TECHNISCHE UNIVERSITÄT MÜNCHEN
Physik Department E21 (Lehrstuhl für Experimentalphysik III)

Investigation of the chiral magnets $NdFe_3(^{11}BO_3)_4$ and MnSi by means of neutron scattering

Dipl. Phys. (Univ.) Marc Janoschek

Vollständiger Abdruck der von der Fakultät für Physik der Technischen Universität München zur Erlangung des akademischen Grades eines

Doktors der Naturwissenschaften (Dr. rer. nat.)

genehmigten Dissertation.

Vorsitzender:	Univ.-Prof. Dr. Andrzej J. Buras
Prüfer der Dissertation:	1. Univ.-Prof. Dr. Peter Böni
	2. Univ.-Prof. Dr. Rudolf Gross

Die Dissertation wurde am 28.7.2008 an der Technischen Universität München eingereicht und durch die Fakultät für Physik am 5.9.2008 angenommen.

Abstract

Recently the field of chiral magnetism gained renewed scientific interest as it was found to be of crucial importance in multiple fields of condensed matter physics. E.g. in the domain of multiferroics helical magnetic order has been successfully identified as driving mechanism for the magneto-electric (ME) effect in several materials like e.g. $RMnO_3$ (with R=Tb, Gd) [KGS$^+$03] and RMn_2O_5 (R=Tb, Dy, Ho) [HPS$^+$04a, HPS$^+$04b] (s. also references [Kim07, CM07]). The ME effect is the coupling of electric and magnetic fields in matter and is therefore interesting both scientifically and as well for technological applications (e.g. sensors, new magnetic memory devices). A further prominent field where chiral magnetism is of current interest are magnetic surfaces or interfaces in layered magnetic systems that naturally break inversion symmetry. The broken inversion symmetry allows for the existence of the Dzyaloshinsky-Moriya interaction [Dzy58, Mor60] that may stabilise helical magnetic order (s. references in [BHvB$^+$07, BR01]). An interesting realisation of such a system is a monolayer of Mn atoms grown on a tungsten (110) substrate. The magnetic moments of the Mn ions in the surface form a magnetic helix as recently observed by Bode *et al.* [BHvB$^+$07] via spin-sensitive scanning tunnelling microscopy (STM). A promising application of chiral magnetism in a two-dimensional system is the construction of a spin field effect transistor(SFET) as it is discussed in reference [HBBB06]. As last example we want to mention the superconductor $CePt_3Si$ in which long-range magnetic order and superconductivity persist simultaneously [BHM$^+$04]. A recent theory developed by Kaur *et al* based on the non-centrosymmetric chemical structure of $CePt_3Si$ claims that the observed magnetic order is possibly helical [KAS05].
Despite the vital interest in chiral magnetism there is still a lack of general concepts that may yield a more collective understanding of the various research topics that are related to chiral magnetism. Therefore it is highly desirable to undertake both further experimental and theoretical studies of systems that display magnetic chirality in order to reveal common properties of chiral magnets. An experimental technique that is highly suitable to investigate chirality in magnetism is neutron scattering. Due to the magnetic moment carried by neutrons the method of neutron scattering generally proves to be a powerful tool to examine magnetic structures and excitations in condensed matter. This is especially true in the case of chiral magnetism, as the use of polarised neutrons provides the unique possibility to directly probe chiral magnetic correlations. Taking advantage of this powerful method we investigated two different magnetic compounds that display magnetic chirality within the framework of this thesis, namely the multiferroic compound $NdFe_3(^{11}BO_3)_4$ and the itinerant helimagnet MnSi.
The compound $NdFe_3(^{11}BO_3)_4$ was recently identified as a multiferroic that shows magnetic field induced ferroelectric phases via the ME effect [ZKK$^+$05, ZVK$^+$06]. It is a member of the family of borates $RM_3(BO_3)_4$ (R = Y,La-Lu, M = Al, Ga, Cr, Fe, Sc) that currently attract much attention because of their special optical properties (e.g. generation of infrared laser action) [Jaq01, HCC$^+$02, CLJ$^+$01] that are important for laser techniques (e.g. for self-frequency-doubling, self-sum-frequency-mixing). Our work

focused on the microscopic magnetic properties and structure that have been investigated only sparsely so far. However, their knowledge is a prerequisite for understanding the ME effect. We investigated the magnetic structure of $NdFe_3(BO_3)_4$ by unpolarised and polarised neutron scattering. As a result of this investigation we identified that $NdFe_3(^{11}BO_3)_4$ orders antiferromagnetically below $T_N = 31$ K. Neutron single crystal and powder diffraction revealed a hexagonal magnetic propagation vector $\boldsymbol{k}^{hex} = [0, 0, \frac{3}{2}]$ corresponding to antiferromagnetic order parallel to the hexagonal c axis. However, below $T_{ICM} \approx 13.5$ K the magnetic structure becomes slightly incommensurate with a propagation vector $\boldsymbol{k}_i^{hex} = [0, 0, \frac{3}{2} + \varepsilon]$ with $\varepsilon(1.6\ K) = 0.00667$. By combined magnetic symmetry analysis and Rietvield fits of the powder diffraction data we identified two magnetic models for the commensurate magnetic phase that fitted our data equally well. By the use of spherical neutron polarimetry we finally revealed that for the correct magnetic model the magnetic moments of both Fe^{3+} and Nd^{3+} are oriented parallel to the basal hexagonal plane and couple antiferromagnetically along the hexagonal c-axis. Additionally the polarised neutron data yields that in the incommensurate magnetic phase below T_{ICM} the magnetic structure is transformed into a long-period antiferromagnetic spiral that propagates parallel to the c-direction with a pitch of approximately 1140 Å. Hence, our investigation clearly showed for the first time that $NdFe_3(^{11}BO_3)_4$ is also a chiral magnet. Furthermore, a high resolution neutron diffraction experiment showed the presence of third order harmonics of the propagation vector in the incommensurate magnetic phase and suggests the evolution of a magnetic soliton lattice below the commensurate to incommensurate phase transition without the application of external forces like magnetic fields or pressure. A soliton is the appearance of localised or topological effects in periodic structures due to the presence of non-linear forces. As the experiment was carried out without the application of external magnetic fields or pressure our results indicate that the antiferromagnetic spiral in $NdFe_3(^{11}BO_3)_4$ is distorted by the magnetic anisotropy in the hexagonal basal plane that was recently reported in reference [TKH$^+$07].

Further we report our work on the cubic itinerant helimagnet MnSi. In zero field the lack of inversion symmetry in MnSi results in a weak Dzyaloshinsky-Moriya interaction, that stabilises a long-wavelength spin spiral with a period of approximately 180 Å along the cubic diagonals below T_c=29.5 K [SCM$^+$83, IEM$^+$85]. Above 6.2 kOe, a ferromagnetic structure is induced, with an ordered magnetic moment of 0.4 μ_B on each Mn site [ISTK77]. Apart from this well understood helical phase MnSi displays a rich magnetic phase diagram showing many peculiarities. This includes a non Fermi-liquid (NFL) phase that was observed above a pressure $p_c \approx 14.6$ kbar [PJL01]. Above p_c a partially ordered magnetic phase was observed using neutron scattering, which revealed strong magnetic scattering intensity on the surface of a sphere in reciprocal space, with a radius corresponding to the modulus of the wave vector of the helical order [PRP$^+$04]. This partial order was interpreted as the unpinning of the helix wave-vector and was found to exist below a characteristic temperature T_0 that vanishes at a pressure $p_0 \approx 21$ kbar. A similar sphere of magnetic scattering is also observed at ambient pressure at $T \gtrsim T_c$ [GMO$^+$05]. Recent theoretical studies by Roessler *et al.* [RBP06] suggest that the Dzyaloshinsky-Moriya interaction may not only stabilise simple helical order, but even more complex

multidimensional, magnetic textures, when the amplitude of the local magnetisation is soft and supports strong longitudinal fluctuations, e.g. near critical phase transitions. It was speculated that the observed magnetic scattering on the sphere at $T \gtrsim T_c$ in MnSi originates from such a magnetic texture. However, Grigoriev *et al.* have interpreted this experimental result as critical scattering from a helimagnet [GMO$^+$05]. We carried out extensive unpolarised and polarised elastic neutron scattering experiments in the temperature regime where the sphere of magnetic intensity is observed in order to clarify the issue of a possible intermediate phase. Our data suggests that the cubic anisotropy energy that locks the direction of the helix decreases significantly above T_c and therefore supports the scenario that the propagation vector of the helix unlocks when the sphere is observed. Further, the fits of the data indicate that the observed magnetic intensity on the sphere can be interpreted as critical scattering of a helimagnet as proposed in [GMO$^+$05].
In addition we have carried out extensive measurements of the dynamical magnetic susceptibility in the helically ordered phase by means of inelastic neutron scattering. Startlingly, despite the extensive measurements of the collective magnetic excitations in the field induced ferromagnetic phase, relatively little attention has been given to the helical phase. For the helical magnetic phase a novel magnetic excitation spectrum has been suggested independently by two theory groups [BKR07, Mal06]. The proposed magnetic excitations emerge in the helical phase as new Goldstone modes - the so-called *helimagnons*. Both groups find an anisotropic dispersion with soft modes linear in q parallel to the propagation vector $\boldsymbol{k}$ and quadratic in q perpendicular to it for small wave vectors near the helical propagation vector. In our measurements we effectively identified a new type of magnetic excitations that show an anisotropic dispersion that is very similar to the prediction by theory. Therefore our results clearly support the existence of the proposed helimagnons.

Acknowledgements

Throughout the different projects of my thesis work I was accompagnied by many people at various places and institutions. Without their advice, guidance and often friendship this work would have certainly suffered. I want to thank:

Prof. Peter Böni for welcoming me at his chair E21 of the Technische Universität München and for giving me the opportunity to continue with the MuPAD project. Thank you for your steady support and the interesting discussions we had. I enjoyed the freedom you offered me for my work.

Dr. Bertrand Roessli for providing me with deep insight in the method of neutron scattering. I really appreciate your constant advice and support, especially with respect to the analysis of our spherical neutron polarimetry results. Also I enjoyed sharing the hobby of photography with you and thus to exchange new pictures and also information about new soft- and hardware.

Prof. Dr. Joel Mesot for welcoming me in the Laboratory for Neutrons Scattering at the Paul Scherrer Institut and for supporting my research work.

Prof. Dr. Christian Pfleiderer for providing me with detailed information and background on MnSi. Your constant input during the discussions about my experimental result was more than helpful. Thanks also for your interest and help concerning the progress of my scientific career.

Dr. Serguei Klimko for the extraordinary work he did by constructing the new version of MuPAD. Without this work parts of my experimental work would have been impossible. It was a real pleasure to continue our colloboration that started during my diploma thesis.

Dr. Murat Ay for helping me on many occasions during work but even more often you were there to listen to me when I went through personal difficulties. You are a real friend and example. Also I am indepted to you for the hospitality you offered me during many stays at the PSI what prevented me from living in the PSI guest house.

Dr. Severian Gvasaliya for helping me throughout many experiments I performed at the PSI and also at the ILL. Thanks for many advices of both professional and

private character. I enjoyed the experiments with you as much as our unfortunetely rare shared private activities.

Dr. Peter Fischer for his deep involvement into the $NdFe_3(BO_3)_4$ project. Your help and advice are kindfully acknowledged. Also I am indepted to your wife and you for the excellent introduction into the gastronomic specialties of Switzerland.

Prof. Dr. Jane Brown for sharing your expert knowledge about spherical neutron polarimetry and magnetic symmetry analysis with me. I appreciate that you were answering my continous questions with detail.

Prof. Dr. Guerman Petrakovskii for providing the $NdFe_3(^{11}BO_3)_4$ crystals.

Dr. Vladimir Pomjakushin for his help and advice concerning magnetic symmetry analysis.

Dr. Ekaterina Pomjakushina for helping me many times to prepare the samples for the experiments.

Florian Bernlochner who worked on the MnSi project as a diploma student. Thanks for the effort and interest you put this research project. It was a pleasure to work with you; I enjoyed our interesting and frequent discussion that were never only limited to physics.

Dr. Sarah Dunsiger for many interesting conversations about physics in general and MnSi specifically. Thanks for your support at many occasions during the last year and also for proofreading this manuscript.

Sebastian Mühlbauer who was always happy to discuss with me about many details of the MnSi experiments. Thanks for introducing me into the treatment of SANS data. Also I enjoyed very the bike tours we did together.

Prof. Dr. Serguei V. Maleyev, Prof. Dr. Achim Rosch & Dr. Benedikt Binz for their theoretical support and input concerning the inelatistic measurements on MnSi.

My collaborators for their support during the experiments that were carried out at three different european neutron sources. Thanks to Sebastian Mühlbauer, Peter Link, Astrid Schneidewind, Lukas Keller, Juerg Schefer, Thomas Keller, Robert Georgii, Martin Boehm and Oksana Zaharko. I also enjoyed the numereous discussions with all you guys during the experiments but also on conferences and meetings.

Dr. Marc Koennecke & Jens Krüger for their work to integrate the MuPAD control routines into the control software of TASP at PSI and MIRA and FRM-II, respectively.

The technical staff at the different institutions and intruments where I performed the experiments for this work. Without the support of the numereous engineers and

technicians many of my experiments would not have been possible. I want to especially mention Walter Latscha, Stefan Fischer, Peter Keller, Roman Bürge, Andreas Mantwill, Reinhard Schwikowski, Eric Bourgeat-Lami, Sebastien Vial and Dirk Etzdorf.

All the people who shared an office with me both at the Paul Scherrer Institut and at the TU München. I enjoyed the nice working atmosphere and many interesting conversations we shared. Thanks to Sabine, Verena, Jay, Beni, Konradin, Sebastian, Shah and Christoph.

All the people of E21 who created a very nice and productive working environment. Special thanks to Barbara for providing the 'female touch' to the institute.

My Roommates for the very nice time we shared while I stayed in Zurich. Thanks to Urs, Arne, Frank, Erich, Tom and Stefan.

My Family not only for supporting me during my whole life but most of all for providing me the freedom and encouragement to realize my own ideas.

My friends Ruben, Doms, Matthias and Jochen, Frank und Eva, Lucija and Marion who provided me with their strong and constant friendship ever since. You supported me in many occasion, each one of you in his own unique way. Thanks for many inspiring conversation, advices, encouragments and the awesum times we shared.

Aude No of course I did not forget you. One should keep the best for the end. Thanks for your love and your understanding. You are a constant source of inspiration and despite the large physical distance between us you were always there when I had to encouter difficult times.

Table 1: Physical constants

Quantity	Name	Value (Unit)
m_n	neutron mass	$1.675{\cdot}10^{-27}$ (kg)
m_p	proton mass	$1.673{\cdot}10^{-27}$ (kg)
m_e	electron mass	$9.109{\cdot}10^{-31}$ (kg)
e	elementary charge	$1.602{\cdot}10^{-19}$ (C)
$\hbar$	Planck constant over 2π	$6.582{\cdot}10^{-16}$ (eV s)
μ_B	Bohr magneton	$9.274{\cdot}10^{-24}$ (J $T^{-}1$)
μ_N	nuclear magneton	$5.051{\cdot}10^{-27}$ (J $T^{-}1$)
μ_0	vacuum permeabilty, magnetic constant	$1.256{\cdot}10^{-6}$ (V s $A^{-}1$ $m^{-}1$)
r_0	classical electron radius	$2.82{\cdot}10^{-15}$ (m)
γ	gyromagnetic ratio of the neutron	1.913 (-)

Table 2: Notation for most imortant physical quantities that were used throughout this thesis work.

Notation	Name
$\boldsymbol{k}_i$, $\boldsymbol{k}_f$	incident and final wave vector of the neutron
$\boldsymbol{Q}$	scattering vector
$\hbar\omega$	energy transfer
$V(\boldsymbol{r})$	neutron scattering potential
b_d	nuclear scattering length of nucleus d
$N_{\boldsymbol{Q}}$	nuclear structure factor
$\boldsymbol{l}$	lattice vector
$\boldsymbol{\tau}$	reciprocal lattice vector
$\exp(-W_d(\boldsymbol{Q}))$	Debye-Waller factor of ion d in unit cell
$F_N(\boldsymbol{Q})$	nuclear unit cell structure factor
$\hat{\boldsymbol{\sigma}}$	Pauli matrices
$\boldsymbol{M}_{\perp\boldsymbol{Q}}$	magnetic interaction vector
$F_d(\boldsymbol{Q})$	magnetic form factor of magnetic ion d
$\boldsymbol{S}_{ld}$	magnetic moment of magnetic ion (l, d)
$\boldsymbol{k}$	magnetic propagation vector
$\boldsymbol{S}_{i\lambda}^{\boldsymbol{k}\nu}$	magnetic Fourier component
$\boldsymbol{P}_0$, $\boldsymbol{P}'$	incident and final polarisation vector
P_{ij}	polarisation tensor
Γ^{ν}	irreducible representation (IR) ν
$\Psi_{\lambda}^{\boldsymbol{k}\nu}$	magnetic basis function for IR ν
$\boldsymbol{S}_{d\lambda}^{\boldsymbol{k}\nu}$	magnetic Fourier component for IR ν and ion d
$\chi_{\alpha\beta}(\boldsymbol{Q}, t)$	magnetic dynamic susceptibility

Contents

Acknowledgements **v**

Tables of physical quantities **viii**

1 Motivation: Chirality and Magnetism **1**
1.1 Chirality . . . 3
1.1.1 Definition of chirality . . . 3
1.1.2 Spins and chiral symmetry . . . 4
1.2 Chiral magnetism . . . 4
1.2.1 The Dzyaloshinsky-Moriya interaction . . . 6
1.2.2 The Bak-Jensen model . . . 8
1.2.3 Magnetic frustration and chirality . . . 11
1.3 Chiral magnetism, 'quo vadis'? . . . 12
1.3.1 Chiral universality class . . . 13
1.3.2 Magnetic surfaces and interfaces . . . 14
1.3.3 Magneto-electric effect . . . 15
1.3.4 Helical Goldstone modes and skyrmion condensate in MnSi . . . 17
1.3.5 Summary . . . 19

2 Neutron scattering **21**
2.1 The neutron scattering cross-section . . . 22
2.2 Nuclear scattering . . . 23
2.2.1 The Fermi pseudopotential . . . 23
2.2.2 Coherent and incoherent scattering . . . 24
2.2.3 Bragg scattering from crystals . . . 25
2.3 Magnetic scattering . . . 27
2.3.1 The magnetic scattering potential . . . 27
2.3.2 The magnetic selection rule . . . 29
2.3.3 Magnetic form factors . . . 30
2.3.4 Magnetic correlation functions . . . 32
2.3.5 Magnetic Bragg scattering . . . 33
2.3.6 Inelastic magnetic scattering . . . 34

2.4 Polarized neutron scattering . . . 36
2.4.1 Polarisation of a neutron beam . . . 36
2.4.2 The Blume-Maleyev equations . . . 38
2.4.3 Polarised neutron scattering on chiral magnets . . . 42
2.4.4 Experimental polarisation . . . 46
2.5 MuPAD . . . 48

3 Magnetic symmetry analysis **53**
3.1 Group theory . . . 53
3.1.1 Definition of groups . . . 53
3.1.2 Irreducible representations . . . 54
3.2 Magnetic representation analysis . . . 55
3.2.1 The propagation vector . . . 56
3.2.2 The little group . . . 56
3.2.3 The magnetic representation . . . 58
3.3 Magnetic Domains . . . 60
3.3.1 Configuration domains . . . 60
3.3.2 180° domains . . . 61
3.3.3 Orientation domains . . . 62
3.3.4 Chirality domains . . . 62

4 Single chirality in the multiferroic $NdFe_3(BO_3)_4$ **65**
4.1 Basic properties . . . 66
4.1.1 Crystal structure . . . 66
4.1.2 Magnetic properties . . . 66
4.1.3 Magneto-electric effect . . . 68
4.2 Experimental work and results . . . 69
4.2.1 Sample preparation . . . 69
4.2.2 Chemical structure refinement . . . 70
4.2.3 Bulk measurements . . . 72
4.2.4 Investigation of the magnetic structure by neutron diffraction . . . 72
4.2.5 Spherical Neutron Polarimetry . . . 89
4.3 Discussion . . . 101

5 The Helimagnet MnSi **107**
5.1 Properties . . . 107
5.1.1 Chemical and magnetic structure . . . 107
5.1.2 Non-Fermi-liquid phase and partial magnetic order . . . 109
5.1.3 Possible intermediate phase and specific heat . . . 113
5.1.4 Magnetic excitations . . . 114
5.2 Theoretical models . . . 117
5.2.1 Intermediate magnetic phase and skyrmions . . . 117
5.2.2 Critical scattering above T_c . . . 119

5.2.3 Goldstone modes in the helical phase . . . 121
5.3 Experimental work and results . . . 126
5.3.1 Samples used for the investigation . . . 127
5.3.2 Investigation of the possible intermediate phase by SANS . . . 127
5.3.3 Spherical neutron polarimetry above T_c . . . 141
5.3.4 Investigation of the helical Goldstone modes . . . 151
5.4 Discussion . . . 159

6 Conclusion and Outlook **163**

Appendix **167**

A Neutron scattering instruments **167**
A.1 Powder diffractometer . . . 167
A.2 Single crystal diffractometer . . . 167
A.3 Triple-axis spectrometer . . . 169
A.4 Small angle neutron scattering . . . 170

B Useful mathematical relationships concerning the neutron polarisation 173
B.1 Statistical errors and background . . . 173
B.2 Relationships between the polarisation, flipping ratio and polarisation efficiency . . . 174

C Final polarisation due to the critical scattering in MnSi **177**

D The neutrons python package **181**
D.1 spfit . . . 183
D.2 tasresfit . . . 184

E Publications **189**

Bibliography **191**

Chapter 1

Motivation: Chirality and Magnetism

Chirality is a property widely spread among entities in nature. The expression chirality itself is derived from the Greek root $\chi\varepsilon\iota\varrho$ (*kheir*) that signifies hand. Looking at our pair of hands we recognise immediately that the left hand is different from the right one. Imagining that we had a left hand instead of our right one that difference becomes even more significant: we would not be able to shake hands with other human beings. However, despite this significant difference between our left and right hand, they also have something in common, they are both hands, e.g. there is no obvious relationship between our right hand and left foot! The special relationship between our two *different* hands is easily understood if we look at their mirror image. In the mirror our right hand becomes a left hand and vice versa as demonstrated in Fig. 1.1(a). Therefore, the mirror image of one of our hands can not be superimposed with the original hand. This is actually the general definition for handedness or chirality. An object that can be superimposed to its mirror image is then called achiral, e.g. a simple bottle.
Already in our every day life we are sourrounded by many objects that are chiral, e.g. screws, or the piglets' tails or snail shells shown in Fig.1.2. However, it turns out that chirality is not only a mere geometrical property but a feature that proved to be of critical importance in major scientific fields. Here we give some selected examples:

- Material science: Carbon nanotubes are tubes that are produced by rolling up monoatomic layers of graphite into tubes. By different choices of the direction along which the tube is rolled up chiral or achiral carbon nanotubes can be produced, respectively. It emerges that several physical properties of carbon nanotubes are completely different if the tube is chiral or not. E.g. the electrical conductance of chiral nanotubes is similar to metals whereas the achiral counterparts behave like semiconductors [SDD98].

- Biology & chemistry: molecules that exist in a left-handed and a right-handed

version are called enantiomers. In ordinary chemical reactions both behave similar, however, when interacting with other chiral objects they behave different depending on their chirality. E.g. many substances used as drugs are chiral; in some cases they only work when the substance is provided in the proper chirality state but often the substance is even toxic when provided with the wrong chirality . Examples for such chiral drugs are penicillin and ethambutol [FL06, wik]. In 2001 the Nobel price for chemistry was assigned to William S. Knowles, Ryoji Noyori and K. Barry Sharpless for their work on chiral catalysts that allow for the production of enantiomers in one pure chirality state [nob01]. Obviously this technique is an important prerequisite for the production of chiral drugs.

- Physics: The weak interaction breaks the conservation of parity as it was shown by Chien-Shiung Wu via the measurement of the directionality of emitted electrons in the β-decay $^{60}_{27}\mathrm{Co} \longrightarrow ^{60}_{28}\mathrm{Ni} + e^- + \overline{\nu}_e$ with respect to the direction of the nuclear Co-spins [WM66]. This experiment showed that all neutrinos have their spins always antiparallel to their direction of movement whereas for antineutrinos the contrary is true. Thus all existing neutrinos are left-handed. Tsung-Dao Lee and Chen Ning Yang who developed the theory for the weak interaction that explains the experimental result received the Nobel price for this achievement in 1957 [nob57].

In this work chirality in magnetism was investigated for selected samples. In this chapter we will first give a proper scientific definition of chirality. Further this property will be introduced into magnetism and a brief historic overview over chirality in magnetism will

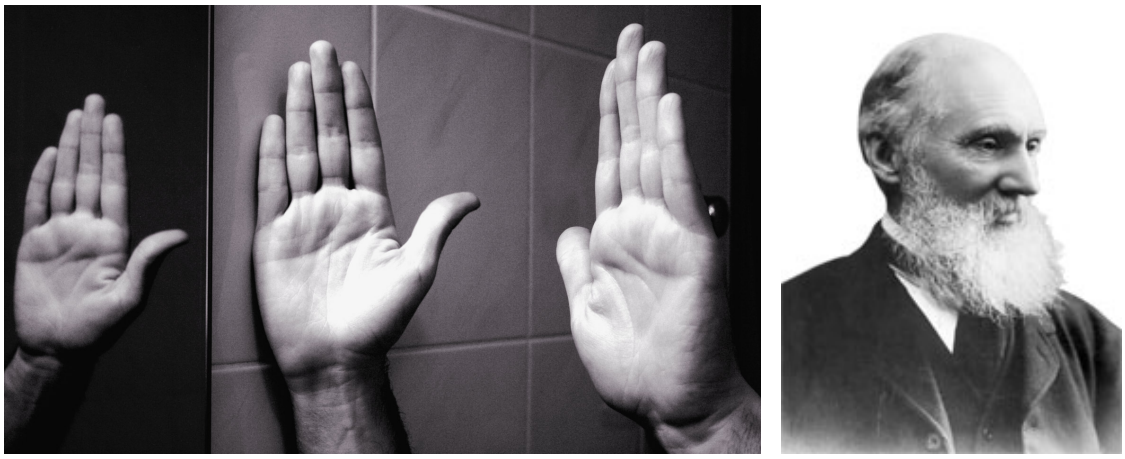

(a) (b)

Figure 1.1: (a) The left (right side of photograph) and right hand (centre) of the author are shown together with the mirror image of his left hand (left side). It is immediately clear that the mirror image of the left hand is similar to the right hand. However, the mirror image of the left hand, namely the right hand cannot be superposed with the original left hand. Thus, our hands are chiral objects. (b) A photograph of Lord Kelvin who defined the property *chirality* for the first time.

(a) (b)

Figure 1.2: Chiral objects in our daily life.

be given. We will conclude the chapter with a set of examples to illustrate the importance of chirality in magnetism that was a major motivation for this work.

1.1 Chirality

1.1.1 Definition of chirality

The first scientific definition of *chirality* goes back on Lord Kelvin (s. Fig. 1.1(b)). In 1884 he stated in the Baltimore Lectures [Kel04]:

> I call any geometrical figure, or group of points, *chiral*, and say that it has chirality, if its image in a plane mirror, ideally realised, cannot be brought to coincide with itself.

Here he also introduced the expression *chirality* for the first time. A demonstration of this statement is shown in Fig. 1.1(a) for the hands of this author. A mathematically more strict definition that is commonly used today is (e.g. [Bar86]):

> An object is chiral if it cannot be transformed into itself by any improper rotation.

An improper rotation is any proper n-fold rotation about an axis followed by an inversion operation [1] where the point of inversion is a point on the rotation axis. Such a symme-

[1] An inversion operation in a Cartesian coordinate frame with respect to the origin is the transformation (x,y,z) $\longmapsto$ (-x,-y,-z). In physics this symmetry transformation is generally referred to as *parity*.

try operation is called a rotoinversion operation [2]. An improper rotation of an object generates a rotation of its mirror image. We note that the mirror reflection Lord Kelvin used in his defintion is equivalent to a rotoinversion where the angle of rotation is 180° and therefore a special case of our more recent definition.

1.1.2 Spins and chiral symmetry

Special care has to be taken when vectors instead of point like objects are transformed by improper rotations. There are two type of vectors with respect to improper rotation. This is most easily seen if we consider a physical quantity like the angular momentum of a particle at position $\boldsymbol{r}$ that moves with momentum $\boldsymbol{p}$. Thus the angular momentum of the particle will be

$$\boldsymbol{L} = \boldsymbol{r} \times \boldsymbol{p}. \tag{1.1}$$

This is shown in Fig. 1.3. Now we apply an inversion symmetry operation to the particle. The position of the particle after the transformation will be $\boldsymbol{r}' = -\boldsymbol{r}$ and its momentum will be $\boldsymbol{p}' = -\boldsymbol{p}$. If we consider the angular momentum after the transformation we get:

$$\boldsymbol{L}' = \boldsymbol{r}' \times \boldsymbol{p}' = (-\boldsymbol{r}) \times (-\boldsymbol{p}) = \boldsymbol{r} \times \boldsymbol{p} = \boldsymbol{L}. \tag{1.2}$$

Hence, the angular momentum of the particle does not change its sign under the inversion transformation whereas its position and momentum do. This is explained in a more descriptive fashion in Fig. 1.3. Vectors that do not change their sign under a inversion operation are called *pseudovectors* or *axial vectors*. In the more general context of all improper rotations a pseudovector is defined as a quantity that transforms like a vector under a proper rotation, but gains an additional sign flip under an improper rotation. All vectors that behave like usual vectors under both proper and improper rotations are called *true* or *polar vectors*.
For this work this is rather important as we deal with chirality in magnetism. Magnetic fields in condensed matter systems are mainly generated by the angular momentum and spins of unpaired electrons that are both pseudovectors.

1.2 Chiral magnetism

Magnetic fields in a crystal are mainly generated by the spins and angular momenta of unpaired electrons of magnetic ions. In order to establish a specific arrangement of the

[2] Equivalently an improper rotation also can be defined as any normal rotation about an axis followed by a mirror reflection with the mirror plane perpendicular to the rotation axis. Such a symmetry operation is called rotoreflection. However, rotoinversions and rotoreflections are identical if they differ in the angle of rotation by 180°, and the point of inversion is in the plane of reflection. Therefore any rotoreflection can be mapped to a rotoinversion.

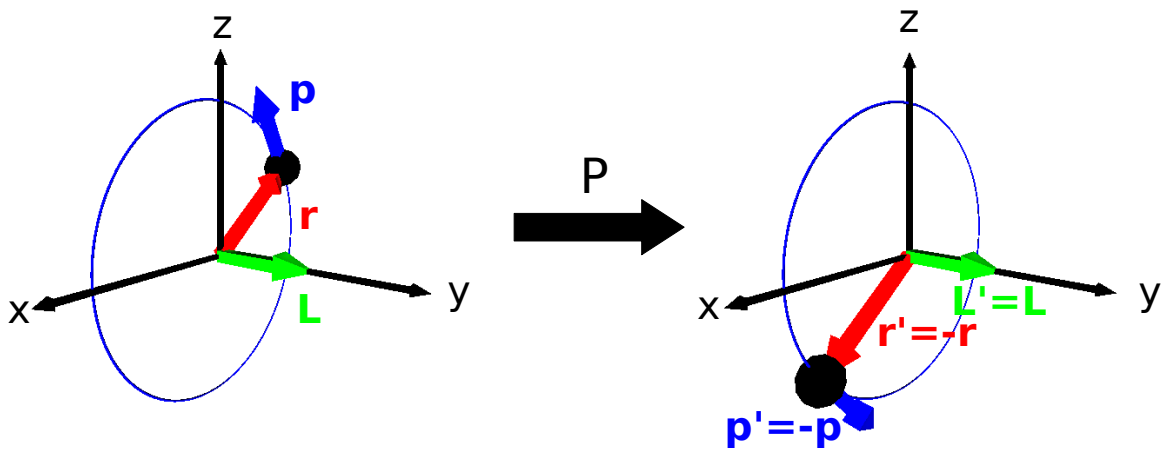

Figure 1.3: In the left viewgraph a particle at position $\boldsymbol{r}$ (red arrow) and with momentum $\boldsymbol{p}$ (blue arrow) is shown. Further the angular momentum of the particle is shown by the arrow in green. The right viewgraph shows the same particle after a parity transformation (inversion) P was applied to it. We immediately see that the positional vector and the momentum of the particle have changed their sign but the sign of the sense of the rotation of the particle remained unchanged. Thus the angular momentum of the particle did not change its sign under the parity transformation. A vector that does not change its sign under improper rotations (thus including the parity transformation) is called a *pseudovector*.

magnetic moments carried by these spins and angular momenta two conditions have to be fulfilled:

- the arrangement of the magnetic moments has to be in agreement with the symmetry of the underlying atomic crystal structure, e.g. the symmetry of the magnetic configuration has to be equivalent or lower than the crystal symmetry (we will consider this fact in more detail in chapter 3).

- the competition of different interactions in the crystal must lead to a minimum in the free energy that stabilises this specific magnetic configuration.

From the definition of chirality in section 1.1.1 we immediately see that for a chiral arrangement of magnetic moments we need to break any improper rotation symmetries. If we imagine the most obvious chiral spin arrangement it will be a magnetic spiral as it is shown in Fig. 1.4. In order to comply with the above conditions a further term in the free energy is required that favours a canted spin arrangement between neighboring moments.

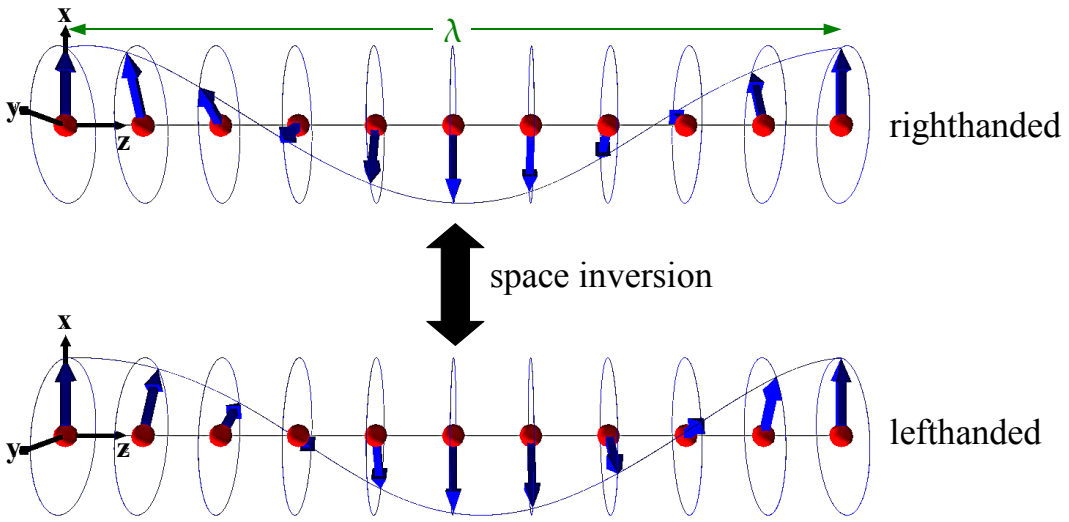

Figure 1.4: A magnetic helix is shown. Such a magnetic ordering is obviously chiral when the definition of section 1.1.1 is applied as shown by the inversion symmetry operation. We note that neighboring moments are mutually canted.

1.2.1 The Dzyaloshinsky-Moriya interaction

The usual magnetic Heisenberg exchange or superexchange [Hei28, And59] interactions described by the Hamiltonian

$$H = J\boldsymbol{S}_i\boldsymbol{S}_j, \tag{1.3}$$

that drive magnetic long range ordering, obviously lead to parallel or antiparallel alignment of neighboring moments depending on the sign of the exchange integral J, as 1.3 is minimal for these spin arrangements. Hence, an additional type of interaction would be necessary to stabilise a magnetic structure like in Fig. 1.4. In 1958 Dzyaloshinksy published an article about his PhD thesis work that reported a phenomenological derivation of a term in the free energy that was able to explain the effect of observed weak ferromagnetism in certain otherwise antiferromagnetic crystals like e.g. Hematite (α-Fe_2O_3)[Dzy58]. This effect might seem unrelated to our problem of chiral magnetic ordering at first sight but as we will see immediately it is closely connected. The weak ferromagnetism in antiferromagnets was a major problem during this period. The observed ferromagnetic moments in these compounds were extremely small and were experimentally found to vary between the limits of 10^{-2}-10^{-5} of the nominal values. The smallness of the spontaneous ferromagnetic moment, however suggested that usual exchange ferromagnetism could not be the source of the observed behaviour. In his work Dzyaloshinsky showed that for Hematite the antiferromagnetic spin arrangement had exactly the same symmetry as a different spin arrangement with mutually canted spins. Then he derived all possible terms in the free energy depending on the spin variables that were consis-

tent with the symmetry class he found before. He was able to prove that one of these terms favours the canted spin arrangement over the antiferromagnetic one and thus is a prerequisite for the observed weak ferromagnetism. The term found by Dzayloshinsky is

$$\boldsymbol{D}(\boldsymbol{S}_i \times \boldsymbol{S}_j), \tag{1.4}$$

where $\boldsymbol{D}$ is a constant vector. Obviously, an interaction between two neighboring spins that would lead to a term like in Eq. 1.4 in the free energy that favours spin canting would also be a good candidate to explain a magnetic spiral like the one in Fig. 1.4. However, Dzyaloshinsky did not clarify the nature of the vector $\boldsymbol{D}$ and how it could be derived.
In 1960 Moriya [Mor60] extended the Anderson theory [And59] for superexchange to include spin-orbit coupling that had been neglected so far. Moriya identified Eq. 1.4 found by Dzyaloshinsky from symmetry arguments as the antisymmetric part[3] in his new model of anisotropic superexchange. As Eq. 1.4 was introduced by Dzyaloshinsky in a phenomenological approach and was identified later by Moriya as a relativistic correction of the superexchange interaction due to spin-orbit coupling it is now commonly known as *Dzyaloshinsky-Moriya interaction* (DMI).
In his publication Moriya also calculated an estimate for the strength of the DMI to be of the order of $(\Delta g/g)$ times the isotropic superexchange interaction, where g is the Landé g-factor and Δg is the deviation from the value for a free electron. Apart from this consideration about the magnitude of $\boldsymbol{D}$, that is generally referred to as *Dzyaloshinsky-Moriya vector* (DM vector), he additionally emphasised that (as Dzyaloshinsky already pointed out) the crystal symmetry is of particular importance for the asymmetric coupling 1.4 as it vanishes in crystals of high symmetry. He considered two single magnetic ions 1 and 2 that are located at the positions A and B, respectively. The point bisecting the straight line AB is denoted as C. He summarised the following symmetry rules:

1. When a centre of inversion is located at C,

$$\boldsymbol{D} = 0.$$

2. When a mirror plane perpendicular to AB passes through C,

$$\boldsymbol{D} \parallel \text{mirror plane or } \boldsymbol{D} \perp \text{AB}.$$

3. When there is a mirror plane including A and B,

$$\boldsymbol{D} \perp \text{mirror plane}.$$

4. When a two-fold rotation axis perpendicular to AB passes trough C

$$\boldsymbol{D} \perp \text{two-fold axis}.$$

5. When there is a n-fold rotation axis ($n \geq 2$) parallel AB

$$\boldsymbol{D} \parallel \text{AB}.$$

[3] antisymmetric under exchange of two spins

When thinking of the definition of chirality in section 1.1.1 it seems natural at first sight that an inversion centre situated in the centre between two spins does not allow the DMI to be present, as inversion is also an improper rotation. We note, however, that Moriya's symmetry rules do not prohibit the presence of neither an inversion centre nor any other improper rotation in the crystal symmetry as they only constrain the symmetry elements that are present in the environment of the two spins that are considered. In other words this means that the presence of the DMI in a magnetic crystal does not necessarily lead to a global chiral magnetic ordering like e.g. the magnetic spiral in Fig. 1.4.

1.2.2 The Bak-Jensen model

Let us consider a real crystal of simple cubic structure, and therefore only one magnetic ion (and magnetic moment) per crystallographic unit cell. If we now assume the magnetic structure to be a magnetic spiral like in Fig. 1.4 we recognise that the periodicity of the lattice (distance between two neighbouring spins) and the magnetic structure are very different: we have to translate through 10 crystallographic unit cells until the magnetic moment is oriented along the same direction as at the starting point. The helical spin arrangement could be thought of as ten different magnetic sublattices where in each of them the moments are rotated about a certain angle $\frac{2\pi}{\lambda}a$ (λ is the period of the helix and a the lattice constant of the cubic crystallographic lattice) around the helix axis and therefore this model is still similar to antiferromagnetic sublattices as in a Néel state only that the period is longer and hence the number of sublattices is bigger (In a Néel state λ would be equal to 2a which is equivalent to two sublattices).
However, we also could image a long period spiral where the magnetic lattice does not match the period of the crystal lattice at all even if we would translate through an infinite number of unitcells. Such a structure is called *incommensurate* with respect to the underlying lattice and is shown in Fig. 1.5. In 1959 Villain [Vil59], Kaplan [Kap59] and Yoshimori [Yos59] independently came up with the idea that such an incommensurate long period superstructure would be possible in antiferromagnetic substances. All of them based their considerations on the symmetric part of the (super-)exchange interaction in Eq. 1.3. Dzyaloshinsky showed in 1964 [Dzy64] that such an incommensurate long period magnetic arrangement is only possible when the DMI is included in order to destabilise the (anti-)ferromagnetic order that is favoured by the exchange interactions. Additionally the crystal has to lack an inversion centre. But there was no real magnetic system for which it could be shown that the mechanism proposed by Dzyaloshinsky was the origin of helical incommensurate long range magnetic ordering.
In 1980 Bak and Jensen [BJ80] were able to explain the long-period ferromagnetic spiral ($\lambda \approx 180$ Å) found experimentally by Ishikawa *et al* [ITBR76] in the itinerant weak ferromagnet MnSi by including the DMI in the free energy. MnSi crystallises in the cubic $P2_13$ structure that possesses no inversion centre. According to the theory of phase transitions of Landau and Lifshitz they expanded the free energy in terms of a slow-varying spin

density $\boldsymbol{S}(\boldsymbol{r})$ that is in agreement with the symmetry of MnSi:

$$\begin{aligned} F(\boldsymbol{r}) &= \frac{1}{2}A(S_x^2+S_y^2+S_z^2)+D\boldsymbol{S}(\nabla\times\boldsymbol{S})+\frac{1}{2}B_1[(\nabla S_x)^2+(\nabla S_y)^2+(\nabla S_z)^2]+ \\ &+ \frac{1}{2}B_2[(\frac{\partial S_x}{\partial x})^2+(\frac{\partial S_y}{\partial y})^2+(\frac{\partial S_z}{\partial z})^2]+\frac{1}{2}C(S_x^2+S_y^2+S_z^2)^2+ \\ &+ \frac{1}{2}E(S_x^4+S_y^4+S_z^4) \end{aligned} \tag{1.5}$$

Here the term A is the ferromagnetic exchange energy, the term D represents the DMI and B_1 and B_2 are first and second order anisotropy terms. Near to T_c the free energy is then usually minimised by periodic structures of the form

$$\boldsymbol{S}(\boldsymbol{r}) = \frac{1}{\sqrt{2}}[\boldsymbol{S}_{\boldsymbol{k}}\exp(i\boldsymbol{k}\boldsymbol{r})+\boldsymbol{S}_{\boldsymbol{k}}^*\exp(-i\boldsymbol{k}\boldsymbol{r})]. \tag{1.6}$$

By substituting Eq. 1.6 into Eq.1.5 we get (to second order in $\boldsymbol{S}_{\boldsymbol{k}}$)

$$\begin{aligned} F(\boldsymbol{k}) &= \frac{1}{2}A|\boldsymbol{S}_{\boldsymbol{k}}|^2+iD\boldsymbol{k}(\boldsymbol{S}_{\boldsymbol{k}}\times\boldsymbol{S}_{\boldsymbol{k}})+\frac{1}{2}B_1k^2|\boldsymbol{S}_{\boldsymbol{k}}|^2+ \\ &+ \frac{1}{2}B_2(k_x^2|\boldsymbol{S}_{\boldsymbol{k}_x}|^2+k_y^2|\boldsymbol{S}_{\boldsymbol{k}_y}|^2+k_z^2|\boldsymbol{S}_{\boldsymbol{k}_z}|^2). \end{aligned} \tag{1.7}$$

By choosing $\boldsymbol{S}_{\boldsymbol{k}} = a_{\boldsymbol{k}} + ib_{\boldsymbol{k}}$ Eq. 1.7 can be minimised when $a_{\boldsymbol{k}} \perp b_{\boldsymbol{k}}$, $|a_{\boldsymbol{k}}| = |b_{\boldsymbol{k}}|$ and $\boldsymbol{k}$ parallel or antiparallel to $a_{\boldsymbol{k}} \times b_{\boldsymbol{k}}$ for $D < 0$ or $D > 0$, which describes a left- and right-handed spiral, respectively. As the D term has full rotational symmetry it does not give any preferred direction for the wavevector $\boldsymbol{k}$. However, it can be fixed by the anisotropic second order term with the coefficient B_2:

$$B_2 < 0 \quad : \quad \boldsymbol{k} \parallel (111) \tag{1.8}$$

$$B_2 > 0 \quad : \quad \boldsymbol{k} \parallel (001). \tag{1.9}$$

On the basis of the experimental results [ITBR76] it was concluded for B_2 in MnSi that $B_2 < 0$ and that it is relatively small in magnitude as the wavevector can experimentally

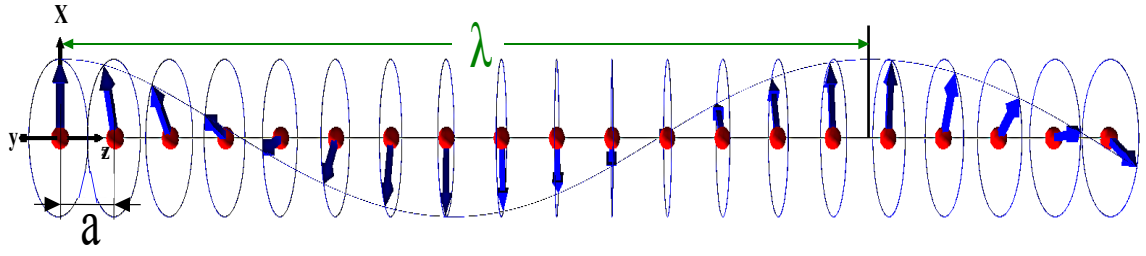

Figure 1.5: A magnetic helix that is incommensurate with respect to the underlying crystal lattice, the lattice periodicity λ of the helix can not be expressed as n times the lattice spacing a.

be moved into any direction by applying a magnetic field. The free energy is then finally described by

$$F(k) = (\frac{1}{2}A - |D|k)|\boldsymbol{S_k}|^2 + (\frac{1}{2}B_1 + \frac{1}{6}B_2)k^2|\boldsymbol{S_k}|^2 \tag{1.10}$$

which is minimised by

$$k = |D|/(B_1 + \frac{1}{3}B_2). \tag{1.11}$$

The long period of the magnetic spiral in MnSi (equivalent to a small magnitude of $\boldsymbol{k}$) then follows from the smallness of D compared to $B_1 + \frac{1}{3}B_2$. In Fig. 1.6 the free energy of Eq. 1.10 is plotted versus k and shows clearly that the ferromagnetic structure with $k = 0$ is unstable. For comparison, the free energy for systems without inversion symmetry (D=0) is also shown (dashed line). We want to point out that a left- and a right-handed magnetic spiral are energetically degenerate. This is immediately clear from Fig. 1.6. However, this means that a further interaction is needed to lift this degeneracy in order to get a system that is completely left- or right-handed. Otherwise this degeneracy must lead to left- and right-handed domains.
The model we described above can be considered as the standard model of long period ferromagnetic helices driven by the DMI and is often referred to as the Bak-Jensen-Model for helical magnetic structures.

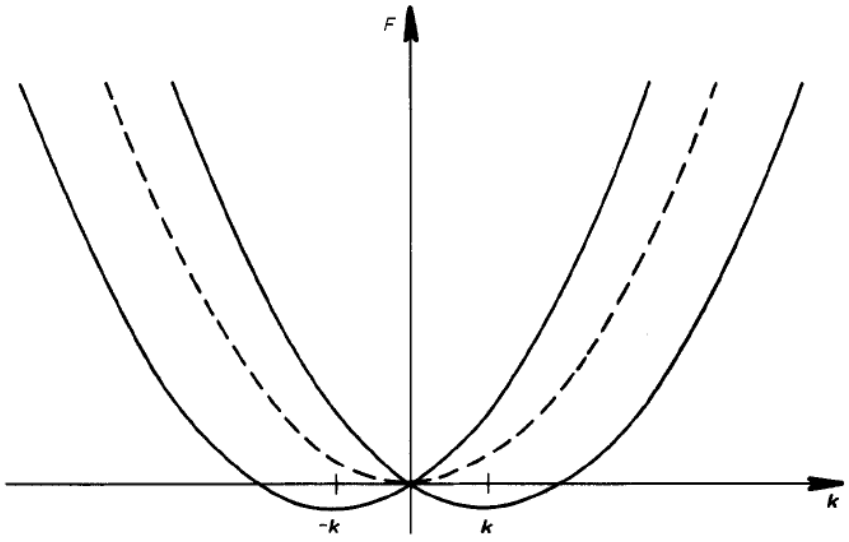

Figure 1.6: Free energy as a function of wavevector k for left-handed and right-handed spirals. The dashed line shows the free energy for a system with inversion symmetry (D=0). The figure is taken from [BJ80].

1.2.3 Magnetic frustration and chirality

There is another possibility that leads to chirality in magnetism that does not involve the DMI. If we consider spins that are located on a triangular lattice this leads to a *frustrated* magnetic order. This is explained in Fig. 1.7(a) that shows a triangular lattice in two dimensions with spins on each corner of the triangle. When the magnetic interaction between neighboring spins is antiferromagnetic there is no solution that allows all three spins to be aligned antiparallel with both of its neighbours. This is called *magnetic frustration*. In order to minimise their magnetic energy the spins tend to align in a so-called 120° spin structure where all the angles between two neighboring spins are arranged to be 120° [4]. Obviously there are two different 120° arrangements and they have different handedness, respectively, as it is shown in Fig. 1.7(b). This kind of chirality that is induced by magnetic frustration was introduced for the first time by Villain in 1977 in a model for a two dimensional spin glass [Vil77].
The chirality in such a system can be mathematically defined by the vector-chirality

$$\kappa = \frac{2}{3\sqrt{3}} \sum_{<i,j>} [\boldsymbol{S}_i \times \boldsymbol{S}_j]_z, \tag{1.12}$$

where one averages the vector product of two spins over three spin pairs (s. e.g. the review article [Kaw98] about frustrated antiferromagnets). For a left-handed triangle $\kappa > 0$

[4] Of course this solution is only possible if the spins are allowed to move freely in the plane of the triangle. E.g. in case of one-component Ising type spins (system possesses easy axis type of magnetic anisotropy) the ground state can not be uniquely determined.

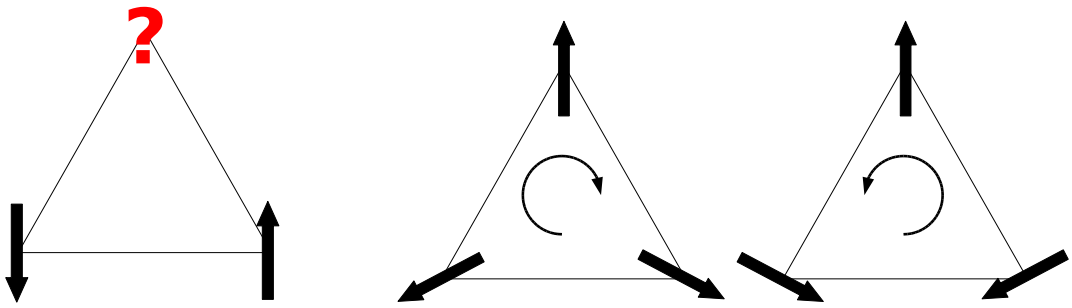

(a) (b)

Figure 1.7: (a) A triangular lattice is shown. If the magnetic interaction between the two neighboring spins is assumed to be antiferromagnetic, there is no possibility to arrange all three spins on the corners of the triangle in such a way that each spin is antiparallel to both of its neighbours. Such a spin configuration is called *frustrated*. (b) The classical 120° spin structure is shown. There are two such structures. In the first one the spins are rotated clockwise if we proceed from one corner of the triangle to the next one in a clockwise direction and the structure is left-handed. In the second the spins are rotated counterclockwise and we call it right-handed.

whereas for a right-handed $\kappa < 0$.
This kind of magnetic frustration appears in layered system, where the triangular layers are stacked on top of each other. Within the layers the magnetic interactions are XY antiferromagnetic type whereas the interaction between the layers is often negligible due to their large distance. A typical example is the stacked triangular antiferromagnet $CsMnBr_3$[PMK+99].
Apart from the magnetic frustration discussed above, in magnetic systems that show non-negligible next-nearest-neighbour interaction frustration can also occur. If the magnetic interactions between nearest neighbours and and next nearest neighbours have a different sign and similar orders of magnitude this obviously leads to frustration as the spin cannot align properly with respect to both interactions. This is illustrated in Fig. 1.8. Such a situation also can lead to helical magnetical ordering. We assume a simple model Hamiltonion on a simple cubic lattice in order to demonstrate this. We consider a ferromagnetic nearest-neighbour interaction in all directions and an antiferromagnetic next-nearest-neighbour interaction along one particular direction, e.g. the z-axis. The Hamiltonian then may be written as

$$H = -J_{NN} \sum_{<i,j>} \boldsymbol{S}_i \boldsymbol{S}_j - J_{NNN} \sum_{<<i,j>>} \boldsymbol{S}_i \boldsymbol{S}_j, \tag{1.13}$$

where the first sum is taken over all nearest-neighbour sites whereas the second sum is only taken over next-nearest-neighbour sites that are situated along the z-direction. The competition between the isotropic ferromagnetic J_{NN} and axial antiferromagnetic J_{NNN} gives rise to spiral magnetic ordering along the z-axis when the ratio $|\frac{J_{NNN}}{J_{NN}}|$ reaches a critical value. As for the magnetic helices driven by the DMI also here the period of the helix is usually incommensurate with respect to the lattice.
Examples for such systems are the rare-earth metals Ho, Dy and Tb [KCWC63, Koe65, KCWW66, DAN67, JM91, Jen96]. They crystallise in the hexagonal-close-packed (hcp) structure and form magnetic spirals along the hexagonal c-axis with the magnetic moments confined inside the basal hexagonal plane. The origin for the frustration in these systems is the long-range Ruderman-Kittel-Kasuya-Yosida (RKKY) interaction [Kit54, Kas56, Yos57, Vle62] that drops as $1/r^3$ and additionally oscillates in sign with distance r which leads to a different sign for nearest and next nearest neighbour interactions.

1.3 Chiral magnetism, 'quo vadis'?

In the preceding sections we have reviewed the mechanisms driving chiral magnetic structures. The occurrence of chiral magnetism by itself seems to be quite well understood. However, in recent years it appears that the formation of chiral magnetism plays a prominent role in multiple related research topics in condensed matter physics. Here we want to give a short overview.

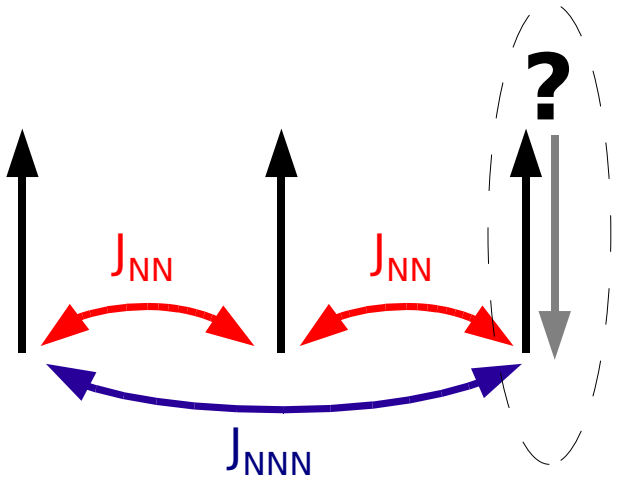

Figure 1.8: Frustration due to non-negligible next nearest neighbour interaction is shown. The exchange integrals for the nearest-neighbour interaction J_{NN} and for the next-nearest-neighbour interaction J_{NNN} are assumed to be of comparable magnitude but of opposite sign. Thus the third spin on the right side is clearly frustrated.

1.3.1 Chiral universality class

Phase transitions of magnetic systems have been studied in great detail both theoretically and experimentally. Due to this extensive work a good understanding of phase transitions of standard ferromagnets and antiferromagnets has been established. The expression 'standard' here denotes that only regular collinear and unfrustrated magnets without quenched disorder are considered. The renormalisation group (RG) theory introduced by Wilson [WK74, Wil83] provided a framework for the calculation of the critical exponents for quantities that indicate a phase transition, e.g. the susceptibility, the specific heat and the order parameter. A central finding within this framework was the concept of *universality* that states that a variety of second-order phase transitions in magnets can be divided in a number of *universality classes* determined only by a few characteristic properties of the systems, namely the spatial dimension d, the symmetry of the order parameter and the range of the considered interaction, but do not depend on the detailed form and magnitude of interactions.[5] Magnetic materials that belong to one single universality class have the same critical exponents independent of their otherwise distinct properties. If only bulk magnetic materials are considered (d = 3) the number of spin components n determine the universality class. More physically the index is interpreted as the dimension of the magnetic anisotropy: n = 1 (Ising), n = 2 (XY) and n = 3 (Heisenberg) signify magnets with easy-axis-type anisotropy, easy-plane-type anisotropy and no anisotropy, respectively. The theoretical predictions for these n-component magnets were found to be correct in many experiments (A good overview for the predicted

[5] A nice introduction is given in section 5.4 of reference [CL95].

and measured critical exponents is given in table 5.4.2 of reference [CL95].).
However, for frustrated, canted or non-collinear magnets the experimental results for the critical exponents are less clear and do not comply with the universality classes in many cases. Further, the theoretical analysis were often somehow inconclusive and sometimes gave conflicting results concerning the nature of the critical behaviour (s. reference [Kaw98] for a clear historical presentation). In the 1980s Kawamura first claimed from symmetry analysis and Monte Carlo simulations that stacked-triangular antiferromagnets like the previously mentioned $CsMnBr_3$ may belong to a novel kind of *chiral universality class* that differs from the standard universality class predicted by RG theory [Kaw85, Kaw86, Kaw87, Kaw86]. Also the helimagnets Ho, Tb and Dy were argued to exhibit identical chiral critical behaviour by the same author [Kaw86, Kaw86]. Despite early experimental studies that agreed with the critical exponents predicted from the new chiral universality scenario for e.g $CsMnBr_3$ there are still both theoretical and experimental issues that do not allow for a final decision about the existence of a chiral universality class. A detailed presentation of these issues is beyond the scope of this work and we refer to the excellent review article [Kaw98] for a complete view of the still active research field (compare [PMK$^+$99, VPSB$^+$01, icvcvIT01].

1.3.2 Magnetic surfaces and interfaces

One emerging field in chiral magnetism are magnetic surface structures or layered magnetic systems. The presence of surfaces or interfaces between layers often breaks the inversion symmetry of a crystal structure and therefore enables the existence of chiral magnetic structures through the DMI. Bogdanov *et al.* developed a phenomenological theory of chiral symmetry breaking in magnetic nanostructures in 2001 [BR01]. They state that surfaced induced chiral symmetry breaking should have a strong impact on the magnetic properties. The chiral symmetry breaking may lead to chiral spatially modulated or localised magnetic structures which were previously associated only with low-symmetry crystals.
First experimental evidence of a magnetic spiral that is established via the DMI on a surface was reported for a monolayer of manganese atoms grown on a tungsten (110) substrate by Bode *et al.* [BHvB$^+$07] via spin-sensitive scanning tunnelling microscopy (STM). As we have seen before the DMI can select magnetic structures of a specific chirality when the inversion symmetry of the complete system is broken. Thus, such surface magnetic structures could become useful in the context of spintronics, as this would enable interaction with a spin-current.
First principle calculations of Heide *et al.* [HBBB06] demonstrate the potential of layered magnetic heterostructures with missing inversion symmetry as future candidates for spin field-effect transistors (compare reference [DD90]). In a two-dimensional electron gas (2DEG) relativistic spin-orbit coupling (DMI) in the presence of an inversion asymmetric electric potential $V(\boldsymbol{r})$ can give rise to a Rashba spin-splitting [Ras60] of an otherwise spin-degenerate electron gas. We note that for this kind of spin-splitting no external mag-

netic field is necessary as the missing inversion symmetry lifts the degeneracy of spin-up and -down energy levels in the 2DEG and therefore $\varepsilon_\uparrow(\boldsymbol{k}) \neq \varepsilon_\downarrow(-\boldsymbol{k})$. Additionally the relativistic movement of the electron transforms the electrical field into a magnetic field in the local frame of reference of the electron. In a classical analogon, the local magnetic field imposes a torque $\boldsymbol{\tau} = \boldsymbol{s} \times \boldsymbol{B}$ on the spin $\boldsymbol{s}$ of the electron and the spin will precesses around the field while moving through the potential $V(\boldsymbol{r})$ (for the full quantum-mechanical derivation see reference [HBBB06]). The precession speed will depend on the strength of the potential and therefore the direction of the spin current passing through the potential can be controlled via an electrical field. This can be used to construct a spin field-effect transistors when ferromagnetic materials for the source and drain of the transistor are used. This is demonstrated in Fig. 1.9.

1.3.3 Magneto-electric effect

The magneto-electric (ME) effect is the coupling of electric and magnetic fields in matter. It was originally discovered by Röntgen in 1888 who observed that a moving dielectric became magnetised when placed in an electric field [Rön88]. Wilson observed the reversed effect, namely the electric polarisation of a moving dielectric in a magnetic field in 1905

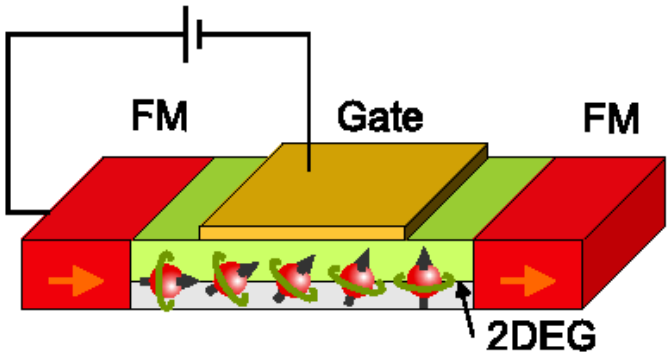

Figure 1.9: A scheme of the a spin field-effect transistor (SFET) is shown (the picture is taken from reference [HBBB06]). The source (spin injector) and the drain (spin analyser) are ferromagnetic metals or semiconductors, with parallel alignment of magnetic moments. The injected spinpolarized electrons with wave vector k move through the 2DEG in the presence of an inversion asymmetric electric potential $V(\boldsymbol{r})$ (e.g. formed by a strained InGaAs/InP heterojunction). As the electrons move from source to drain their spins precess about a precession axis, which arises from spin-orbit interaction (compare text). The precession speed is tunable via the gate voltage that changes the potential $V(\boldsymbol{r})$. The current through the device is large if the electron spin at the drain points in the initial direction and thus parallel to the spin analyser, and small if the direction is reversed. Here an intermediate situation is depicted. We emphasise that for a given gate voltage the spins form a stationary magnetic helix even though the electrons propagate through the potential.

[Wil05]. Already in 1894 it was argued by Curie from symmetry considerations that the ME effect should also exist for non-moving materials [Cur94]. As electric and magnetic fields are not invariant under (space) inversions and time reversal, respectively, we can deduce that if an electric and and a magnetic field should couple inside a crystal neither inversion nor time reversal can be symmetry operations (compare [Kho06, Fie05]). The time-reversal symmetry can be broken by movement (as in the historic Röntgen experiment), by application of an external field or intrinsically via long-range magnetic ordering in the crystal. Dzaloshinskii [Dzy59] derived for the first time the explicit violation of time-reversal for the specific system Cr_2O_3 and predicted a ME effect that was subsequently experimentally confirmed by Astrov [Ast60]. Even though the potential of the ME effect for new applications in electronics, e.g. as electrical field controlled magnetic memory devices, was immediately recognised after this observation (compare [WA73]), there are still relatively few materials that are known to display a ME effect and additionally the observed effect is generally weak. This is because for a strong ME coupling the material must be a strong ferroelectric and ferromagnetic material (compare e.g. [Fie05]). The class of materials showing this property is commonly referred to as multiferroics[6] [Sch94]. However, ferroelectricity and magnetism seem to be mutually exclusive in many materials. Most of the materials that display ferroelectricity are transition metal oxides in which the transition metal ions have empty d shells because they like to form covalent bonds with neighboring oxygens. This bonds involve a shift of the ions that leads to electric polarisation. In contrast, magnetism implies partially filled d shells, since the spins of completely field shells cancel each other and hence do not lead to the formation of magnetism. This matter is discussed in more depth in the references [Hil00, Kho06].
However, the (ME) effect was subject of renewed interest in recent years [Kho06, Fie05]. This is due to the discovery of new materials that display large ME effects via a change of direction or sign reversal of the electric polarisation when a magnetic field is applied. Examples for these materials are different manganates $RMnO_3$ (with R=Tb, Gd) [KGS$^+$03] and RMn_2O_5 (R=Tb, Dy, Ho) [HPS$^+$04a, HPS$^+$04b] but also $Ni_3V_2O_8$[LHK$^+$05] and $MnWO_4$[TAT$^+$06]. Interestingly enough all these systems have in common that the large ME effect is observed within magnetic phases with spiral magnetic structures. E.g. $TbMnO_3$ undergoes a paraelectric to ferroelectric phase transition at $T_C \approx 28$ K when its magnetic structure changes from a sinusoidally modulated collinear to a spiral magnetic structure [KHJ$^+$05]. As the absence of inversion symmetry is a necessary prerequisite for ferroelectricity this can be understood qualitatively as the former magnetic structure possesses inversion symmetry whereas it is broken by the latter.
In 2005 Katsura, Nagaosa, and Balatsky (KNB) suggested a mechanism to explain ferroelectricity induced by the magnetic ordering of a material [KNB05]. In this model electric polarisation

$$\boldsymbol{P}_i = A \cdot \boldsymbol{e}_{i,j} \times (\boldsymbol{S}_i \times \boldsymbol{S}_j), \tag{1.14}$$

is generated by the overlap of electronic wave functions of neighbouring atomic sites i and

[6] We note that the term multiferroic is not limited to (anti-)ferromagnets and ferroelectrics but also involves ferroelastics. A multiferroic displays two or more of this ferroic ordering phenomena.

j which possess mutually canted spins $\boldsymbol{S}_i$ and $\boldsymbol{S}_j$. $\boldsymbol{e}_{i,j}$ denotes the vector between both atoms and A is a coupling constant determined by the spin exchange interaction and the spin-orbit interaction (DMI). Recently, Yamasaki *et al.* demonstrated by means of polarised neutron diffraction that the chirality of the spiral magnetic structure of $TbMnO_3$ in the ferroelectric phase can be switch from right-handed to left-handed by applying an electrical field along the crystallographic c axis [YSG+07]. This electric field induced change of the magnetic structure could be completely explained within the KNB model. The KNB model does not involve lattice degrees of freedom in order to explain the development of electric polarisation in $TbMnO_3$ in the spiral magnetic phase. The arising polarisation is explained in terms of polarised electronic orbitals. In a more recent theoretical treatment by Sergienko *et al.* [SD06] it was shown that the presence of the DMI may also lead to a shift of the oxygen with respect to the Mn ions in $TbMnO_3$ which would explain the strong coupling between ferroelectric and magnetic degrees of freedom in this compound.
In 2006 Mostovoy [Mos06] introduced a phenomenological theory motivated by symmetry considerations that explains not only the observed polarisation in $TbMnO_3$ but also reproduces the phase diagram observed by Kimura *et al.* [KGS+03]. In a system without inversion symmetry a coupling term that is linear in the gradient of the magnetisation $\boldsymbol{M}(\nabla \cdot \boldsymbol{M})$ is allowed and the magnetically induced polarisation is[7]:

$$\boldsymbol{P} \propto \gamma \left[\boldsymbol{M}(\nabla \cdot \boldsymbol{M}) - (\boldsymbol{M} \cdot \nabla)\boldsymbol{M}\right]. \tag{1.15}$$

We assume that the magnetisation forms a spiral of the form

$$\boldsymbol{M}(\boldsymbol{r}) = M_1 \boldsymbol{e}_x \cos(\boldsymbol{k}\boldsymbol{r}) + M_2 \boldsymbol{e}_y \sin(\boldsymbol{k}\boldsymbol{r}), \tag{1.16}$$

where $\boldsymbol{k}$ is the propagation vector of the spiral and $\boldsymbol{e}_i$ with i=x, y, z are unit vectors in a Cartesian coordinate frame. For the electric polarisation induced by the magnetisation we therefore find

$$\boldsymbol{P} \propto \gamma M_1 M_2 (\boldsymbol{e}_z \times \boldsymbol{k}). \tag{1.17}$$

Here $\boldsymbol{e}_z$ is obviously equal to $\boldsymbol{e}_x \times \boldsymbol{e}_y$. This signifies that only when the propagation vector of the helix is parallel to the plane in which the magnetisation rotates a electric polarisation is observed. This corresponds to the situation observed for $TbMnO_3$. We note that in this model the electrical polarisation has not to be driven by the DMI but also can rise from helical ordering due to frustration (compare section 1.2.3).
For a detailed overview of systems showing a ME effect that is driven by helical magnetic ordering we refer to the two review articles [Kim07, CM07].

1.3.4 Helical Goldstone modes and skyrmion condensate in MnSi

MnSi is an itinerant helimagnet that crystallises in the cubic $P2_13$ structure that possesses no inversion symmetry. In zero field, its magnetic structure below T_c=29.5 K is

[7] The given expression is for cubic crystal symmetry.

a long-period ferromagnetic spiral with the propagation vector $\boldsymbol{k} = (2\pi/a)(\zeta, \zeta\,\zeta)$ with $\zeta = 0.016$ resulting in a period of approximately 180 Å [SCM$^+$83, RBFE02] along the [111] direction. Above 6.2 kOe, a ferromagnetic structure is induced, with an ordered magnetic moment of 0.4 μ_B on each Mn site [ISTK77].
The magnetic excitation spectrum of MnSi has been studied extensively in the field-induced ferromagnetic [ISTK77, TBE$^+$98, SBE$^+$99] and the paramagnetic phase [INFS82, INU$^+$85]. The observed collective spin-waves that merge into the so-called Stoner continuum of single particle spin flip excitations are well explained when MnSi is considered as a weakly ferromagnetic Fermi liquid (FL) [LT85, Mor85]. Startlingly, to the best of our knowledge no investigations of the excitations of the helical magnetic ground state at ambient pressure and low temperature have been reported.
However, recently a novel magnetic excitation spectrum has been suggested independently by two theory groups for the helical magnetic phase in MnSi [BKR07, Mal06]. They predict that the presence of the DMI leads to a new type of helical Goldstone modes coupled to the emergence of the helical state which they called *helimagnons*, in analogy to ferromagnons and antiferromagnons. Both groups find an anisotropic dispersion with soft modes linear in q parallel to the propagation vector $\boldsymbol{k}$ and quadratic in q perpendicular to it.
Besides to the helical magnetic order that is well understood (compare e.g. section 1.2.2) MnSi displays many peculiarities that are so far unexplained. Belitz *et al* have stated [BKR07] that the only obvious difference of MnSi with respect to other itinerant ferromagnets is the presence of the weak DMI that gives rise to the helical magnetic ordering. Therefore the presence of the proposed helimagnons may explain these non-understood features. They include a non-Fermi-liquid (NFL) phase above a critical pressure p_c of 14.6 kbar [PJL01] that extends from a few mK to a crossover temperature of approximately 12 K and a partial magnetic order that only exists in a pocket of the NFL phase above p_c[PRP$^+$04]. The partial order was interpreted as the unpinning of the helix wavevector. A detailed review of the non-understood properties of MnSi will be given in chapter 5.
A further experimental result on MnSi that currently attracts a lot of interest is that in SANS measurements at $T \gtrsim T_c$ a sphere of intensity is observed with a radius corresponding to the propagation vector $\boldsymbol{k}$ of the helix. The appearance of the sphere may be interpreted as the unpinning of the helix propagation vector. This fact presently attracts high interest and triggered theoretical considerations that explain the sphere of magnetic intensity by an intermediate phase between the helical and the paramagnetic phase. In MnSi the intermediate phase may be triggered by soft longitudinal magnetic fluctuations, that favour the appearance of multi-dimensional magnetic textures. Rößler *et al.* [RBP06] predict that the magnetic state may form *skyrmion* patterns in this phase, i.e. complex multidimensional, magnetic textures. Their calculations show that the skyrmion condensate may only be stable when a variation of the amplitude of the magnetisation is allowed. The helimagnons predicted above might be the soft modes leading to this new intermediate phase.
We emphasise that even though MnSi that is generally considered as good candidate for

a model system of a helical magnet, it shows many features that are not well-understood. However, theoretical models described above predict that the majority of them is directly connected to the DMI and therefore to the inherent chiral magnetism of MnSi. Ultimately, if the proposed helimagnons are identified as the typical excitation spectrum of a helimagnet this will help to elucidate the properties of other helical magnets as well. Therefore further experimental studies to resolve these issues are desirable.

1.3.5 Summary

We showed that the concept of chiral magnetism is of relevance in a wide range of research topics in condensed matter physics that are interesting both for technological reasons as well as for fundamental research. Apart from the fields described above, where the relevance of chiral magnetism was already clearly identified, there is also indication that magnetic chirality is of importance in the field of non-centrosymmetric superconductors like e.g. $CePt_3Si$ (s. references [BHM+04, FAKS04, KAS05]. This example underlines that the futher understanding of magnetic chirality is of rather general importance.
Despite the obvious key role of chirality within the different domains so far little attention has been given to magnetic chirality in a more general view. A more detailed study of chiral magnetic systems may reveal common properties or mechanisms that would lead to a better understanding in all research topics that involve chiral magnetism.
In the next two chapters we will demonstrate that unpolarised and polarised neutron scattering (chapter 2) in combination with magnetic symmetry analysis (chapter 3) is an ideal tool to study chiral magnetism. During this work we carried out extensive investigations on two compounds that involve magnetic chirality by means of neutron scattering: the multiferroic $NdFe_3(BO_3)_4$ (chapter 4) and the itinerant helimagnet MnSi (chapter 5).

Chapter 2

Neutron scattering

Since the 1960s elastic and inelastic neutron scattering have been proved to be an invaluable tools to study static and dynamic microscopic properties in condensed matter systems. This success is due to the characteristic properties of cold to thermal neutrons:

- Due to their wavelength λ being of the same order as interatomic distances in solids and liquids (typically a few Å), interference effects occur in the scattering process which yield information on the structure of the scattering system.
- Being uncharged particles, neutrons only interact with the scattering system via nuclear forces. Therefore there is no Coulomb barrier to overcome. Neutrons can penetrate deeply in the sample and therefore provide information about bulk properties. In difference to X-ray scattering the scattering length is no monotonic function of the atomic number. It varies strongly for neighbouring nuclei in the table of elements. This is advantageous when light elements are of interest.
- Energies of thermal neutrons ($E_n = \frac{81.81}{\lambda^2}$[meV] with λ in Å) and of elementary excitations in condensed matter are of the same order of magnitude. By analysing the energy transfer of neutrons onto the sample in the scattering process, sample dynamics can be studied easily.
- Due to its magnetic moment the neutron interacts with the magnetic fields generated by the electrons of a magnetic sample. On account of this the neutron scattering cross-section does not only include nuclear contributions but also magnetic ones and thus neutrons are highly suitable probes to investigate magnetic properties.

In this chapter we will introduce the basic concepts in neutron scattering. In the field of magnetism the use of polarised neutron beams, i.e. all neutron spins in the beam are mutually parallel, even adds to the amount of information that can be extracted from a neutron scattering experiment. We will see that this is especially usefull in the field of chiral magnetism. Hence, special attention will be given to the method of neutron polarisation analysis.

2.1 The neutron scattering cross-section

In a typical neutron scattering experiment a beam of neutrons with well-defined incident momentum $\hbar\boldsymbol{k}_i$ is impinged on the sample to be investigated. Due to the interactions between the sample and the neutrons will be scattered to a different state with final momentum $\hbar\boldsymbol{k}_f$. The conservation laws for momentum and energy consequently result in the equations

$$\begin{aligned} \hbar\boldsymbol{Q} &= \hbar(\boldsymbol{k}_i - \boldsymbol{k}_i) \\ \hbar\omega &= E_i - E_f = \frac{\hbar^2}{2m_n}(k_i^2 - k_f^2), \end{aligned} \tag{2.1}$$

for the momentum and the energy transfer that are experienced by the neutrons in the scattering process, respectively. m_n is the mass of the neutron. By measuring the probability that neutrons are scattered from an initial state with neutron wave vector $\boldsymbol{k}_i$ into a final state with wave vector $\boldsymbol{k}_f$ for a number of different combinations of ($\boldsymbol{Q}$, ω), conclusions about the special form of the interaction potential of a distinct sample can be drawn. This probability can be derived by means of Fermi's golden rule and is described by the partial differential neutron scattering cross-section [Lov84, Squ78] given by

$$\frac{d^2\sigma}{d\Omega dE'} = \frac{k_f}{k_i}\left(\frac{m}{2\pi\hbar^2}\right)^2 \sum_{n,\sigma_i} p_n p_\sigma \sum_{n',\sigma_f} \left|\langle \boldsymbol{k}_f\sigma_f, n'|V|\boldsymbol{k}_i,\sigma_i,n\rangle\right|^2 \delta(\hbar\omega + E_n - E_{n'}). \tag{2.2}$$

Here we use k_i/σ_i and k_f/σ_f to describe the wave number and spin of the neutrons before and after the scattering process, respectively, whereas the initial and final state of the scattering system (sample) are given by the quantum numbers n and n'. The initial states n of the scattering system occur with the probability $p_n = e^{-En/k_BT}/\sum_n e^{-En/k_BT}$ at a distinct temperature T. If a beam of unpolarised neutrons is assumed, the probabilities for the up and down states of the neutrons spins are equal. Therefore $p_\sigma = \frac{1}{2}$ for all σ. Averaging over n and σ takes into account all possible initial states before the scattering process, while summing over n and σ' considers all possible final states after the scattering process. The matrix element $\langle \ldots \rangle$ describes the transition probability from initial states (n, $\boldsymbol{k}_i$, σ_i) of the total system (neutron & sample) to final states (n', $\boldsymbol{k}_f$, σ_f) due to the interaction potential V according to Fermi's golden rule. The δ-function assures the conservation of energy during the scattering process. The factor $\mathrm{k}_i/\mathrm{k}_f$ is due to the fact that the cross-section is defined as the ratio of the outgoing and incoming neutron currents. We note that therefore the partial differential cross-section is the neutron intensity scattered into a solid angle $d\Omega$ and with energies between E' and $E' + dE'$.

2.2 Nuclear scattering

2.2.1 The Fermi pseudopotential

A neutron interacts with matter via the nuclear force. The range of the nuclear interaction is of the order of 1-10 fm. The scattering potential of a nucleus j situated at position R_j is described via the *Fermi pseudopotential* given by

$$V_j(\boldsymbol{r}) = \frac{2\pi\hbar^2}{m} b_j \delta(\boldsymbol{r} - \boldsymbol{R_j}), \tag{2.3}$$

where m is the mass of the neutron and b_j the scattering length of this nucleus [Lov84, Squ78]. The potential therefore is described by an point-like interaction which is well justified by the fact that the wavelength of cold to thermal neutrons is much larger than the range of the nuclear force, namely $\lambda \cong$ 1-10 Å. The wave function of a neutron scattered via the nuclear interaction can be consequently entirely described by S-waves (l=0) when analysed in terms of partial waves.
The scattering potential of an ensemble of several nuclei (e.g. in a liquid or crystal) then can be described by a sum over the potentials of individual nuclei j

$$V(\boldsymbol{r}) = \frac{2\pi\hbar^2}{m} \sum_j b_j \delta(\boldsymbol{r} - \boldsymbol{R_j}). \tag{2.4}$$

We see that due to the short range nature of the nuclear force $\boldsymbol{k}_f \cdot \boldsymbol{r_0} \ll 1$ (r_0 the range of the nuclear force) is always satisfied and the kinematic Born approximation can be applied to calculate the matrix element in Eq. 2.2. Hence, the wave functions for the scattered neutrons are approximated as plane waves $e^{i\boldsymbol{k}_f \cdot \boldsymbol{r}}$. Together with Eq. 2.4 the matrix element can be evaluated to be (s. e.g. [Squ78] for a complete derivation)

$$|\langle \boldsymbol{k}_f, n' | V(\boldsymbol{r}) | \boldsymbol{k}_i, n \rangle|^2 \;=\; \left(\frac{2\pi\hbar^2}{m}\right)^2 \left| \sum_j b_j \langle n' | \exp(i\boldsymbol{Q} \cdot \boldsymbol{R}_j) | n \rangle \right|^2, \tag{2.5}$$

where $\boldsymbol{Q}$ is the scattering vector as defined by Eq. 2.1 and we have neglected the spin state of the neutron as appropriate for an unpolarised beam. The δ-function for the energy conservation in the cross-section 2.2 can be rewritten in an integral form via

$$\delta(\hbar\omega + E_n - E_{n'}) = \frac{1}{2\pi\hbar} \int dt \exp\{i(E_{n'} - E_n)t/\hbar\} \exp(-i\omega t). \tag{2.6}$$

Using additionally the fact that the states n of the scattering system are eigenfunctions of $\hat{H}$ with the eigenvalues E_n ($\hat{H}|n\rangle = E_n|n\rangle$) the position operators $\boldsymbol{R}_j$ can be written as time-dependent Heisenberg operators $\boldsymbol{R}_j(t) = \exp(iHt/\hbar)\boldsymbol{R}_j \exp(-iHt/\hbar)$ [Squ78].

The final expression obtained for the nuclear partial differential neutron scattering cross-section is then

$$\frac{d^2\sigma}{d\Omega dE'} = \frac{k_f}{k_i}\frac{1}{2\pi\hbar}\sum_{j,j'} b_j b_{j'} \int dt \langle \exp\{-i\boldsymbol{Q}\cdot\boldsymbol{R}_{j'}(0)\}\exp\{i\boldsymbol{Q}\cdot\boldsymbol{R}_j(t)\}\rangle \exp(-i\omega t), \quad (2.7)$$

where $\langle A\rangle = \sum_n p_n \langle n|A|n\rangle$ denotes the thermal average over an operator A at temperature T (remember $p_n = e^{-En/k_BT}/\sum_n e^{-En/k_BT}$).
Finally we define the *nuclear structure factor* $N_{\boldsymbol{Q}}(t) = \sum_j b_j \exp\{i\boldsymbol{Q}\cdot\boldsymbol{R}_j(t)\}$ that will be used in later chapters and allows to rewrite Eq. 2.7 in the short form

$$\frac{d^2\sigma}{d\Omega dE'} = \frac{k_f}{k_i}\frac{1}{2\pi\hbar}\int dt \langle N^\dagger_{\boldsymbol{Q}}(0) N_{\boldsymbol{Q}}(t)\rangle \exp(-i\omega t). \quad (2.8)$$

2.2.2 Coherent and incoherent scattering

The scattering length b_j depends on the distinct nucleus and additionally on the spin state of the nucleus-neutron system. A neutron has a spin $\sigma = \frac{1}{2}$ and a nucleus may have a spin I and consequently the total spin of the system can take two values $I + \frac{1}{2}$ or $I - \frac{1}{2}$ and the scattering length is written as

$$b_j^{\pm} = b_j + B\sigma\cdot I, \quad (2.9)$$

where the term $B\sigma\cdot I$ is the dipole interaction between the neutron and the nuclear spin. We see that for isotopes with non-zero spin I two distinct scattering lengths exist for $\sigma = \pm\frac{1}{2}$, respectively. Further, the scattering length b_j varies for different isotopes of an element as different isotopes possess different spin I. In a real sample an a priori unknown distribution of different nuclei and isotopes is present and we have to average over all possible scattering lengths b_j

$$\frac{d^2\sigma}{d\Omega dE'} = \frac{k_f}{k_i}\frac{1}{2\pi\hbar}\sum_{j,j'} \overline{b_j b_{j'}} \int dt \langle \exp\{-i\boldsymbol{Q}\cdot\boldsymbol{R}_{j'}(0)\}\exp\{i\boldsymbol{Q}\cdot\boldsymbol{R}_j(t)\}\rangle \exp(-i\omega t). \quad (2.10)$$

The average $\overline{b_j b_{j'}}$ can be separated into two parts, namely

$$\left(\frac{d^2\sigma}{d\Omega dE'}\right)_{coh} = \frac{\sigma_{coh}}{4\pi}\frac{k_f}{k_i}\frac{1}{2\pi\hbar}\sum_{j,j'}\int dt \langle \exp\{-i\boldsymbol{Q}\cdot\boldsymbol{R}_{j'}(0)\}\exp\{i\boldsymbol{Q}\cdot\boldsymbol{R}_j(t)\}\rangle \exp(-i\omega t) \quad (2.11)$$

and

$$\left(\frac{d^2\sigma}{d\Omega dE'}\right)_{inc} = \frac{\sigma_{inc}}{4\pi}\frac{k_f}{k_i}\frac{1}{2\pi\hbar}\sum_{j}\int dt \langle \exp\{-i\boldsymbol{Q}\cdot\boldsymbol{R}_j(0)\}\exp\{i\boldsymbol{Q}\cdot\boldsymbol{R}_j(t)\}\rangle \exp(-i\omega t), \quad (2.12)$$

that are called the *coherent* and *incoherent* cross-section, respectively [Squ78]. Here we have defined $\sigma_{coh} = 4\pi(\bar{b})^2$ and $\sigma_{inc} = 4\pi\{\overline{b^2} - (\bar{b})^2\}$. The coherent cross-section describes correlations between the same nucleus at different times and different nuclei at different times and hence gives rise to interference effects. The incoherent cross-section describes only correlations of the same nucleus at different times and therefore does not lead to interference effects.
The information that is of interest in condensed matter systems, namely the correlations between different particles at the same time (structural information) and at different times (information about excitations) are contained only in the coherent part of the cross-section. The incoherent cross-section gives rise to scattering intensity that is isotropic and adds to the experimental background. Therefore, we will only consider the coherent part in the following[1].

2.2.3 Bragg scattering from crystals

All specimen investigated in this work are single or polycrystals (powders) and therefore it is interesting to analyse Eq. 2.7 for the case of crystals. For simplicity we will consider only Bravais crystals with one atom per unit cell. The vectors $\boldsymbol{a}_1$, $\boldsymbol{a}_2$ and $\boldsymbol{a}_3$ define the unit cell and we can write any lattice vector $\boldsymbol{l}$ as a linear combination of them:

$$\boldsymbol{l} = l_1\boldsymbol{a}_1 + l_2\boldsymbol{a}_2 + l_3\boldsymbol{a}_3, \tag{2.13}$$

with l_i being integers. The volume of the unit cell is $v_0 = \boldsymbol{a}_1 \cdot (\boldsymbol{a}_2 \times \boldsymbol{a}_3)$. Additionally we define reciprocal lattice vectors $\boldsymbol{\tau}_j$ that fulfil the equation $\boldsymbol{a}_i \cdot \boldsymbol{\tau}_j = 2\pi\delta_{ij}$ as

$$\boldsymbol{\tau}_1 = \frac{2\pi}{v_0}(\boldsymbol{a}_2 \times \boldsymbol{a}_3), \quad \boldsymbol{\tau}_2 = \frac{2\pi}{v_0}(\boldsymbol{a}_3 \times \boldsymbol{a}_1), \quad \boldsymbol{\tau}_3 = \frac{2\pi}{v_0}(\boldsymbol{a}_1 \times \boldsymbol{a}_2). \tag{2.14}$$

We take into account the thermal movement of the atoms in the lattice by writing their positional operators as $\boldsymbol{R}_l(t) = \boldsymbol{l} + \boldsymbol{u}_l(t)$ where $\boldsymbol{u}_l$ denotes the displacement from the equilibrium position $\boldsymbol{l}$.
In a Bravais lattice the correlation between nuclei at positions l and l' only depends on their distance $\boldsymbol{l} - \boldsymbol{l}'$ and the sum over l in the cross-section is identical for each l' [Squ78]. Thus we may put l = 0 and find

$$\begin{aligned} & \sum_{l,l'} \langle \exp\{-i\boldsymbol{Q}\cdot\boldsymbol{R}_{l'}(0)\} \exp\{i\boldsymbol{Q}\cdot\boldsymbol{R}_l(t)\}\rangle \\ = \; & N \sum_{l} \exp(i\boldsymbol{Q}\cdot\boldsymbol{l}) \langle \exp\{-i\boldsymbol{Q}\cdot\boldsymbol{u}_0(0)\} \exp\{i\boldsymbol{Q}\cdot\boldsymbol{u}_l(t)\}\rangle \\ = \; & N \sum_{l} \exp(i\boldsymbol{Q}\cdot\boldsymbol{l}) \langle \exp U \exp V\rangle, \end{aligned} \tag{2.15}$$

[1] However, in some cases even the incoherent cross-section is useful, e.g. to determine the density of states of phonons (compare [Squ78]).

where N is the number of nuclei in the crystal and in the last step we defined $U = -i\boldsymbol{Q}\cdot\boldsymbol{u}_0(0)$ and $V = i\boldsymbol{Q}\cdot\boldsymbol{u}_l(t)$. Here we only considered the coherent cross-section 2.11. If the interatomic forces are assumed to be linear the theory of normal modes can be applied to describe the motion of the atoms in the crystal. We will not consider this in detail here and only use the result $\langle \exp U \exp V\rangle = \exp\langle U^2\rangle \exp\langle UV\rangle$ that can obtained by the theory of normal modes [Squ78]. The term $\exp\langle U^2\rangle = \exp\langle(-\boldsymbol{Q}\cdot\boldsymbol{u}_0(0))^2)\rangle = \exp(-2W(\boldsymbol{Q}))$ is called the *Debye-Waller or B factor* and describes uncorrelated thermal motion of atoms [Deb13, Wal23]. It leads to a reduction in scattering intensity towards large $\boldsymbol{Q}$. The term $\exp\langle UV\rangle$ can be expanded in

$$\exp\langle UV\rangle = 1 + \langle UV\rangle + \frac{1}{2!}\langle UV\rangle^2 + \dots. \tag{2.16}$$

The zeroth order term gives rise to elastic scattering (atoms do not move) and the nth term for n≠0 gives the cross-section for n-phonon processes. In this work phonons will not be considered and we will only write out the cross-section for the zeroth order term. For zeroth order the scattering is elastic and thus $|\boldsymbol{k}_i| = |\boldsymbol{k}_f|$ and the cross-section is

$$\begin{aligned}\left(\frac{d\sigma}{d\Omega}\right)_{coh,el} &= \frac{\sigma_{coh}}{4\pi} N \exp(-2W(\boldsymbol{Q})) \sum_l \exp(i\boldsymbol{Q}\cdot\boldsymbol{l}) \\ &= \frac{\sigma_{coh}}{4\pi} N \frac{(2\pi)^3}{v_0} \exp(-2W(\boldsymbol{Q})) \sum_\tau \delta(\boldsymbol{Q}-\boldsymbol{\tau}),\end{aligned} \tag{2.17}$$

where in the last step the identity $\sum_l \exp(i\boldsymbol{Q}\cdot\boldsymbol{l}) = \frac{(2\pi)^3}{v_0}\sum_{\boldsymbol{\tau}} \delta^3(\boldsymbol{Q}-\boldsymbol{\tau})$ was used [Squ78]. From Eq. 2.17 we see that scattering is only observed when $\boldsymbol{Q} = \boldsymbol{k}_i - \boldsymbol{k}_f = \boldsymbol{\tau}$. This condition is an equivalent description of Bragg's law in reciprocal space (s. Fig. 2.1 for details)

$$\tau = 2k\sin\theta. \tag{2.18}$$

If we write $k = k_i = k_f = \frac{2\pi}{\lambda}$ and $\tau = n\frac{2\pi}{d}$ where λ is the wavelength of the neutron and d the lattice spacing of the crystal we obtain Bragg's law

$$n\lambda = 2d\sin\theta. \tag{2.19}$$

We note that for non-Bravais crystals the derivation above is easily extended by introducing the *nuclear unit-cell structure factor* [Squ78] given by

$$F_N(\boldsymbol{Q}) = \sum_d \bar{b}_d \exp(i\boldsymbol{Q}\cdot\boldsymbol{d}) \exp(-W_d), \tag{2.20}$$

into the cross-section. Here the vector $\boldsymbol{d}$ describes the position and $\exp(-W_d(\boldsymbol{Q})) = \exp\langle(-\boldsymbol{Q}\cdot\boldsymbol{u}_d(0))^2)\rangle$ the Debye-Waller factor of the dth atom in the unit cell. Hence, the coherent cross-section for a non-Bravais crystal is obtained by replacing $\frac{\sigma_{coh}}{4\pi}\exp(-2W(\boldsymbol{Q}))$ (s. Eq. 2.17) by $F_N^\dagger(\boldsymbol{Q})F_N(\boldsymbol{Q})$.

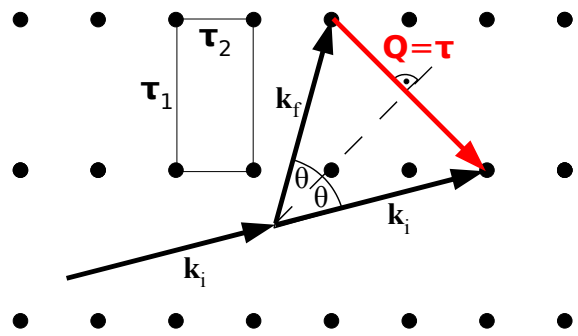

Figure 2.1: Bragg scattering in reciprocal space is illustrated. If d is the lattice constant of the scattering plane in real space then we can write $Q = \tau = \frac{2\pi}{d}$. Further, with $k_i = k_f = k$ we find $\frac{\tau}{2} = k\sin(\theta)$.

2.3 Magnetic scattering

2.3.1 The magnetic scattering potential

The magnetic interaction of the neutron with the sample is the interplay between the magnetic dipole moment of the neutron carried by its spin and the magnetic fields generated by the electrons of the sample. The operator corresponding to the magnetic dipole moment of the neutron is given by

$$\boldsymbol{\mu}_n = -\gamma\mu_N\hat{\boldsymbol{\sigma}}, \tag{2.21}$$

$$\text{where } \mu_N = \frac{e\hbar}{2m_p} \tag{2.22}$$

is the *nuclear magneton*. m_p is the mass of the proton and e its charge. $\gamma = 1.913$ is the *gyromagnetic ratio* of the neutron. $\hat{\boldsymbol{\sigma}}$ are the Pauli-matrices defined by

$$\hat{\sigma}_x = \begin{pmatrix} 0 & 1 \\ 1 & 0 \end{pmatrix}, \hat{\sigma}_y = \begin{pmatrix} 0 & -i \\ i & 0 \end{pmatrix}, \hat{\sigma}_z = \begin{pmatrix} 1 & 0 \\ 0 & -1 \end{pmatrix}. \tag{2.23}$$

The interaction of the magnetic dipole moment of the neutron with a magnetic field B is

$$V_m = -\boldsymbol{\mu}_N \cdot \boldsymbol{B}. \tag{2.24}$$

The magnetic field generated by the sample is composed of two parts. We imagine an electron with spin $\boldsymbol{s} = \frac{1}{2}\hat{\boldsymbol{\sigma}}$ and with momentum $\boldsymbol{p}$ (compare Fig. 2.2):

- The magnetic dipole moment of the electron $\boldsymbol{\mu}_e = -2\mu_B\boldsymbol{s}$ produces the magnetic field

$$\boldsymbol{B}_s = \boldsymbol{\nabla} \times \boldsymbol{A}, \quad \boldsymbol{A} = \frac{\mu_0}{4\pi}\frac{\boldsymbol{\mu}_e \times \boldsymbol{R}}{R^3}, \tag{2.25}$$

at a distance $\boldsymbol{R}$ from the electron (s. Fig.2.2). Here $\mu_B = \frac{e\hbar}{2m_e}$ is the Bohr magneton and m_e is the mass of the electron.

- Since the electron represents a moving charge of magnitude e it additionally generates the magnetic field

$$\boldsymbol{B_L} = -\frac{\mu_0}{4\pi}\frac{2\mu_B}{\hbar}\frac{\boldsymbol{p}\times\boldsymbol{R}}{R^3}. \tag{2.26}$$

at the point $\boldsymbol{R}$. Here $\boldsymbol{L} = \boldsymbol{R}\times\boldsymbol{p}$ is the angular momentum of the electron and we consequently denote this field by $\boldsymbol{B}_L$.

In total the magnetic interaction potential is then given by

$$V_m = -\frac{\mu_0}{4\pi}\gamma\mu_N 2\mu_B\hat{\boldsymbol{\sigma}}\cdot(\boldsymbol{W_s}+\boldsymbol{W_L}), \tag{2.27}$$

where $\boldsymbol{W}_s = \boldsymbol{\nabla}\times(\frac{\boldsymbol{s}\times\boldsymbol{R}}{R^3})$ and $\boldsymbol{W}_L = \frac{1}{\hbar}\frac{\boldsymbol{p}\times\boldsymbol{R}}{R^3}$ [Squ78]. Equivalent to the nuclear cross-section the matrix element in Eq. 2.2 can be evaluated for the magnetic potential V_m. We consider electrons at positions $\boldsymbol{r}_i$ with spin $\boldsymbol{s}_i$ and momentum $\boldsymbol{p}_i$. The expression found for the matrix element is then [Lov84]

$$\begin{aligned}\langle\boldsymbol{k}_f|\boldsymbol{W}_{si}+\boldsymbol{W}_{Li}|\boldsymbol{k}_i\rangle &= 4\pi\boldsymbol{M}_{\perp\boldsymbol{Q}},\\ \boldsymbol{M}_{\perp\boldsymbol{Q}} &= \sum_i \exp(i\boldsymbol{Q}\cdot\boldsymbol{r}_i)\left\{\hat{\boldsymbol{Q}}\times(\boldsymbol{s_i}\times\hat{\boldsymbol{Q}})+\frac{i}{\hbar Q}(\boldsymbol{p_i}\times\hat{\boldsymbol{Q}})\right\},\end{aligned} \tag{2.28}$$

where $\boldsymbol{M}_{\perp\boldsymbol{Q}}$ is called the *magnetic interaction vector*, and $\hat{\boldsymbol{Q}}$ is an unit vector parallel to $\boldsymbol{Q}$ and we only considered the position dependent part of V_m.
A more demonstrative representation of Eq. 2.28 can be derived (s. chapter 7.2 of reference [Squ78]) where the magnetic interaction vector is expressed as a function of the local magnetisation density $\boldsymbol{M}(\boldsymbol{r})$ of the sample at the point $\boldsymbol{r}$:

$$\boldsymbol{M}_{\perp\boldsymbol{Q}} = \hat{\boldsymbol{Q}}\times(\boldsymbol{M}_{\boldsymbol{Q}}\times\hat{\boldsymbol{Q}}) \tag{2.29}$$

$$\boldsymbol{M}_{\boldsymbol{Q}} = -\frac{1}{2\mu_B}\int \boldsymbol{M}(\boldsymbol{r})\exp(i\boldsymbol{Q}\boldsymbol{r})d^3r. \tag{2.30}$$

$\boldsymbol{M}_{\boldsymbol{Q}}$ is called the *magnetic structure factor* and is proportional to the Fourier transform of $\boldsymbol{M}(\boldsymbol{r})$. Hence, information about the microscopic magnetisation of a sample can be obtained by measuring the distribution of magnetic neutron scattering intensity.
In a last step it can be shown (s. chapter 7.2 in [Squ78]) that if the evaluation of the sum over final neutron spin states and the average over initial spin states (s. Eq. 2.2) for unpolarised neutrons ($p_\sigma = \frac{1}{2}$ for both spin states, up and down), the following identity is obtained

$$\sum_{\sigma_i,\sigma_f} p_\sigma\left|\langle\sigma_f,n'|\hat{\boldsymbol{\sigma}}\cdot\boldsymbol{M}_{\perp\boldsymbol{Q}}|\sigma_i,n\rangle\right|^2 = \sum_\alpha\langle n|M^{\alpha\dagger}_{\perp\boldsymbol{Q}}|n'\rangle\langle n'|M^{\alpha}_{\perp\boldsymbol{Q}}|n\rangle, \tag{2.31}$$

where $\alpha = x, y, z$. The complete magnetic cross-section for unpolarised neutron beams is finally obtained by inserting Eqs. 2.27 and 2.31 into the general Eq. 2.2

$$\begin{aligned}\frac{d^2\sigma}{d\Omega dE'} &= (\gamma r_0)^2 \frac{k_f}{k_i} \sum_{n,n'} p_n \sum_{\alpha} \langle n|M^{\alpha\dagger}_{\perp \boldsymbol{Q}}|n'\rangle\langle n'|M^{\alpha}_{\perp \boldsymbol{Q}}|n\rangle \delta(\hbar\omega + E_n - E_{n'}) \\ &= (\gamma r_0)^2 \frac{k_f}{k_i} \sum_{\alpha,\beta} (\delta_{\alpha\beta} - \hat{Q}_\alpha \hat{Q}_\beta) \sum_{n,n'} p_n \langle n|M^{\alpha\dagger}_{\boldsymbol{Q}}|n'\rangle\langle n'|M^{\beta}_{\boldsymbol{Q}}|n\rangle \delta(\hbar\omega + E_n - E_{n'}).\end{aligned} \tag{2.32}$$

$r_0 = 2.82 \cdot 10^{-15} m$ is a collection of all the multiplying factors in Eqns. 2.27, 2.28 and 2.2 and corresponds to the *classical electron radius*.

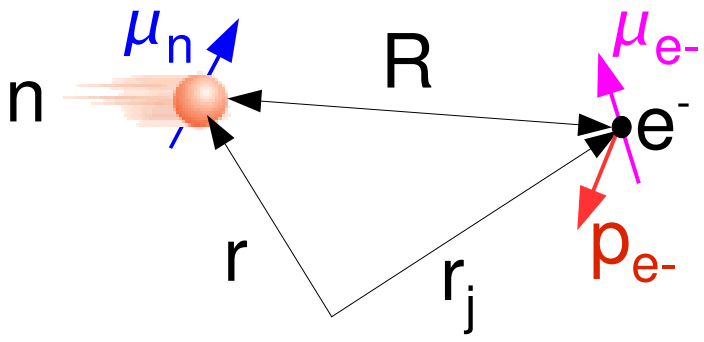

Figure 2.2: Magnetic Scattering: The neutron at position $\boldsymbol{r}$ is scattered by the magnetic field in the sample generated by the spin $\boldsymbol{s}$ and momentum $\boldsymbol{p}$ of electrons at $\boldsymbol{r}_j$

2.3.2 The magnetic selection rule

From Eq. 2.29 a useful geometric selection rule can be easily derived. The evaluation of Eq. 2.29 shows that the magnetic interaction vector $\boldsymbol{M}_{\perp \boldsymbol{Q}}$ is the projection of the magnetic structure factor $\boldsymbol{M}_{\boldsymbol{Q}}$ onto a plane that is perpendicular to the scattering vector $\boldsymbol{Q}$. This proofs that only components of $\boldsymbol{M}_{\boldsymbol{Q}}$ perpendicular to $\boldsymbol{Q}$ contribute to the scattering process as shown in Fig.2.3(a). The magnetic selection rule is a natural consequence of the magnetic interaction being a dipole interaction. When magnetic scattering is analysed it is therefore useful to define a local frame of reference that rotates together with the scattering vector $\boldsymbol{Q}$:

$$\begin{array}{lll} x & \parallel & \boldsymbol{Q} \\ y & \perp & \boldsymbol{Q} \quad \text{in the scattering plane} \\ z & \perp & \boldsymbol{Q} \quad \text{out of the scattering plane} \end{array} \tag{2.33}$$

The coordinate frame is defined in Fig. 2.3(b). In that frame of reference $\boldsymbol{M}_{\perp \boldsymbol{Q}}$ has only non-zero components along the y- and z-axis. In this work it will be further denoted as *analysis frame*. We will see later that this coordinate frame is especially helpful for polarisation analysis experiments.

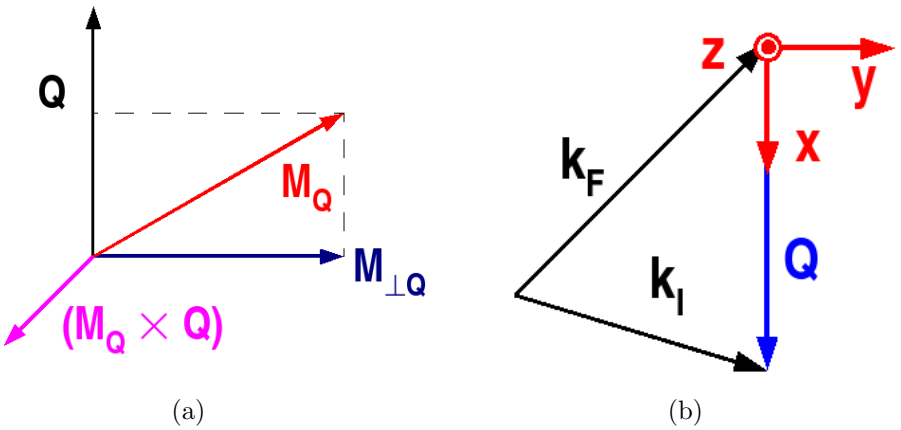

(a) (b)

Figure 2.3: (a) The magnetic selection rule: Only components of $\boldsymbol{M}_{\boldsymbol{Q}}$ perpendicular to $\boldsymbol{Q}$ contribute the scattering process. (b) The basic frame of reference for polarization analysis: $\boldsymbol{k}_i$ and $\boldsymbol{k}_f$ are the initial and final wavevectors of the neutrons; the coordinates are defined with respect to $\boldsymbol{Q}$.

2.3.3 Magnetic form factors

We consider a non-Bravais crystal with magnetic atoms at the positions $\boldsymbol{R}_{ld}$, where l and d signify the unit cell and the position of the ion within this unit cell respectively (s. Eq. 2.20). Then, we can write the position of the νth unpaired electron with spin $\boldsymbol{s}_\nu$ of the ion at $\boldsymbol{R}_{ld}$ as

$$\boldsymbol{r}_i = \boldsymbol{l} + \boldsymbol{d} + \boldsymbol{r}_\nu = \boldsymbol{R}_{ld} + \boldsymbol{r}_\nu, \tag{2.34}$$

where $\boldsymbol{r}_\nu$ is the relative distance of the electron to the ion. Additionally we make the following assumptions:

- The Heitler-London model is valid, therefore the umpaired electrons are close to the equilibrium positions of the magnetic ions.
- The total angular momentum L and the total spin S are good quantum numbers and therefore LS coupling is assumed.

We want to distinguish between two cases. First we look at the situation when the total angular momentum is L=0.[2] Then the magnetic structure factor $\boldsymbol{M}_{\boldsymbol{Q}}$ is only characterised

[2]This is a valid assumption for the magnetic elements in the iron group where the orbital momentum is quenched by crystal fields.

by its spin part and [Lov84]

$$\begin{aligned}\langle n'|\boldsymbol{M_Q}|n\rangle &= \langle n'|\sum_{l,d}\exp(i\boldsymbol{Q}\cdot\boldsymbol{R}_{ld})\sum_{\nu(d)}\exp(i\boldsymbol{Q}\cdot\boldsymbol{r}_\nu)\boldsymbol{s}_\nu|n\rangle \\ &= F_d(\boldsymbol{Q})\langle n'|\sum_{l,d}\exp(i\boldsymbol{Q}\cdot\boldsymbol{R}_{ld})\boldsymbol{S}_{ld}|n\rangle \qquad (2.35)\\ \text{where}\quad F_d(\boldsymbol{Q}) &= \int s_d(\boldsymbol{r})\exp(i\boldsymbol{Q}\cdot\boldsymbol{r})d^3r. \qquad (2.36)\end{aligned}$$

Here $s_d(\boldsymbol{r})$ is the density of the unpaired electrons in the ion d normalised to their number. $F_d(\boldsymbol{Q})$ is called the *magnetic form factor*. The introduction of the magnetic form factor allows to consider all electrons of one magnetic ion at position $\boldsymbol{R}_{ld}$ together and regard $\boldsymbol{S}_{ld}$ as the *total spin* of this ion.
For magnetic ions with $L \neq 0$ [3] a similar result can be derived. In this case the magnetic form factor in Eq. 2.36 is replaced by:

$$\begin{aligned}\frac{1}{2}gF_d(\boldsymbol{Q}) &= \frac{1}{2}g_S\Im_0 + \frac{1}{2}g_L(\Im_0+\Im_2), \qquad (2.37)\\ \text{where}\quad g &= g_S+g_L,\\ g_S &= 1+\frac{S(S+1)-L(L+1)}{J(J+1)},\\ g_L &= 1+\frac{L(L+1)-S(S+1)}{2J(J+1)},\\ \Im_n &= 4\pi\int_0^\infty j_n(Qr)r^2dr.\end{aligned}$$

Here g is the Landé splitting factor and $j_n(Qr)$ are nth order spherical Bessel-functions. In the case of $L \neq 0$ the operator $\boldsymbol{S}_{ld}$ has to regarded as the total angular momentum of the considered magnetic ion [Squ78, Lov84]. The magnetic form factors can be approximated by analytical functions. The functions are ($s = \frac{Q}{4\pi}$)

$$\begin{aligned}\langle j_0(s)\rangle &= A\exp(-as^2)+B\exp(-bs^2)+C\exp(-cs^2)+D \quad \text{for} \quad l=0\\ \langle j_l(s)\rangle &= As^2\exp(-as^2)+Bs^2\exp(-bs^2)+Cs^2\exp(-cs^2)+Ds^2 \quad \text{for} \quad l\neq 0.\end{aligned} \qquad (2.38)$$

The corresponding parameters for 3d and 4d transition metal electrons, the 4f and 5f electrons of rare-earth and actinide ions, respectively are tabulated in [Bro04]. We see that due to the magnetic form factors the neutron intensity falls of exponentially as a function of Q^2 and therefore magnetic scattering is only observable in a limited Q-range. This is demonstrated for the magnetic ion Mn^{3+} in Fig. 2.4.

[3] e.g. ions of the rare earth group.

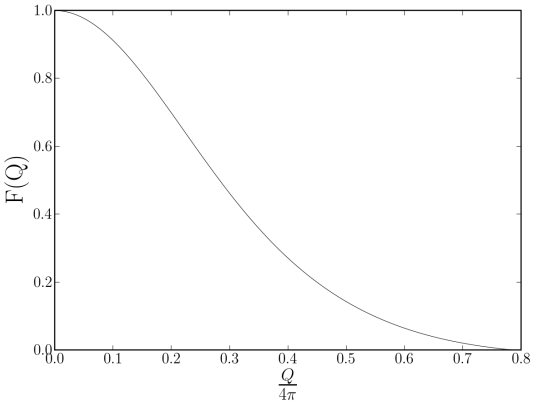

Figure 2.4: The magnetic form factor $F_d(\boldsymbol{Q})$ of the magnetic ion Mn^{3+} is shown.

2.3.4 Magnetic correlation functions

Similar to the nuclear cross-section time-dependent Heisenberg operators can be introduced into the magnetic cross-section when the δ-function for energy conservation is rewritten in correspondence with Eq. 2.6. The expression obtained for the magnetic cross-section is [Squ78]

$$\begin{aligned}\frac{d^2\sigma}{d\Omega dE'} &= \frac{(\gamma r_0)^2}{2\pi\hbar}\frac{k_f}{k_i}\sum_{\alpha,\beta}(\delta_{\alpha\beta}-\hat{Q}_\alpha\hat{Q}_\beta)\sum_{l'd'ld}\frac{1}{4}g_{d'}g_d F^*_{d'}(\boldsymbol{Q})F_d(\boldsymbol{Q}) \\ &\quad\times\int\langle\exp\{-i\boldsymbol{Q}\cdot\boldsymbol{R}_{l'd'}(0)\}\exp\{i\boldsymbol{Q}\cdot\boldsymbol{R}_{ld}(t)\}\rangle\langle S^{\alpha\dagger}_{l'd'}(0)S^{\beta}_{ld}(t)\rangle\exp(-i\omega t),\end{aligned} \tag{2.39}$$

where the time dependent spin operator was defined as $S^\alpha_{ld}(t)=\exp(iHt/\hbar)S^\alpha_{ld}\exp(-iHt/\hbar)$ and we used the expression for the magnetic form factor derived in the previous section. We define the following nuclear and magnetic correlation functions

$$\begin{aligned}I_{jj'}(\boldsymbol{Q},t) &= \langle\exp\{-i\boldsymbol{Q}\cdot\boldsymbol{R}_{l'd'}(0)\}\exp\{i\boldsymbol{Q}\cdot\boldsymbol{R}_{ld}(t)\}\rangle \\ &= I_{jj'}(\boldsymbol{Q},\infty)+I'_{jj'}(\boldsymbol{Q},t) \qquad (2.40)\\ J_{jj'}(t) &= \langle S^{\alpha\dagger}_{l'd'}(0)S^{\beta}_{ld}(t)\rangle = J_{jj'}(\infty)+J'_{jj'}(t). \qquad (2.41)\end{aligned}$$

Here j stands for the combination of l,d. In a second step we divided both correlation functions in a time-independent part at $t=\infty$[4] and a time-dependent part. From this separation into time-dependent and -independent part four different kind of scattering processes can be distinguished:

1. The term $I_{jj'}(\boldsymbol{Q},\infty)J_{jj'}(\infty)$ leads to elastic magnetic scattering. By probing this scattering term the magnetic structure of the sample can be determined by measur-

[4] At the time $t=\infty$ all excitations are faded out.

ing the magnetic Bragg intensities and comparing them with the intensities calculated from different magnetic models.

2. The term $I_{jj'}(\boldsymbol{Q},t)J_{jj'}(\infty)$ is the origin for magneto-vibrational scattering. Here phonons are excited in the sample during the scattering process via the magnetic interaction instead of the nuclear interaction. It will not be considered further in this work.

3. $I_{jj'}(\boldsymbol{Q},t)J_{jj'}(t)$ gives rise to scattering that is inelastic in both the spin and the phonon system. This term will also not be considered in this work.

4. Purely magnetic inelastic scattering is generated via the term $I_{jj'}(\boldsymbol{Q},\infty)J_{jj'}(t)$. No lattice vibrations are excited in this case. Hence, the measurement of this scattering contribution allows to investigate magnetic excitations in a sample.

We consider the first and the last expressions in more detail as they will be used troughout this work.

2.3.5 Magnetic Bragg scattering

We will now derive a general expression for elastic magnetic scattering described by the term $I_{jj'}(\boldsymbol{Q},\infty)J_{jj'}(\infty)$. We have already mentioned in section 1.2.2 that magnetic structures can be incommensurate with the underlying chemical lattice. The periodicity Λ of a magnetic structure in real space can be expressed via the so-called *propagation vector* $\boldsymbol{k}$ where $k = \frac{2\pi}{\Lambda}$ [INO91] and an expansion in Fourier modes. We will specify the concept of the propagation vector further in chapter 3. The total spin (or total angular momentum) of a magnetic ion on the site d in the unit cell l is then expressed as

$$\begin{aligned}
\langle \boldsymbol{S}_{ld} \rangle &= \boldsymbol{R}_d^{\boldsymbol{k}} \cos\left(\boldsymbol{k}\cdot\boldsymbol{l}+\phi_d\right) + \boldsymbol{I}_d^{\boldsymbol{k}} \sin\left(\boldsymbol{k}\cdot\boldsymbol{l}+\phi_d\right) \\
&= \frac{\boldsymbol{R}_d^{\boldsymbol{k}}}{2}\left(e^{i(\boldsymbol{k}\cdot\boldsymbol{l}+\phi_d)} + e^{-i(\boldsymbol{k}\cdot\boldsymbol{l}+\phi_d)}\right) + \frac{\boldsymbol{I}_d^{\boldsymbol{k}}}{2i}\left(e^{i(\boldsymbol{k}\cdot\boldsymbol{l}+\phi_d)} - e^{-i(\boldsymbol{k}\cdot\boldsymbol{l}+\phi_d)}\right) \\
&= \underbrace{\frac{(\boldsymbol{R}_d^{\boldsymbol{k}} - i\boldsymbol{I}_d^{\boldsymbol{k}})}{2} e^{i\phi_d}}_{\equiv \boldsymbol{S}_d^{\boldsymbol{k}}} e^{i\boldsymbol{k}\cdot\boldsymbol{l}} + \underbrace{\frac{(\boldsymbol{R}_d^{\boldsymbol{k}} + i\boldsymbol{I}_d^{\boldsymbol{k}})}{2} e^{-i\phi_d}}_{\equiv \boldsymbol{S}_d^{-\boldsymbol{k}}} e^{-i\boldsymbol{k}\cdot\boldsymbol{l}}
\end{aligned} \tag{2.42}$$

$\boldsymbol{R}_d^{\boldsymbol{k}}$ and $\boldsymbol{I}_d^{\boldsymbol{k}}$ are the real and imaginary part of the *magnetic Fourier mode* $\boldsymbol{S}_d^{\boldsymbol{k}}$ for the propagation vector $\boldsymbol{k}$. ϕ_d defines a phase with respect to the origin. By different choices of $\boldsymbol{S}_d^{\boldsymbol{k}}$ and $\boldsymbol{k}$ different magnetic structures with different periodicities can be modelled. The expression for the cross-section is generally evaluated separately for the two distinct Fourier components for the two propagation vector $\boldsymbol{k}$ and $-\boldsymbol{k}$, respectively [INO91]. For

$\boldsymbol{k}$ we find (for the magnetic structure we replace $\boldsymbol{l}$ by $\boldsymbol{R}_{l'd'}$, compare Eq.2.15)

$$\begin{aligned}
&\sum_{jj'} I_{jj'}(\boldsymbol{Q},\infty)J_{jj'}(\infty) \\
&= \sum_{l'd'ld} \langle \exp\{-i\boldsymbol{Q}\cdot\boldsymbol{R}_{l'd'}(0)\}\exp\{i\boldsymbol{Q}\cdot\boldsymbol{R}_{ld}(\infty)\}\rangle \langle S_{d'}^{\boldsymbol{k}\alpha\dagger} e^{-i\boldsymbol{k}\cdot\boldsymbol{R}_{l'd'}(0)} S_d^{\boldsymbol{k}\beta} e^{i\boldsymbol{k}\cdot\boldsymbol{R}_{ld}(\infty)}\rangle \\
&= N\sum_l \exp\{i(\boldsymbol{Q}+\boldsymbol{k})\cdot\boldsymbol{l}\}\sum_{dd'} \exp(-W_{d'}(\boldsymbol{Q}))\exp(-W_d(\boldsymbol{Q}))\exp(-i\boldsymbol{Q}\cdot\boldsymbol{d'})\exp(i\boldsymbol{Q}\cdot\boldsymbol{d}) S_{d'}^{\boldsymbol{k}\alpha\dagger} S_d^{\boldsymbol{k}\beta} \\
&= \sum_\tau \delta(\boldsymbol{Q}+\boldsymbol{k}-\boldsymbol{\tau})\sum_{dd'} \exp(-W_{d'}(\boldsymbol{Q}))\exp(-W_d(\boldsymbol{Q}))\exp(-i\boldsymbol{Q}\cdot\boldsymbol{d'})\exp(i\boldsymbol{Q}\cdot\boldsymbol{d}) S_{d'}^{\boldsymbol{k}\alpha\dagger} S_d^{\boldsymbol{k}\beta},
\end{aligned} \tag{2.43}$$

and for $-\boldsymbol{k}$ respectively

$$\sum_\tau \delta(\boldsymbol{Q}-\boldsymbol{k}-\boldsymbol{\tau})\sum_{dd'} \exp(-W_{d'}(\boldsymbol{Q}))\exp(-W_d(\boldsymbol{Q}))\exp(-i\boldsymbol{Q}\cdot\boldsymbol{d'})\exp(i\boldsymbol{Q}\cdot\boldsymbol{d}) S_{d'}^{-\boldsymbol{k}\alpha\dagger} S_d^{-\boldsymbol{k}\beta}. \tag{2.44}$$

We used the results in Eqs 2.15, 2.17 and 2.20 obtained for nuclear scattering in order evaluate the sum over l and l'. The full expression for both terms taking into account the magnetic form factors and all prefactors is given by

$$\begin{aligned}
\left(\frac{d\sigma}{d\Omega}\right)_{mag,el} &= N(\gamma r_0)^2 \frac{(2\pi)^3}{v_0} \sum_{\boldsymbol{\tau}} \sum_{\{\boldsymbol{k}\}} \sum_{\alpha,\beta} (\delta_{\alpha\beta} - \hat{Q}_\alpha \hat{Q}_\beta) F_M^{\boldsymbol{k}\alpha\dagger} F_M^{\boldsymbol{k}\beta} \delta(\boldsymbol{Q}-\boldsymbol{k}-\boldsymbol{\tau}), \\
\text{where} \quad \boldsymbol{F}_M^{\boldsymbol{k}} &= \sum_d g_d F_d(\boldsymbol{Q}) \exp(-W_d(\boldsymbol{Q}))\exp(i\boldsymbol{Q}\cdot\boldsymbol{d})\boldsymbol{S}_d^{\boldsymbol{k}},
\end{aligned} \tag{2.45}$$

is the *magnetic structure factor*. The sum over $\{\boldsymbol{k}\}$ is over both propagation vectors. From the δ-function we see that when neutrons are scattered from an incommensurate magnetic structure the magnetic intensity appears at satellite positions $\boldsymbol{Q} = \boldsymbol{\tau} \pm \boldsymbol{k}$ relative to the nuclear Bragg peaks at $\boldsymbol{\tau}$ (s. Fig 2.5). When several $\boldsymbol{k}$-vectors are present in the magnetic structure the sum over $\{\boldsymbol{k}\}$ is extended over all of them. If the magnetic structure is commensurate with the chemical lattice $\boldsymbol{k} = 0$ (e.g. for a simple ferromagnet) and the magnetic scattering appears at $\boldsymbol{Q} = \boldsymbol{\tau}$ and in Eq. 2.45 we will have $\boldsymbol{S}_d^0 = \boldsymbol{R}_d^0$ (compare Eq. 2.42) and $\delta(\boldsymbol{Q}-\boldsymbol{k}-\boldsymbol{\tau}) \longrightarrow \delta(\boldsymbol{Q}-\boldsymbol{\tau})$.

2.3.6 Inelastic magnetic scattering

We will relate the inelastic term $I_{jj'}(\boldsymbol{Q},\infty)J_{jj'}(t)$ to the magnetic dynamic susceptibility and to the magnetisation of a magnetic sample. The corresponding inelastic magnetic

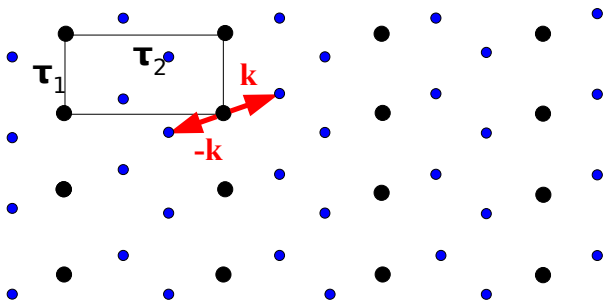

Figure 2.5: A incommensurate magnetic structure with propagation vector $\boldsymbol{k}$ is illustrated in reciprocal space.

cross-section is

$$\left(\frac{d^2\sigma}{d\Omega dE'}\right)_{mag,inel} = \frac{(\gamma r_0)^2}{2\pi\hbar}\frac{k_f}{k_i}\sum_{\alpha,\beta}(\delta_{\alpha\beta}-\hat{Q}_\alpha\hat{Q}_\beta)\sum_{l'd'ld}\frac{1}{4}g_{d'}g_d F^*_{d'}(\boldsymbol{Q})F_d(\boldsymbol{Q}) \times \int\langle\exp\{-i\boldsymbol{Q}\cdot\boldsymbol{R}_{l'd'}(0)\}\exp\{i\boldsymbol{Q}\cdot\boldsymbol{R}_{ld}(\infty)\}\rangle\langle S^\alpha_{l'd'}(0)S^\beta_{ld}(t)\rangle\exp(-i\omega t). \tag{2.46}$$

We will quickly review some results of statistical quantum mechanics which we will use in the following. We consider a quantum mechanical system whose ground state is described by the Hamiltonian H_0. If an external force $F(t)$ couples to the operator B of the system we can write the new Hamiltonian H of the system like

$$H = H_0 + H'(t) = H_0 - F(t)B, \tag{2.47}$$

where $F(t) = 0$ for $t \leqslant t_0$. It can be shown [Sch97] that the response of the system in the observable $\langle A\rangle$ due to the perturbation is given by

$$\Delta\langle A(t)\rangle = \langle A(t)\rangle - \langle A\rangle_0 = \int dt'\chi_{AB}(t-t')F(t'). \tag{2.48}$$

Here the *dynamic susceptibility* or *linear response function* is defined by

$$\chi_{AB}(t-t') = \frac{i}{\hbar}\Theta(t-t')\langle[A(t),B(t')]\rangle_0, \tag{2.49}$$

namely the expectation of the commutator of the two Heisenberg operators $A(t)$ and $B(t')$ (with respect to the Hamiltonian H_0). The introduced Heavyside step-function Θ conserves causality. Finally we will use the *fluctuation-dissipation-theorem* [Lov84, Sch97]

$$Im(\chi_{AB}(\omega)) = \hbar\pi G_{AB}(\omega)\left[\exp\left(-\frac{\hbar\omega}{k_BT}\right)-1\right], \tag{2.50}$$

here $G_{AB}(t) = \langle A(0)B(t)\rangle$. $\chi_{AB}(\omega)$ and $G_{AB}(\omega)$ are the Fourier transforms of $\chi_{AB}(t)$ and $G_{AB}(t)$. From Eq. 2.46 we can define an operator (s. reference [Lov84] for details)

$$T^{\alpha}(\boldsymbol{Q},t) = \sum_{ld} \frac{1}{2} g_d F_d(\boldsymbol{Q}) \exp(-W_d(\boldsymbol{Q})) \exp\left\{-i\boldsymbol{Q}\cdot(\boldsymbol{l}-\boldsymbol{d})\right\} \boldsymbol{S}_{ld}(t) \tag{2.51}$$

and therefore find for

$$G_{\alpha\beta}(\boldsymbol{Q},t) = \langle T^{\alpha}_{\boldsymbol{Q}}(0) T^{\beta}_{-\boldsymbol{Q}}(t)\rangle. \tag{2.52}$$

Together with Eq. 2.50 and by taking into account the integration in time the inelastic magnetic cross-section can be rewritten as

$$\left(\frac{d^2\sigma}{d\Omega dE'}\right)_{mag,inel} = -\frac{(\gamma r_0)^2}{\pi\hbar}\frac{k_f}{k_i}\left\{n(\omega)+1\right\}\sum_{\alpha,\beta}(\delta_{\alpha\beta}-\hat{Q}_{\alpha}\hat{Q}_{\beta})Im(\chi_{\alpha\beta}(\boldsymbol{Q},\omega)), \tag{2.53}$$

where we defined $n(\omega) = \left\{\exp\left(\frac{\hbar\omega}{k_B T}\right) - 1\right\}^{-1}$ as the *Bose-Einstein function*. The factor $\{n(\omega)+1\}$ takes into account the Bose-Einstein statistics of excited quasi-particles. We note that we have related the magnetic inelastic cross-section to the magnetic dynamic susceptibility

$$\chi_{\alpha\beta}(\boldsymbol{Q},t) = \frac{(2\mu_B)^2}{N}\frac{i}{\hbar}\langle[T^{\alpha}_{\boldsymbol{Q}}(0)T^{\beta}_{-\boldsymbol{Q}}(t)]\rangle \tag{2.54}$$

that is the response of the magnetisation of the sample to an applied magnetic field B. Through this relationship the microscopic information obtained in a neutron scattering experiment can be compared to the results of macroscopic probes that measure the sample magnetisation or the magnetic susceptibility.

2.4 Polarized neutron scattering

2.4.1 Polarisation of a neutron beam

A neutron spin represents a spin-$\frac{1}{2}$-system that is generally expressed as the state vector

$$\chi = a\chi_{\uparrow} + b\chi_{\downarrow} = a\begin{pmatrix}1\\0\end{pmatrix} + b\begin{pmatrix}0\\1\end{pmatrix} \tag{2.55}$$

which describes the superposition of eigenstates being parallel or antiparallel to the chosen quantisation axis in a two-dimensional Hilbert space H_2. From now on they will be called the *up* and *down states*, respectively. $|a|^2$ and $|b|^2$ are the probabilities of the system being in the up or the down state. Because the probability that the system is in any of these two state is 1 the normalisation condition

$$\chi^{\dagger}\chi = |a|^2 + |b|^2 = 1 \tag{2.56}$$

has to be fulfilled.
The polarisation of a single neutron is defined as a unit vector pointing in the direction of the neutron spin, given by the expectation value of the Pauli-matrices defined in Eq. 2.23 (s. also [Lov84]):

$$\begin{aligned} \boldsymbol{P} &\equiv < \hat{\boldsymbol{\sigma}} >= \chi^\dagger \hat{\boldsymbol{\sigma}} \chi = Tr(\hat{\varrho}\hat{\boldsymbol{\sigma}}), \\ \text{where} \quad \hat{\varrho} &= \chi\chi^\dagger = \begin{pmatrix} |a|^2 & ab^* \\ ba^* & |b|^2 \end{pmatrix} \end{aligned} \tag{2.57}$$

is the density matrix operator which defines the probability of a certain spin state [Fan57]. If the following valid choice

$$a = \cos\frac{\theta}{2} e^{i\frac{\phi}{2}} \qquad b = \sin\frac{\theta}{2} e^{-i\frac{\phi}{2}} \tag{2.58}$$

is used then we find for the polarisation of the neutron

$$\boldsymbol{P} = \begin{pmatrix} 2\Re(a^*b) \\ 2\Im(a^*b) \\ |a|^2 - |b|^2 \end{pmatrix} = \begin{pmatrix} \sin\theta\cos\phi \\ \sin\theta\sin\phi \\ \cos\theta \end{pmatrix} = \hat{\boldsymbol{n}}, \tag{2.59}$$

where $\hat{\boldsymbol{n}}$ is a unit vector defined in spherical coordinates (θ, ϕ). This geometrical interpretation of a general spin-$\frac{1}{2}$-state is called the *Bloch-representation*. We see that a single neutron is always fully polarised. The polarization of a neutron beam is then

$$\boldsymbol{P} = \frac{1}{N}\sum_i \boldsymbol{P}_i = << \hat{\boldsymbol{\sigma}} >>_{beam}, \tag{2.60}$$

where N is the number of neutrons in the beam and $\boldsymbol{P}_i$ is their corresponding polarization. Therefore the polarization is defined as a property of a neutron beam. This statistical quantity will be measured by averaging over all neutrons in the beam. For an *unpolarised beam* $\boldsymbol{P_0}$ is then zero; for a *completely polarised beam* $|\boldsymbol{P_0}| = 1$; and for a *partially polarised beam* $0 < |\boldsymbol{P_0}| < 1$.
The direction of the polarisation vector can be manipulated by means of magnetic fields:

- In a homogeneous magnetic field $\boldsymbol{B}$ the components of the polarisation that are perpendicular to the field direction start to precess around the field axis (s. e.g [Wil88, Mez93]) as described by the action

$$\frac{d\boldsymbol{P}(t)}{dt} = -\gamma_L(\boldsymbol{P}(t) \times \boldsymbol{B}). \tag{2.61}$$

  This is called *Larmor-precession*. The precession frequency is called *Larmor frequency* and is given by $\omega_L = \frac{\gamma e}{m_p} B = \gamma_L B$ where $\gamma_L = 2\pi \cdot 2913 \frac{rad}{sG}$.

- From Eq. 2.61 we see that the direction parallel to the magnetic field $\boldsymbol{B}$ is conserved. If the direction of the magnetic field is rotated slowly with respect to Larmor frequency $\omega \ll \omega_L$ then the component of the polarisation vector that is parallel to $\boldsymbol{B}$ will be turned with the field direction [Güt32, Cyw06]. This is called an *adiabatic transition* and is illustrated in Fig. 2.6.

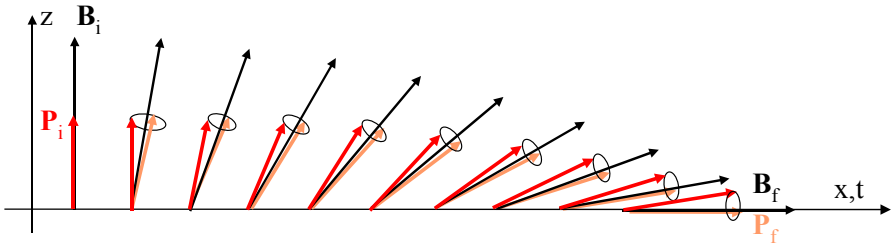

Figure 2.6: An adiabatic transition of the polarisation vector: the polarization vector precesses with ω_L around the magnetic field that is turned with a frequency $\omega \ll \omega_L$.

2.4.2 The Blume-Maleyev equations

If the incident beam of neutrons is polarised new terms in the equations for the neutron cross-section derived in the previous sections appear. In Eq. 2.2 the average over the spin states of the neutrons incident of the sample has to be evaluated taking into account the polarisation of the neutron beam properly. The cross-section we want to evaluate is

$$\frac{d^2\sigma}{d\Omega dE'} = \frac{k_f}{k_i}\frac{1}{2\pi\hbar}\int dt \sum_{\sigma_i,\sigma_f} p_\sigma \langle\sigma_i|V^\dagger_{\boldsymbol{Q}}(0)|\sigma_f\rangle\langle\sigma_f,|V_{\boldsymbol{Q}}(t)|\sigma_i\rangle \exp(-i\omega t),$$
$$\text{where} \qquad V_{\boldsymbol{Q}}(t) = \langle \boldsymbol{k}_f|V(t)|\boldsymbol{k}_i\rangle = N_{\boldsymbol{Q}}(t) + (\gamma r_0)\hat{\boldsymbol{\sigma}}\cdot \boldsymbol{M}_{\perp\boldsymbol{Q}}(t). \tag{2.62}$$

Here we already expressed the scattering potentials in terms of Heisenberg operators (s. section 2.2.1) with help of Eq. 2.6 and used the results obtained for the evaluation of nuclear and magnetic potentials before. The density matrix in Eq. 2.57 can be expressed through

$$\hat{\varrho} = \sum_{\sigma_i,\sigma_f} p_\sigma |\sigma\rangle\langle\sigma|, \tag{2.63}$$

if it is diagonal [Lov84]. The sum and average over the spin states then are represented by

$$\sum_{\sigma_i,\sigma_f} p_\sigma \langle\sigma_i,|V^\dagger_{\boldsymbol{Q}}(0)|\sigma_f\rangle\langle\sigma_f,|V_{\boldsymbol{Q}}(t)|\sigma_i\rangle = \sum_{\sigma_i}\langle\sigma_i|V^\dagger_{\boldsymbol{Q}}(0)V_{\boldsymbol{Q}}(t)\hat{\varrho}|\sigma_i\rangle = Tr(\hat{\varrho}V^\dagger_{\boldsymbol{Q}}(0)V_{\boldsymbol{Q}}(t)) \tag{2.64}$$

and therefore we can rewrite the cross-section as

$$\frac{d^2\sigma}{d\Omega dE'} = \frac{k_f}{k_i}\frac{1}{2\pi\hbar}\int dt Tr(\hat{\varrho}V^\dagger_{\boldsymbol{Q}}(0)V_{\boldsymbol{Q}}(t))\exp(-i\omega t). \tag{2.65}$$

This expression was evaluated in the 1960s by various contributors [IM62, Blu63, Izy63, Blu64, SB68] by use of the density matrix formalism that allows to calculate the mean values of properties of systems, such as neutron beams, which consist of an incoherent superposition of particles in different pure states. The formalism is described in [Fan57]. Here we only give the result of this complex derivation:

$$\begin{aligned}\frac{d^2\sigma}{d\Omega dE'} &= \frac{k_f}{k_i}\frac{1}{2\pi\hbar}\int dt\Big\{ \\ &\langle N_{\boldsymbol{Q}} N_{\boldsymbol{Q}}^\dagger\rangle + && \text{pure nuclear contribution} \\ &+(\gamma r_0)^2\langle \boldsymbol{M}_{\perp\boldsymbol{Q}}\boldsymbol{M}_{\perp\boldsymbol{Q}}^\dagger\rangle + && \text{pure magnetic contribution} \\ &+(\gamma r_0)\boldsymbol{P_0}\left[\langle N_{\boldsymbol{Q}}^\dagger \boldsymbol{M}_{\perp\boldsymbol{Q}}\rangle + \langle \boldsymbol{M}_{\perp\boldsymbol{Q}}^\dagger N_{\boldsymbol{Q}}\rangle\right] - && \text{nuclear-magnetic interference} \\ &-i(\gamma r_0)\boldsymbol{P_0}\langle \boldsymbol{M}_{\perp\boldsymbol{Q}}\times\boldsymbol{M}_{\perp\boldsymbol{Q}}^\dagger\rangle && \text{chiral magnetic contribution} \\ &\Big\}\exp(-i\omega t), \end{aligned} \tag{2.66}$$

where $\boldsymbol{P_0}$ is the polarization vector of the incident beam. We readily divided the cross-section in four different terms. The first two are independent of the initial polarisation vector $\boldsymbol{P_0}$ and therefore are also non-zero for an unpolarised beam. They are the pure nuclear and magnetic contribution. The last two terms are linearly dependent on $\boldsymbol{P_0}$ and are only non-zero if $\boldsymbol{P_0} \neq 0$. The third term is known as the *nuclear-magnetic interference term* and appears when nuclear and magnetic contributions appear at the same position in ($\boldsymbol{Q}$, ω)-space (e.g. for a ferromagnet). The last term is the *chiral contribution* that is only present when helical magnetic structures or fluctuations exist in the sample. This will be demonstrated later. We note, that by using a polarised beam more information can be gained compared to the unpolarised situation.
Additionally the spin state of the neutrons may change during the scattering process due to the magnetic interaction and consequently the polarisation of the beam $\boldsymbol{P_0} = \langle\hat{\boldsymbol{\sigma}}\rangle$ is changed. The expectation of $\hat{\boldsymbol{\sigma}}$ after the scattering process and therefore the final polarisation is given by

$$\boldsymbol{P'} = \frac{Tr(\hat{\varrho}V_{\boldsymbol{Q}}^\dagger\hat{\boldsymbol{\sigma}}V_{\boldsymbol{Q}})}{Tr(\hat{\varrho}V_{\boldsymbol{Q}}^\dagger V_{\boldsymbol{Q}})}, \tag{2.67}$$

where the denominator normalises the expression to the probability that any scattering process takes place. The full expression is then

$$\boldsymbol{P'}\frac{d^2\sigma}{d\Omega dE'} = \frac{k_f}{k_i}\frac{1}{2\pi\hbar}\int dt Tr(\hat{\varrho}V_{\boldsymbol{Q}}^\dagger(0)\hat{\boldsymbol{\sigma}}V_{\boldsymbol{Q}}(t))\exp(-i\omega t). \tag{2.68}$$

Again the evaluation of the trace over the neutron spin states [IM62, Blu63, Izy63, Blu64, SB68] leads to the expression for the *final polarization vector* after the scattering process:

$$\begin{aligned}\boldsymbol{P'}\frac{d^2\sigma}{d\Omega dE'} &= \frac{k_f}{k_i}\frac{1}{2\pi\hbar}\int dt\Big\{\boldsymbol{P_0}\langle N_{\boldsymbol{Q}}N_{\boldsymbol{Q}}^\dagger(t)\rangle - (\gamma r_0)^2\boldsymbol{P_0}\langle \boldsymbol{M}_{\perp\boldsymbol{Q}}\boldsymbol{M}_{\perp\boldsymbol{Q}}^\dagger(t)\rangle + \\ &+ (\gamma r_0)^2\langle(\boldsymbol{P_0}\boldsymbol{M}_{\perp\boldsymbol{Q}}^\dagger(t))\boldsymbol{M}_{\perp\boldsymbol{Q}}\rangle + (\gamma r_0)^2\langle \boldsymbol{M}_{\perp\boldsymbol{Q}}^\dagger(t)(\boldsymbol{P_0}\boldsymbol{M}_{\perp\boldsymbol{Q}})\rangle + \\ &+ (\gamma r_0)\left(\langle N_{\boldsymbol{Q}}^\dagger\boldsymbol{M}_{\perp\boldsymbol{Q}}(t)\rangle + \langle \boldsymbol{M}_{\perp\boldsymbol{Q}}^\dagger N_{\boldsymbol{Q}}(t)\rangle\right) + \\ &+ i(\gamma r_0)\boldsymbol{P_0}\times\left(\langle \boldsymbol{M}_{\perp\boldsymbol{Q}}^\dagger N_{\boldsymbol{Q}}(t)\rangle - \langle N_{\boldsymbol{Q}}^\dagger\boldsymbol{M}_{\perp\boldsymbol{Q}}(t)\rangle\right) + \\ &+ i(\gamma r_0)^2\langle \boldsymbol{M}_{\perp\boldsymbol{Q}}\times\boldsymbol{M}_{\perp\boldsymbol{Q}}^\dagger(t)\rangle\Big\}\exp(-i\omega t). \end{aligned} \tag{2.69}$$

The Eqs 2.66 and 2.69 are known as the *Blume-Maleyev equations*. Before we discuss the different contributions present in Eq. 2.69 we will rewrite it in tensor form for convenience [Bro01, JKR$^+$07]:

$$\boldsymbol{P'} \;=\; \tilde{\boldsymbol{P}}\boldsymbol{P_0} + \boldsymbol{P''}, \tag{2.70}$$

where $\boldsymbol{P_0}$ and $\boldsymbol{P'}$ are again the initial polarisation vector before the scattering process and the final polarisation vector after the scattering process, respectively. $\tilde{\boldsymbol{P}}$ and $\boldsymbol{P''}$ are given by the following equations:

$$\sigma\tilde{\boldsymbol{P}} = \begin{pmatrix} (N-M^y-M^z) & iI^z & -iI^y \\ -iI^z & (N+M^y-M^z) & M_{mix} \\ iI^y & M_{mix} & (N-M^y+M^z) \end{pmatrix}, \qquad \sigma\boldsymbol{P''} = \begin{pmatrix} C \\ R^y \\ R^z \end{pmatrix}. \tag{2.71}$$

σ denotes the neutron cross-section for polarised neutrons from Eq. 2.66 and is rewritten as

$$\sigma \;\equiv\; \frac{d^2\sigma}{d\Omega dE'} = \underbrace{N + M^y + M^z}_{\text{independent of } \boldsymbol{P_0}} \; \underbrace{- P_0^x C + P_0^y R^y + P_0^z R^z}_{\text{dependent on } \boldsymbol{P_0}}. \tag{2.72}$$

All the terms included in Eqs. 2.71, 2.72 are determined by the nuclear structure factor $N_{\boldsymbol{Q}}(t)$ and the magnetic interaction vector $\boldsymbol{M}_{\perp\boldsymbol{Q}}(t)$ and are summarised in Table 2.1. They are given in the analysis frame defined in Eq. 2.33.

By investigating this new form for the final polarisation vector in Eqs. 2.71 and 2.71 we can directly identify that $\tilde{\boldsymbol{P}}$ describes the rotation of $\boldsymbol{P_0}$ due to the interaction with the sample whereas and $\boldsymbol{P''}$ takes into account that the sample can also polarise the neutron beam.

The measured quantity is the polarization matrix, namely the components of the final polarization vector after the scattering process for all three directions of the incident beam polarization,

$$\mathrm{P}_{ij} = (P_{i0}\tilde{P}_{ji} + P''_j)/|\boldsymbol{P_0}|, \tag{2.73}$$

where i and j $(i, j = x, y, z)$ denote the directions of the incident and final polarization vectors, respectively.

A *polarization analysis* experiment gives additional information compared to just measuring the neutron scattering cross-section in Eq. 2.72. The additional data can be used to disentangle the different contributions to the scattering cross-section for each point in $(\mathbf{Q}, \omega)$-space. In an unpolarised neutron scattering experiment the purely nuclear and purely magnetic contributions are superposed whereas all the other contributions are cancelled due to the unpolarised incident beam (s. Eq. 2.72).

In order to demonstrate the meaning of the polarisation tensor we investigate it for a simple case. We assume that we determine the polarisation tensor on a pure magnetic reflection of a simple collinear antiferromagnet. Then, without loss of generality the magnetic interaction vector has the form

$$\boldsymbol{M}_{\perp\boldsymbol{Q}} = m\left[\hat{e}_y\cos(\alpha) + \hat{e}_z\sin(\alpha)\right], \tag{2.74}$$

where the $\hat{e}_i$ ($i = x, y, z$) are unit vectors in the analysis frame defined in Eq. 2.33[5] and α is the angle between $\boldsymbol{M}_{\perp\boldsymbol{Q}}$ and the y-axis as also denoted in Fig. 2.7. m is a real number denoting the magnitude of the interaction vector on the specific reflection. Further on a pure magnetic reflection all terms in Eqs. 2.71, 2.72 including the nuclear structure factor $N_{\boldsymbol{Q}}$ are equal to zero, namely N, $R^{y/z}$ and $I^{y/z}$. The other terms can be easily calculated (for a more clear presentation we will set $(\gamma r_0)^2 = 1$ for the calculation):

- $M^y + M^z = m^2\cos^2(\alpha) + m^2\sin^2(\alpha) = m^2$.
- $-M^y + M^z = -(M^y - M^z) = -m^2\cos^2(\alpha) + m^2\sin^2(\alpha) = -m^2\cos(2\alpha)$.
- $M_{mix} = m^2\cos(\alpha)\sin(\alpha) + m^2\sin(\alpha)\cos(\alpha) = m^2\sin(2\alpha)$.
- $C = 0$ as $\boldsymbol{M}_{\perp\boldsymbol{Q}}$ is real and therefore $\boldsymbol{M}_{\perp\boldsymbol{Q}} \parallel \boldsymbol{M}^{\dagger}_{\perp\boldsymbol{Q}}$.

In conclusion we obtain the polarisation tensor

$$\sigma = m^2 \quad \text{and} \quad \mathrm{P} = \begin{pmatrix} -1 & 0 & 0 \\ 0 & \cos(2\alpha) & \sin(2\alpha) \\ 0 & \sin(2\alpha) & -\cos(2\alpha) \end{pmatrix}. \tag{2.75}$$

The interpretation of this polarisation tensor is that the component of the initial polarisation vector that is parallel to x, and thus to $\boldsymbol{Q}$, is always perfectly flipped, whereas the y and z components are rotated by 180° around the magnetic interaction vector $\boldsymbol{M}_{\perp\boldsymbol{Q}}$. This is summarised in Fig. 2.7. We see that by evaluating the polarisation tensor the direction of the magnetic interaction vector with respect to the crystallographic axis can be determined. By doing so for a for a few magnetic reflections the direction of the magnetic moments often can be extracted. However, it contains no information about the magnitude of the moments[6].

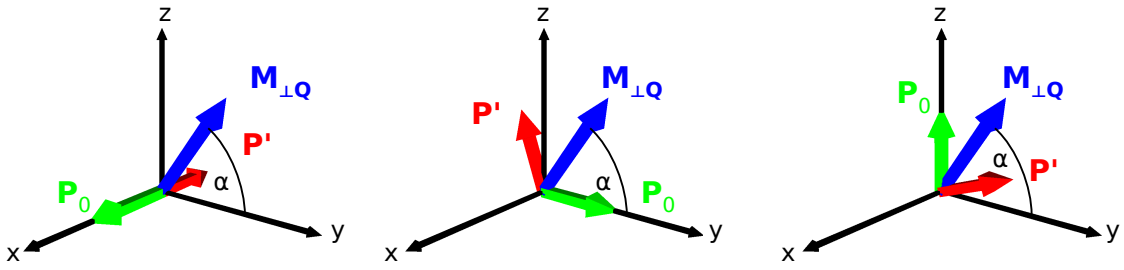

Figure 2.7: The change of the polarisation vector in the scattering process on a pure magnetic reflection with a magnetic interaction vector of the form denoted in Eq. 2.74 is shown. The three view panels show the effect on the polarisation for the x-, y- and z-component of the polarisation vector (from left to the right), respectively.

[5] Remember in this frame the x-component of $\boldsymbol{M}_{\perp\boldsymbol{Q}}$ is per definition equal to zero.
[6] At least on pure magnetic reflections.

Table 2.1: Terms contained in Eqs. 2.71,2.72; $\langle \hat{A}_{\boldsymbol{Q}} \hat{B}^{\dagger}_{\boldsymbol{Q}} \rangle_{\omega} = \frac{1}{2\pi\hbar} \int dt \exp(-i\omega t) \langle \hat{A}_{\boldsymbol{Q}} \hat{B}^{\dagger}_{\boldsymbol{Q}}(t) \rangle$ (e.g. s. [Mal99])are inelastic correlation functions; $\boldsymbol{Q}$ is the scattering vector and $\hbar\omega$ the energy transfer; k_i and k_f denote the magnitude of the wavevector of incident and scattered neutrons, respectively; x, y, z denote the three directions in space according to Eq. 2.33. By performing the limit $\lim_{t\to\infty} \langle A_{\boldsymbol{Q}} B^{\dagger}_{\boldsymbol{Q}}(t) \rangle = \langle A_{\boldsymbol{Q}} \rangle \langle B^{\dagger}_{\boldsymbol{Q}} \rangle$ the terms used for elastic scattering can be obtained.

Item	correlation functions	description
N	$\frac{k_f}{k_i} \langle N_{\boldsymbol{Q}} N^{\dagger}_{\boldsymbol{Q}} \rangle_{\omega}$	nuclear contribution
$M^{y/z}$	$(\gamma r_0)^2 \frac{k_f}{k_i} \langle M^{y/z}_{\perp \boldsymbol{Q}} M^{\dagger y/z}_{\perp \boldsymbol{Q}} \rangle_{\omega}$	y- and z-components of the magnetic contribution.
$R^{y/z}$	$(\gamma r_0) \frac{k_f}{k_i} \langle N^{\dagger}_{\boldsymbol{Q}} M^{y/z}_{\perp \boldsymbol{Q}} \rangle_{\omega} + \langle M^{\dagger y/z}_{\perp \boldsymbol{Q}} N_{\boldsymbol{Q}} \rangle_{\omega}$	real parts of the nuclear-magnetic interference term.
$I^{y/z}$	$(\gamma r_0) \frac{k_f}{k_i} \langle N^{\dagger}_{\boldsymbol{Q}} M^{y/z}_{\perp \boldsymbol{Q}} \rangle_{\omega} - \langle M^{\dagger y/z}_{\perp \boldsymbol{Q}} N_{\boldsymbol{Q}} \rangle_{\omega}$	imaginary parts of the nuclear-magnetic interference term.
C	$i(\gamma r_0)^2 \frac{k_f}{k_i} (\langle M^{y}_{\perp \boldsymbol{Q}} M^{\dagger z}_{\perp \boldsymbol{Q}} \rangle_{\omega} - \langle M^{z}_{\perp \boldsymbol{Q}} M^{\dagger y}_{\perp \boldsymbol{Q}} \rangle_{\omega})$	chiral contribution
M_{mix}	$(\gamma r_0)^2 \frac{k_f}{k_i} (\langle M^{y}_{\perp \boldsymbol{Q}} M^{\dagger z}_{\perp \boldsymbol{Q}} \rangle_{\omega} + \langle M^{z}_{\perp \boldsymbol{Q}} M^{\dagger y}_{\perp \boldsymbol{Q}} \rangle_{\omega})$	mixed magnetic contribution or magnetic-magnetic interference term

2.4.3 Polarised neutron scattering on chiral magnets

In order to demonstrate the usefulness of polarisation analysis for the investigation of helical magnets we now consider the neutron scattering cross-section for a single magnetic helix as it was calculated from the Bak-Jensen model in section 1.2.2. For this purpose we consider a cubic lattice with one single magnetic ion situated at the origin of the chemical unit cell, so we will neglect the index d used for non-Bravais lattices here. Furthermore, we will not take into account a magnetic form factor in this example. The magnetic helix is chosen to have a magnetic propagation vector $\boldsymbol{k} = k\hat{e}_z$. According to Eq. 2.42 we choose $\boldsymbol{R_k} = a\hat{e}_x$ and $\boldsymbol{I_k} = b\hat{e}_y$ and $\phi = 0$. Here $\hat{e}_i$ with i = x, y, z are unit vectors in the Cartesian coordinate system that is spanned by the cubic crystallographic axes. Therefore the magnetic helix is defined by:

$$\begin{aligned} \langle \boldsymbol{S}_l \rangle &= a\hat{e}_x \cos(\boldsymbol{k}\cdot\boldsymbol{l}) + b\hat{e}_y \sin(\boldsymbol{k}\cdot\boldsymbol{l}) \\ &= \underbrace{\frac{(a\hat{e}_x - ib\hat{e}_y)}{2}}_{\equiv \boldsymbol{S^k}} e^{i\boldsymbol{k}\cdot\boldsymbol{l}} + \underbrace{\frac{(a\hat{e}_x + ib\hat{e}_y)}{2}}_{\equiv \boldsymbol{S^{-k}}} e^{-i\boldsymbol{k}\cdot\boldsymbol{l}} \end{aligned} \tag{2.76}$$

We note that for $a = b$ or $a \neq b$ we have a circular or elliptical helix, respectively. For educational reasons we will consider two more cases, namely:

- $a = 1$ and $b = 0$: This corresponds to a simple amplitude modulated structure, where the magnetic moment is not turned when one propagates through the crystal.
- $\boldsymbol{R^k} = a\hat{e}_x$ and $\boldsymbol{I^k} = b\hat{e}_z$: This corresponds to a cycloidical magnetic structure, where

the magnetic moments also rotates as for a helix, however in a plane that is parallel to the propagation vector.

All the different cases are demonstrated in table 2.2. We will now calculate the cross-section and polarisation tensor for the different structures for illustration. As the magnetic scattering is dependent on the orientation of the magnetic structure factor with respect to the scattering vector $\boldsymbol{Q}$ we will do so for a specific position in reciprocal space. We chose to calculate the relevant quantities for the special case of the two magnetic satellites around the nuclear Bragg reflection (0,0,1), namely $\boldsymbol{Q}_{\pm} = (0, 0, 1 \pm k)$ and $\boldsymbol{Q}$ will be parallel to the propagation vector $\boldsymbol{k} = k\hat{e}_z$ for both reflections. Hence, according to the magnetic selection rule (s. section 2.3.2) the magnetic interaction vector $\boldsymbol{M}_{\perp \boldsymbol{Q}}$ will only have non-zero components in the x and y direction in the crystal coordinate frame. From Eq. 2.45 we see that

$$\boldsymbol{M}_{\perp \boldsymbol{Q}} = \hat{\boldsymbol{Q}} \times (\boldsymbol{S}^{\boldsymbol{k}} \times \hat{\boldsymbol{Q}}), \tag{2.77}$$

for a Bravais lattice (the Debye-Waller-factor and the magnetic form factor are neglected). For the further calculation in terms of the Eqs. 2.70, 2.71 and 2.72 $\boldsymbol{M}_{\perp \boldsymbol{Q}}$ needs to be expressed in the polarisation analysis reference frame defined in Eq. 2.33, where we define the scattering plane to be parallel to the crystallographic x and z directions. Finally, we note that as we consider pure magnetic Bragg reflections here, all terms containing the nuclear structure factor $N_{\boldsymbol{Q}}$ are zero: $N = R^{y/z} = I^{y/z} = 0$.
All the terms necessary for the calculation together with the results are summarised in table 2.2 for both reflections $\boldsymbol{Q}_{\pm} = (0, 0, 1 \pm k)$ and we only discuss the results here:

- From the calculated expressions for the cross-sections we see that using unpolarised neutrons ($\boldsymbol{P}_0 = 0$) the four distinct structures would give identical terms for both reflections. Therefore it would not be possible to distinguish the structures from each other. The calculated intensities are not identical for different models, however, the difference is only a scale factor. This indicates that to get identical intensities for all models the size of the magnetic moment would have to be different for each model. Further, we note, that by measuring the intensities on multiple magnetic Bragg reflections one may distinguish between the models due to different mutual orientation of $\boldsymbol{S}^{\boldsymbol{k}}$ and $\hat{\boldsymbol{Q}}$.

- For the amplitude modulated structure and the cycloid the chiral term is equal to zero whereas for the circular helix and the elliptical helix it is non-zero. The chiral term is not generally zero for the cycloid; here it only vanishes due to the orientation of $\boldsymbol{S}^{\pm \boldsymbol{k}} = \frac{(a\hat{e}_x \mp ia\hat{e}_z)}{2}$ with respect to $\hat{\boldsymbol{Q}} = \boldsymbol{Q}_{\pm} = (0, 0, 1 \pm k)$: the z-component of $\boldsymbol{S}^{\pm \boldsymbol{k}}$ is removed due to the magnetic selection rule. Measuring the polarisation tensor on a different magnetic reflection where $\boldsymbol{Q}$ is nearly perpendicular to $\boldsymbol{S}^{\pm \boldsymbol{k}}$, i.e $\boldsymbol{Q} = (0, 5, \pm k)$ would reveal a chiral term. However, for the amplitude modulated structure $C = 0$ always. Hence, measuring the cross-section on both satellites around one or two distinct nuclear Bragg reflections with different orientations of $\boldsymbol{Q}$ and with a incident neutron beam that is polarised parallel to $\boldsymbol{Q}$ (x direction)

Table 2.2: Four different modulated structures are demonstrated for a simple cubic crystal. The corresponding magnetic Fourier components $\boldsymbol{S}^{\pm\boldsymbol{k}}$ and magnetic interaction vectors are summarised for the two magnetic satellite reflections $\boldsymbol{Q}_{\pm} = (0, 0, 1 \pm k)$. Finally, the cross-section and the polarisation tensor are provided, together with the quantities used to calculate them (s. Eqs 2.70, 2.71 and 2.72 and table 2.1).

Name	Ampl. modulated	Circular helix	Elliptical helix	Cycloid
Figure	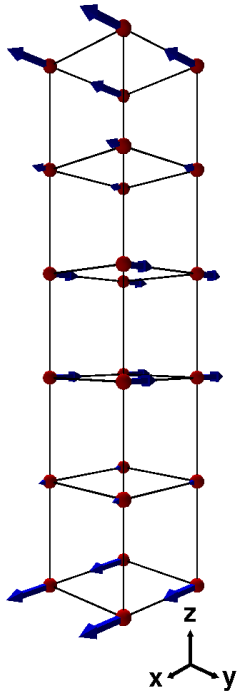	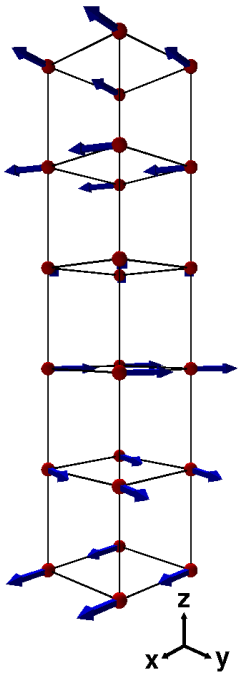	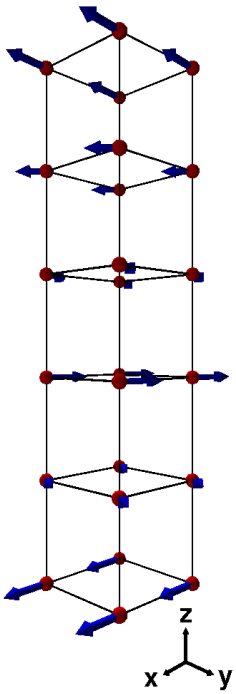	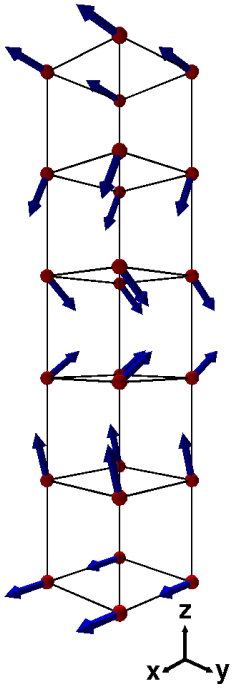
$\boldsymbol{Q}_{+} = (0, 0, 1 + k)$				
$\boldsymbol{S^k}$	$\frac{a\hat{e}_x}{2}$	$\frac{(a\hat{e}_x - ia\hat{e}_y)}{2}$	$\frac{(a\hat{e}_x - ib\hat{e}_y)}{2}$	$\frac{(a\hat{e}_x - ia\hat{e}_z)}{2}$
$\boldsymbol{M}_{\perp\boldsymbol{Q}}$	$(0, \frac{a}{2}, 0)$	$(0, \frac{a}{2}, -\frac{ia}{2})$	$(0, \frac{a}{2}, -\frac{ib}{2})$	$(0, \frac{a}{2}, 0)$
M^y	$(\gamma r_0)^2 \frac{a^2}{4}$	$(\gamma r_0)^2 \frac{a^2}{4}$	$(\gamma r_0)^2 \frac{a^2}{4}$	$(\gamma r_0)^2 \frac{a^2}{4}$
M^z	0	$(\gamma r_0)^2 \frac{a^2}{4}$	$(\gamma r_0)^2 \frac{b^2}{4}$	0
M^{mix}	0	0	0	0
C	0	$-(\gamma r_0)^2 \frac{a^2}{2}$	$-(\gamma r_0)^2 \frac{ab}{2}$	0
$\frac{d\sigma}{d\Omega}$	$(\gamma r_0)^2 \frac{a^2}{4}$	$(\gamma r_0)^2 \frac{a^2}{2}(1 + P_0^x)$	$(\gamma r_0)^2 (\frac{a^2+b^2}{4} + P_0^x \frac{ab}{2})$	$(\gamma r_0)^2 \frac{a^2}{4}$
P_{ij}	$\begin{pmatrix} -1 & 0 & 0 \\ 0 & 1 & 0 \\ 0 & 0 & -1 \end{pmatrix}$	$\begin{pmatrix} -1 & 0 & 0 \\ -1 & 0 & 0 \\ -1 & 0 & 0 \end{pmatrix}$	pol. tensor provided in table 2.3	$\begin{pmatrix} -1 & 0 & 0 \\ 0 & 1 & 0 \\ 0 & 0 & -1 \end{pmatrix}$
$\boldsymbol{Q}_{-} = (0, 0, 1 - k)$				
$\boldsymbol{S^{-k}}$	$\frac{a\hat{e}_x}{2}$	$\frac{(a\hat{e}_x + ia\hat{e}_y)}{2}$	$\frac{(a\hat{e}_x + ib\hat{e}_y)}{2}$	$\frac{(a\hat{e}_x + ia\hat{e}_z)}{2}$
$\boldsymbol{M}_{\perp\boldsymbol{Q}}$	$(0, \frac{a}{2}, 0)$	$(0, \frac{a}{2}, +\frac{ia}{2})$	$(0, \frac{a}{2}, +\frac{ib}{2})$	$(0, \frac{a}{2}, 0)$
M^y	$(\gamma r_0)^2 \frac{a^2}{4}$	$(\gamma r_0)^2 \frac{a^2}{4}$	$(\gamma r_0)^2 \frac{a^2}{4}$	$(\gamma r_0)^2 \frac{a^2}{4}$
M^z	0	$(\gamma r_0)^2 \frac{a^2}{4}$	$(\gamma r_0)^2 \frac{b^2}{4}$	0
M^{mix}	0	0	0	0
C	0	$+(\gamma r_0)^2 \frac{a^2}{2}$	$+(\gamma r_0)^2 \frac{ab}{2}$	0
$\frac{d\sigma}{d\Omega}$	$(\gamma r_0)^2 \frac{a^2}{4}$	$(\gamma r_0)^2 \frac{a^2}{2}(1 - P_0^x)$	$(\gamma r_0)^2 (\frac{a^2+b^2}{4} - P_0^x \frac{ab}{2})$	$(\gamma r_0)^2 \frac{a^2}{4}$
P_{ij}	$\begin{pmatrix} -1 & 0 & 0 \\ 0 & 1 & 0 \\ 0 & 0 & -1 \end{pmatrix}$	$\begin{pmatrix} 1 & 0 & 0 \\ 1 & 0 & 0 \\ 1 & 0 & 0 \end{pmatrix}$	pol. tensor provided in table 2.3	$\begin{pmatrix} -1 & 0 & 0 \\ 0 & 1 & 0 \\ 0 & 0 & -1 \end{pmatrix}$

Table 2.3: The missing polarisation tensor in table 2.2 for the elliptical helix is provided for the two magnetic Bragg reflections $\boldsymbol{Q}_{\pm} = (0, 0, 1 \pm k)$. We denote $\alpha = \frac{a}{b}$.

	$\boldsymbol{Q}_{-} = (0, 0, 1 + k)$	$\boldsymbol{Q}_{-} = (0, 0, 1 - k)$
P_{ij}	$\begin{pmatrix} \frac{-(\alpha^2+1)P_0^x-2\alpha}{\alpha^2+1+2\alpha P_0^x} & 0 & 0 \\ -\frac{2\alpha}{\alpha^2+1} & \frac{\alpha^2-1}{\alpha^2+1} & 0 \\ -\frac{2\alpha}{\alpha^2+1} & 0 & \frac{1-\alpha^2}{\alpha^2+1} \end{pmatrix}$	$\begin{pmatrix} \frac{-(\alpha^2+1)P_0^x+2\alpha}{\alpha^2+1-2\alpha P_0^x} & 0 & 0 \\ +\frac{2\alpha}{\alpha^2+1} & \frac{\alpha^2-1}{\alpha^2+1} & 0 \\ +\frac{2\alpha}{\alpha^2+1} & 0 & \frac{1-\alpha^2}{\alpha^2+1} \end{pmatrix}$

allows to identify whether the structure exhibits a magnetic chirality or not.

- Additionally, we note that the chiral term changes sign for the two corresponding satellites $\boldsymbol{Q}_{\pm} = (0, 0, 1 \pm k)$. This is not due to a different chirality of the two satellites but rather corresponds to a single-handed screw that is screwed and unscrewed[7]. This means that by measuring the intensities on both satellites one can in principle conclude whether the helix is left- or right-handed. However, as we need to pay attention to domains: often right- and left-handed magnetic spirals are energetically degenerate in centrosymmetric crystals. This leads to equally populated chiral domains and the observed chiral term becomes equal to zero in this case, as left- and right-handed spirals have a different sign in the chiral term on a specific reflection.

- If additionally the polarisation tensor is measured it is even possible to distinguish between the different helices shown. The circular helix always perfectly polarises the beam along the x-direction in the polarisation coordinate frame. For the elliptical helix additional yy and zz elements are observed and the final polarisation along the x-axis depends on the ratio $\alpha = \frac{a}{b}$. By comparing the yy and zz elements with Eqs. 2.70 and 2.71 we additionally see that the respective sign of the two terms also determines along which axis a and b are oriented. Finally, if the polarisation tensor is measured on different magnetic satellites with distinct orientations of $\boldsymbol{S}^{\pm \boldsymbol{k}}$ with respect to $\hat{\boldsymbol{Q}}$ allows to identify in which plane the magnetic moments rotate when the helix propagates through the crystal.

In conclusion we have demonstrated that polarised neutrons and most of all full polarisation analysis are highly suitable tools to investigate chiral magnetism. We note, that the power of polarisation analysis lies in determining the direction of the magnetic moments. In order to get additional information of their respective size additional integrated intensities have to be determined by powder or single crystal neutron diffraction. Also, if more than one magnetic ion is present in the unit cell chiral terms can be observed even if the moments on each single site do not form a helical structure, since in neutron scattering the total magnetic moment of the unit cell is observed and this may form a magnetic spiral even for such cases. Finally, we want to highlight that in case magnetic domains (s.

[7]For the process of unscrewing the sense of rotation is changed with respect to the observer, however also the propagation direction changes and therefore the chirality is identical for both processes.

chapter 3) or multiple magnetic ions are present in a magnetic crystal, the determination of magnetic structures can be challenging even with the use of polarised neutrons.

2.4.4 Experimental polarisation

The neutrons produced in a neutron source have no preferred direction for their spins, i.e. a general neutron beam is unpolarised. There are basically three methods, which are commonly used to polarise a neutron beam.

^{3}He polarisers polarise the neutron beam via the spin-dependent absorption cross-section of spin-polarised ^{3}He gas for neutrons $\sigma_\pm = \sigma_0 \pm \sigma_p$ where the $\pm$-cases denote the orientation of the neutron spin with respect to the spin-polarisation of the gas. The transmission of such a ^{3}He filter is described by

$$t^\pm = \exp[-\tilde{N} d(\sigma_0 \pm \sigma_p/\sigma_0)], \tag{2.78}$$

where $\tilde{N}$ and d are the atomic concentration of the gas and the thickness of the filter, respectively [TR95].

Single crystal polarisers make use of the presence of the term $\sigma \boldsymbol{P''}$ in Eq. 2.71 that polarises the beam.[8] E.g. non-zero terms $R^{y/z}$ are present for centrosymmetric ferromagnetic single crystals without ferromagnetic domains. A mono-domain state is generally achieved by applying a magnetic field to the crystal. If they additionally have the property $(\gamma r_0)|\boldsymbol{M}_{\perp \boldsymbol{Q}}| = |N_{\boldsymbol{Q}}|$ on a specific Bragg reflection then the beam is fully polarised parallel to the direction of the applied field after the reflection at the crystal [Wil88]. Examples for crystals with this property are the (111) reflection of the Heusler compound Cu_2MnAl (d-spacing 3.43 Å) and the the (200) reflection of the alloy $Co_{0.92}Fe_{0.08}$ (d-spacing 1.76 Å).

Polarising (super-)mirrors. The angle of total reflection for neutrons from a magnetised ferromagnetic thin film is given by

$$\theta^\pm = \lambda \sqrt{N(b \pm p)/\pi}, \tag{2.79}$$

where λ is the neutron wavelength, N is the nuclear density and b and p are the nuclear and magnetic scattering length, respectively. The + and − case describe the reflection angle for neutrons having spin antiparallel or parallel to the direction of the magnetisation of the film. For the ideal case $b = p$ all reflected neutrons are polarised. Reflection angles are very small for thermal and cold neutrons and depend on the wavelength of the neutrons (e.g. $\theta \approx 0.4°$ for $\lambda \approx 4$ Å and $Fe_{50}Co_{48}V_2$ as magnetised film). This problem is usually solved by producing films of multiple magnetic and non-magnetic layers, called supermirrors. Typical combinations of materials are Fe/Si, Co/Si and $Fe_{50}Co_{48}V_2/TiNi_x$. Often multilayers are used in

[8] For an unpolarised incident beam ($\boldsymbol{P}_0$) the part $\tilde{\boldsymbol{P}}$ in Eq. 2.71 does not contribute.

devices called benders. Multiple multilayer-wafers (up to a few hundred) are pressed in a curved shape, e.g. S- or C-form, in order to polarise the beam completely by multiple reflections. As wafers transparent substrate material (e.g. Si) is used, on which the supermirror is deposited by sputtering techniques. Such a device is placed downstream of the monochromator of the experiment (compare also [Bön00]).

After the scattering process at the sample, the final polarization can be measured with a similar device as is used for polarising the beam. Since different components of the Pauli-operators do not commute, i.e.

$$[\hat{\sigma}_x, \hat{\sigma}_y] = 2i\hat{\sigma}_z \quad \text{and cyclical,} \tag{2.80}$$

only the projection of the polarization vector on the quantisation axis of the analyser can be measured. E.g. for a supermirror the magnetisation direction of the film represents the quantisation axis for the neutrons spins. Without loss of generality we define that this axis is parallel to the z-axis. Then all the spins will collapse to states being parallel (up) or antiparallel (down) with respect to the z axis. The distribution of the spins into these two states will fulfil the condition (s. Eq. 2.59)

$$P'_z = <\hat{\sigma}_z> = |a|^2 - |b|^2, \tag{2.81}$$

where $|a|^2$ and $|b|^2$ are the probabilities for the spins being in the up or down state respectively. We define the neutron intensities scattered into a detector situated behind the supermirror for the magnetisation being parallel or antiparallel to the z-axis as I^+ and I^-. Then the ratios between the two intensities I^+ and I^- determine the probabilities for the neutrons being in up and down state and therefore also the experimental polarisation:

$$|a|^2 = \frac{I^+}{I^+ + I^-} \quad \text{and} \quad |b|^2 = \frac{I^-}{I^+ + I^-} \quad \Longrightarrow P'_z = \frac{I^+ - I^-}{I^+ + I^-}. \tag{2.82}$$

Thus, experimentally, the polarization is defined as the projection of the polarization vector on an axis defined by the applied quantisation axis of the measurement device. We note that often instead of reversing the magnetisation direction of the supermirror a π-*flipper* is used. This device is installed upstream of the polarisation-analyser and rotates the polarization vector by π around an axis perpendicular to the quantisation axis of the analyser by using a magnetic field (s. Eq. 2.61) and therefore has an identical effect.
When non-ideal polarises, analysers and flippers are used in an experiment this has to be considered when comparisons to a model for a magnetic structure are performed. This is done by calculating the general polarisation dependent intensities that are corrected for the polarising and flipping efficiencies for all devices and then calculating the intensities by

$$P^+ = \frac{I^{+i+j} - I^{+i-j}}{I^{+i+j} + I^{+i-j}} \qquad \text{and} \qquad P^- = \frac{I^{-i+j} - I^{-i-j}}{I^{-i+j} + I^{-i-j}}, \tag{2.83}$$

where P^+ and P^- are the experimental polarisations for the initial polarisation before the scattering process being *up* or *down* respectively and i,j = x,y,z according the defined analysis frame (s. Eq. 2.33). The intensities are calculated via

$$\begin{aligned} I^{+i+j} &= I_0\big[P_2(P_1\sigma^{+i+j}+(1-P_1)\sigma^{-i+j})+(1-P_2)(P_1\sigma^{+i-j}+(1-P_1)\sigma^{-i-j})\big] \\ I^{-i+j} &= I_0\big[P_2(P_1\varepsilon_1\sigma^{-i+j}+(1-P_1\varepsilon_1)\sigma^{+i+j})+(1-P_2)(P_1\varepsilon_1\sigma^{-i-j}+(1-P_1\varepsilon_1)\sigma^{+i-j})\big] \\ I^{+i-j} &= I_0\big[P_2\varepsilon_2(P_1\sigma^{+i-j}+(1-P_1)\sigma^{-i-j})+(1-P_2\varepsilon_2)(P_1\sigma^{+i+j}+(1-P_1)\sigma^{-i+j})\big] \\ I^{-i-j} &= I_0\big[P_2\varepsilon_2(P_1\varepsilon_1\sigma^{-i-j}+(1-P_1\varepsilon_1)\sigma^{+i-j})+(1-P_2\varepsilon_2)(P_1\varepsilon_1\sigma^{-i+j}+(1-P_1\varepsilon_1)\sigma^{+i+j})\big]. \end{aligned} \tag{2.84}$$

P_1 (ε_1) and P_2 (ε_2) are the polarising (flipping) efficiencies of the polarisers (flippers) before and after the sample, respectively, and $\sigma^{i,j} = |\langle\sigma_j|N_{\boldsymbol{Q}}(t) + (\gamma r_0)\sigma\boldsymbol{M}_{\perp\boldsymbol{Q}}(t)|\sigma_i\rangle|^2$[Bro06]. In the Eqs. 2.84 the efficiencies for the polarisers (flippers) take into account that the beam is not fully polarised (flipped) by the devices and therefore mix the corresponding 'up' and 'down' channels for the polarisation correctly via the adequate transition matrix elements $\sigma^{i,j}$. We note that $0.5 < P_1, P_2, \varepsilon_1, \varepsilon_2 < 1$ must be true always. For $P_1 = P_2 = \varepsilon_1 = \varepsilon_2 = 1$ the method above is equivalent to calculating the polarisation tensor via the Blume-Maleyev equations defined in Eqs. 2.70, 2.71 and 2.72.[9]

2.5 MuPAD

As the major technique used during the course of this work was neutron polarisation analysis we will review the device used for the experiments here. The additionally employed types of neutron scattering instruments are summarised in appendix A.
In the previous sections we have considered all necessary elements to carry out a polarisation analysis experiment. However, we additionally have to take into account that careful control of the polarization vector throughout the whole experimental setup is necessary in a polarization analysis experiment as magnetic stray fields in the environment of the instrument may depolarise or rotate the polarization vector. This fact becomes more evident when we consider a polarised neutron beam with wavelength of 1 Å (corresponding to a velocity of 3956 $\frac{m}{s}$) travelling a distance of 0.5 m (in the range of typical distances between polariser and sample) through a homogeneous field of 300 mG (magnitude of Earth's magnetic field!). In this case the components of the polarization vector perpendicular to the field axis will be already rotated by $\approx 40°$ (s. Eq. 2.61). In *classical longitudinal polarization analysis* [MRK69], the depolarisation of the beam by residual magnetic fields is prevented by the application of a magnetic guide field along the polarised neutron beam. However, this setup only allows the projection of the final polarization vector onto the direction of the guide field to be determined. Any component of the polarization turned into a direction perpendicular to the guide field upon the scattering process will be depolarised. Hence only the three diagonal terms of the polarization tensor may be determined. However, in order to handle the scientific cases presented above the

[9] For a more detailed discussion of the efficiencies see appendix B.2.

information of the six off-diagonal terms is additionally needed.
As an alternative the neutron polarization can be conserved when any residual fields are removed from the sample environment by a zero field chamber. Then any component of the final polarization vector may be determined and the full polarization tensor can be measured. This method is known as *spherical neutron polarimetry* (SNP) (For a complete introduction see reference [Bro05]). The first device using this technique to perform routine SNP measurements at finite scattering angles was CryoPAD (**Cryo**genic **P**olarization **A**nalysis **D**evice), presented by Tasset et al. [Tas89] in 1989. It is based on a zero field chamber, realised through a double superconducting Meissner-shield.
However, for all polarisation analysis experiments conducted within this work a new alternative SNP option was used that employs a mu-metal sample chamber to create a zero field environment that conserves the direction of the polarization vector throughout the instrument. The device was developed by Janoschek et al. and is called MuPAD (**Mu**-Metal **P**olarisation **A**nalysis **D**evice)[Jan04, JKR$^+$07]. The chamber mainly consists of a double layered mu-metal cylinder in which a standard ILL orange cryostat or a FRM-II closed cycle cryostat can be hosted inside the zero field region. With this setup a shielding factor $S = B_o/B_i = 1000 - 3000$ depending on the direction can be achieved inside the zero field chamber, where B_o and B_i are the fields outside and inside of the chamber, respectively. An overview of the chamber is given in Fig. 2.9.
As a polarised neutron beam cannot traverse a mu-metal layer of several mm thickness without serious losses in intensity and polarization the beam has to enter the zero field chamber through apertures in the mu-metal. To avoid depolarisation when the neutrons travel through these apertures and additionally to avoid that magnetic residual fields can penetrate into the zero field chamber through the entrance and exit apertures coupling coils (CCs) are used. Neutrons reach the zero field region with their spins parallel to the guide field of the coupling coil. The transition from the outer guide field to the field of the coupling coil is adiabatic, whereas the transition from the field of the coupling coil into the screened area is strictly nonadiabatic, in order to conserve the spin direction inside the zero field region. The non-adiabatic transition is achieved by passing the neutrons through the wires of the coupling coil; outer stray fields are avoided by a mu-metal yoke closely wrapped around the coupling coil. Variation of the scattering angle requires a splitting of the double mu-metal cylinder. The gap between the two cylinder parts can be closed section by section by an automated pneumatic system of mu-metal lamellas (see Fig. 2.9) according to the scattering angle.
To control the polarization vector of the incident and scattered neutrons a set of two *precession coils* (PCs) is used for the incoming and outgoing beam, respectively. They are hosted in two extensions to the zero field chamber, called *arms* in the following. The double mu-metal shields of the arms are connected mechanically and magnetically to the inner and outer mu-metal cylinder of the central chamber, respectively, assuring a zero field environment for these coils (Fig. 2.9). The arm at the entrance side of MuPAD is fixed with respect to the mu-metal cylinders, whereas the arm at the exit side moves on a rail system together with the opening for the scattered neutrons provided by the automatic mu-metal lamella system. The two CCs are mounted inside the zero field arms

(Fig. 2.9). The PCs are installed inside the zero field arms and special care was taken to ensure that the return fields of the precession coils cannot influence the polarization vector of the neutron beam (s. references [Jan04, JKR+07] for technical details). This way, a precise control of the polarization vector in all directions is achieved. The interplay of all precession and coupling coils is shown in Fig. 2.8. A neutron beam polarised along the z-direction enters the zero field region via the entrance CC. The two outer PC's control the orientation of the polarization with respect to the scattering plane. The two inner PC's turn the polarization within the scattering plane either along and/or perpendicular to $\boldsymbol{Q}$. This setup allows full and precise control of the polarisation vector of the neutron beam incident on the sample and of the scattered neutron beam as well. Hence, all terms of terms P_{ij} of the polarisation tensor (s. Eq. 2.70) can be measured. A photograph of MuPAD is shown in Fig. 2.10.

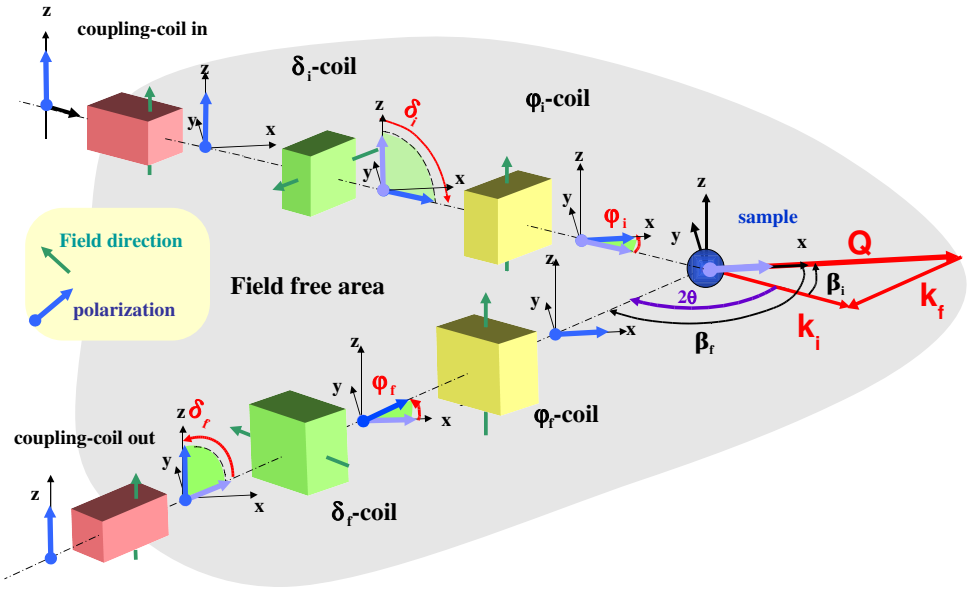

Figure 2.8: The setup of MuPAD is shown schematically. A neutron beam polarised along the z-direction enters into the zero field chamber denoted by the grey shaded area through the incident coupling coil. The polarization vector is turned by two precession coils with homogeneous fields perpendicular to each other in order to be aligned along the x-direction. It is scattered on a non-magnetic Bragg peak of a sample (this case was chosen due to the simplicity of the picture). Therefore the polarization vector is not changed during the scattering process. Now the second pair of precession coils downstream of the sample is used to turn the x-component of the final polarization in the direction of the analyser axis (z-axis). This component is guided out of the zero field chamber to the analyser by the exit coupling coil. Thus in this configuration the term P_{xx} of the polarization tensor is measured. By using other combinations of precession angles in the coils all terms P_{ij} of the polarisation tensor (s. Eq. 2.70) are measured.

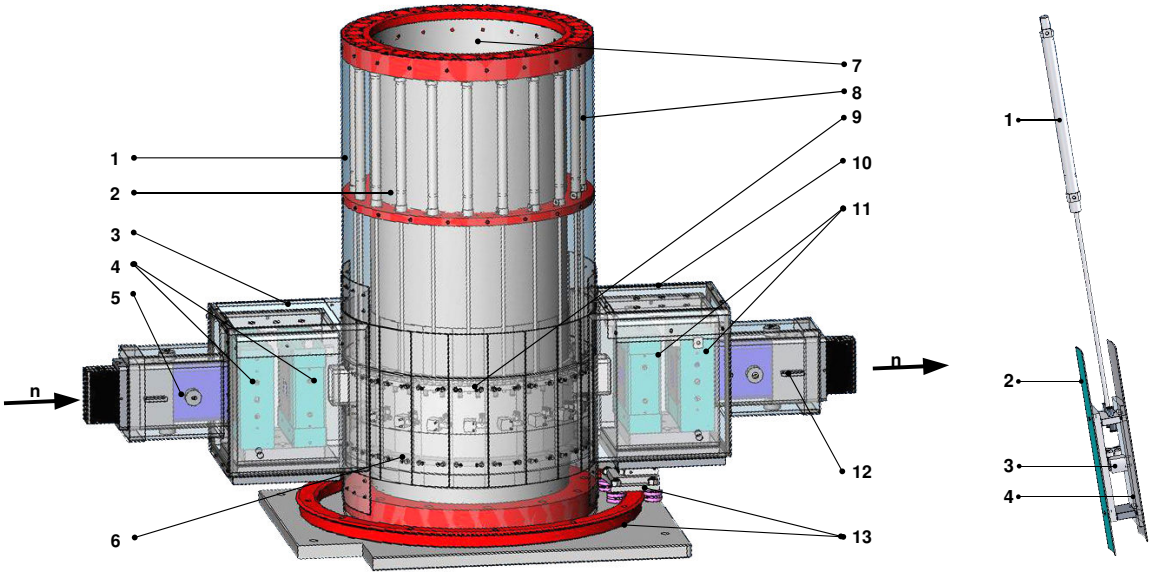

(a) (b)

Figure 2.9: A technical drawing of the MuPAD device is shown. (a) **n** denotes the direction of the neutron beam. The following details are specified: (1) outer mu-metal shield (2) inner mu-metal shield (3) primary fixed arm out of double mu-metal shielding hosting all coils for the incoming neutron beam (4) precession coils for manipulation of the polarization vector incident on the sample (5) coupling coil to conserve the polarization vector of the incoming beam (6) mu-metal lamellas for automatic closure of the beam slit when the scattering vector is changed (7) top hole for insertion of standard ILL orange or FRM-II closed cycle cryostats (8) non-magnetic pneumatic cylinders which move mu-metal lamellas (9) sample position in chamber (10) secondary moving arm which hosts coils for the outgoing neutron beam; arm is moved together with the host spectrometer (11) precession coils for manipulation of the final polarization vector (12) coupling coil to conserve the polarization vector of the outgoing beam (13) non-magnetic rail system on which the moving secondary arm is mounted. (b) A detailed view of the pneumatic lamella system for automatic closure of the zero field chamber is shown: (1) pneumatic cylinder which moves lamellas up and down (2) inner mu-metal lamella to magnetically close inner cylinder of chamber (3) cylinder which spreads inner and outer lamella towards the inner and outer mu-metal shield to assure good magnetic contact when the chamber is closed (4) outer mu-metal lamella.

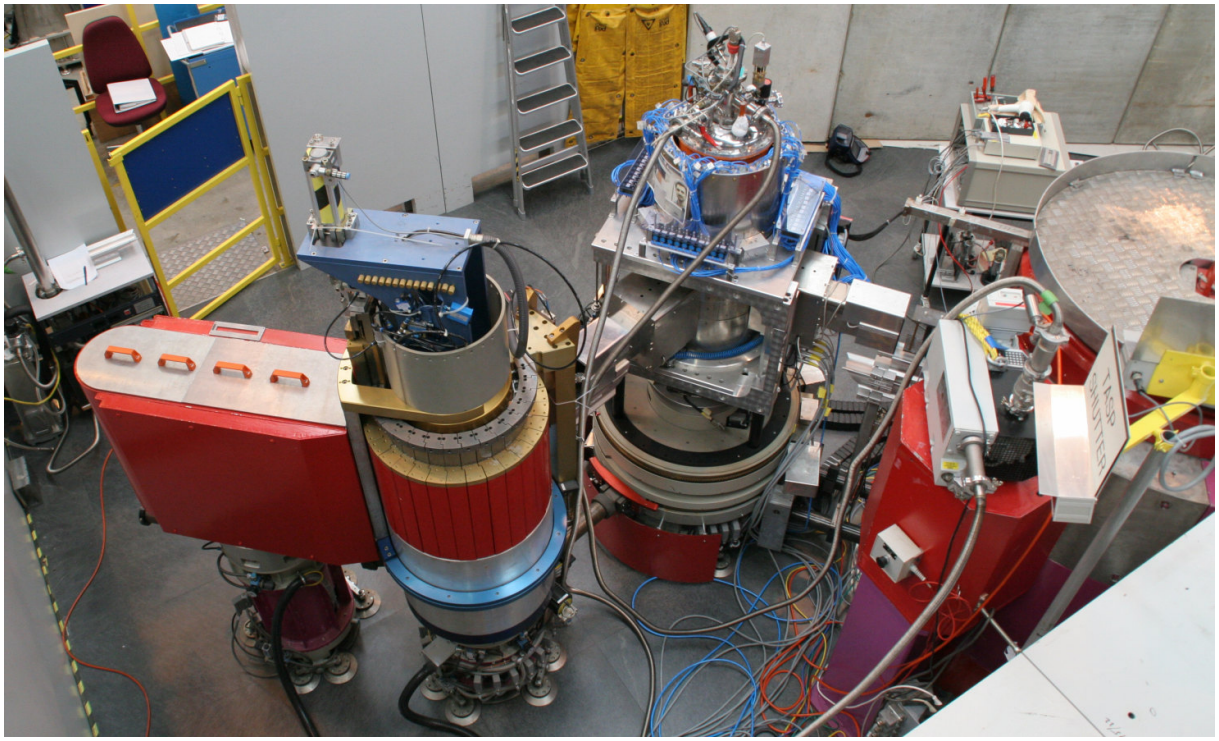

Figure 2.10: A photograph of MuPAD installed on the triple-axis spectrometer TASP [SRB01] at the continuous spallation neutron source SINQ of Paul Scherrer Institut is shown.

Chapter 3

Magnetic symmetry analysis

In this work polarised and unpolarised neutron diffraction techniques were used to determine the microscopic magnetic structure of two different compounds. The determination of magnetic structures by means of neutron scattering is significantly facilitated when symmetry considerations are employed in the analysis of the data. In this chapter the use of group theory in the analysis of magnetic structures will be established. Additionally we use this theoretical framework to discuss the possible emergence of different types of magnetic domains when the symmetry of the magnetic structure is lower compared to the symmetry of the chemical structure.

3.1 Group theory

3.1.1 Definition of groups

Magnetic symmetry analysis is based on group theory. In the mathematical sense a group is defined as follows [Cot90]:

A group (G, $*$) is a set G with a binary operation $*$ that satisfies the following four axioms:

1. **Closure:** For all elements g_1, g_2 in G, the result of $g_1 * g_2$ is also in G.
2. **Associativity:** For all g_1, g_2 and g_3 in G, $(g_1 * g_2) * g_3 = g_1 * (g_2 * g_3)$.
3. **Identity element:** There exists an element e in G such that for all g in G, $e * g = g * e = g$.
4. **Inverse element:** For each g_1 in G, there exists an element g_2 in G such that $g_1 * g_2 = g_2 * g_1 = e$, where e is the identity element.

All (chemical) crystal structures can be grouped into the so-called 230 *space groups*. A space group is a group of symmetry operations, e.g. rotations, rotation-inversions, translations, that describe the symmetry of a given crystal. All space groups are tabulated in reference [Hah06]. It turns out that the space groups form groups in a mathematical sense since their elements, namely the symmetry operations, rigorously satisfy the group axioms. Hence, the mathematical framework of group theory is also applicable to space groups.

3.1.2 Irreducible representations

A symmetry operation is most conveniently represented in terms of a matrix. E.g. it may be expressed by a 3×3 matrix that transforms the coordinates of an atom according to the symmetry operation. Any system of matrices $\Gamma(g)$ related to each element g that complies with the same multiplication rules as they are valid for the group G is called *a representation of the group G*. The dimension of the matrices $\Gamma(g)$ signifies the dimension of the representation. For a given group generally a multitude of equivalent representations exists that are related to each other via unitary transformations U[1]:

$$U\Gamma(g)U^{-1} = \tilde{D}(g). \tag{3.1}$$

If a unitary transformation exists that transforms the matrices $\Gamma(g)$ in such a way that the resulting matrices $\tilde{\Gamma}(g)$ have block-diagonal form, then the resulting blocks in the matrices multiply independently and hence fulfil the same multiplication rules then the original matrices. Therefore the blocks form themselves a representation of the group g that has a reduced dimension compared to the original representation. In the case that no unitary transformation exists that can reduce $\Gamma(g)$ to block-diagonal form the representation is called *a irreducible representation* [INO91]. The original reducible representation can be expanded into the irreducible representations via

$$\Gamma = \sum_{\nu} n_\nu \Gamma^\nu, \tag{3.2}$$

where n_ν denotes how often the νth irreducible representations is contained in Γ.
When a physical problem is considered it is expressed in terms of some variables φ_λ ($\lambda = 1, \ldots, p$) that correspond to the specific problem, e.g. in our case the positions of the atoms in the crystal or the direction of the magnetic moments. The action of a symmetry operation g upon some function of the coordinates $\boldsymbol{r}$[2] is defined by [INO91]

$$T(g)\varphi(\boldsymbol{r}) = \varphi(g^{-1}\boldsymbol{r}) \equiv \varphi'(\boldsymbol{r}), \tag{3.3}$$

[1]Representations that cannot be transformed into each other via unitary transformations are termed nonequivalent.

[2]These a not necessarily the coordinates of space but rather the coordinates of the coordinate frame that was defined for the specific physical problem.

where $T(g)$ denotes the operator corresponding to the symmetry operation g in the space of the functions φ_λ. Hence, the functions φ_λ are the unit vectors of the p-dimensional space of functions W related to the specific physical problem. The physical quantities $\varphi(\boldsymbol{r})$ that correspond to vectors in W can be expressed as linear combinations of the p unit vectors φ_λ. Therefore, we can rewrite Eq. 3.3 as

$$T(g)\varphi_\lambda(\boldsymbol{r}) = \varphi'(\boldsymbol{r}) = \sum_\mu \Gamma_{\mu\lambda}(g)\varphi_\mu(\boldsymbol{r}), \tag{3.4}$$

where $\Gamma_{\mu\lambda}(g)$ is a representation of the group G in the space of functions W. The functions $\varphi_\lambda(\boldsymbol{r})$ can be transformed into each other via the symmetry operations and the specific form of the transformation in the space W is given by the matrices $\Gamma_{\mu\lambda}(g)$.
This signifies that if an unitary transformation U exists that reduces the matrix representations $\Gamma_{\mu\lambda}(g)$, also the functions $\varphi_\lambda(\boldsymbol{r})$ split up into independent subsystems of functions

$$\Psi_\lambda(\boldsymbol{r}) = \sum_\mu U_{\mu\lambda}\varphi_\mu(\boldsymbol{r}), \tag{3.5}$$

that do not intersect in the case of symmetry transformations. Hence, finding the irreducible representations Γ^ν is equivalent to expressing the initial physical variables $\varphi_\lambda(\boldsymbol{r})$ through the symmetrized linear combinations in Eq. 3.5 that are called the *basis functions of the irreducible representation* of the group G in the basis space W.
We emphasise that due to this method the number of free physical parameters is often significantly reduced as the parameters that are found to be related by symmetry are no longer independent. E.g. in the case of structure determination with neutrons no longer all possible atomic positions are fitted independently but only those, that are not related by symmetry. In group theory a method called the *projection operator* is used to obtain the basis functions of the irreducible representations (for a complete derivation see [INO91]). The projection operator is defined as:

$$\Psi_\lambda \equiv P\varphi = \frac{1}{n(G)} \sum_{g\epsilon G} \Gamma^{*\nu}_{\mu\lambda}(g)T(g)\varphi \quad (\lambda = 1, \ldots, l_\nu), \tag{3.6}$$

where $n(G)$ is the total number of symmetry elements of the group G and l_ν is the dimension of irreducible representation Γ^ν. Thus, for a given space group the problem can always be reduced via the projection operator that projects the original problem onto the lower dimensional space of the symmetric basis functions of the irreducible representations.

3.2 Magnetic representation analysis

For the symmetry analysis of magnetic structures two facts have to be taken into account additionally. In section 1.1.2 we have already learned that spins and thus also magnetic

moments are pseudo vectors and therefore behave different under improper rotations. Further, many magnetic structures are long-periodic modulated structures (compare sections 1.2.2, 2.4.3 and table I in reference [Izy84]) that are difficult to describe within the normal crystallographic space groups as the magnetic unit cells are then often incommensurate with the chemical lattice. This problem is circumvented by using the concept of magnetic propagation vectors that we will describe in the following. The consequent application of the concept then allows the construction of symmetrized basis functions for the magnetic structure.

3.2.1 The propagation vector

We have already used the concept of a magnetic propagation vector in sections 1.2.2, 2.3.5 and 2.4.3 to describe magnetic structures with a periodicity Λ that is different from the underlying chemical lattice without specifying it in detail. Generally periodic physical variables $\Psi^{\boldsymbol{k}}(\boldsymbol{r})$ that have to comply with the underlying crystal lattice that is defined by lattice translation $\boldsymbol{l}$ (compare section 2.2.3 and especially Eq. 2.13) have to fulfil the following condition [INO91]

$$T(\boldsymbol{l})\Psi^{\boldsymbol{k}}(\boldsymbol{r}) = \exp(-i\boldsymbol{k}\cdot\boldsymbol{l})\Psi^{\boldsymbol{k}}(\boldsymbol{r}), \tag{3.7}$$

where $T(\boldsymbol{l})$ is the action of a lattice translation operation on the space of functions W. This is equivalent to Bloch's theorem for wave functions of electrons in a periodic potential. The most general solutions for Eq. 3.7 and therefore the basis functions for the group of translations are the Bloch functions

$$\Psi^{\boldsymbol{k}}(\boldsymbol{r}) = u_{\boldsymbol{k}}(\boldsymbol{r})\exp(i\boldsymbol{k}\cdot\boldsymbol{l}), \tag{3.8}$$

where $u_{\boldsymbol{k}}$ denotes a periodic function with the periods of the non-inverted lattice. We see from Eq. 3.7 that the function $\Psi^{\boldsymbol{k}}(\boldsymbol{r})$ is transformed into itself with the accuracy of the numerical phase $\exp(-i\boldsymbol{k}\cdot\boldsymbol{l})$ under the action of a pure translation operation $T(\boldsymbol{l})$. Thus, the propagation vector is used to propagate the function $\Psi^{\boldsymbol{k}}(\boldsymbol{r})$ that is periodic in $\boldsymbol{r}$ from the zeroth to the nth cell, where $\boldsymbol{l}$ is the translational vector interconnecting the two cells.

3.2.2 The little group

We have seen in the preceding section that the translation operations contained in the elements of a space group G do not change the function $\Psi^{\boldsymbol{k}}(\boldsymbol{r})$. Now, we want to investigate the action of the remaining rotational symmetry operations. For convenience we will express the symmetry operations in the Wigner-Seitz notation in which all symmetry operations g that belong to a given space group are divided into two distinct parts, namely

the rotational part h and its *accompanying translation* $\boldsymbol{\tau}_h$[3]. The symmetry operation is then denoted as $g = \{h|\boldsymbol{\tau}_h\}$. The multiplication the of elements is then defined via

$$\{\alpha|\boldsymbol{\tau}_\alpha\}\{\beta|\boldsymbol{\tau}_\beta\} = \{\alpha\beta|\alpha\boldsymbol{\tau}_\beta + \boldsymbol{\tau}_\alpha\} \quad \text{and} \quad \{h|\boldsymbol{\tau}_h\}^{-1} = \{h^{-1}| - h^{-1}\boldsymbol{\tau}_h\}. \tag{3.9}$$

The most general form of a symmetry operation g is then $\{h|\boldsymbol{\tau}_h + \boldsymbol{l}_n\}$ where $\boldsymbol{l}_n$ is an additional lattice translation from the zeroth to the nth cell. We therefore find that $\{h|\boldsymbol{\tau}_h + \boldsymbol{l}_n\}\Psi^{\boldsymbol{k}}(\boldsymbol{r}) = \Psi'(\boldsymbol{r})$. To understand the nature of this new function we will apply a pure translation to it [INO91]:

$$\begin{aligned} T(\boldsymbol{l})\Psi'(\boldsymbol{r}) &= \{1|\boldsymbol{l}\}\Psi'(\boldsymbol{r}) = \{1|\boldsymbol{l}\}\{h|\boldsymbol{\tau}_h + \boldsymbol{l}_n\}\Psi^{\boldsymbol{k}}(\boldsymbol{r}) = \\ &= \{h|\boldsymbol{\tau}_h + \boldsymbol{l}_n\}\{1|h^{-1}\boldsymbol{l}\}\Psi^{\boldsymbol{k}}(\boldsymbol{r}) = \{h|\boldsymbol{\tau}_h + \boldsymbol{l}_n\}\exp(-i\boldsymbol{k}\cdot h^{-1}\boldsymbol{l})\Psi^{\boldsymbol{k}}(\boldsymbol{r}) = \\ &= \exp(-i\boldsymbol{k}h^{-1}\cdot\boldsymbol{l})\{h|\boldsymbol{\tau}_h + \boldsymbol{l}_n\}\Psi^{\boldsymbol{k}}(\boldsymbol{r}) = \exp(-ih\boldsymbol{k}\cdot\boldsymbol{l})\Psi'(\boldsymbol{r}). \end{aligned} \tag{3.10}$$

Here 1 is the identity operation. By comparison with Eq. 3.7 we see that $\Psi'(\boldsymbol{r})$ is also a Bloch function. Instead of the propagation vector $\boldsymbol{k}$ a new propagation vector $h\boldsymbol{k}$ generated from symmetry appears in the phase of the Bloch function and we can rewrite the former expression for $\Psi'(\boldsymbol{r})$ to

$$\{h|\boldsymbol{\tau}_h + \boldsymbol{l}_n\}\Psi^{\boldsymbol{k}}(\boldsymbol{r}) = \Psi^{h\boldsymbol{k}}. \tag{3.11}$$

Consequently, the Bloch functions in Eq. 3.8 also serve as basis functions for the whole space group G containing translational and rotational symmetry operators.
Additionally, Eq. 3.11 demonstrates that all pure rotational operators h_L contained in G generate a set of propagation vectors $1\boldsymbol{k}$, $h_1\boldsymbol{k}$, $h_2\boldsymbol{k}$, ... from the original propagation vector $\boldsymbol{k}$[4]. This set is called the *star of the propagation vector* (denoted by $\{\boldsymbol{k}\}$) and contains all nonequivalent propagation vectors that are generated from the rotational elements of the space group G. The propagation vectors contained in $\{\boldsymbol{k}\}$ are called *the arms of the star* $\boldsymbol{k}_L = h_L\boldsymbol{k}$ and l_k denotes the number of arms. The number of arms cannot be larger than the number of elements in the *point group* G^0 of the crystal, that is the subgroup of G that only contains the pure rotational operators.
All symmetry elements g in G that leave the propagation vector unchanged are elements of the *little group* that is generally denoted by $G_{\boldsymbol{k}}$. Naturally $G_{\boldsymbol{k}}$ is a subgroup of G (and not of G^0) that contains all translational operators but only rotational operators that leave $\boldsymbol{k}$ invariant. We can expand G in terms of $G_{\boldsymbol{k}}$.

$$G = \sum_{L=1}^{l_k} g_L G_{\boldsymbol{k}}, \tag{3.12}$$

[3]Some of the symmetry elements, e.g. screw-rotations or gliding reflections inherently contain translations. Additionally a translation may be present, when the symmetry operation is not centred at the origin.

[4]Translations are not considered since the propagation vector starts from the centre of the Brillouin zone and thus are not affected by translations.

where g_L is the element-representative of the expansion.
Similarly to the procedure for the space group G described in section 3.1.2 irreducible representations for the littel group by $\mathrm{G}_{\boldsymbol{k}}$ can be derived that we will denote with $\gamma^{\boldsymbol{k}\nu}$ and its dimension with l_ν. Hence, for each irreducible representation l_ν basis functions $\Psi_\lambda^{\boldsymbol{k}\nu}(\boldsymbol{r}) = u_{\boldsymbol{k}\lambda}^\nu(\boldsymbol{r})\exp(i\boldsymbol{k}\cdot\boldsymbol{l})$ $(\lambda = 1,\ldots,l_\nu)$ exist. However, Eq. 3.11 compromises that elements g of the space group G that are applied to such a basis function (Bloch function) generate new basis functions with a distinct propagation vector $\boldsymbol{k}_L$ that belongs to the same star. Therefore the space group is characterised by an irreducible representation of the entire star $\{\boldsymbol{k}\}$ that is called $\Gamma^{\{\boldsymbol{k}\}\nu}$. This signifies that each irreducible representation $\gamma^{\boldsymbol{k}\nu}$ of a little group $\mathrm{G}_{\boldsymbol{k}}$ induces an irreducible representation $\Gamma^{\{\boldsymbol{k}\}\nu}$ of the entire space group. The basis functions of the space group are formed of the basis functions of all arms of the star $\Psi_1^{\boldsymbol{k}_1\nu},\ldots,\Psi_{l_\nu}^{\boldsymbol{k}_1\nu},\Psi_1^{\boldsymbol{k}_2\nu},\ldots,\Psi_{l_\nu}^{\boldsymbol{k}_2\nu},\ldots,\Psi_1^{\boldsymbol{k}_{l_k}\nu},\ldots,\Psi_{l_\nu}^{\boldsymbol{k}_{l_k}\nu}$. The relation between $\gamma^{\boldsymbol{k}\nu}$ and $\Gamma^{\{\boldsymbol{k}\}\nu}$ is expressed mathematically via [INO91] the formula

$$\Gamma_{L\lambda,M\mu}^{\{\boldsymbol{k}\}\nu}(g) = \gamma_{\lambda\mu}^{\boldsymbol{k}\nu}(g_L^{-1}gg_M) = \begin{cases} 1, & \text{if } \; g_L^{-1}gg_M \in G_{\boldsymbol{k}} \\ 0, & \text{otherwise,} \end{cases} \tag{3.13}$$

where $\lambda,\mu = 1,\ldots,l_\nu$ and L and M are numbers of the according arm of the star. Thus, it sufficient to know the irreducible representations of the little group $\mathrm{G}_{\boldsymbol{k}}$ and map them via Eq. 3.13 to the irreducible representation of the space group. The matrices $\gamma^{\boldsymbol{k}\nu}$ are tabulated for all 230 space groups in reference [Kov65] via the *projective representation* γ_{pr}^ν that is only valid for the zeroth block (no translation, i.e. for the little group $G_{\boldsymbol{k}}^0$ of the point group G^0) but that can be converted back by the equation [INO91]:

$$\gamma^{\boldsymbol{k}\nu}(g) = \gamma_{pr}^\nu(h)\exp(-i\boldsymbol{k}\cdot\boldsymbol{\tau}_h) \quad (g = \{h|\boldsymbol{\tau}_h\}). \tag{3.14}$$

3.2.3 The magnetic representation

The projection operator defined in Eq. 3.6 together with the relation defined in Eqs. 3.13 easily allows the construction of the basis functions for a given physical function $\varphi(\boldsymbol{r})$ for all 230 space groups. However, we still do not know the action of the symmetry operators $T(g)$ in Eq. 3.6 onto the specific physical function that describes a magnetic structure. This will be derived in the following.
A magnetic structure is described by magnetic moments that are situated at the positions of the magnetic ions in the crystal. We introduce a $3\sigma_m N$-dimensional vector (σ_m is the number of magnetic ions in the unit cell) that describes the magnetic structure

$$\varphi_{\boldsymbol{k}}^{d\beta} = \sum\nolimits_n^{\oplus} \sigma_0^{d\beta}\exp(i\boldsymbol{k}\cdot\boldsymbol{l}_n), \tag{3.15}$$

where the sum over n is a direct sum over all N cells of the crystal. $\sigma_0^{d\beta}$ is a 3σ-dimensional vector in which only the component that denotes the β-component (e.g. β = x, y, z) of the magnetic moment of the dth magnetic ion in the zeroth cell is equal to one whereas

all other components are equal to zero. The phase factor $\exp(i\boldsymbol{k}\cdot\boldsymbol{l}_n)$ accounts for the propagation of the structure in accordance with Eq. 3.7.
Now we can investigate the action of $T(g)$ on the functions in Eq. 3.15. This action will be two-fold as it will move the position of the magnetic ion and additionally will change the direction of the magnetic moment. The application of $g=\{h|\boldsymbol{\tau}_h\}$ on the position $\boldsymbol{r}_d$ of the magnetic ion d in the zeroth cell gives

$$g\boldsymbol{r}_d = h\boldsymbol{r}_d + \boldsymbol{\tau}_h = \boldsymbol{r}_{d'} + \boldsymbol{a}_p(g,d), \tag{3.16}$$

where $\boldsymbol{r}_{d'}$ is the position of magnetic ion d'. The magnetic ion will be generally moved to a position outside the zeroth cell which is denoted by $\boldsymbol{a}_p(g,d)$ that is the connection vector between the zeroth cell and the new cell and is called the *return translation*. Thus the function Eq. 3.15 will receive an additional phase factor $\exp[-i\boldsymbol{k}\cdot\boldsymbol{a}_p(g,d)]$ upon application of g in accordance with Eq. 3.7.
For the action of $T(g)$ on the magnetic moment we have to consider that magnetic moments are pseudo vectors and therefore behave different under improper rotations. We will denote the component β of the magnetic moment of the magnetic ion d as $\boldsymbol{S}_d^\beta$. Since according to Eq. 3.16 the magnetic ion d is transformed into the magnetic ion d' the same is valid for the respective moments and in addition to the rotation the magnetic moment will collect the phase factor $\exp[-i\boldsymbol{k}\cdot\boldsymbol{a}_p(g,d)]$. Thus, we find for the application of g

$$g\boldsymbol{S}_d^\beta = \delta_h R^h_{\alpha\beta}\boldsymbol{S}_{d'}^\beta \exp[-i\boldsymbol{k}\cdot\boldsymbol{a}_p(g,d)], \tag{3.17}$$

where $R^h_{\alpha\beta}$ is a rotation matrix corresponding to the rotational part of g and δ_h is the determinant of $R^h_{\alpha\beta}$ that takes into account the transformation properties of pseudo vectors under improper rotations[5].
This allows us to formulate the action of $T(g)$ on Eq.3.15 as [INO91]

$$T(g)\varphi_{\boldsymbol{k}}^{d\beta} = \sum_{d'\alpha}\{\gamma_m^{\boldsymbol{k}}(g)\}_{d'\alpha,d\beta}\varphi_{\boldsymbol{k}}^{d'\alpha}, \tag{3.18}$$

$$\text{where}\quad \{\gamma_m^{\boldsymbol{k}}(g)\}_{d'\alpha,d\beta} = \exp[-i\boldsymbol{k}\cdot\boldsymbol{a}_p(g,d)]\delta_h R^h_{\alpha\beta}\delta_{d',gd}. \tag{3.19}$$

Here the Kronecker symbol $\delta_{d',gd}$ describes the permutation of the magnetic ions due to Eq. 3.16 with gd being a short form of $g\boldsymbol{r}_d$. Finally, by introducing Eqs. 3.13 and 3.18 into the projection operator in Eq. 3.6 the basis functions of the *magnetic irreducible presentation* are obtained as [INO91]

$$\Psi_\lambda^{\boldsymbol{k}\nu} = \sum\nolimits_n^{\oplus}\sum\nolimits_{d=1}^{\sigma_M\oplus}\boldsymbol{S}_{d\lambda}^{\boldsymbol{k}\nu}\exp(i\boldsymbol{k}\cdot\boldsymbol{l}_n), \tag{3.20}$$

$$\text{where}\quad \boldsymbol{S}_{d\lambda}^{\boldsymbol{k}\nu} = \sum_{h\in G_{\boldsymbol{k}}^0}\gamma_{\lambda[\mu]}^{\boldsymbol{k}\nu}(g)\exp[-i\boldsymbol{k}\cdot\boldsymbol{a}_p(g,d)]\delta_{d',gd}\delta_h\begin{pmatrix}R^h_{x[\beta]}\\ R^h_{y[\beta]}\\ R^h_{z[\beta]}\end{pmatrix}, \tag{3.21}$$

[5]The determinants of the rotation matrices corresponding to proper and improper rotations are equal to 1 and -1 respectively.

where the two direct sums are over all N cells of the crystal and over each magnetic ion i in the unit cell. The indices in square brackets are fixed. The $\boldsymbol{S}_{d\lambda}^{\boldsymbol{k}\nu}$ have the physical meaning of magnetic moments forming a magnetic structure with propagation vector $\boldsymbol{k}$. Therefore they can be identified with the *magnetic Fourier modes* that we already defined in section 2.3.5 in order to describe a magnetic structure.
We note that for the calculation of the basis functions $\Psi_{\lambda}^{\boldsymbol{k}\nu}$ only the knowledge of the propagation vector $\boldsymbol{k}$ (that can be experimentally observed in neutron scattering, s. section 2.3.5), the position of the magnetic ions in the primitive cell of a magnetic structure and the space group of the crystal (in order to know the irreducible presentations of the little group $\gamma_{\lambda\mu}^{\boldsymbol{k}\nu}(g)$ from the tables in [Kov65]) are necessary. The set of magnetic basis function $\Psi_{\lambda}^{\boldsymbol{k}\nu}$ then describes all magnetic structures that are in agreement with the symmetry of the crystal structure. The real magnetic structure can be described as a linear combination of these magnetic basis functions with complex mixing coefficients $\mathrm{C}_{\lambda}^{\boldsymbol{k}\nu}$. The magnetic structure of the crystal then can be found by fitting the magnetic model corresponding to the linear combination of the basis functions to the observed magnetic diffraction pattern. Thus, the only task that has to be performed in order to identify the real magnetic structure is to find the proper irreducible representation ν and the corresponding mixing coefficients $\mathrm{C}_{\lambda}^{\boldsymbol{k}\nu}$ that give the best agreement with the observed data.
Nowadays the magnetic basis functions that give an initial model for fitting the magnetic structure can be calculated by computer programs that only need the propagation vector, the position of the magnetic ions and the space group of the crystal as input parameters, examples are the programs MODY [SBP04] and BASIREPS [RC06].
We emphasise that the basis functions in Eq. 3.20 are in general complex. However, as a physical quantity the magnetic structure is real. This is no inconsistency since in general the propagation vectors $\boldsymbol{k}$ and $-\boldsymbol{k}$ exist in a pair (compare e.g. reference [Izy84]) and their related basis functions are considered together as we already used it in section 2.3.5 which leads to a real magnetic structure (compare Eq. 2.42).

3.3 Magnetic Domains

We have seen that the symmetry of a magnetic structure that develops in a crystal has in general lower symmetry compared to the symmetry of the crystal. This leads to the formation of magnetic domains. Here we will summarise the different types of possible domains and some of their consequences on magnetic structure determination.

3.3.1 Configuration domains

In section 3.2.2 we have shown that some of the rotational symmetry elements in the point group G^0 belonging to a crystal do not leave the propagation vector invariant. These point group elements generate a new arm of the star $\{\boldsymbol{k}\}$ and lead to so-called *configuration* or

$\boldsymbol{k}$-*domains*, that is domains linked to another arm $\boldsymbol{k}_L$ of the star.
As an example we can consider the compound MnSi that was also investigated in this work. The crystal structure of MnSi belongs to the cubic spacegroup $P2_13$. The corresponding point group is 23 and contains 12 symmetry operations. The application of these symmetry operations on the magnetic propagation vector of MnSi that is equal to $\boldsymbol{k} = (2\pi/a)[\zeta, \zeta\,\zeta]$ with $\zeta = 0.016$ leads to an overall number of four different propagation vectors. This is demonstrated in table. 3.1.
Since configuration domains only lead to additional reflections they do not hinder the determination of a magnetic structure.

Table 3.1: In table we show the action of the 12 elements of point group 23 of MnSi onto the magnetic propagation vector of MnSi $\boldsymbol{k} = [\zeta, \zeta\,\zeta]$ with $\zeta = 0.016$. The point group operators are given in the Jones-Faithful notation (JFN) and names are given in the notation of Kovalev [Kov65] and the International tables of Crystallography (IT)[Hah06].

Kovalev	IT	Symm. Op. (JFN)	Action on $\boldsymbol{k}$
h_1	1	x,y,z	[0.0160, 0.0160, 0.0160]
h_9	3_{111}	z,x,y	[0.0160, 0.0160, 0.0160]
h_5	3^{-1}_{111}	y,z,x	[0.0160, 0.0160, 0.0160]
h_4	2_z	-x,-y,z	[-0.0160, -0.0160, 0.0160]
h_{10}	$3^{-1}_{1\bar{1}1}$	z,-x,-y	[-0.0160, -0.0160, 0.0160]
h_7	$3_{\bar{1}11}$	-y,z,-x	[-0.0160, -0.0160, 0.0160]
h_3	2_y	-x,y,-z	[-0.0160, 0.0160, -0.0160]
h_{12}	$3^{-1}_{\bar{1}11}$	-z,-x,y	[-0.0160, 0.0160, -0.0160]
h_6	$3_{11\bar{1}}$	y,-z,-x	[-0.0160, 0.0160, -0.0160]
h_2	2_x	x,-y,-z	[0.0160, -0.0160, -0.0160]
h_{11}	$3^{-1}_{11\bar{1}}$	-z,x,-y	[0.0160, -0.0160, -0.0160]
h_8	$3_{1\bar{1}1}$	-y,-z,x	[0.0160, -0.0160, -0.0160]

3.3.2 180° domains

When the magnetic moments in different parts of a crystal are related via a time reversal symmetry operation *180° domains* will be observed. The time reversal symmetry implies that all the moments in one part of the crystal have reversed direction compared to the moments in the other part. This is because the emergence of spontaneous magnetisation in a crystal breaks the time inversion symmetry, however, in the absence of an external magnetic field both directions related via the time reversal are energetically degenerate.
If all signs of the magnetic moments in a magnetic structure are reversed also the sign of the magnetic interaction vector in Eq. 2.28 is reversed. For a magnetic structure with a non-zero propagation vector the two domains cannot be distinguished in a neutron scattering experiment since for this case only terms of the form $M^i_{\perp\boldsymbol{Q}} M^{\dagger j}_{\perp\boldsymbol{Q}}$ (i,j=y,z) are observed, that are identical regardless of the sign of the moment. However, for a magnetic

structure with zero propagation vector nuclear and magnetic scattering appear at the same position. When the experiment is performed with polarised neutrons nuclear-magnetic interference terms of the form $N^{\dagger}_{\boldsymbol{Q}} M^{i}_{\perp \boldsymbol{Q}}$ appear in both the polarised cross-section and as well in the polarisation tensor (compare Eqs. 2.71 and 2.72) that change their sign when the direction of the magnetic moments is reversed. If real or imaginary nuclear-magnetic interference terms will be observed depends on the exact magnetic structure and we refer to reference [Bro05] for a complete discussion.

3.3.3 Orientation domains

The little group $\mathrm{G}_{\boldsymbol{k}}$ defined in section 3.2.2 is the group of all symmetry operations that leave the propagation vector invariant. The real magnetic structure of a crystal has a magnetic space group M that is a subgroup of $\mathrm{G}_{\boldsymbol{k}}$. Therefore M has the same or lower symmetry than $\mathrm{G}_{\boldsymbol{k}}$. It has lower symmetry when some of the mixing coefficients $\mathrm{C}^{\boldsymbol{k}\nu}_{\lambda}$ of the magnetic basis functions $\Psi^{\boldsymbol{k}\nu}_{\lambda}$ have to be set equal to zero in order to describe the magnetic structure via the basis functions for a single irreducible representation ν. Consequently, all the symmetry operations contained in $\mathrm{G}_{\boldsymbol{k}}$ but not in M will transform the magnetic structure in a new magnetic structure and hence generate additional domains. These domains are called *orientation domains* or *spin domains (s-domains)*.
Regardless of the fact that the magnetic structure will be different for each domain, the magnetic scattering from all orientation domains will be observed at identical positions in reciprocal space, since they all possess the same periodicity. Thus, when the magnetic cross-section or the the polarisation tensor are calculated from a magnetic structure with present orientation domains this has to be considered and we have to average over the domains via [Bro05]

$$\mathrm{P}_{ij} = \sum_{l} \eta_l \mathrm{P}^{l}_{ij} = \sum_{l} \eta_l (P_{i0} \tilde{P}^{l}_{ji} + P^{l''}_{j})/|\boldsymbol{P_0}| \tag{3.22}$$

where η_l is the population of the domain l and $\sum_l \eta_l = 1$ has to be fulfilled. Generally the presence of orientation domains leads to a depolarisation of the neutron beam. This is demonstrated in Fig. 3.1. Therefore, the polarisation tensor is a useful quantity to determine the presence of magnetic orientation domains.

3.3.4 Chirality domains

In section 1.2 we demonstrated that a helical magnetic structure breaks the spatial inversion symmetry due to its chirality. Thus the magnetic space group M of such a structure will not contain the inversion symmetry element. If the underlying crystal structure is centrosymmetric and therefore does contain the inversion symmetry element *chirality domains* can occur that correspond to a situation where in one part of the crystal the

magnetic structure is right-handed whereas it is left-handed in a second part (compare Fig. 1.4).
If a magnetic structure that has a unique handedness is investigated with polarised neutrons the chiral term C in Eqs. 2.71 and 2.72 will be non-zero as has been discussed in section 2.4.3. But as the chiral term reverses its sign when a right-handed structure is changed to be left-handed it will be equal to zero if both chirality domains are equally populated. If the two domains are however unequally populated the chiral term will be only reduced and the population of both domains can be determined [Bro05].

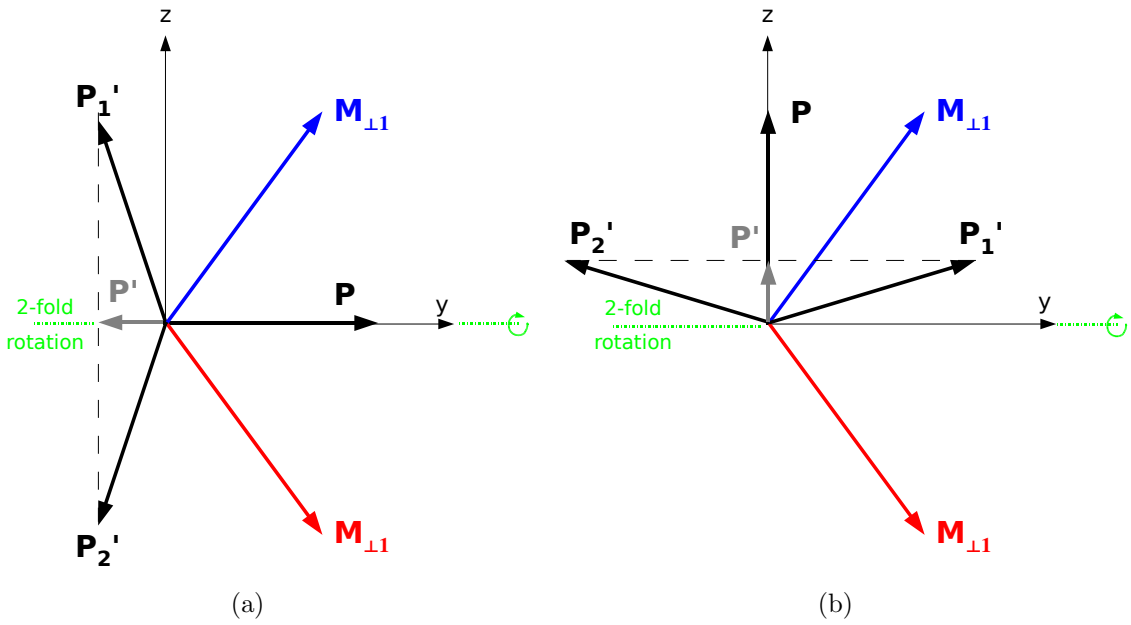

Figure 3.1: From section 2.4.2 we know that on a pure magnetic reflection the polarisation vector rotates around $\boldsymbol{M}_{\perp \boldsymbol{Q}}$ (for $\boldsymbol{M}_{\perp \boldsymbol{Q}} \parallel \boldsymbol{M}^{\dagger}_{\perp \boldsymbol{Q}}$). We assume a magnetic structure that has two orientation domains that are related via a two-fold rotation axis parallel to the y-axis in the figure. Consequently the magnetic interaction vectors $\boldsymbol{M}_{\perp 1}$ and $\boldsymbol{M}_{\perp 2}$ are also related via the same two fold rotation as it is shown in both figures. The polarisation vector $\boldsymbol{P}$ will rotate around the corresponding magnetic interaction vector for each of the domains and two distinct final polarisation vectors $\boldsymbol{P}'_1$ and $\boldsymbol{P}'_2$ are obtained, respectively. When they are averaged according to Eq. 3.22 with equal domain populations η the total final polarisation vector $\boldsymbol{P}'$ is obtained. It is significantly reduced compared to the initial polarisation vector $\boldsymbol{P}$ and therefore depolarised. In (a) the situation is shown for the initial polarisation vector $\boldsymbol{P}$ being parallel to the two-fold rotation axis whereas in (b) it is perpendicular to it. The drawings were adapted from reference [Bro05].

Chapter 4

Single chirality in the multiferroic $NdFe_3(BO_3)_4$

$NdFe_3(BO_3)_4$ is a highly fascinating material because it displays a range of interesting physical properties. It is a member of the family of borates $RM_3(BO_3)_4$ (R = Y,La-Lu, M = Al, Ga, Cr, Fe, Sc) that currently attract much attention because of their special optical properties. Rare earth ions in general and Nd^{3+} in particular have excellent characteristics to generate infrared laser action and to serve in nonlinear optics. Nd^{3+} doped $YAl_3(BO_3)_4$ (YAB)or $GdAl_3(BO_3)_4$ (GAB) crystals or the concentrated crystal $NdAl_3(BO_3)_4$ (NAB) are of great interest as they show strong optical absorption around 750 and 800 nm so that they can be easily pumped by commercial laser diodes [Kam81, Kam96]. When pump and laser radiation are propagating in a nonlinear host, they may interact with each other providing the possibility of generating visible laser radiation [Boy92]. E.g. for YAB, GAB and NAB it was shown that they perform excellent as self-frequency-doubling, self-sum-frequency-mixing and, thus as microchip laser materials [Jaq01, HCC$^+$02, CLJ$^+$01]. These materials are interseting for scientific applications like quantum computing but also for commercial devices like compact red, green and blue (RGB) laser devices that may be used in highly portable video projectors or similar devices. Further it was speculated that the replacement of the nonmagnetic Al^{3+} ion by the magnetic Fe^{3+} may result in new optoelectronic applications like e.g. Faraday devices [CKP$^+$04].
The two members $GdFe_3(BO_3)_4$ and $NdFe_3(BO_3)_4$ of this borate family are additionally interesting with respect to there magnetic properties due to competing magnetic sublattices. This is especially fascinating as both materials were recently identified as multiferroics showing magnetic field induced ferroelectric phases via the ME effect [ZKK$^+$05, ZVK$^+$06]. However the magnetic properties of the borates were much less studied than the optical ones.
The knowledge of the microscopic magnetic properties and structure is thus highly desirable for the family of $RFe_3(BO_3)_4$, especially for the understanding of the ME effect. In this chapter we present our experimental investigation of the magnetic struc-

ture of $NdFe_3(BO_3)_4$ by mainly neutron scattering. We have chosen $NdFe_3(BO_3)_4$ over $GdFe_3(BO_3)_4$ as model for group of materials $RFe_3(BO_3)_4$ as Gd has a large absorption cross-section for neutrons and therefore is rather unsuitable for structure determination.

4.1 Basic properties

Before we start with the description of our experiments and results we will briefly discuss the basic properties of the family of iron borates $RFe_3(BO_3)_4$.

4.1.1 Crystal structure

The iron borates $RFe_3(BO_3)_4$ (R = Y,La-Lu) crystallise in the trigonal space group R32 (group no. 155 in the international tables of crystallography), that is they belong to the structural type of the mineral huntite $CaMg_3(BO_3)_4$ [CCGP$^+$97]. This structure is missing a centre of inversion. In table 4.1 we give the structural parameters for $NdFe_3(BO_3)_4$ obtained from our sample[1]. The structure is composed of isolated RO_6 distorted trigonal prisms and smaller FeO_6 octahedra that form layers with a R-Fe distance of ≈ 3.78 Å. The RO_6 polyhedra are interconnected inside the layers by corner sharing with triangular BO_3 groups of two different types and the FeO_6 groups. The FeO_6 groups form one-dimensional helical chains along the c-axis with Fe-Fe distances of ≈ 3.18 Å. The layers formed from the FeO_6 and RO_6 polyhydra are shown in Fig. 4.1. Rare earth iron borates of heavy rare earth atoms (Eu-Ho,Gd,Tb) and of Y undergo a structural phase transition to the space group $P3_121$ at a temperature T_s. The temperature T_s of the phase transition was found to increase with the ionic radius of the rare earth atom from $T_s = 88$ K for Eu to 445 K for Y by following an anomaly in the specific heat that was associated to the structural phase transition [HDI$^+$03].

4.1.2 Magnetic properties

Measurements in a SQUID revealed a peak in the magnetic susceptibility for the entire group of iron borates. The peak was attributed to the onset of antiferromagnetic order [HDI$^+$03]. The corresponding ordering temperature T_N at which the peak is ovserved depends on the ionic radius of the R site and varies from 22 K for R = La to 40 K for R = Tb.
Up to now the most detailed studies were performed on $GdFe_3(BO_3)_4$. For $GdFe_3(BO_3)_4$ the structural phase transition from $P3_121$ to R32 is observed at $T_s = 156$ K [KFM$^+$05]. The magnetic ordering temperature is $T_N = 36$ K and results in antiferromagnetic ordering of the magnetic moments of the Fe^{3+} ions in adjacent hexagonal ab-planes. The

[1] We will discuss the table in more detail in the experimental section.

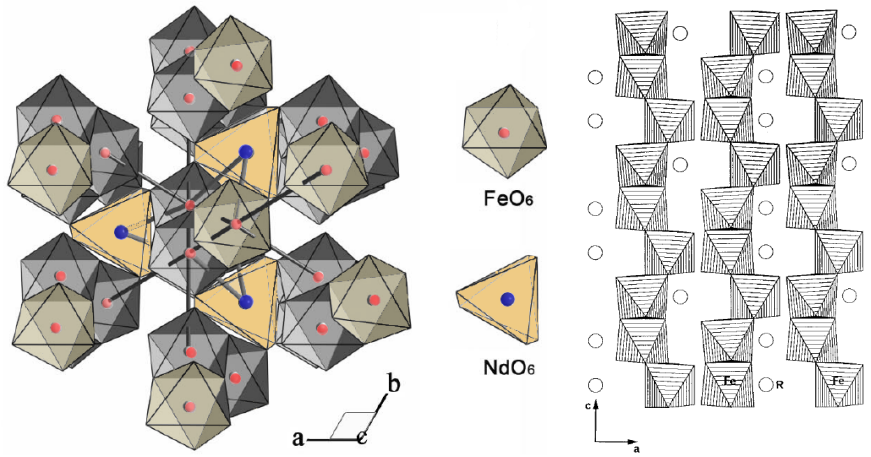

(a) (b)

Figure 4.1: (a) The crystal structure of $RFe_3(BO_3)_4$ is shown. We only display the RO_6 and FeO_6 polyhedra present in the structure, the B ions are neglected. The polyhedra in light pastel colours are situated in the top ab layer shown in the viewgraph. We see that three FeO_6 octahedra are interconnected by one common ReO_6 prism. The FeO_6 groups form helical chains along the c axis as illustrated in (b) ((a) is taken from [PCS$^+$07] whereas (b) is from [CCGP$^+$97]).

magnetic moments are confined in the basal plane and form a 120°-structure. A second magnetic transition is observed at $T_{SR} = 9$ K where it is assumed that the Fe^{3+} magnetic moments reorient along the hexagonal c axis. They couple still antiferromagnetically between adjacent hexagonal planes but magnetic moments are oriented ferromagnetically for neighboring helical iron chains. Additionally they are aligned antiferromagnetically with respect to the moments of the Gd^{3+} ions within each layer [BBG$^+$03, PPBB04]. However, this magnetic structure is just based on modelling magnetic susceptibility and antiferromagnetic resonance data.
Even though the neutron powder diffraction results of Ritter *et al* [RBV$^+$07] on $TbFe_3(BO_3)_4$ were published after our experimental work was finished we want to briefly discuss them here for completeness of our description. They find an ordering temperature T_N of 40 K in agreement with [HDI$^+$03]. The magnetic structure derived from the neutron scattering data is equivalent to the one for $GdFe_3(BO_3)_4$ below the spin orientation transition temperature T_{SR}: both Fe^{3+} and Tb^{3+} moments align parallel to the crystallographic c-axis and order antiferromagnetically along this direction. Within one ab-layer the moments in all three helical Fe^{3+} chains are aligned mutually ferromagnetic, but the alignment with respect to Tb^{3+} is antiferromagnetic. The values found for the ordered magnetic moments are $\mu_{Fe^{3+}} = 3.94\ \mu_B$ and $\mu_{Tb^{3+}} = 8.54\ \mu_B$.
Campà *et al* performed DC magnetic susceptibility measurements using a SQUID on $NdFe_3(BO_3)_4$ [CCGP$^+$97]. They found two peaks in the magnetic susceptibility at 32 K and 6 K respectively. They proposed that the higher temperature is connected to the

onset of ordering within the Fe^{3+} sublattice whereas below 6 K they assumed that both Fe^{3+} and Nd^{3+} possess three-dimensional antiferromagnetic order. Later the Neél temperature $T_N = 33(1)$ K was confirmed by Chukalina *et al* by means of infrared absorption spectroscopy [CKP+04]. However, they were unable to observe any anomaly at lower temperatures and therefore proposed simultaneous magnetic ordering of both sublattices at T_N. We see that the existing results on the magnetic structure of $NdFe_3(BO_3)_4$ are limited and additionally contradictionary. Therefore, the performance of neutron diffraction experiments in order to find the exact magnetic structure of $NdFe_3(BO_3)_4$ is highly desirable.

4.1.3 Magneto-electric effect

In two members of the family of iron borates a ME effect has been observed recently. For $GdFe_3(BO_3)_4$ a strong enhancement of the dielectric constant measured along the crystallographic a-axis was observed when a magnetic field was applied along the a- or c-axis [YLS+06] as shown in Fig. 4.2. The enhancement is observed between T_N and T_{SR} and between T_M and T_{SR} if the field is applied along the a-axis or c-axis, respectively. Here, $T_M = 10$K is an anomaly in the dielectric constant that is observed upon heating the crystal. Additionally, Zvezdin *et al* reported that below T_{SR} a magnetic field induced ferroelectric polarisation develops that is accompanied by a jump in the magnetostriction [ZKK+05].
The same authors reported an equivalent effect for $NdFe_3(BO_3)_4$. Below a temperature $T_{ME} \approx 25$ K a high ferroelectric polarisation along the a-axis was observed when a magnetic field was applied parallel to the a or b axis. A value of about -320 $\mu C/m^2$ of electric

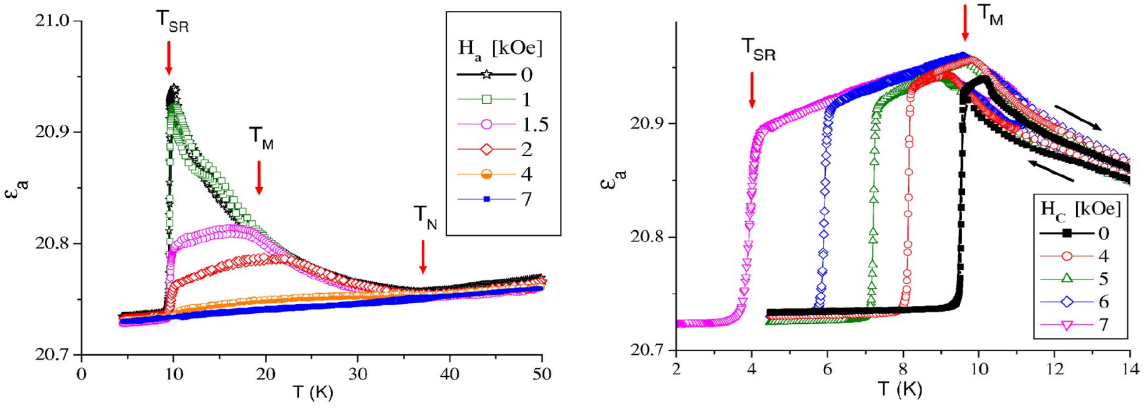

(a) (b)

Figure 4.2: The dielectric constant ε_a of $GdFe_3(BO_3)_4$ measured along the a-axis is shown as a function of temperature for different magnetic fields applied parallel to (a) the a-axis and (b) the c-axis [YLS+06].

polarisation for magnetic fields above 80 kOe was measured. This is about 30 times larger than for $GdFe_3(BO_3)_4$)[ZVK$^+$06]. The experimental data is shown in Fig. 4.3. We note that T_{ME} does not correspond to any magnetic transition temperature observed so far unlike for $GdFe_3(BO_3)_4$.

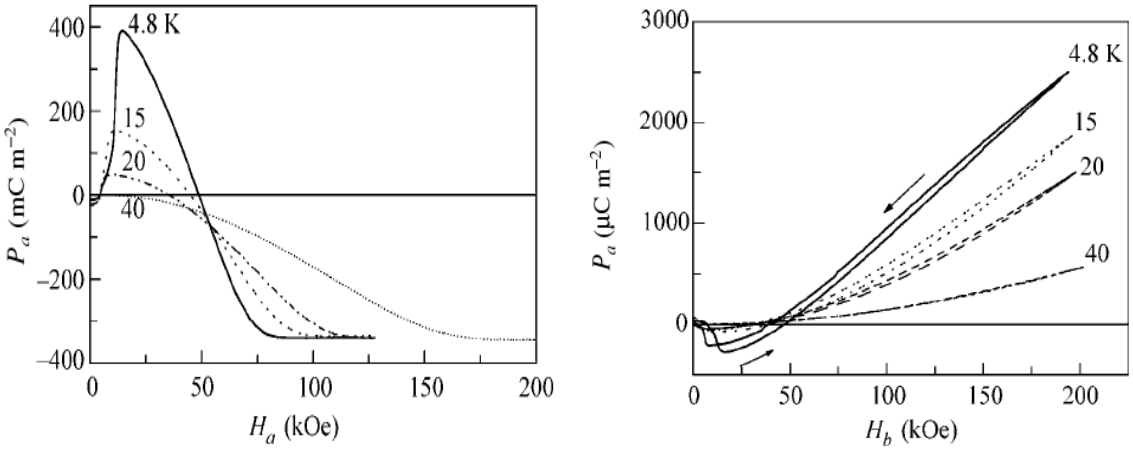

(a) (b)

Figure 4.3: The electric polarisation of $NdFe_3(BO_3)_4$ measured along the a-axis as a function of magnetic field for different isotherms is shown for (a) the magnetic field parallel to the a-axis and (b) parallel to the b-axis[ZKK$^+$05].

4.2 Experimental work and results

All the experimental work performed within the framework of this thesis was performed only on one member of the family of iron borates, namely on $NdFe_3(BO_3)_4$. We investigated the magnetic structure of this compound mainly by unpolarized and polarized neutron diffraction.

4.2.1 Sample preparation

Because of the strong neutron absorption by natural boron, samples with ^{11}B enriched to 99% were prepared at the Institute of Physics at Krasnoyarsk by the group of Prof. Petrakovskii. The single crystals $NdFe_3(^{11}BO_3)_4$ were grown from solution in a melt [BKT04] of 75 mass% (Bi_2 Mo_3 O_{12} + $3^{11}B_2O_3$ + $0.6Nd_2O_3$) + 25 mass% $NdFe_3(^{11}BO_3)_4$. The saturation temperature was $T_s \approx 920$ °C, and the concentration (n) dependence of T_s was $dT_s/dn = 5$ °C/mass%. The flux with mass of 150 g was prepared by melting at the temperature of 1100 °C of the oxides Bi_2O_3, MoO_3, $^{11}B_2O_3$, Fe_2O_3 and Nd_2O_3, using a platinum crucible. The flux was kept at this temperature for 10 h for homogenization.

Afterwards the temperature of the flux was decreased to T = T_s + 7 ° C, the platinum rod with four seeds was settled down in the flux and the rotation of 30 revolutions per minute of the rod was switched on. After 10 min the temperature was decreased to T = T_s -10 ° C. Then the temperature was decreased with velocity of 1-3 °C/24 h. The total duration of the crystal growth was about 14 days. Thus crystals with linear dimensions up to 12 mm were prepared.
Some of the crystals were used to produce powder samples for the neutron powder diffraction experiments by grinding them into fine powder in a mill.

4.2.2 Chemical structure refinement

The quality of the sample that was enriched with ^{11}B was verified by determining its chemical structure by neutron, laboratory X-rays and synchrotron radiation. All structural refinements described hereafter were performed with a recent version of the program suite Fullprof [RC06] where the internal scattering lengths were used.
We investigated a small fraction of the $NdFe_3(^{11}BO_3)_4$ powder sample at room temperature on a Siemens D-500 laboratory x-ray powder diffractometer available at the Paul Scherrer Institut (PSI). For the measurement the $\theta/2\theta$ geometry with rotating flat sample and Cu K_α radiation were used. The measured x-ray diffraction pattern can be excellently fitted in the powder profile matching mode [RC06](goodness of fit $\chi^2 = 3.5$) on the basis of space group R32, yielding the lattice parameters listed in table 4.1. Still, close to the first Bragg peak (1, 0, 1), there is additional intensity which is visible as a shoulder towards higher scattering angles that may be due to a trace of $Nd(OH)_3$. Otherwise the sample seems to be the expected single-phase borate material. On the other hand, fits with the chemical structure model published in [CCGP$^+$97] reveal very strong preferred orientation along the direction [1, 0, 1] and produce only moderate agreement between observation and calculation.
In order to further investigate these issues measurements on the high resolution powder diffractometer at the Swiss SLS synchrotron of PSI were undertaken. The powder sample was filled into a cylindrical glass capillary of approximately 0.3 mm diameter and 0.9 mm length and was measured at 308 K with synchrotron radiation of wavelength λ = 0.708 27(5) Å. The sample had been rotating during the measurement. The final average diffraction pattern covers the scattering angle range from 3.519° to 70.151° with an angular step of 0.004°. Surprisingly, the synchrotron measurements showed no evidence for the presence of other phases or additional line splittings. The observed Bragg peaks could be will indexed on the basis of space group R32 with the hexagonal lattice parameters given in table 4.1.
Finally also neutron powder diffraction measurements at room temperature were performed at the high resolution powder neutron diffractometer HRPT [FFK$^+$00] at the

Table 4.1: Structural parameters of $NdFe_3(BO_3)_4$, refined from the HRPT neutron diffraction data (λ = 1.8857(5) Å) at room temperature (n), compared to laboratory (x) and synchrotron x-rays (s) as well as to the single-crystal x-ray results of reference [CCGP$^+$97] (ref). Space group R32 (no. 155). B = isotropic temperature factor. Within brackets estimated standard deviations are given. Agreement values [RC06] concerning weighted profile intensities R_{wp} = 6.8%, statistically expected value R_{exp} = 2.2%, goodness of fit χ^2 = 10.3 and concerning integrated nuclear neutrons intensities R_{Bn} = 7.5%

Lattice parameters (Å):		$a_{hex,n}$ =	9.589(1)	$c_{hex,n}$ =	7.612(1)
		$a_{hex,x}$ =	9.5878(3)	$c_{hex,x}$ =	7.6103(3)
		$a_{hex,s}$ =	9.588(1)	$c_{hex,s}$ =	7.611(1)
		$a_{hex,ref}$ =	9.578(1)	$c_{hex,ref}$ =	7.605(3) [CCGP$^+$97]
Atom	Site	x	y	z	B (Å^2)
Nd	3a	0	0	0	0.38(7)
Fe	9d	0.5500(2)	0	0	0.1[a]
[CCGP$^+$97]		0.5511(1)			
B1	3b	0	0	0.5	0.47(4)
B2	9e	0.4463(3)	0	0.5	0.47(4)
		0.446(1)			
O1	9e	0.8539(4)	0	0.5	0.66(3)
		0.8557(6)			
O2	9e	0.5948(3)	0	0.5	0.66(3)
		0.5903(8)			
O3	18f	0.4546(2)	0.1448(2)	0.5174(3)	0.66(3)
		0.4511(6)	0.1453(6)	0.5188(6)	

[a] Fixed, as it tended to negative values.

continuous spallation neutron source SINQ at PSI. A cylindrical vanadium container[2] of 8 mm diameter was filled with the powder sample to 55 mm in height under He gas atmosphere. For the neutron wavelength of 1.8857(5) Å the sample transmission has been measured, yielding the product of linear absorption coefficient μ and sample radius r: μr = 0.344. Due to the used Ge monochromator of HRPT higher order contamination of the neutron beam were negligible. As neutrons are, in contrast to x-rays, particularly sensitive to light atoms such as boron and oxygen, a powder profile refinement of the HRPT data for room temperature was also made starting from the structure model published in [CCGP$^+$97]. Corresponding refined structural parameters are summarised in table 4.1. In addition the neutron powder diffraction patterns suggest certain problems related to preferred orientation or insufficient powder averaging even though the sample was ro-

[2]The coherent neutron scattering cross-section for vanadium is 0.01838(12) b and therefore negligible. It scatters neutrons mainly incoherently (incoherent cross-section σ_{inc} = 5.08(6). As incoherent scattering is independent from the scattering angle (s. section 2.2.2) and only will add a constant background, vanadium is generally used as container material in neutron powder diffraction.

tated during the measurements. Usually the former effect is negligible in neutron powder diffraction. By employing the March approach for preferred orientation [RC06], we were able to improve the fits significantly. However, in contrast to the x-ray refinement no well defined preferred orientation direction could be identified and finally it has been fixed to the direction [0, 0, 1]. 101 reflections contribute to the neutron diffraction pattern, compared to 27 parameters used in the refinement (six for the background polynomial). Within error limits, the lattice parameters of the present $NdFe_3(^{11}BO_3)_4$ sample determined by x-ray and neutron diffraction agree, but are somewhat larger than the values published in [CCGP$^+$97] for $NdFe_3(BO_3)_4$. The positional parameters are in reasonable agreement with those published by Campá *et al* [CCGP$^+$97].

4.2.3 Bulk measurements

In addition to the neutron scattering experiments we also performed bulk measurements. The temperature dependence of specific heat C_p of polycrystalline $NdFe_3(^{11}BO_3)_4$ was determined using a PPMS measurement system from Quantum Design at Paul Scherrer Institut in the temperature range from approximately 3 to 152 K. From about 15 to 43 K a measurement in an external magnetic field of 9 T has also been performed. The results are shown in Fig. 4.4. There is a clear peak observed in C_p at approximately $T_N = 30.1(2)$ K which we attribute to the onset of magnetic long-range order in agreement with [CCGP$^+$97, CKP$^+$04]. The peak position does not change upon cooling or heating and is also independent of magnetic fields up to 9 T. This implies that the coupling between the magnetic structure of $NdFe_3(^{11}BO_3)_4$ and external magnetic fields is relatively weak compared to the exchange interactions that stabilise the magnetic ordering.
Magnetic susceptibility measurements were made by means of a SQUID at the Institute of Physics at Krasnoyarsk on a single crystal of $NdFe_3(BO_3)_4$ in the temperature range from 4.2 to 224 K. The magnetic field was applied parallel and perpendicular to the hexagonal c-axis in order to determine the magnetic anisotropy of the system. The data are presented in Fig. 4.5 and demonstrate that the magnetic anisotropy in $NdFe_3(BO_3)_4$ has easy plane character inside the hexagonal ab-plane. The peak seen in both curves at approximately 31(1) K also suggests the onset of antiferromagnetic order. Below approximately 15 K there is again an increase of the magnetic susceptibility for lower temperatures. Both temperatures are marked with a red doted line in Fig. 4.5. The observed increase of the magnetic susceptibility indicates that the magnetic structure may change at 15 K. Finally, the peak at 6 K, reported in [CCGP$^+$97], is not seen.

4.2.4 Investigation of the magnetic structure by neutron diffraction

In order to study the magnetic structure of $NdFe_3(^{11}BO_3)_4$ below the magnetic phase transition at $T_N \approx 31$ K that was observed in the bulk measurements the powder sample

was cooled down to T = 1.6 K inside a standard ILL orange cryostat [ora]. The low-temperature measurements were made on the cold-neutron powder diffractometer DMC [FKSK00] at the SINQ spallation source at the PSI that is dedicated to magnetic structure determination. The experiments were performed with the neutron wavelength λ = 2.4526(5) Å and a pyrolytic graphite filter was used in order to eliminate higher order contamination in the neutron beam. A stationary sample was used in a first set of measurements, however, in order to reduce preferred orientation effects or rather to obtain a

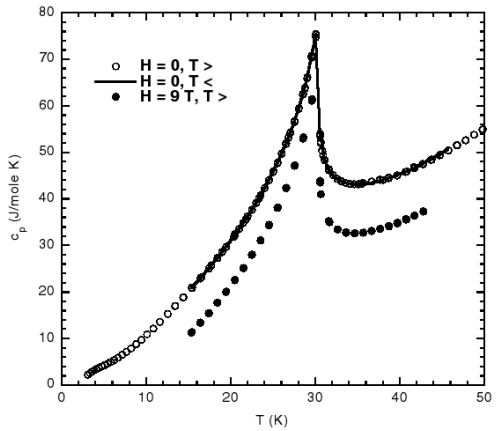

Figure 4.4: Temperature dependence of the specific heat of polycrystalline $NdFe_3(^{11}BO_3)_4$, measured on the PPMS (Quantum Design) at Paul Scherrer Institut. For clarity the data points in an external magnetic field of 9 T have been shifted by -10 units. T > and < indicate increasing and decreasing temperature, respectively. The figure has been published in reference [FPS+06].

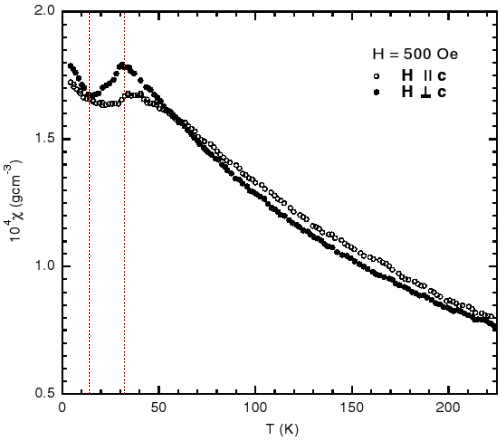

Figure 4.5: Anisotropy of magnetic susceptibility, measured by means of a SQUID at the Institute of Physics at Krasnoyarsk on a $NdFe_3(BO_3)_4$ single crystal with magnetic field H applied parallel and perpendicular to the hexagonal c-direction. The red lines denote the position of the peak associated with antiferromagnetic ordering and the increase of the susceptibilities inside the antiferromagnetic phase, respectively (s. text) [FPS+06].

better powder averaging over crystallite grains a second set of measurements were conducted with a rotating sample. In the latter case the sample was cooled in a closed cycle refrigerator from CTI-Cryogenics [cti]. This procedure improved the quality of the data and the fits considerably.
In addition a single crystal of approximate dimensions 8 x 8 x 8 mm^3 of $NdFe_3(^{11}BO_3)_4$ was investigated on the thermal four-circle neutron diffractometer TriCS [SKM$^+$00] at SINQ in the single-detector mode of operation at temperatures down to approximately 5 K, using a neutron wavelength $\lambda = 1.1809(4)$ Å. Here also the sample was cooled inside a closed cycle refrigerator.
The same single crystal was reinvestigated on the triple-axis spectrometer TASP [SRB01] situated at the end position of a cold super mirror guide of SINQ. The spectrometer was operated in its elastic mode in a high resolution setup with fixed incident and final wave vector $k_f = 1.2$ Å^{-1}. Additionally 20' Soller collimators were installed in the incident beam, in front of the analyzer and the detector. The second order contamination was removed from the beam by means of a beryllium filter that was inserted between the sample and the analyser. The use of a triple-axis spectrometer for diffraction experiments is justified by the excellent signal-to-noise ratio that is achieved by the use of an additional analyser crystal.
Similar to the refinement of the chemical structure, again all diffraction data were analysed with the program FullProf [RC06] where the internal tables for the magnetic form factors (compare section 2.3.3) were used.

4.2.4.1 Determination of the propagation vectors

The powder diffraction patterns measured at DMC show additional magnetic peaks for temperatures $T \lesssim 30$ K, that is clear evidence for magnetic long-range ordering in $NdFe_3(^{11}BO_3)_4$. This is demonstrated in Fig. 4.6 where the measured powder diffraction patterns are shown as a function of temperature. Fig. 4.7(a) shows a single pattern as observed at T = 20 K. Powder profiles that only contain the magnetic intensities were obtained by substracting the intensities that were observed at T = 50 K which is well above the magnetic phase transition at T_N. As example we show the profile for T =1.6 K in Fig. 4.7(b). The additional magnetic peaks could be well indexed with a commensurate magnetic propagation vector $\boldsymbol{k}_{hex} = [0,0,\frac{3}{2}]$ for all temperatures below T_N.
The single crystal diffraction data measured at TriCS yields the same magnetic propagation vector $\boldsymbol{k}_{hex} = [0,0,\frac{3}{2}]$ for temperatures $T \gtrsim 19$ K. The identified magnetic peaks such as (-1, 0, $\frac{1}{2}$) = (-1, 0, $\frac{3}{2}$) are observed as satellites $\pm\boldsymbol{k}_{hex}$ of nuclear Bragg peaks that comply with the triganal R lattice condition -H + K + L = 3n, n = integer.
For temperatures $T \lesssim 19$ K a splitting of the magnetic peak (-1,0, $\frac{1}{2}$) was observed in ω-scan. This is illustrated in Fig. 4.8. Due to the limited $\boldsymbol{Q}$-resolution of Trics operated at $\lambda = 1.1809(4)$ Å and the observed small splitting we reinvestigated the temperature dependence of the propagation vector on TASP with the high resolution setup described above. The crystal was oriented in scattering plane containing the reciprocal axis b^*(K)

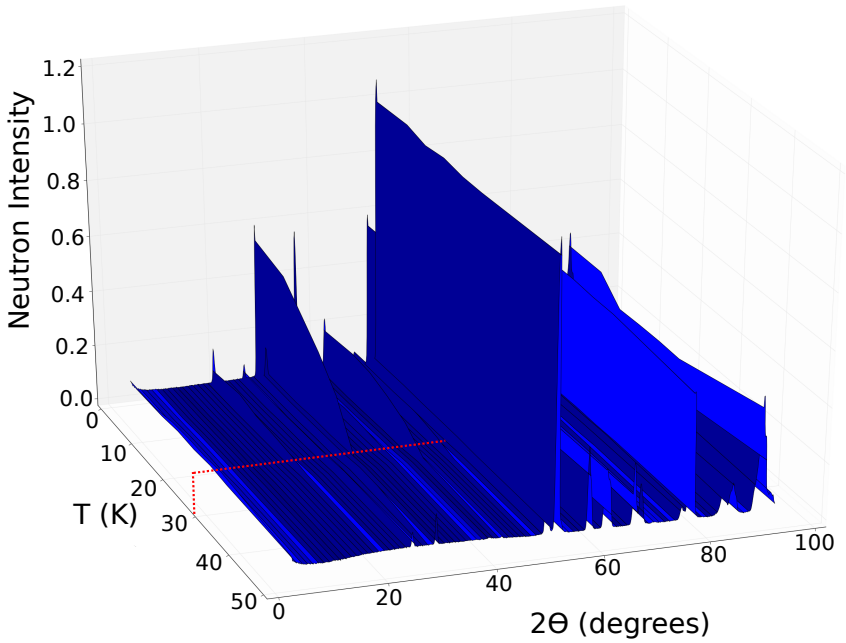

Figure 4.6: The temperature dependence of the neutron diffraction profiles measured at DMC are shown. The red line marks the temperature T $\lesssim$ 30 K where additional magnetic peaks are observed due to long-range magnetic order.

and c*(L). We performed elastic $\boldsymbol{Q}$-scans along the reciprocal L-direction for different values of K around the reciprocal space position $(0,0,\frac{3}{2})$ at T = 1.6 K. The result is shown in Fig. 4.9(a) and clearly demonstrates that the slight incommensurability associated to the observed splitting corresponds to a propagation vector $\boldsymbol{k}^i_{hex} = [0,0,\frac{3}{2} + \varepsilon]$ where the value of the splitting was determined to be $\varepsilon = 0.00667$.
Additionally we performed elastic $\boldsymbol{Q}$-scans along the reciprocal L-direction (for K = 0) as a function of temperature as shown in Fig.4.9(b). The propagation vector is commensurate down to the temperature $T_{ICM} \approx 13.5$ K and the magnetic Bragg reflections splits into two incommensurate satellite peaks. Here we estimated T_{ICM} as the temperature in Fig.4.9(b) where the maximum intensity of the commensurate magnetic reflection is reached and then starts to decrease as the reflection splits up into the two incommensurate satellite peaks. The observed splitting of magnetic Bragg reflection is temperature dependent and can be well described via $k_z = \frac{3}{2} + \varepsilon$ where

$$\varepsilon = 1.6 \cdot 10^{-3} |(T_{ICM} - T)|^{0.58}. \tag{4.1}$$

Hence, from now on, we will denote the temperature regimes between T_N and T_{ICM} commensurate magnetic (CM) phase and the temperature range below T_{ICM} as incommensurate magnetic (ICM) phase. We note that the temperature $T_{ICM} \approx 13.5$ K that was determined for the CM to ICM phase transition is in good agreement with the temperature where the magnetic susceptibility increases again for low temperatures (s. Fig. 4.5).

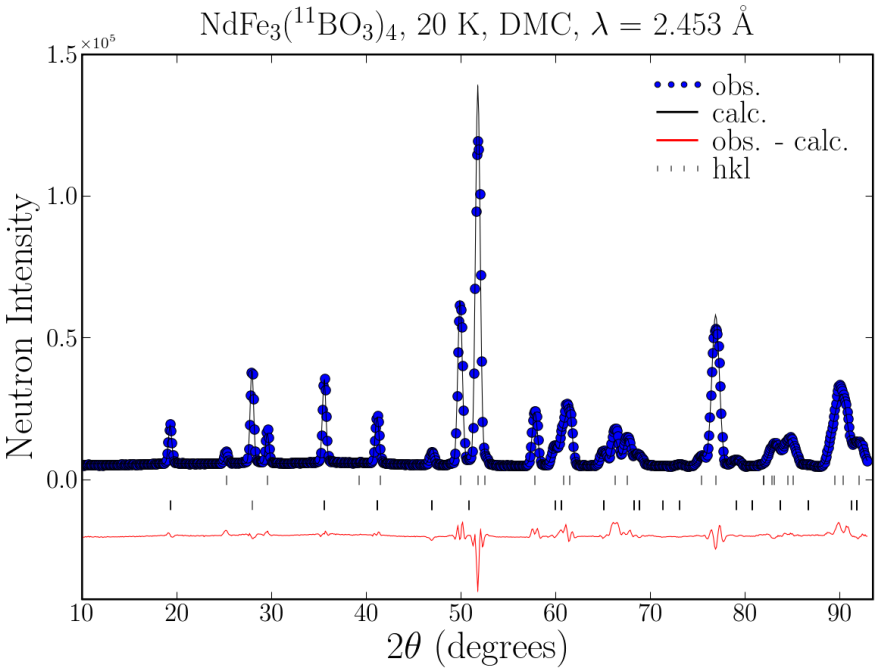

(a)

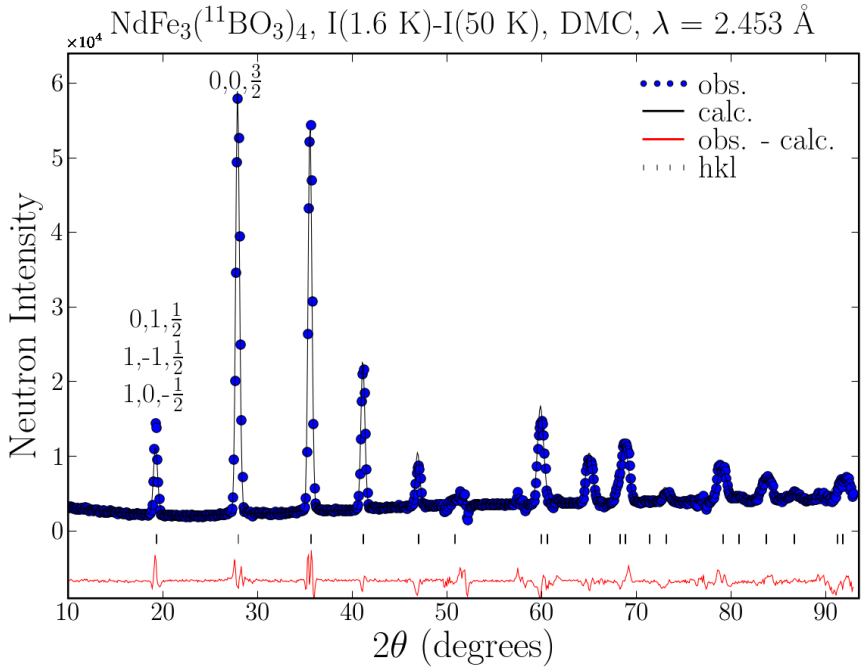

(b)

Figure 4.7: (a) Observed (points, angular step 0.1°), calculated (black line) and difference neutron diffraction pattern (difference of observed and calculated intensity, red line) of $NdFe_3(^{11}BO_3)_4$ at 20 K. The upper and lower vertical bars show nuclear and magnetic Bragg peak positions, respectively. (b) Here the neutron diffraction pattern measured at 50 K in the paramagnetic phase was subtracted from the pattern observed at 1.6 K in order to obtain a diffraction pattern containing only magnetic peaks.

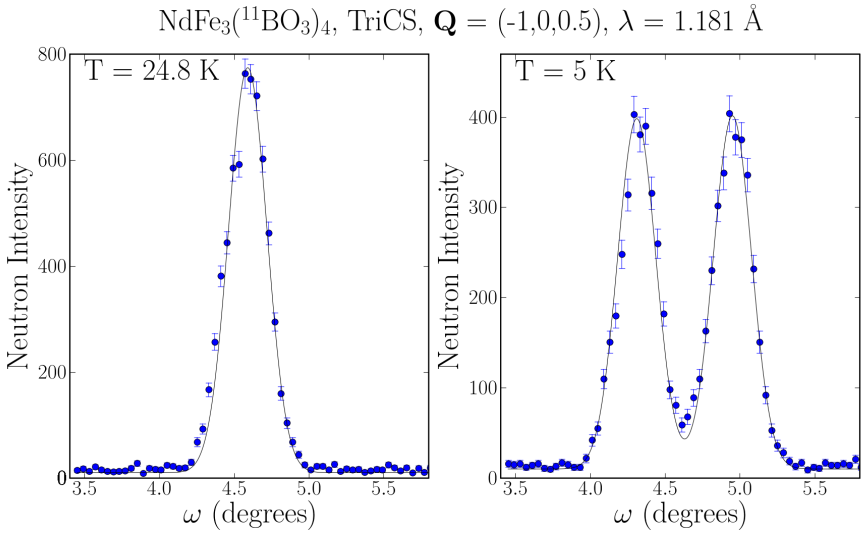

Figure 4.8: An ω-scan (turning around the b-axis) over the (-1, 0, $\frac{1}{2}$) magnetic reflection of $NdFe_3(^{11}BO_3)_4$ is shown for T = 24.8 K (left panel) and for T = 5 K (right panel), respectively.

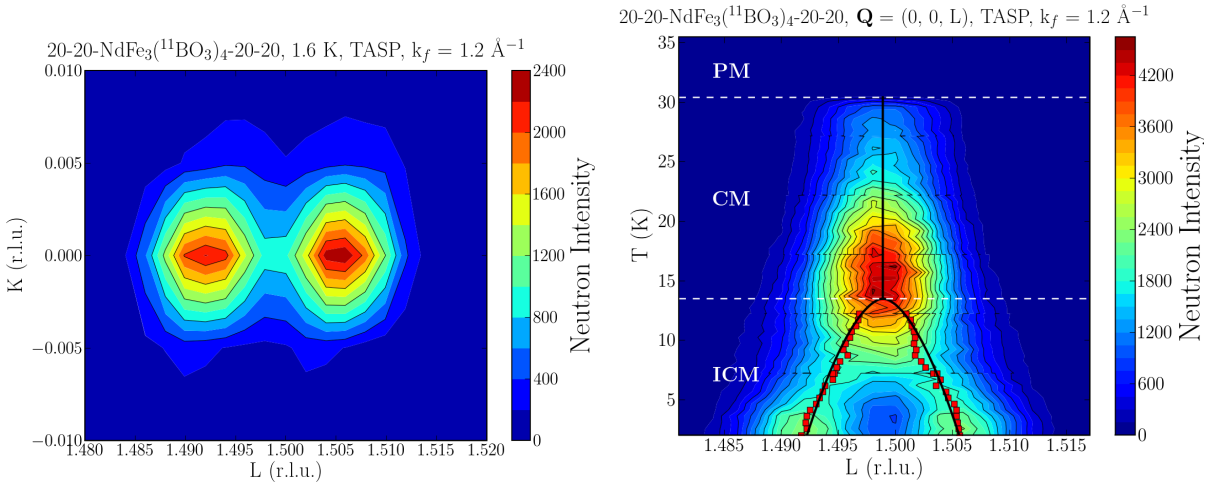

(a) (b)

Figure 4.9: (a) The figure shows a contour map of the neutron intensity around the position (0,0,$\frac{3}{2}$) in reciprocal space determined at T = 1.6 K by means of elastic $\boldsymbol{Q}$-scans along the reciprocal L-direction for different values K on the triple-axis spectrometer TASP. (b) he figure shows a contour map of the neutron intensity around the reciprocal lattice position (0,0,$\frac{3}{2}$) in elastic $\boldsymbol{Q}$-scans along the reciprocal L-direction as a function of temperature determined on the triple-axis spectrometer TASP. The red points are the peak positions of the incommensurate magnetic Bragg reflections as determined by fits of Gaussian peaks to the measured scans. The black curves below the splitting of the propagation vectors are described by the formula $k_z = \frac{3}{2} + \varepsilon$ where $\varepsilon = 1.6 \cdot 10^{-3}|(T_{ICM} - T)|^{0.58}$. Here PM denotes the paramagnetic phase, CM the commensurate magnetic phase and ICM the incommensurate magnetic phase, respectively.

Further elastic $\boldsymbol{Q}$-scans were carried out around the reciprocal space position (0,-1,0.5) along L. They are presented in Fig. 4.10. In addition to the principal magnetic satellites also reflections at higher order harmonics were observed as emphasised in the Figs. 4.10 (b) to (d). Their shift with respect to $\boldsymbol{k}_{hex}$ was found to be $3\,\varepsilon = 0.02$. The integrated intensity of the third order harmonics is largest near the transition temperature T_{ICM} and decreases fast as a function of decreasing temperature. We note that the integrated intensity of the principle satellites remains approximately constant down the lowest temperature.

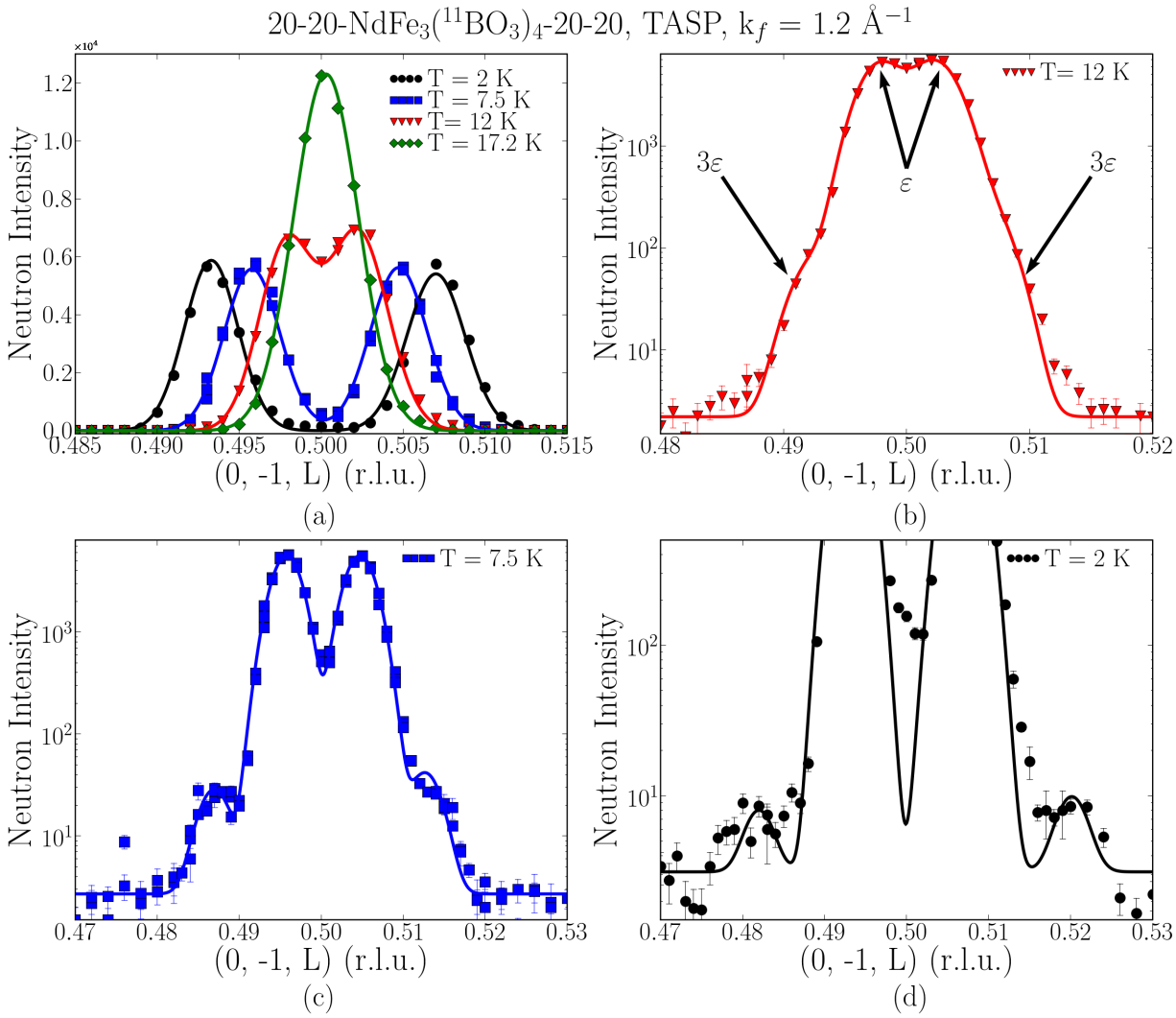

Figure 4.10: (a) Q-scans over the (0,-1,0.5) magnetic Bragg for different temperatures are shown. In the panels (b) to (d) the development of third order satellites is observed. Their shift from the commensurate position is three times larger than for the first order peaks. The solid lines are fits to the data with multiple Gaussian profiles.

4.2.4.2 Magnetic representational analysis

We have seen in section 3.2 that with the knowledge of the propagation vector $\boldsymbol{k}$, the position of the magnetic ions in the primitive cell of a magnetic structure and the space group of the paramagnetic phase all possible magnetic structures that are in agreement with the symmetry of the chemical structure can be calculated. We obtained the basis functions for $NdFe_3(^{11}BO_3)_4$ by means of the programs MODY [SBP04] and BASIREPS [RC06]. For the calculation of the basis functions the primitive cell has to be considered [IN79]. For $NdFe_3(^{11}BO_3)_4$ the primitive cell is rhombohedral as the unit cell of the space group R32 is described in a hexagonal setting together with three rhombohedral lattice centering translations R (+(0,0,0; 2/3, 1/3, 1/3; 1/3, 2/3, 2/3)). We note that this is also the reason why we indexed the magnetic reflections with a propagation vector $\boldsymbol{k}^{hex}$ = [0, 0, $\frac{3}{2}$] that is larger than a single hexagonal reciprocal lattice translation along the crystallographic c-axis. With respect to the rhombohedral cell the propagation vector is $\boldsymbol{k}_{rh}$ = [$\frac{1}{2}$, $\frac{1}{2}$, $\frac{1}{2}$] which corresponds to antiferromagnetic ordering along the hexagonal c-axis. Further the magnetic Fourier modes $\boldsymbol{S}_{d\lambda}^{\boldsymbol{k}\nu}(0)$ (s. Eq. 3.19) for the corresponding basis functions $\Psi_{\lambda}^{\boldsymbol{k}\nu}$ that are consequently only valid for the zeroth primitive cell can be propagated to the nth cell via the relation

$$\boldsymbol{S}_{d\lambda}^{\boldsymbol{k}\nu}(\boldsymbol{t}) = \boldsymbol{S}_{d\lambda}^{\boldsymbol{k}\nu}(0)\exp(i2\pi\boldsymbol{k}\boldsymbol{t}), \tag{4.2}$$

where $\boldsymbol{t}$ is the translational vector interconnecting the zeroth and the nth cell and $\boldsymbol{k}$ is the propagation vector (compare Eq. 3.7). This involves that the magnetic ions related by the rhombohedral translations R are not longer equivalent as in the paramagnetic phase but differ by phase factors $2\pi\mathbf{k}_{hex}\mathbf{t}$ according to these translations. Keeping this in mind, we discuss in the following only the symmetry relations for the first of these three R sublattices in the hexagonal frame as the others can then be easily obtained via Eq. 4.2. The primitive rhombohedral cell of $NdFe_3(^{11}BO_3)_4$ contains for magnetic ions: three Fe^{3+} ions situated at the positions (x,0,0), (0,x,0) and (1-x,1-x,0) with x = 0.55 (they are correlated via the two three-fold rotation axes parallel to the x-axis, and are therefore in the same orbit) and one Nd^{3+} ion at (0,0,0). The program MODY [SBP04] provided with these positional parameters calculated the magnetic basis functions. In tables 4.2 and 4.3 we present the results for the commensurate and incommensurate propagation vectors respectively in the form of the magnetic Fourier modes that are associated with the basis functions $\Psi_{\lambda}^{\boldsymbol{k}\nu}$.
The representational analysis for the commensurate propagation vector $\boldsymbol{k}^{hex}$ = [0, 0, $\frac{3}{2}$] yields three irreducible representations Γ^1, Γ^2 and Γ^3. Γ^1 and Γ^2 are one-dimensional whereas Γ^3 is a two-dimensional representation. We want to briefly describe the magnetic structures that are described by the corresponding magnetic Fourier modes (s. table 4.2). Before we start the discussion we want to remind of the definition of the indices associated with the magnetic Fourier modes $\boldsymbol{S}_{d\lambda}^{\boldsymbol{k}\nu}$ (s. also section 3.2.3). Here ν denotes the number of the irreducible representation, d the number of the associated magnetic ion in the zeroth cell and λ is the number of the corresponding basis function. As we know from the bulk

Table 4.2: Irreducible representations Γ^ν and magnetic Fourier modes $\boldsymbol{S}^{\boldsymbol{k}\nu}_{d\lambda}$ (with components along the hexagonal basic translations), as obtained from the program MODY [SBP04] for $\boldsymbol{k}_{hex}$ = [0,0,$\frac{3}{2}$], a = exp($i\pi/3$), b = exp($i\pi/6$). Note that the irreducible representation Γ^3 is two dimensional. We consider this by introducing the index m via $\lambda \longrightarrow \lambda m$.

(a) Character table for the irreducible representations Γ^ν

Sym. op.	1	3^+	3^-	$2_{[010]}$	$2_{[100]}$	$2_{[110]}$
Γ^1	1	1	1	1	1	1
Γ^2	1	1	1	-1	-1	-1
Γ^3	$\begin{pmatrix} 1 & 0 \\ 0 & 1 \end{pmatrix}$	$\begin{pmatrix} -a & 0 \\ 0 & -a^* \end{pmatrix}$	$\begin{pmatrix} -a & 0 \\ 0 & -a^* \end{pmatrix}$	$\begin{pmatrix} 0 & 1 \\ 1 & 0 \end{pmatrix}$	$\begin{pmatrix} 0 & -a^* \\ -a & 0 \end{pmatrix}$	$\begin{pmatrix} 0 & -a^* \\ -a & 0 \end{pmatrix}$

(b) Fe sublattice (there is only one orbit): representation $\Gamma = \Gamma^1 + 2\Gamma^2 + 3\Gamma^3$

	atom 1 (x, 0, 0)	atom 2 (0, x, 0)	atom 3 (1-x, 1-x, 0)	
λ (Γ^1)	$\boldsymbol{S}^{\boldsymbol{k}1}_{1\lambda}$	$\boldsymbol{S}^{\boldsymbol{k}1}_{2\lambda}$	$\boldsymbol{S}^{\boldsymbol{k}1}_{3\lambda}$	
1	(1,0,0)	(0,1,0)	(-1,-1,0)	
λ (Γ^2)	$\boldsymbol{S}^{\boldsymbol{k}2}_{1\lambda}$	$\boldsymbol{S}^{\boldsymbol{k}2}_{2\lambda}$	$\boldsymbol{S}^{\boldsymbol{k}2}_{3\lambda}$	
1	($\frac{1}{2}$,1,0)	(-1,-$\frac{1}{2}$,0)	($\frac{1}{2}$,-$\frac{1}{2}$,0)	
2	(0,0,1)	(0,0,1)	(0,0,1)	
λm (Γ^3)	$\boldsymbol{S}^{\boldsymbol{k}3}_{1\lambda m}$	$\boldsymbol{S}^{\boldsymbol{k}3}_{2\lambda m}$	$\boldsymbol{S}^{\boldsymbol{k}3}_{3\lambda m}$	(modes multiplied by 2)
1a	(1,0,0)	(0,-a,0)	(a*,a*,0)	
1b	(-a*,0,0)	(0,-a,0)	(-1,-1,0)	
2a	(0,1,0)	(a,a,0)	-(a*,0,0)	
2b	(a*,a*,0)	(-a,0,0)	(0,1,0)	
3a	(0,0,1)	(0,0,-a)	-(0,0,-a*)	
3b	(0,0,a*)	(0,0,a)	(0,0,-1)	

(c) Nd sublattice: representation $\Gamma = \Gamma^2 + \Gamma^3$

	atom 1 (0, 0, 0)	
λ (Γ^2)	$\boldsymbol{S}^{\boldsymbol{k}2}_{1\lambda}$	
1	(0,0,1)	
λm (Γ^3)	$\boldsymbol{S}^{\boldsymbol{k}3}_{1\lambda m}$	(modes multiplied by $2\sqrt{3}$)
1a	(b*,-i,0)	
1b	(-b*,-b,0)	

measurements in section 4.2.3 that the magnetic easy directions are perpendicular to the hexagonal c-axis, we will only consider Fourier modes with moments inside the ab-plane.

- The magnetic modes $\boldsymbol{S}_{d1}^{\boldsymbol{k}1}$ for the representation Γ^1 are real for the Fe sublattice and for the Nd sublattice this representation does not occur. The basis function for the three Fe^{3+} ions form a 120°-structure in the ab-plane (the basis functions are given in the hexagonal crystal coordinate frame).
- The basis functions for Γ^2 are also real. The magnetic modes $\boldsymbol{S}_{d1}^{\boldsymbol{k}2}$ for the Fe sublattice also form a 120°-structure but are rotated by 60° with respect to Γ^1. The magnetic modes $\boldsymbol{S}_{d2}^{\boldsymbol{k}2}$ for the Fe sublattice and $\boldsymbol{S}_{d1}^{\boldsymbol{k}2}$ for the Nd sublattice describe structures which have the moments parallel to the hexagonal c-axis. Consequently these will not be considered here.
- For Γ^3 all magnetic modes apart from $\boldsymbol{S}_{d3a}^{\boldsymbol{k}3}$ and $\boldsymbol{S}_{d3a}^{\boldsymbol{k}3}$ (that describe configurations with moments parallel to the c-axis and will not be considered) describe general spiral configurations with moments confined in the ab-plane.

Due to the propagation vector $\boldsymbol{k}^{hex} = [0,\ 0,\ \frac{3}{2}]$ the magnetic moments are ordered antiferromagnetically between adjacent ab-layers for all irreducible representations.
For the incommensurate case with propagation vector $\boldsymbol{k}_{hex}^{i} = [0,0,\frac{3}{2} + \varepsilon]$, similarly three irreducible representations, namely Γ^1, Γ^2 and Γ^3, exist. All of them are one dimensional: Γ^1 is real, and the other two are conjugate complex. The basis functions of Γ^1 describe a magnetic structure with moments that are now amplitude modulated along the c-axis instead of simple antiferromagnetic structure due to the slightly incommensurate propagation vector for both Fe and Nd sublattices. Γ^2 and Γ^3 both describe spiral structures (s. table 4.3).
As the irreducible representations that yielded the best fits for the commensurate and incommensurate phase were Γ^3 and Γ^2 respectively, we will consider their corresponding magnetic structures in more detail. We first investigate the incommensurate phase. For the Nd sublattice there is only one magnetic Fourier mode associated with Γ^2, namely $\boldsymbol{S}_{d1}^{\boldsymbol{k}2}$ that only has non-zero components parallel to the hexagonal basal plane. As the basis function corresponding to $\boldsymbol{S}_{d3}^{\boldsymbol{k}2}$ for the Fe sublattices describes a magnetic structure with moments parallel to the c-axis we will only use $\boldsymbol{S}_{d1}^{\boldsymbol{k}2}$ and $\boldsymbol{S}_{d2}^{\boldsymbol{k}2}$. Because of the incommensurate propagation vector the basis function for both $+\boldsymbol{k}$ and $-\boldsymbol{k}$ are given in table 4.3. However, in the present case we can always make the magnetic modes associated with $-\boldsymbol{k}$ complex conjugated to the ones associated with $+\boldsymbol{k}$ by using the following linear combinations for both Fe and Nd sites:

$$\begin{aligned} \boldsymbol{S}_{d1}^{-\boldsymbol{k}2'} &= -a\boldsymbol{S}_{d1}^{-\boldsymbol{k}2} \\ \boldsymbol{S}_{d2}^{-\boldsymbol{k}2'} &= a(\boldsymbol{S}_{d1}^{-\boldsymbol{k}2} + \boldsymbol{S}_{d2}^{-\boldsymbol{k}2}), \end{aligned} \tag{4.3}$$

where a = $\exp(i\pi/3)$. Now we can construct the magnetic Fourier modes for the Fe sublattice from a linear combination of the modes $\boldsymbol{S}_{d1}^{\boldsymbol{k}2}$ and $\boldsymbol{S}_{d2}^{\boldsymbol{k}2}$ as

$$\boldsymbol{S}_{d,Fe}^{\boldsymbol{k}} = C_1\boldsymbol{S}_{d1}^{\boldsymbol{k}2} + C_2\boldsymbol{S}_{d2}^{\boldsymbol{k}2} \tag{4.4}$$

with complex mixing coefficients C_1 and C_2. Thus, the general solution for the magnetic moments on the Fe sublattice generated from the irreducible representation Γ^2 is then

$$\begin{aligned} \boldsymbol{S}_{d,Fe}(\boldsymbol{t}) &= \boldsymbol{S}^{\boldsymbol{k}}_{d,Fe} exp(i2\pi \boldsymbol{kt}) + \boldsymbol{S}^{-\boldsymbol{k}}_{d,Fe} exp(-i2\pi \boldsymbol{kt}) \\ &= \boldsymbol{R}^{\boldsymbol{k}}_{d,Fe} \cos(2\pi \boldsymbol{kt}) + \boldsymbol{I}^{\boldsymbol{k}}_{d,Fe} \sin(2\pi \boldsymbol{kt}), \end{aligned} \tag{4.5}$$

where we defined $\boldsymbol{R}^{\boldsymbol{k}}_{d,Fe} = 2Re(\boldsymbol{S}^{\boldsymbol{k}}_{d,Fe})$ and $\boldsymbol{I}^{\boldsymbol{k}}_{d,Fe} = -2Im(\boldsymbol{S}^{\boldsymbol{k}}_{d,Fe})$ in accordance with Eq. 2.42. This defines a general elliptical spiral for all three Fe moments with moments confined in the ab-plane that propagates along the c-axis ($\boldsymbol{k} = \boldsymbol{k}^i_{hex} = [0,0,\frac{3}{2} + \varepsilon]$) and whose specific appearance depends on the choice of C_1 and C_2 via $\boldsymbol{R}^{\boldsymbol{k}}_{d,Fe}$ and $\boldsymbol{I}^{\boldsymbol{k}}_{d,Fe}$ (compare section 2.4.3).
There is one choice of C_1 and C_2 that appears to be especially appealling. If we choose $C_2 = C_1 \exp(-i\pi/3) = a^*$ the magnetic moments of all three Fe^{3+} ions are parallel (s. Eq. 4.4 and also table 4.3):

$$\begin{aligned} \boldsymbol{S}^{\boldsymbol{k}}_{1,Fe} &= C_1 \left[(1,0,0) + a^*(0,1,0)\right] = C_1(1,a^*,0) \\ \boldsymbol{S}^{\boldsymbol{k}}_{2,Fe} &= C_1 \left[(0,-a,0) + a^*(a,a,0)\right] = C_1(1,a^*,0) \\ \boldsymbol{S}^{\boldsymbol{k}}_{3,Fe} &= C_1 \left[(a^*,a^*,0) + a^*(a^*,0,0)\right] = C_1(1,a^*,0) \end{aligned} \tag{4.6}$$

By introducing this result in Eq. 4.5 and by using the coefficient $C_1 = S_{Fe} \exp(-i\pi/6) \exp(-i\alpha_{Fe})$[3] we obtain the following magnetic structure for all three Fe moments:

$$\begin{aligned} \boldsymbol{S}_{Fe}(\boldsymbol{t}) &= S_{Fe} \left[(\sqrt{3},0,0)\cos(2\pi \boldsymbol{kt} + \alpha_{Fe}) + (1,2,0)\sin(2\pi \boldsymbol{kt} + \alpha_{Fe})\right] \\ &= S_{Fe} \left[\sqrt{3}\boldsymbol{e}_x \cos(2\pi \boldsymbol{kt} + \alpha_{Fe}) + (\boldsymbol{e}_x + 2\boldsymbol{e}_y)\sin(2\pi \boldsymbol{kt} + \alpha_{Fe})\right], \end{aligned} \tag{4.7}$$

where $\boldsymbol{e}_x$ and $\boldsymbol{e}_y$ are unit vectors along the crystallographic a and b directions (remember the basis functions were given in the hexagonal coordinate frame). We also introduced an arbitrary phase angle α_{Fe} that determines the direction of the moments inside the hexagonal plane. Eq. 4.5 describes a spiral with constant moment amplitude in the orthogonal basis.
For the Nd sublattice the result can be obtained more easy as there is only one magnetic Fourier mode associated with Γ^2, namely

$$\boldsymbol{S}^{\boldsymbol{k}}_{Nd} = C_3 \boldsymbol{S}^{\boldsymbol{k}2}_1 = (b^*, -i, 0), \tag{4.8}$$

where $b = \exp(i\pi/6)$ and we dropped the subscript d since there is only one Nd^{3+} ion. By defining $C_3 = S_{Nd} \exp(-i\alpha_{Nd})$ and $\boldsymbol{R}^{\boldsymbol{k}}_{Nd} = 2Re(\boldsymbol{S}^{\boldsymbol{k}}_{Nd})$ and $\boldsymbol{I}^{\boldsymbol{k}}_{Nd} = -2Im(\boldsymbol{S}^{\boldsymbol{k}}_{Nd})$, similar to the case for the Fe^{3+}, we get the magnetic configuration for the magnetic moments on the Nd site as

$$\begin{aligned} \boldsymbol{S}_{Nd}(\boldsymbol{t}) &= S_{Nd} \left[(\sqrt{3},0,0)\cos(2\pi \boldsymbol{kt} + \alpha_{Nd}) + (1,2,0)\sin(2\pi \boldsymbol{kt} + \alpha_{Nd})\right] \\ &= S_{Nd} \left[\sqrt{3}\boldsymbol{e}_x \cos(2\pi \boldsymbol{kt} + \alpha_{Nd}) + (\boldsymbol{e}_x + 2\boldsymbol{e}_y)\sin(2\pi \boldsymbol{kt} + \alpha_{Nd})\right]. \end{aligned} \tag{4.9}$$

[3]The choice of the additional imaginary phase $\exp(-i\pi/6)$ is just for convenience as then the moments for α_{Fe}=0 are parallel to a-axis for $\boldsymbol{t}$=0.

Table 4.3: Irreducible representations Γ^ν and magnetic Fourier modes $\boldsymbol{S}_{d\lambda}^{\boldsymbol{k}\nu}$ (with components along the hexagonal basic translations) for the incommensurate phase, as obtained from the program MODY [SBP04] for $\boldsymbol{k}_{hex}^i = [0,0,\frac{3}{2}+\varepsilon]$, a = exp($i\pi/3$), b = exp($i\pi/6$).

(a) Character table for the irreducible representations Γ^ν

Sym. op./Irred. rep.	1	3^+	3^-
Γ^1	1	1	1
Γ^2	1	-a*	-a
Γ^3	1	-a	-a*

(b) Fe sublattice (there is only one orbit): representation $\Gamma = 3\Gamma^1 + 3\Gamma^2 + 3\Gamma^3$

		Γ^1		Γ^2		Γ^3	
Atom d (position)	λ	$\boldsymbol{S}_{d\lambda}^{\boldsymbol{k}1}$	$\boldsymbol{S}_{d\lambda}^{-\boldsymbol{k}1}$	$\boldsymbol{S}_{d\lambda}^{\boldsymbol{k}2}$	$\boldsymbol{S}_{d\lambda}^{-\boldsymbol{k}2}$	$\boldsymbol{S}_{d\lambda}^{\boldsymbol{k}3}$	$\boldsymbol{S}_{d\lambda}^{-\boldsymbol{k}3}$
1 (x, 0, 0)	1	(1,0,0)	(1,0,0)	(1,0,0)	(-a*,0,0)	(1,0,0)	(-a,0,0)
	2	(0,1,0)	(-1,-1,0)	(0,1,0)	(a*,a*,0)	(0,1,0)	(0,a,0)
	3	(0,0,1)	(0,0,-1)	(0,0,1)	(0,0,a*)	(0,0,1)	(0,0,a)
2 (0, x, 0)	1	(0,1,0)	(0,1,0)	(0,-a,0)	(0,-a,0)	(0,-a*,0)	(0,-a*,0)
	2	(-1,-1,0)	(1,0,0)	(a,a,0)	(-a,0,0)	(a*,a*,0)	(-a*,0,0)
	3	(0,0,1)	(0,0,-1)	(0,0,-a)	(0,0,a)	(0,0,-a*)	(0,0,a*)
3 (1-x, 1-x, 0)	1	(-1,-1,0)	(-1,-1,0)	(a*,a*,0)	(-1,-1,0)	(a,a,0)	(-1,-1,0)
	2	(1,0,0)	(0,1,0)	(-a*,0,0)	(0,1,0)	(-a,0,0)	(0,1,0)
	3	(0,0,1)	(0,0,-1)	(0,0,-a*)	(0,0,-1)	(0,0,-a)	(0,0,-1)

(c) Nd sublattice (modes multiplied by $\sqrt{3}$): representation $\Gamma = \Gamma^1 + \Gamma^2 + \Gamma^3$

		Γ^1		Γ^2		Γ^3	
Atom d (position)	λ	$\boldsymbol{S}_{d\lambda}^{\boldsymbol{k}1}$	$\boldsymbol{S}_{d\lambda}^{-\boldsymbol{k}1}$	$\boldsymbol{S}_{d\lambda}^{\boldsymbol{k}2}$	$\boldsymbol{S}_{d\lambda}^{-\boldsymbol{k}2}$	$\boldsymbol{S}_{d\lambda}^{\boldsymbol{k}3}$	$\boldsymbol{S}_{d\lambda}^{-\boldsymbol{k}3}$
1 (0, 0, 0)	1	(0,0,1)	(0,0,-1)	(b*,-i,0)	(b*,b,0)	(b,i,0)	(b,b*,0)

We see that the Nd ions always form a spiral with constant moment amplitude in contrast to the Fe sublattice.

For the commensurate case we anticipate the results of our fits and will not go in much detail with the possible configurations through mixing all possible basis functions in table 4.2. We only note that by using the irreducible representation Γ^3 and only considering a linear combination of the Fourier modes $\boldsymbol{S}_{d1a}^{\boldsymbol{k}3}$ and $\boldsymbol{S}_{d2a}^{\boldsymbol{k}3}$ and setting the mixing coefficients $C_{\lambda m}$ for all other basis functions to zero the same magnetic configurations as for the incommensurate structure can be constructed. The only difference is that due to the commensurate propagation vector the magnetic spiral configurations in Eqs. 4.7 and 4.9 reduce to magnetic structures where the moments inside one ab-layer are arranged ferromagnetically but order antiferromagnetically between adjacent layers.

Before we start to describe the fits to the identified magnetic models we want to deal with a subtlety concerning the calculation of magnetic intensities in the CM phase. Two

vectors $\boldsymbol{Q}_1$ and $\boldsymbol{Q}_2$ in reciprocal space are considered as equivalent if $\boldsymbol{Q}_1 - \boldsymbol{Q}_2 = \boldsymbol{\tau}$ where $\boldsymbol{\tau}$ is a reciprocal lattice vector. In the CM phase the propagation vector is $\boldsymbol{k} = \boldsymbol{k}^{hex} = [0,\ 0,\ 3/2]$ and $\boldsymbol{k}^{hex} - (-\boldsymbol{k}^{hex}) = [0, 0, 3] = 3c^*$, that is indeed a reciprocal lattice vector. Hence $\boldsymbol{k}^{hex}$ is equivalent to $-\boldsymbol{k}^{hex}$ and we find that the equation

$$\boldsymbol{\tau}_1 + \boldsymbol{k} = \boldsymbol{\tau}_2 - \boldsymbol{k} = \boldsymbol{Q}_0 \tag{4.10}$$

can be always fulfilled for this case. Additionally, as we will show in the following, the magnetic structure factor is different from what we derived in Eq. 2.45. We consider a general periodic magnetic structure as in Eq. 2.42 but under the assumption that Eq. 4.10 holds true. The expression for elastic magnetic scattering is then (cf. section 2.3.4):

$$\begin{aligned}
&\sum_{jj'} I_{jj'}(\boldsymbol{Q},\infty) J_{jj'}(\infty) \\
= &\sum_{l'd'ld} \langle \exp\{-i\boldsymbol{Q}\cdot\boldsymbol{R}_{l'd'}(0)\} \exp\{i\boldsymbol{Q}\cdot\boldsymbol{R}_{ld}(\infty)\}\rangle \\
&\quad \times \langle (S_{d'}^{\boldsymbol{k}\alpha\dagger} e^{-i\boldsymbol{k}\cdot\boldsymbol{R}_{l'd'}(0)} + S_{d'}^{-\boldsymbol{k}\alpha\dagger} e^{i\boldsymbol{k}\cdot\boldsymbol{R}_{l'd'}(0)})(S_d^{\boldsymbol{k}\beta} e^{i\boldsymbol{k}\cdot\boldsymbol{R}_{ld}(\infty)} + S_d^{-\boldsymbol{k}\beta} e^{-i\boldsymbol{k}\cdot\boldsymbol{R}_{ld}(\infty)})\rangle \\
= &\sum_{l'd'ld} \langle \exp\{-i\boldsymbol{Q}_0\cdot\boldsymbol{R}_{l'd'}(0)\} \exp\{i\boldsymbol{Q}_0\cdot\boldsymbol{R}_{ld}(\infty)\}\rangle \langle (S_{d'}^{\boldsymbol{k}\alpha\dagger} + S_{d'}^{-\boldsymbol{k}\alpha\dagger})(S_d^{\boldsymbol{k}\beta} + S_d^{-\boldsymbol{k}\beta})\rangle \\
= &\sum_{\tau} \delta(\boldsymbol{Q}-\boldsymbol{Q}_0) \sum_{dd'} \exp(-W_d(\boldsymbol{Q}_0)) \exp(-W_{d'}(\boldsymbol{Q}_0)) \exp(i\boldsymbol{Q}_0\cdot\boldsymbol{d}) \exp(i\boldsymbol{Q}_0\cdot\boldsymbol{d'}) \\
&\quad \times (S_{d'}^{\boldsymbol{k}\alpha\dagger} + S_{d'}^{-\boldsymbol{k}\alpha\dagger})(S_d^{\boldsymbol{k}\beta} + S_d^{-\boldsymbol{k}\beta}).
\end{aligned} \tag{4.11}$$

For the details of evaluating the sums over l and l' we refer again to Eqs. 2.15,2.17 and 2.20. With the definitions for $\boldsymbol{S}^{\boldsymbol{k}}$ and $\boldsymbol{S}^{-\boldsymbol{k}}$ made in Eq. 2.42 we obtain

$$\begin{aligned}
\boldsymbol{S}_d^{\boldsymbol{k}} + \boldsymbol{S}_d^{-\boldsymbol{k}} &= \frac{(\boldsymbol{R}_d^{\boldsymbol{k}} - i\boldsymbol{I}_d^{\boldsymbol{k}})}{2} e^{i\phi_d} + \frac{(\boldsymbol{R}_d^{\boldsymbol{k}} + i\boldsymbol{I}_d^{\boldsymbol{k}})}{2} e^{-i\phi_d} \\
&= \boldsymbol{R}_d^{\boldsymbol{k}} \cos(\phi_d) + \boldsymbol{I}_d^{\boldsymbol{k}} \sin(\phi_d).
\end{aligned} \tag{4.12}$$

Finally by resubstituting $\boldsymbol{Q}_0 = \boldsymbol{\tau} - \boldsymbol{k}$ we obtain the elastic magnetic cross-section for the case of $\boldsymbol{k}$ being equivalent to $-\boldsymbol{k}$ as

$$\left(\frac{d\sigma}{d\Omega}\right)_{mag,el} = N(\gamma r_0)^2 \frac{(2\pi)^3}{v_0} \sum_{\boldsymbol{\tau}} \sum_{\alpha,\beta} (\delta_{\alpha\beta} - \hat{Q}_\alpha \hat{Q}_\beta) F_M^{\boldsymbol{k}\alpha\dagger} F_M^{\boldsymbol{k}\beta} \delta(\boldsymbol{Q} - \boldsymbol{k} - \boldsymbol{\tau}), \tag{4.13}$$

where the sum over $\boldsymbol{k}$ and $-\boldsymbol{k}$ has to be explicitly removed (compare Eq. 2.45) and the magnetic structure factor has changed to

$$\boldsymbol{F}_M^{\boldsymbol{k}} = \sum_d g_d F_d(\boldsymbol{Q}) \exp(-W_d(\boldsymbol{Q})) \exp(i\boldsymbol{Q}\cdot\boldsymbol{d}) \{\boldsymbol{R}_d^{\boldsymbol{k}} \cos(\phi_d) + \boldsymbol{I}_d^{\boldsymbol{k}} \sin(\phi_d)\}. \tag{4.14}$$

The results in Eqs. 4.13 and 4.14 imply that only one magnetic satellite exists exactly as has been observed in the neutron diffraction experiments in the CM phase. The single

satellite reflection corresponds to the observed collinear antiferromagnetic ordering where the magnetic moments in adjacent hexagonal planes are aligned antiferromagnetically. We note that even though we have described this structure in spiral configuration (s. Eqs 4.7 and 4.9) the commensurate propagation vector describes an antiferromagnetic order along the c axis with a real magnetic structure factor.
The program FullProf used for the fits of the neutron powder diffraction data considers the Eqs. 4.13 and 4.14 properly in case of $\boldsymbol{k}$ and $-\boldsymbol{k}$ being equivalent in order to calculate the intensities for the magnetic Bragg reflections.

4.2.4.3 Magnetic structure determination

The magnetic models for the magnetic structure of $NdFe_3(^{11}BO_3)_4$ obtained in the previous section by symmetry analysis were fitted to the measured powder diffraction data by the program Fullprof [RC06]. The models we used to fit the data at 2 K (difference I(2 K)-I(50 K), s. Fig. 4.7) are defined in the Eqs. 4.5 and 4.9. We used a general approach were both C_1 and C_2 defining the magnetic structure of the Fe sublattice were allowed to vary. We will call this model the *'free Fe moment model'* in the following. The imaginary phase of C_1 was fixed to zero as one cannot determine the phase shift of the modulated magnetic structure with respect to the crystal lattice from powder diffraction data which is averaged over all direction. The fit with five free parameters Re(C_1), Re(C_2), Im(C_2), Re(C_3) and Im(C_3) gave the ratio C_2 / C_1 = 1.02exp($-i0.44\pi$), which is quite close to the value of exp($-i\pi/3$) expected for the parallel Fe moments. The angles between the Fe moments amount to $\approx 10°$, while the sizes of the magnetic moments are 1, 0.8 and 0.75 for the three Fe sites, respectively, normalised to the magnetic moment of the first atom. The direction of the Nd-moment with respect to the Fe moments in the hexagonal basal plane was refined to 83° , 64° and 70° for the three Fe moments. The goodness of fit [RC06] yielded by this magnetic model is $\chi^2 = 15.4$. However, the assumption of equal Fe moments is physically more reasonable for a non-metallic compound and does not contradict to the measured powder neutron diffraction data. By fixing $C_2 = C_1$ exp($-i\pi/3$), the goodness of fit only decreased marginally to $\chi^2 = 16.8$. In this constant magnetic moment case there are only three adjustable parameters, two values of the ordered magnetic moments and an angle between them. Both corresponding commensurate magnetic structures are shown in Fig. 4.12. This second model will consequently be denoted as *'constant Fe moment model'*.
Ultimately, we used Eq. 4.7 for the Fe sublattice, and therefore the 'constant Fe moment model', for the profile analyses of the DMC powder neutron intensities of $NdFe_3(^{11}BO_3)_4$. This approach resulted in good fits of the magnetic neutron intensities, however, it was limited by the previously mentioned texture problems (in particular of the strongest nuclear Bragg peak). In view of the rather limited q-range of the DMC patterns at the long neutron wavelength λ = 2.453 Å, we fixed the positional parameters at the values summarised in table 4.1 with an overall temperature factor B = 0 and used only 10 and 14 parameters (three for the background polynomial) for nuclear and magnetic refinements,

respectively. Best agreements were obtained by using separate preferred orientation parameters for the nuclear and magnetic intensities. As these corrections are smaller in the case of magnetic intensities, the discussed problems of the nuclear fits are probably partially associated with deviations in the distributions of the boron and oxygen atoms from the assumed structure model. In the case of a nonoscillating sample we therefore worked with magnetic difference neutron diffraction patterns, visually determined background values and used the lattice parameters determined at 15 K. Typical corresponding fits are illustrated in Fig. 4.7. The temperature dependence of the resulting ordered magnetic Fe and Nd moments of $NdFe_3(^{11}BO_3)_4$ are illustrated in Fig. 4.11. The final parameters for both magnetic model as obtained in the fits and the corresponding agreement factors are summarised in table 4.4.

We want to emphasise that the fit of the powder diffraction data was performed with a fixed commensurate propagation vector $\boldsymbol{k}_{hex} = [0,0,\frac{3}{2}]$ even in the temperature range below T_{ICM} where the incommensurate propagation vector $\boldsymbol{k}^i_{hex} = [0,0,\frac{3}{2} + \varepsilon]$ was observed in the single crystal diffraction experiments. At T = 1.6 K an attempt was made to refine the incommensurate propagation vector $k^i_{hex} = [0, 0, k_z]$ resulting in the value $k_z = 1.5058(1)$. Even though the other free model parameters (size of the Fe and Nd moments and the angle between the two sublattices in the hexagonal plane α^{Nd}) did not change within the precision of the analysis (compare the last two lines of table 4.4) χ^2 increased from 13 to 18. This indicates that within the resolution of DMC at neutron wavelength $\lambda = 2.453$ Å the magnetic structure appears to be still as commensurate.

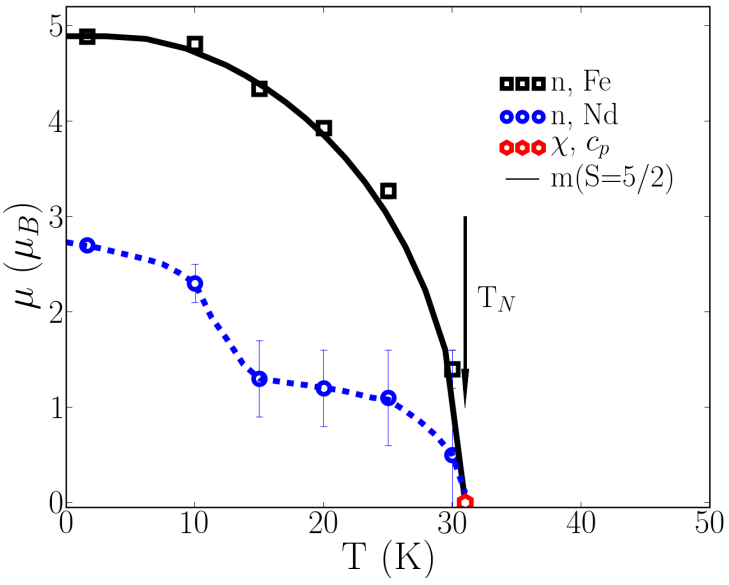

Figure 4.11: Temperature dependencies of the ordered magnetic Fe and Nd moments with error bars according to estimated standard deviations for the 'constant Fe moment model', see table 4.4. The black solid and blue dashed lines are the expected magnetisation (m) curve for S = 5/2 [Dar67] and a guide to the eye, respectively.

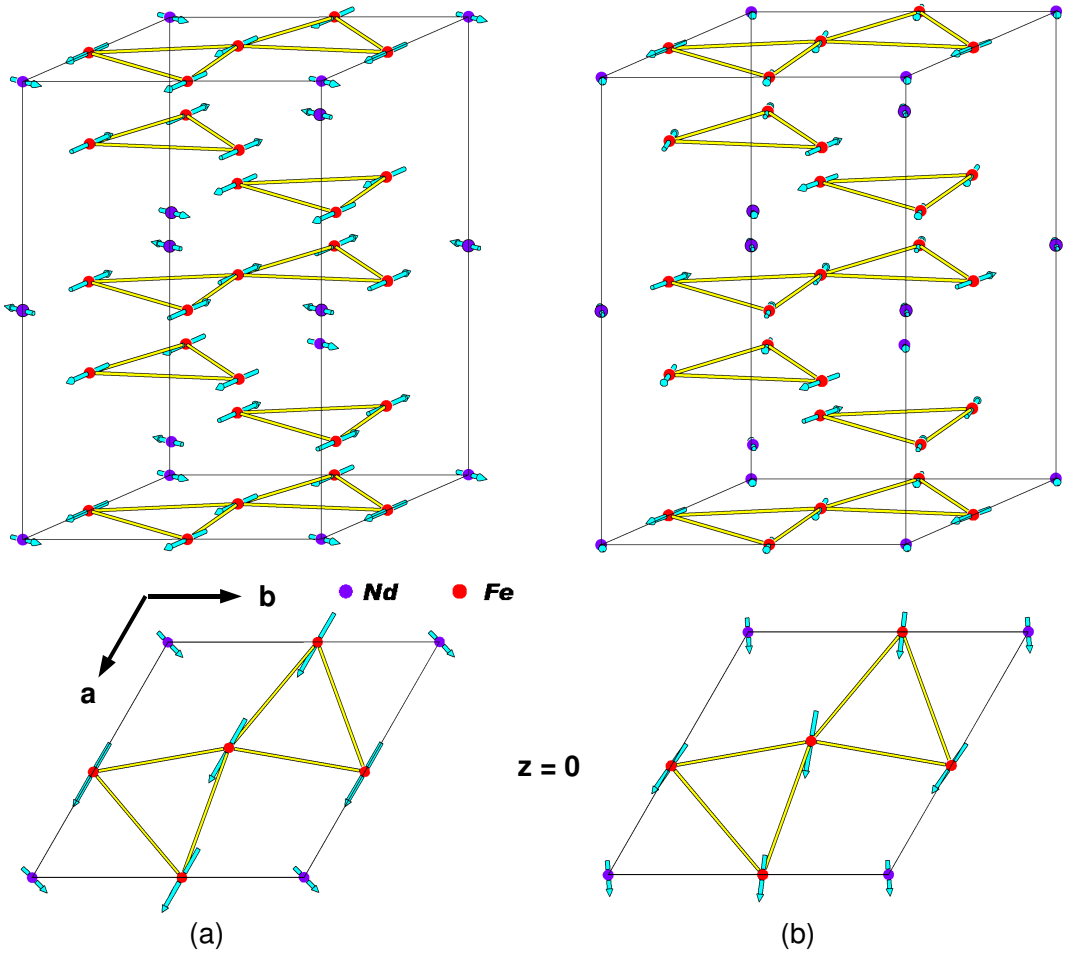

Figure 4.12: The hexagonal magnetic unit cell of $NdFe_3(^{11}BO_3)_4$ at 20 K, plotted with the program ATOMS [Dow06]. We note that it is doubled along the crystallographic c axis with respect to the chemical unit cell. In (a) the magnetic structure corresponding to the 'constant Fe moment model' is illustrated ($C_2 = C_1 \exp(-i\pi/3)$) whereas (b) shows the magnetic structure where C_1 and C_2 were fitted independently ('free Fe moment model'). The difference between the two structures can be seen most clearly if a hexagonal basal plane is considered as shown in the respective lower view graphs for the layer z = 0. The magnetic moments on the three Fe positions have all slightly different angles.

Table 4.4: Experimental details, resulting ordered magnetic moments μ and agreement values of the neutron powder profile fits of $NdFe_3(^{11}BO_3)_4$ as a function of temperature, measured on DMC, based on the commensurate magnetic unit cell. In (a) the parameters are summarised for the 'constant Fe moment model'. The angle α_{Fe} of the Fe sublattice has been fixed at zero. At 15 K the lattice parameters have been determined as $a_{hex} = 9.594(1)$ Å and $c_{hex} = 7.603(1)$ Å. Note the essential improvements of fits to the nuclear structure (R_{Bn}) due to sample oscillation. With respect to Eqs. 4.7 and 4.9 $S^{\boldsymbol{k}} = \mu$. R_{Bn} and R_{Bm} are conventional R-factors concerning integrated nuclear and magnetic neutron intensities, respectively [RC06]. (b) For comparison we also give the parameters of the 'free Fe moment model'. For convenience the magnetic moment size calculated from the fit parameters C_i is added for this model.

(a) 'constant Fe-moment model'

T (K)	Sample motion	μ_{Fe} (μ_B)	μ^{Nd} (μ_B)	α^{Nd} (deg)	χ^2	R_{Bn}	R_{Bm}
50	No	0	0		176	15.0	
30	Osc.	1.4(2)	0.5(1.1)	77[b]	77	8.9	47.9
25	Osc.	3.27(8)	1.1(5)	77(3)	61	8.1	11.5
20	Osc.	3.93(7)	1.2(4)	75(3)	57	7.9	7.8
15	Osc.	4.34(6)	1.3(4)	69(4)	55	7.8	6.3
10	No	4.81(4)	2.3(2)	58(1)	20		9.8
1.6	No	4.89(3)[c]	2.7(1)	47(1)	15		8.0
a		4.89(4)	2.7(2)	46(2)	18		10.7

[a] $k^i_{hex} = [0, 0, k_z]$, refined to $k_z = 1.5058(1)$ at 1.6 K.
[b]Fixed value.
[c]Note the expected value $\mu_{Fe} = 5\ \mu_B$ for free Fe^{3+} ions.

(b) 'free Fe-moment model'

T (K)	C_1	$Re(C_2)$	$Im(C_2)$	$Re(C_3)$	$Im(C_3)$	μ_{Fe1} (μ_B)	μ_{Fe2} (μ_B)	μ_{Fe3} (μ_B)	μ_{Nd} (μ_B)	χ^2	R_{Bm}
20	2.7(2)	-0.3(2)	-2.7(2)	0.8(7)	1.4(2)	2.9	1.9	3.4	1.2	54.6	7.62
1.6	3.7(1)	0.7(2)	-3.7(1)	1.2(7)	2.7(1)	3.4	3.1	4.1	2.3	15.4	8.14

4.2.5 Spherical Neutron Polarimetry

Even though the assumption of equally sized Fe moments is physically more reasonable for a non-metallic compound such as $NdFe_3(^{11}BO_3)_4$, only more detailed measurements by means of spherical neutron polarimetry (SNP) may allow to decide for the correct structure. These measurements seem to be especially desirable as the agreement factors were better for the fits of the free moment model compared to the constant moment model. As we have seen in the section 2.4 SNP allows to obtain the maximum amount of information about a magnetic structure.
The SNP option MuPAD [JKR+07] (compare also section 2.5) available at the continuous spallation source SINQ at the PSI was mounted on TASP [SRB01] in order to perform full polarisation analysis on $NdFe_3(^{11}BO_3)_4$. A photograph of this setup is shown in Fig. 2.10. In order to polarise the neutron beam and to analyse the final polarisation of the beam two polarising supermirror benders were used as spin polariser and analyser after the monochromator and in front of the analyser, respectively. A final wave vector $k_f = 1.97$ Å^{-1} (corresponding to a wavelength λ of 3.18 Å) was chosen to maximise both the intensity and the polarisation of the neutron beam. No additional filter for second order suppression was used because the benders already act as filters.
For this measurement the single crystal was oriented the same way as for the unpolarised diffraction experiments, namely with the reciprocal axis b*(K) and c*(L) within the scattering plane.

4.2.5.1 Polarisation matrices in the commensurate magnetic phase

In the CM magnetic phase we measured polarisation tensors for all accessible magnetic reflections for the temperatures T = 20, 25 and 30 K in $NdFe_3(^{11}BO_3)_4$. Since the polarisation tensors do not depend on temperature for T $\geq$ 20 K only the data for T = 20 K is given in table 4.5. All magnetic polarisation tensors shown in table 4.5 are measured on purely magnetic reflections (i.e. the propagation vector $\boldsymbol{k} \neq 0$) and therefore the terms including nuclear contributions are equal to zero (N = $R_y = R_z = I_y = I_z = 0$, s. also section 2.4.2). From the measured polarisation tensors several constraints on the magnetic structure can be derived:

1. For the magnetic reflection (0,0,-1.5) the scattering vector $\boldsymbol{Q}$ is directed parallel to the crystallographic c direction. Hence, the magnetic interaction vector only contains components in the basal plane. $\boldsymbol{P'}_{xx}$ (=(-M_y-M_z)/(M_y+M_z)) is fully polarised whereas $\boldsymbol{P'}_{yy}$ (=(M_y-M_z)/(M_y+M_z)) and $\boldsymbol{P'}_{zz}$ (=(-M_y+M_z)/(M_y+M_z)) are fully depolarised. This would foremost lead to the assumption $M_y \approx M_z$ but as the elements $\boldsymbol{P'}_{yz}$ and $\boldsymbol{P'}_{zy}$ are also equal to zero it also suggests the presence of spin domains in the basal plane (cf. section 2.4.2 for the meaning of the tensor elements).

2. On the magnetic reflection (0,4,0.5) the scattering vector $\boldsymbol{Q}$ is approximately parallel to the reciprocal b* axis. As the z axis which is perpendicular to the scattering plane

lies always within the basal hexagonal plane in the chosen scattering geometry the y-axis is approximately parallel to the crystallographic c axis ($\sphericalangle(y, c) \approx 15°$). The polarisation tensor shows $\boldsymbol{P'}_{xx} \approx \boldsymbol{P'}_{yy} \approx -\boldsymbol{P'}_{zz}$ which indicates that $M_y \approx 0$ and hence the magnetic interaction vector is directed along z. Therefore the magnetic moments are confined in the basal plane which is also in agreement with measurements of the magnetic susceptibility and the magnetic model found by neutron powder diffraction (compare Figs. 4.5 and 4.12).

3. On all measured Bragg peaks the elements yx and zx are equal to zero. This implies that the magnetic structure is not chiral at all or that it is a chiral structure with equally populated chiral domains.

These constraints are in agreement with both magnetic structures that yielded good fits of neutron powder diffraction data as described in the previous section, namely (1) the 'constant Fe moment model' and (2) 'free Fe moment model'. Therefore to decide between the two models we will need to calculate the polarisation tensors from the models and compare them to the measured values.

4.2.5.2 Possible magnetic domains

As the measurements were performed on a single crystal specimen we also have to consider possible magnetic domains. The presence of such domains in the basal plane is evident due to the constraint (i) in the previous section. In section 3.3 we have seen how the reduction of the symmetry of the magnetic structure compared to the chemical structure can lead to different types of domains.
The point group 32 (C_v) corresponding to the space group R32 of $NdFe_3(^{11}BO_3)_4$ contains six symmetry elements, namely **1** (identity), 3^+, 3^- (3-fold rotation around c-axis), $2_{[010]}$, $2_{[100]}$ and $2_{[110]}$ (2-fold rotations). The commensurate propagation vector $\boldsymbol{k}_{hex} = [0,\ 0,\ \frac{3}{2}]$ of $NdFe_3(^{11}BO_3)_4$ is invariant with respect to all six symmetry elements and therefore there is only one $\boldsymbol{k}$-domain and the little group $G_{\boldsymbol{k}}$ associated with $\boldsymbol{k}_{hex}$ includes all 6 point group elements.
As the magnetic structure of $NdFe_3(^{11}BO_3)_4$ has a non-zero propagation vector 180°-domains cannot be distinguished and therefore will not be considered in the following (s. section 3.3.2).
In Fig. 4.13 the action of all six symmetry elements onto the three Fe^{3+}-ions and the single Nd^{3+}-ion in the rhombohedral primitive cell is shown for the constant moment model. We see that basically all symmetry elements lead to an orientation domain (depending on the angle α_{Nd} between the Fe and Nd magnetic moments). E.g. the two 3-fold axes lead to orientation domains with spins that are rotated by 120° in the basal plane. The same is valid for the Nd sublattice. This finally means that six orientation domains have to be taken into account when our models are compared to the data.

Table 4.5: Polarisation tensors on all accessible magnetic Bragg reflections of $NdFe_3(^{11}BO_3)_4$ are shown for T = 20 K. The column $\boldsymbol{P}_0$ and $\boldsymbol{P'}$ denote the direction of the initial and final polarisation vector, respectively. The subscripts of $\boldsymbol{P'}$ signify the polarisation tensors that were measured (*meas*) and calculated (*calc*) from the two distinct magnetic models models. The errors provided for the measured values are statistical errors that were calculated via Eq. B.4. Further (1) denotes the 'constant Fe moment model' whereas (2) is the 'free Fe moment model'. The polarisation tensor elements marked in red demonstrate where model (2) does not match the data. The shown polarisation tensors were calculated as an average over the present orientation domains. This is demonstrated for the reflection (+0.0, +0.0, −1.5) in table 4.8.

				$\boldsymbol{P'}_{meas}$			$\boldsymbol{P'}_{calc}(1)$			$\boldsymbol{P'}_{calc}(2)$		
H	K	L	$\boldsymbol{P}_0$	x	y	z	x	y	z	x	y	z
+0.0	+2.0	−0.5	+x	−0.861(3)	+0.073(6)	+0.042(6)	−0.870	+0.000	−0.000	−0.867	+0.000	+0.000
			+y	−0.059(6)	−0.659(4)	−0.050(6)	−0.012	−0.665	−0.031	−0.013	−0.568	−0.200
			+z	+0.043(6)	−0.050(6)	+0.655(4)	−0.012	−0.031	+0.665	−0.013	−0.200	+0.568
			-x	+0.876(3)	−0.026(6)	−0.031(6)	+0.867	+0.000	+0.000	+0.862	+0.000	−0.000
			-y	+0.034(6)	+0.659(4)	+0.059(6)	−0.012	+0.665	+0.031	−0.013	+0.568	+0.200
			-z	−0.081(6)	+0.043(6)	−0.655(4)	−0.012	+0.031	−0.665	−0.013	+0.200	−0.568
+0.0	+0.0	−1.5	+x	−0.872(2)	+0.057(4)	+0.119(4)	−0.869	+0.000	+0.000	−0.869	+0.000	+0.000
			+y	−0.010(4)	+0.010(4)	+0.019(4)	−0.000	+0.000	−0.000	+0.000	+0.000	+0.000
			+z	−0.032(4)	+0.020(4)	−0.007(4)	+0.000	−0.000	−0.000	+0.000	+0.000	−0.000
			-x	+0.872(2)	−0.058(3)	−0.115(3)	+0.869	+0.000	+0.000	+0.869	+0.000	+0.000
			-y	−0.043(4)	−0.018(4)	−0.017(4)	−0.000	−0.000	+0.000	+0.000	−0.000	−0.000
			-z	−0.019(4)	−0.023(4)	+0.017(4)	+0.000	+0.000	+0.000	+0.000	−0.000	+0.000
+0.0	+4.0	+0.5	+x	−0.853(7)	+0.06(1)	+0.01(1)	−0.868	+0.000	+0.000	−0.869	+0.000	+0.000
			+y	−0.05(1)	−0.837(8)	−0.05(1)	+0.006	−0.869	+0.006	−0.005	−0.866	+0.060
			+z	+0.03(1)	−0.02(1)	+0.826(8)	+0.006	+0.006	+0.869	−0.005	+0.060	+0.866
			-x	+0.850(7)	+0.02(1)	+0.03(1)	+0.869	+0.000	+0.000	+0.868	+0.000	+0.000
			-y	−0.01(1)	+0.807(8)	+0.08(1)	+0.006	+0.869	−0.006	−0.005	+0.866	−0.060
			-z	−0.08(1)	+0.08(1)	−0.851(7)	+0.006	−0.006	−0.869	−0.005	−0.060	−0.866
+0.0	−2.0	−2.5	+x	−0.871(4)	+0.068(7)	+0.107(7)	−0.874	−0.000	+0.000	−0.821	−0.000	+0.000
			+y	−0.092(7)	−0.081(7)	−0.012(7)	−0.054	−0.093	−0.013	+0.099	−0.108	−0.055
			+z	−0.017(7)	−0.006(7)	+0.100(7)	−0.054	−0.013	+0.093	+0.099	−0.055	+0.108
			-x	+0.876(4)	−0.045(7)	−0.102(7)	+0.858	+0.000	−0.000	+0.875	−0.000	−0.000
			-y	−0.005(7)	+0.085(7)	+0.030(7)	−0.054	+0.093	+0.013	+0.099	+0.108	+0.055
			-z	−0.064(7)	+0.030(7)	−0.087(7)	−0.054	+0.013	−0.093	+0.099	+0.055	−0.108
+0.0	+1.0	−2.5	+x	−0.860(8)	+0.07(2)	+0.11(2)	−0.870	+0.000	+0.000	−0.860	+0.000	−0.000
			+y	−0.04(2)	−0.08(2)	+0.01(2)	−0.008	−0.028	+0.000	−0.043	−0.264	+0.263
			+z	−0.04(2)	−0.01(2)	+0.11(2)	−0.008	+0.000	+0.028	−0.043	+0.263	+0.264
			-x	+0.851(8)	−0.07(2)	−0.10(1)	+0.868	−0.000	+0.000	+0.847	+0.000	+0.000
			-y	−0.02(2)	+0.10(2)	+0.02(2)	−0.008	+0.028	−0.000	−0.043	+0.264	−0.263
			-z	−0.03(2)	+0.02(2)	−0.05(2)	−0.008	−0.000	−0.028	−0.043	−0.263	−0.264
+0.0	+1.0	+0.5	+x	−0.876(3)	+0.037(7)	+0.084(7)	−0.867	+0.000	+0.000	−0.868	+0.000	−0.000
			+y	−0.078(7)	−0.485(6)	−0.083(7)	+0.015	−0.395	−0.001	−0.055	−0.472	−0.329
			+z	+0.069(7)	−0.062(7)	+0.481(6)	+0.015	−0.001	+0.395	−0.055	−0.329	+0.472
			-x	+0.880(3)	−0.009(7)	−0.044(7)	+0.870	−0.000	−0.000	+0.847	+0.000	+0.000
			-y	+0.010(7)	+0.495(6)	+0.079(7)	+0.015	+0.395	+0.001	−0.055	+0.472	+0.329
			-z	−0.101(7)	+0.070(7)	−0.478(6)	+0.015	+0.001	−0.395	−0.055	+0.329	−0.472

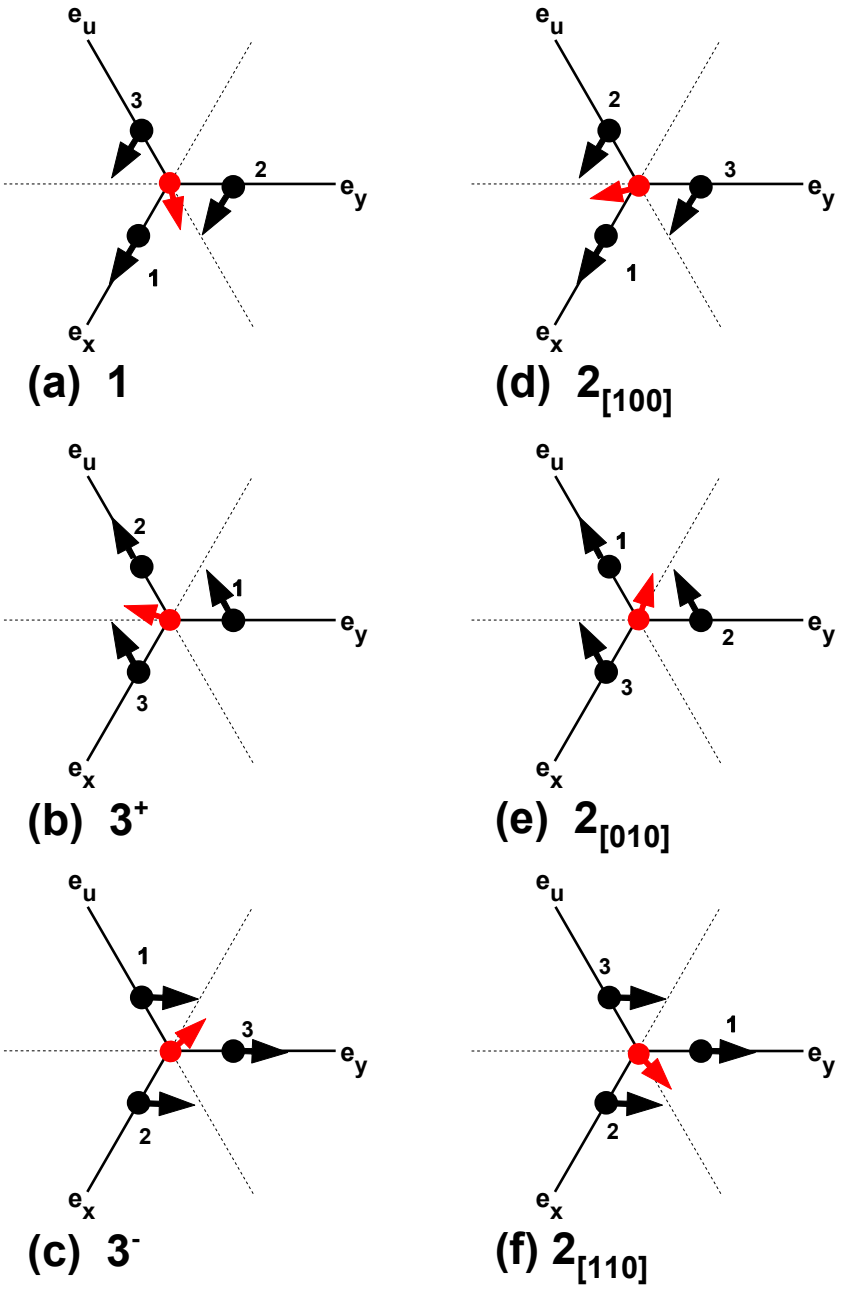

Figure 4.13: The action of all six symmetry elements that leave the propagation vector $\boldsymbol{k}_{hex}$ = [0, 0, $\frac{3}{2}$] in the CM phase invariant is shown. The axes $\boldsymbol{e}_x$ and $\boldsymbol{e}_y$ are unit vectors parallel to the hexagonal crystallographic axes a and b. $\boldsymbol{e}_u$ is a unit vector that is antiparallel to the reciprocal axis b*. The red arrow indicates the magnetic moment of the Nd^{3+} ion whereas the black arrows are the magnetic moments of the three Fe^{3+}-ions in rhombohedral primitive cell of $NdFe_3(^{11}BO_3)_4$. The magnetic structure corresponds to the 'constant Fe moment model' as it was refined from the neutron powder diffraction results.

We note, however, that in the incommensurate phase only the two three-fold rotations and the identity are members of the little group as the two-fold rotations transform the incommensurate propagation vector $\boldsymbol{k}^i_{hex} = [0,\ 0,\ \frac{3}{2} + \varepsilon]$ into $-\boldsymbol{k}^i_{hex} = [0,\ 0,\ -(\frac{3}{2} + \varepsilon)]$. In the incommensurate phase we consequently only have to consider three 120°-domains generated by these symmetry operations.

4.2.5.3 Fit of the polarisation tensors

Before we start to discuss the fits to the measured polarisation tensors we want to explain the implications of $\boldsymbol{k}$ and $-\boldsymbol{k}$ being equivalent in the CM phase. As we have seen in Eq. 4.14 the magnetic structure factor is real for this case. Since the chiral term is $C = i(\gamma r_0)^2 \frac{k_f}{k_i}(\langle M^y_{\perp \boldsymbol{Q}} M^{\dagger z}_{\perp \boldsymbol{Q}}\rangle_\omega - \langle M^z_{\perp \boldsymbol{Q}} M^{\dagger y}_{\perp \boldsymbol{Q}}\rangle_\omega)$ it can be only non-zero when the magnetic structure factor is complex and $\boldsymbol{M}_{\perp \boldsymbol{Q}} \nparallel \boldsymbol{M}^\dagger_{\perp \boldsymbol{Q}}$. In other words, due to the antiparallel alignment of magnetic moments on consequent magnetic layers no chiral contribution can be generated in the cross-section, which is in accordance with (iii). This is valid from both possible magnetic models.
In order to fit the two possible magnetic models that were identified in the preceding sections to the experimentally observed polarisation tensors the program *spfit* was used. It was written in PYTHON [vRD01] by the author of this work. The program can calculate the polarisation tensor on multiple reflections from a chemical and magnetic structure defined in an input file. The program is able to distinguish between the magnetic structure factors for non-equivalent and equivalent $\boldsymbol{k}$ as they were defined in Eqs.2.45 and 4.14, respectively. A least-squares algorithm is used within the program to fit the magnetic structure to the data. The program is described in more detail in appendix D.
Further we need to cope with the reduced modulus of the polarisation vector due to non-ideal polarisers and flippers as it was described in section 2.4.4. The polarisation tensor for the purely nuclear Bragg reflection (0,0,-3) presented in table 4.7 shows that the maximum polarisation of the beam is 0.87. On a pure nuclear peak the polarisation vector should be unchanged. If we assume that the polariser and analyser perform equally well we can estimate that each of the devices generates a beam polarisation $P_b = \sqrt{0.87}$ = 0.93. Using Eq. B.8 the polarisation efficiencies of both benders is then calculated as $P_1 = P_2 = (2P_b - 1) \approx 0.966$. The polarisation tensors were therefore calculated within the used program via Eqs. 2.83 and 2.84 with P_1 and P_2 set to the estimated value. The influence of the flipping efficiency of the four precession coils used in the SNP-option MuPAD (s. section 2.5) are difficult to determine as the magnetic fields generated in the coils in order to turn the polarisation vector are different for each polarisation tensor element P_{ij} and additionally depend on the position in reciprocal space of the host spectrometer. Therefore we assumed the flipping efficiencies to be $\varepsilon_1 = \varepsilon_2 = 1$ what leads to good results.
Finally we carried out least-squares fits for both the 'constant Fe moment model' and the 'free Fe moment model'. We employed the exact models as established by the powder fits for T =20 K in the previous section as a starting point of the fits (s. table 4.4 for param-

eters). Parameters that cannot be determined from the polarisation tensors, e.g. lattice constants and atomic positions and Debye-Waller factors, were consequently fixed in the fits. Since SNP is generally insensitive to absolute moment sizes in case of pure magnetic reflections the magnitude of the magnetic moments for the Fe and Nd ions obtained in the powder fits were used and fixed. Both models completely failed to explain the SNP-data when no orientation domains were considered. Therefore, the six orientation domains with equal population were assumed for the calculation of the polarisation tensors according to Eq. 3.22. This increased the agreement between the data and calculation significantly as demonstrated for the magnetic reflection (0, 0, -1.5) and the 'constant Fe moment model' in table 4.8. The rotation matrices that were used to generate the magnetic structure for each orientation domain from the original structure are given in table 4.6.
The results of the fits are shown together with the measured polarisation tensors in table 4.5. The 'free Fe moment model' was not able to explain the measured polarisation tensors on the two magnetic reflection (0, 2, -0.5), (0, 1, -2.5) and (0, 1, 0.5) as marked by the red entries in table 4.5. The agreement between model and data could not be improved by fits. Here we note that our general experience with fits of SNP data during this work was that, when the model was not already near to the proper solution it was not possible to improve it significantly.
For the 'constant Fe moment model' the angle α_{Nd} was set to the starting value of 75° as obtained in the powder fit and then was allowed to vary. The fit yielded a systematic dependence of the 'yy' and 'zz' elements of the polarisation tensor of the magnetic reflection (0, 1, 0.5) on the angle α_{Nd} as demonstrated in Fig. 4.14. A similar but weaker dependence is also found in the 'yz' and 'zy' elements of the reflection (0, 2, -0.5), (0, 4, 0.5) and (0, 1, -2.5). The angular dependence of the polarisation tensor elements in Fig. 4.14 shows that the best agreement between data and model is obtained when the angle α_{Nd} between the Nd and Fe moments is either 0° or 180°. Here the latter is physically more reasonable. The resulting polarisation tensors on all magnetic reflections can be found in table 4.5.
Attempts to additionally determine the orientation of the Fe magnetic moments via the angle α_{Fe} gave no conclusive results. The angle α_{Fe} describes the absolute orientation of the magnetic moments in the crystallographic ab-plane with respect to chemical structure. Thus, the indeterminacy of α_{Fe} is most probabably related to the presence of the six orientation domains in the hexagonal basal plane. Finally, all fits were performed with α_{Fe} fixed at zero.
In summary our SNP data is in perfect agreement with the 'constant Fe moment model' in the commensurate phase when the angle between the magnetic moments of the Nd and Fe ions is set to zero. Concerning the six orientation domains we want to emphasise that in the case of $\alpha_{Nd} = 0$ the magnetic configurations obtained by application of the three symmetry operations $2_{[010]}$, $2_{[100]}$ and $2_{[110]}$ are identical to the configurations obtained by **1**, 3^+ and 3^- as can be seen in Fig. 4.13. Hence, in this case it is enough to consider the three orientation domains associated with **1**, 3^+ and 3^- as the degree of symmetry reduction is lower.
In consideration that $\alpha_{Nd} = 0°$ is favoured by our SNP data that is more sensitive on the

Table 4.6: The table shows the symmetry matrices corresponding to the six symmetry operators of the point group C_v that were used to generate the orientation domains for the calculation of the polarisation tensors. The matrices are given in a right-handed Cartesian coordinate system where the x and z axes are parallel to the crystallographic a and c axes, respectively.

1	3^+	3^-
$\begin{pmatrix} 1 & 0 & 0 \\ 0 & 1 & 0 \\ 0 & 0 & 1 \end{pmatrix}$	$\begin{pmatrix} -\frac{1}{2} & -\frac{\sqrt{3}}{2} & 0 \\ \frac{\sqrt{3}}{2} & -\frac{1}{2} & 0 \\ 0 & 0 & 1 \end{pmatrix}$	$\begin{pmatrix} -\frac{1}{2} & \frac{\sqrt{3}}{2} & 0 \\ -\frac{\sqrt{3}}{2} & -\frac{1}{2} & 0 \\ 0 & 0 & 1 \end{pmatrix}$
$2_{[010]}$	$2_{[100]}$	$2_{[110]}$
$\begin{pmatrix} -\frac{1}{2} & -\frac{\sqrt{3}}{2} & 0 \\ -\frac{\sqrt{3}}{2} & \frac{1}{2} & 0 \\ 0 & 0 & -1 \end{pmatrix}$	$\begin{pmatrix} 1 & 0 & 0 \\ 0 & 1 & 0 \\ 0 & 0 & -1 \end{pmatrix}$	$\begin{pmatrix} -\frac{1}{2} & \frac{\sqrt{3}}{2} & 0 \\ \frac{\sqrt{3}}{2} & \frac{1}{2} & 0 \\ 0 & 0 & -1 \end{pmatrix}$

Table 4.7: The polarisation tensor measured on the pure nuclear Bragg reflection (0,0,-3) is shown. The polarisation elements on the diagonal of the polarisation tensor are reduced from 1 due to non-ideal polarisers.

	$\boldsymbol{P'}$		
$\boldsymbol{P}_0$	x	y	z
+x	+0.882	−0.090	−0.133
+y	+0.072	+0.874	−0.102
+z	+0.152	+0.024	+0.872
-x	−0.873	+0.011	+0.165
-y	−0.013	−0.882	+0.121
-z	−0.102	−0.087	−0.890

Table 4.8: The measured and calculated polarisation tensor for the magnetic Bragg reflection (0,0,-1.5) is shown. The calculated polarisation tensor is averaged over the polarisation tensors for each of the six present magnetic orientation domains according to Eq. 3.22. The domains were assumed to be equally populated and hence the population factors η_i were set equal to 1/6.

Sym. Op./P_{ij}	xx	xy	xz	yx	yy	yz	zx	zy	zz
1	−0.869	+0.000	+0.000	−0.000	−0.859	−0.128	+0.000	−0.128	+0.859
3^+	−0.869	+0.000	+0.000	−0.000	+0.319	+0.808	−0.000	+0.808	−0.319
3^-	−0.869	+0.000	+0.000	−0.000	+0.541	−0.679	−0.000	−0.679	−0.541
$2_{[010]}$	−0.869	+0.000	+0.000	+0.000	−0.859	−0.128	+0.000	−0.128	+0.859
$2_{[100]}$	−0.869	+0.000	+0.000	−0.000	+0.541	−0.679	−0.000	−0.679	−0.541
$2_{[110]}$	−0.869	+0.000	+0.000	+0.000	+0.319	+0.808	+0.000	+0.808	−0.319
sum	−0.869	+0.000	+0.000	−0.000	+0.000	+0.000	−0.000	+0.000	−0.000
measured:	−0.872	+0.057	+0.119	−0.010	+0.010	+0.019	−0.032	+0.020	−0.007

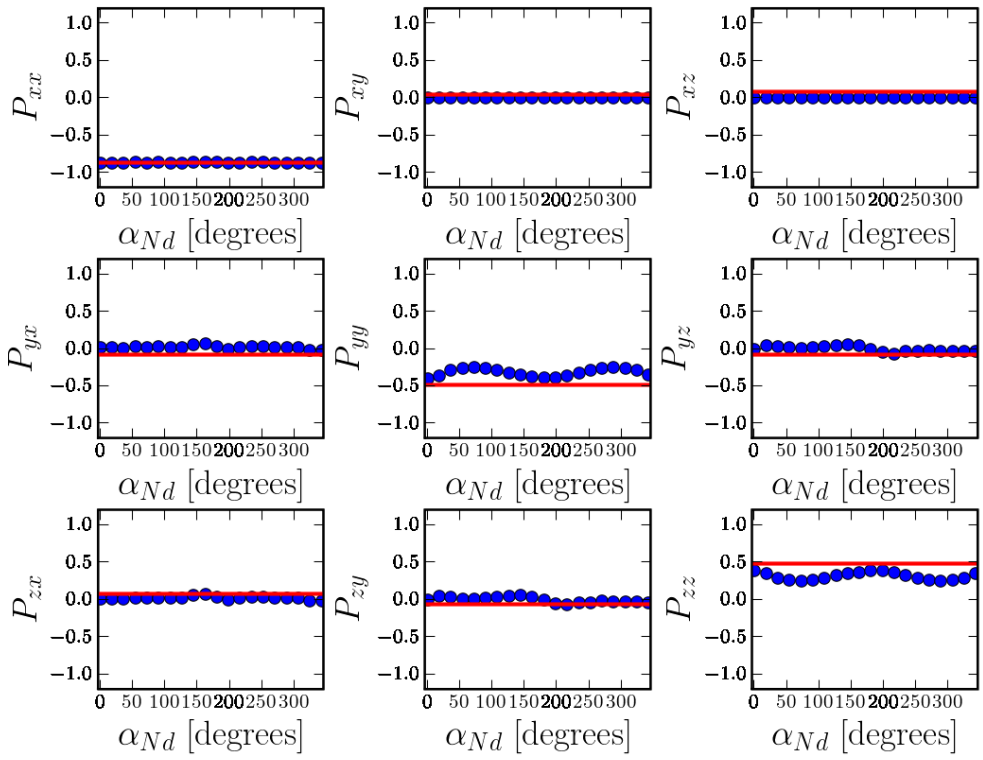

Figure 4.14: The figure shows the dependence of the polarisation tensor elements of the magnetic reflection (0, 1, 0.5) on the angle α_{Nd} for the 'constant Fe moment model'. The red line denotes the measured value whereas the blue dots are the calculated values.

direction of the magnetic moment we repeated the Rietveld refinements of the powder data for the 'constant Fe moment model' (compare section 4.2.4.3), however, the magnetic moments on the Fe and Nd sublattices were fixed to be parallel. The result of the fits are summarised in table 4.9. The agreement factors are essentially unchanged by this measure. The major difference is that the magnetic moment on the Nd sublattice is reduced from 2.7 μ_B to 1.51 μ_B at 1.6 K. The magnetic moments as a function of temperatures are shown in Fig. 4.15. We conclude that the 'constant Fe moment model' with the angle set to $\alpha_{Nd} = 0°$ provides the best description for the combination of the neutron powder and SNP data.

4.2.5.4 Incommensurate phase

The $\boldsymbol{Q}$-resolution of the polarised setup on TASP is naturally limited since the benders perform significantly worse with respect to transmission and also polarising efficiency at wave vectors smaller than $k_f = 1.97$ Å^{-1}. In order to be able to observe the small splitting

Table 4.9: The table shows the results of the Rietvield refinement of the powder data for the 'constant Fe moment model' that were carried out in section 4.2.4.3, however with the constraint that the angle between the magnetic moments on the Fe and Nd sites is fixed at $\alpha_{Nd} = 0°$.

T (K)	Sample motion	μ_{Fe} (μ_B)	μ^{Nd} (μ_B)	χ^2	R_{Bn}	R_{Bm}
30	Osc.	1.46(6)	0.1(1)	77	8.9	48.7
25	Osc.	3.43(3)	0.14(6)	62	8.2	9.8
20	Osc.	4.00(3)	0.23(5)	57	7.9	7.7
15	Osc.	4.41(3)	0.36(5)	55	7.8	6.4
10	No	5.07(3)	0.98(3)	18		8.9
1.6	No	5.09(3)[a]	1.51(1)	14		8.0

[a]Note the expected value $\mu_{Fe} = 5\ \mu_B$ for free Fe^{3+} ions.

($\varepsilon = 0.00667$ (r.l.u.) $\equiv$ 0.0055Å^{-1}) of the magnetic Bragg reflections in the ICM phase of $NdFe_3(^{11}BO_3)_4$ an excellent $\boldsymbol{Q}$-resolution is necessary. The relatively moderate Q-resolution associated with $k_f = 1.97$ Å^{-1} is not sufficient to measure seperate polarisation tensors on the magnetic satellites $\pm\boldsymbol{k}_i^{hex}$ and consequently a superposition of intensities from both satellites will be observed. However, by performing polarised Q-scans over the magnetic satellites around the position (0,0,-1.5) in reciprocal space it is still possible to extract some important information about the magnetic structure in the ICM magnetic phase.

From Eq. 2.72 we know how the observed contributions in neutron scattering depend on the the direction of the initial polarisation vector of the neutron beam $\boldsymbol{P}_0$. By turning the initial polarisation vector P_0 parallel (antiparallel) to the x direction (thus parallel or antiparallel to $\boldsymbol{Q}$) the following scattering cross-sections are obtained:

$$\begin{aligned} \sigma(\boldsymbol{P}_0 = \pm\boldsymbol{e}_x) &= N + M^y + M^z \mp C \\ \Rightarrow \sigma(\boldsymbol{P}_0 = +\boldsymbol{e}_x) - \sigma(\boldsymbol{P} = -\boldsymbol{e}_x) &= (N + M^y + M^z - C) - (N + M^y + M^z + C) \\ &= -2C. \end{aligned} \tag{4.15}$$

Hence, the difference between the intensities, which are measured with the initial polarisation parallel and antiparallel to x is proportional to the chiral contribution to the cross-section, which only appears if the magnetic structure is chiral (compare section 2.4.3). We carried out elastic $\boldsymbol{Q}$-scans along the L direction around the reciprocal space position (0, 0, -1.5) as shown in Fig. 4.16. In our experimental setup the second polariser downstream of the sample that is employed as polarisation analyser was still mounted. Therefore, four polarised $\boldsymbol{Q}$-scans with corresponding intensities I_{ij} (i,j=incident/final polarisation vector direction) instead of two like in Eq. 4.15 had to be performed and the respective cross-sections are related via

$$\begin{aligned} \sigma(\boldsymbol{P}_0 = +\boldsymbol{e}_x) &= (I_{xx}) + (I_{x-x}) \\ \sigma(\boldsymbol{P}_0 = -\boldsymbol{e}_x) &= (I_{-xx}) + (I_{-x-x}). \end{aligned} \tag{4.16}$$

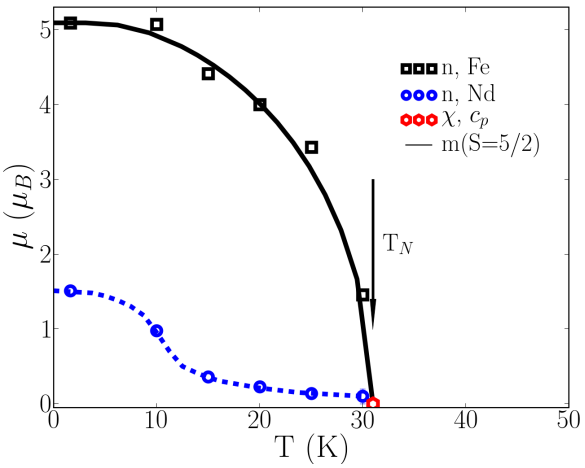

Figure 4.15: Temperature dependence of the ordered magnetic Fe and Nd moments as obtained from the Rietveld refinement of the powder data for α_{Nd} fixed at 0° is shown (s. text for details). The black full and blue dashed lines are the expected magnetisation (m) curve for S = 5/2 [Dar67] and a guide to the eye, respectively.

As shown in Fig. 4.16(a) the polarised scans allow to separate the resolution limited peak at (0,0,-1.5) in two satellites (0,0,0)-$\boldsymbol{k}_i^{hex}$ (I_{-xx}) and (0,0,-3)+$\boldsymbol{k}_i^{hex}$ (I_{x-x}). The scans were performed at T = 1.5 K where the second order satellites are negligible (compare Fig. 4.10) and hence are not considered here. The difference $\sigma(\boldsymbol{P}_0 = +\boldsymbol{e}_x) - \sigma(\boldsymbol{P}_0 = -\boldsymbol{e}_x) = (I_{xx}) + (I_{x-x}) - (I_{-xx}) + (I_{-x-x})$ is provided in Fig. 4.16(b). Since two distinct extrema with opposite signs for the two satellites can be distinguished in the observed difference several constraints for the magnetic structure below T_{ICM} can be derived:

- First, the observation of chiral terms on the satellites proves that the magnetic structure that we have shown to be a collinear antiferromagnet along the crystallographic c-axis with moments in the hexagonal basal plane transforms to a antiferromagnetic long-period spiral. The moments are therefore almost antiferromagnetic in adjacent ab-layers and are slightly rotated by a small angle from layer to layer.
- The chiral term on the satellite associated with the propagation vector +$\boldsymbol{k}_i^{hex}$ has a different sign with respect to the chiral term on the satellite associated with the propagation vector -$\boldsymbol{k}_i^{hex}$ which is typical for a helix. We have seen in chapter 2 that dependent on the handedness of the spiral the chiral term will have positive and negative sign on the satellite associated with $\boldsymbol{k}$ and $-\boldsymbol{k}$ respectively, or vice versa. This implies that if magnetic spirals with both handednesses would exist in equally populated chiral-domains then we would see zero intensity in the difference scan shown Fig. 4.16(b). Therefore we conclude that we have at least unequally populated chiral domains where one handedness is preferred over the other one.

In order to investigate this further we performed calculations of the magnetic intensities where we assumed the 'constant Fe moment model' for the calculation of the intensities,

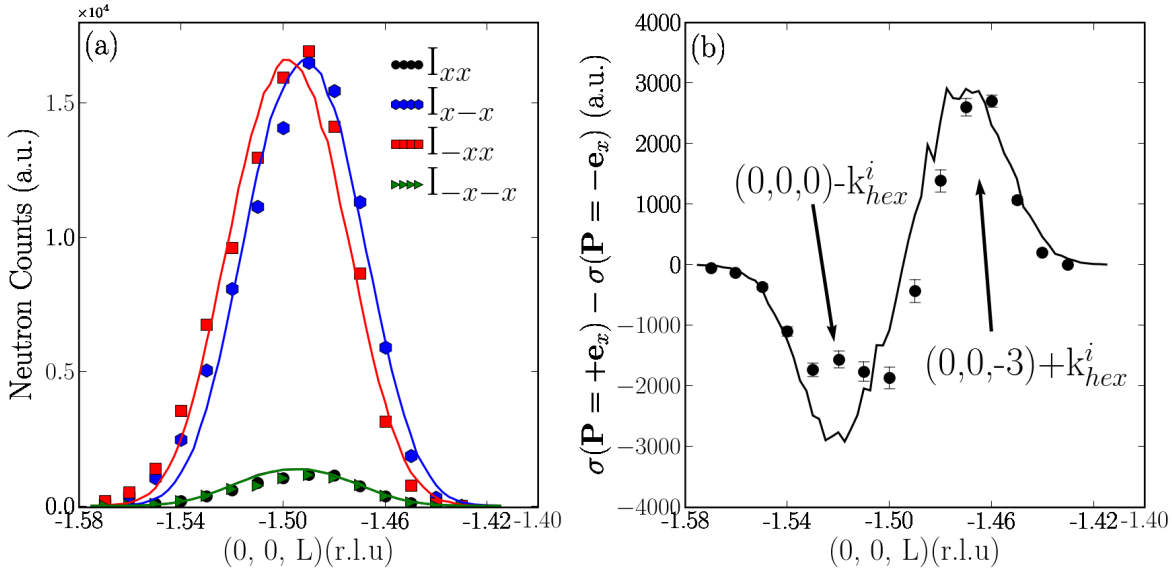

Figure 4.16: (a) Q-scans in the polarised mode over the magnetic Bragg satellites (0,0,0)-$\boldsymbol{k}_i^{hex}$ and 0,0,-3)+$\boldsymbol{k}_i^{hex}$ at T = 1.5 K are shown. (b) The difference for intensities with the initial polarisation vector directed parallel and antiparallel to $\boldsymbol{Q}$ for the same Q-scan are shown. This difference is directly proportional to the chiral contribution to the scattering cross-section as shown in Eq. 4.15.

however together with the incommensurate $\boldsymbol{k}_i^{hex}$ that leads a small rotation of the magnetic moments between neighbouring layers. We calculated the integrated intensities for the four measured polarisation channels 'xx', 'x-x', '-xx' and '-x-x' for both satellites (0,0,0)-$\boldsymbol{k}_i^{hex}$ and (0,0,-3)+$\boldsymbol{k}_i^{hex}$, where we used $\varepsilon = 0.0667$ in $\boldsymbol{k}_{hex}^i = [0, 0, \frac{3}{2} + \varepsilon]$ as deduced from our high resolution diffraction data. The calculated integrated intensities are given in table 4.10(a) for the case of only one single chirality domain. For comparison we give the measured integrated intensities from the scans for the four polarisation channels in table 4.10(b). First of all the calculated values reproduce the correct sign for the difference of the intensities that represents the chiral contribution to the cross-section. But due to the limited resolution of the setup the measured values are integrated over both peaks and cannot be compared directly to the calculations. This is especially true for the difference of the intensities. However, we can make some assumptions that will allow for a comparison. We will assume that

- the measured integrated intensity in the channel '-xx' is only due to the peak at (0,0,0)-$\boldsymbol{k}_i^{hex}$. This assumption is justified as the measured points (red in Fig. 4.16(a)) are shifted towards the direction of this peak.

- the measured integrated intensity in the channel 'x-x' is only due to the peak at (0,0,-3)+$\boldsymbol{k}_i^{hex}$. This assumption is justified by an identical argument (blue points in Fig. 4.16(a)).

- the channels 'xx' and '-x-x' are equally contributed from both satellite reflection as they are centred on top of each other and between the other two channels (green and black points in Fig. 4.16(a)).

With these assumptions we compare intensity ratios for both peaks. For instance the calculated ratio I^c_{x-x}/I^c_{xx} for the magnetic Bragg reflection (0,0,-3)+$\boldsymbol{k}_i^{hex}$ amounts to 23.98. The measured ratio with respect to our model assumptions is $I^m_{x-x}/(I^c_{xx}/2) = 28.22$ (the division by 2 is due to the last assumption). For the second satellite (0,0,0)-$\boldsymbol{k}_i^{hex}$ we find the calculated ratio $I^c_{-xx}/I^c_{-x-x} = 24.11$ and the measured ratio $I^m_{-xx}/(I^c_{-x-x}/2) = 28.33$. This signifies that our model of a sinlge antiferromagnetic helix with the magnetic moments parallel to the hexagonal basal plane that propagates along the hexagonal c axis reproduces our data well.
In addition we verified our assumptions by performing a convolution of the calculated integrated intensities with the resolution of the spectrometer in a simulation. For this purpose the intensities were multiplied with delta-functions positioned at the satellite positions and we calculated the intensities in the four polarisation channels via convoluting these Bragg peaks with the spectrometer resolution. The resolution of the spectrometer was calculated with the program *tasresfit* for each point in the scan. The program was written by Florian Bernlochner and the author of this work and is described in the appendix D. The result of the simulations are the solid lines in Fig. 4.16. To match the intensity a scale factor was introduced in the calculation. The only parameters varied in the calculation were the populations of the two chiral domains described above and the scale factor. The best agreement was found with populations of 15 and 85%. However, this deviation from a 100% populated is probably due to the difficulties we had to match the peak shape of reflections in the scan properly, which affects especially the difference calculated therefrom. Therefore, we think that within our experimental resolution the assumption of a single chiral domain is justified.

Table 4.10: (a) Integrated intensities for the magnetic satellite reflections in the ICM phase as calculated from the constant Fe moment model, however, with the incommensurate $\boldsymbol{k}_i^{hex}$. For the calculation we assumed that only one single chiral domain is populated. (b) Measured integrated intensities for the $\boldsymbol{Q}$-scan in Fig. 4.16(a) in the different polarisation channels. For the comparison see the text.

(a)

Peak	I^c_{xx}	I^c_{x-x}	I^c_{-xx}	I^c_{-x-x}	$\sigma(\boldsymbol{P}_0 = +\boldsymbol{e}_x) - \sigma(\boldsymbol{P} = -\boldsymbol{e}_x)$
(0,0,0)-$\boldsymbol{k}_i^{hex}$	5.71	0.24	137.07	5.71	-136.84
(0,0,-3)+$\boldsymbol{k}_i^{hex}$	5.73	137.44	0.24	5.73	137.20

(b)

I^m_{xx}	I^m_{x-x}	I^m_{-xx}	I^m_{-x-x}
66.2	934.0	946.0	65.9

4.3 Discussion

Our investigation on $NdFe_3(^{11}BO_3)_4$ combines the results of macroscopic measurements and a detailed neutron diffraction study with unpolarised and polarised neutrons. The magnetic susceptibility results showed that the magnetic anisotropy is of easy plane type with the magnetic moments confined in the hexagonal basal plane. Below $T_N \approx 30$ K, additional Bragg reflections were observed in neutron powder diffraction that could be well indexed by means of a magnetic propagation vector $\boldsymbol{k}^{hex} = [0, 0, \frac{3}{2}]$. This is a clear signature of the long range magnetic ordering present in $NdFe_3(^{11}BO_3)_4$ below T_N. The magnetic transition temperature derived from the neutron scattering data is in good agreement with the transition temperature observed in the magnetic susceptibility as well as in the specific heat. An additional magnetic phase transition at $T_{ICM} \approx 13.5$ K, where the commensurate magnetic structure becomes incommensurate could be identified in high resolution diffraction experiments via the observed splitting of the magnetic reflections. The splitting yields an incommensurate propagation vector $\boldsymbol{k}_i^{hex} = [0, 0, \frac{3}{2} + \varepsilon]$ where $\varepsilon(1.6\ K)$ was determined to be 0.00667.
In the CM phase, two models for the magnetic structure of $NdFe_3(^{11}BO_3)_4$ that explain the neutron powder diffraction data equally well were established by means of combined magnetic representation analysis and fits to the powder data. The additional application of spherical neutron polarimetry allowed to decide that the correct model for the magnetic structure is given by equally-sized and directed magnetic moments on all three Fe sites that are parallel to the hexagonal basal plane. Magnetic moments in adjacent planes are collinear and antiferromagetically coupled. Further our SNP data suggests that the magnetic moments on the Nd sites are parallel to the moments on the Fe ions. This mutual magnetic orientation of Fe and Nd magnetic moments is also in agreement with recent measurements of the magnetic susceptibility and corresponding theoretical calculations (s. reference [VDK07] and references 1-4 therein). However, we note that the preliminary analysis of more recent data measured on a second sample at HEIDI at FRM-II (that has not been considered in this work) favour a non-zero angle of approximately 45° at 1.6 K between the magnetic moments of the Fe and Nd ions within the hexagonal basal plane. Yet, the result from the single crystal experiments suffer from problems with extinction due to a rather large crystal and additionally the SNP data is more sensitive to the orientation of magnetic moments. Moreover, the angle between the moments of the Fe and Nd sublattices may is sample dependent.
At T = 1.6 K the magnetic moment of the Fe^{3+} ions amounts to approximately 5.1 μ_B (4.9 μ_B if a non-zero angle between Fe and Nd sublattices is assumed), which is closed to the value for free Fe^{3+}. The temperature dependence of the magnetic moments for the Fe^{3+} ions is approximately described by the magnetisation curve for S = 5/2 [Dar67]. The magnetic moment of the Nd^{3+} sublattices saturates at 1.51 μ_B (2.7 μ_B if a non-zero angle between Fe and Nd sublattices is assumed), and is therefore reduced from the value 3.3-3.7 μ_B for free Nd^{3+} (s. e.g. [Blu01]), which is supposable due to the crystal fields that were observed and calculated in reference [PCS+07]. Further it is interesting to note

that the temperature dependence of the magnetic moments for Nd^{3+} displays a sudden jump below 15 K. On the one hand this increase may be associated with the commensurate to incommensurate phase transition at $T_{ICM} \approx 13.5$ K. On the other hand it might indicate a small paramagnetic contribution of the Nd sublattice as proposed in [TKH+07] which would be agreement with the increase observed in the magnetic susceptibility data in 15 K.

Due to the tiny splitting of the propagation vector, the CM and ICM phase cannot be distinguished within the resolution of the powder diffractometer DMC that was employed for the measurements. Hence no statement about the change of the magnetic structure in the ICM phase can be made from the neutron powder data. But the polarized $\boldsymbol{Q}$-scan performed in the ICM phase clearly demonstrates the presence of a chiral contribution in the magnetic cross-section. The intensities on the incommensurate magnetic peaks could be well explained via the magnetic model that was found for the CM phase simply by introducing the incommensurate propagation vector. This suggest that the magnetic structure transforms into a long-period antiferromagnetix helix that propagates along the hexagonal c axis. The incommensurate magnetic propagation vector $\boldsymbol{k}_i^{hex} = [0, 0, \frac{3}{2} + \varepsilon]$ is therefore associated with a rotation of the magnetic moments about $180° + \gamma$ around the c axis between adjacent hexagonal planes that are interrelated via trigonal translations. The measured value of the splitting $\varepsilon = 0.00667$ corresponds to $\gamma \approx 0.8°$ and the full period of the helix amounts to approximately 1140 Å. The mere observation of a chiral contribution signifies unequally populated chirality domains (s. section 3.3.4). Our data shows suggest that only one of the two chirality domains exists. The antiferromagnetic helix in the ICM phase of $NdFe_3(^{11}BO_3)_4$ therefore exists with a unique handedness. A single chirality domain is in principle not expected, since left- and right-handed spirals are energetically degenerate (compare section 3.3.4), however in the case of $NdFe_3(^{11}BO_3)_4$ this might be related to the fact that the chemical structure is non-centrosymmetric. This is similar to the magnetic helices in MnSi or UPtGe [Bro01] that both possess no inversion symmetry.

The observation of third order harmonics of the magnetic satellites at the positions $(0, 0, 3/2 \pm 3\varepsilon)$ additionally suggest the formation of a magnetic soliton lattice in $NdFe_3(^{11}BO_3)_4$. A soliton is the appearance of localized or topological defects in periodic structures due to the presence of non-linear forces. Such non-linear forces can be due to a external magnetic field that interacts with the magnetic moments or due to magnetic anisotropy. The free energy for a regular magnetic helix that includes an anisotropy energy of order n in the basal plane perpendicular to the propagation vector parallel to z direction has the form [IL83]

$$F = \frac{1}{V} \int d\boldsymbol{r} \left\{ \gamma\eta^2 (\frac{d\phi}{dz})^2 + \sigma\eta^2 \frac{d\phi}{dz} + \omega\eta^n \cos(n\phi) \right\}, \tag{4.17}$$

where η and ϕ are the modulus and phase of the two-component magnetic order parameter that describes the magnetic moments that are parallel to the basal plane. Here the first term describes the exchange interaction, the second term is the Dzyaloshinsky-Moriya

interaction[4] and the last term is the n-th order crystallographic anisotropy energy.
Until now no explicit statement about the existence of the DMI in $NdFe_3(^{11}BO_3)_4$ has been made. However, as $NdFe_3(^{11}BO_3)_4$ is non-centrosymmetric the presence of the DMI is allowed from symmetry. Therefore, the formation of the observed magnetic helix is possibly driven by the DMI.
The Euler-Lagrange equation for Eq. 4.17 is given by the so-called sine-Gordon equation:

$$\frac{d^2}{dz^2}(n\phi) \quad + \quad v_n \sin(n\phi), \tag{4.18}$$

$$\text{where} \quad v_n \quad = \quad \frac{\omega}{\gamma}\frac{\eta^{n-2}n}{2}. \tag{4.19}$$

The solution of this equation is expressed in terms of elliptic function

$$n\frac{\phi}{2} = am(qz,\kappa), \quad q = \frac{v_n^{1/2}}{\kappa}. \tag{4.20}$$

Here κ is the modulus of the elliptic function. For small v_n ($\frac{\omega}{\gamma} \longrightarrow 0$) this solution can be expanded in an asymptotic series [IL83]

$$\phi = kz + \frac{v_1}{k^2}\sin(kz) + \frac{v_n}{nk^2}\sin(nkz) + \ldots, \tag{4.21}$$

and additionally one obtaines the following expression for the propagation vector:

$$k = \frac{|\sigma|}{\gamma} - \frac{v_1^2\gamma^3}{2|\sigma|^3} - \frac{v_m^2\gamma^3}{2n^2|\sigma|^3}. \tag{4.22}$$

In the absence of a magnetic anisotropy Eqs. 4.21 and 4.22 describe a regular helix with propagation vector of modulus k that propagates parallel to the z-directions. However, if the anisotropy energy is switched on the helix is distorted by additional sine modulations parallel to z. This is illustrated in Fig. 4.17 for a second order magnetic anisotropy.
The neutron scattering cross-section from a magnetic soliton lattice is expressed by [IL83]:

$$\begin{aligned}
\frac{d\sigma}{d\Omega} &= S^2 \sum_{\boldsymbol{\tau}} (J_0^x(\boldsymbol{k}))^2 (1-\hat{Q}_x^2)\delta^3(\boldsymbol{Q}-\boldsymbol{\tau}) + \\
&+ S^2 \sum_{+,-} \sum_{\boldsymbol{\tau}} \sum_{p=1}^{\infty} \left\{ (J_p^x(\boldsymbol{k}))^2 (1-\hat{Q}_x^2) + (J_p^y(\boldsymbol{k}))^2 (1-\hat{Q}_y^2) \right\} \delta^3(\boldsymbol{Q} \pm p\boldsymbol{k} - \boldsymbol{\tau}), \\
\text{where} \quad & J_0^x(\boldsymbol{k}) = -\frac{v_1}{2k^2}, \\
& J_1^x(\boldsymbol{k}) = \frac{1}{2} - \frac{3v_1^2}{32k^4} - \frac{v_n^2}{8(nk)^4}, \quad J_1^y(\boldsymbol{k}) = \frac{1}{2} - \frac{5v_1^2}{32k^4} - \frac{v_n^2}{8(nk)^4}, \\
& J_{n\pm1}^{x,y}(\boldsymbol{k}) = \pm\frac{v_n}{4n^2k^2}.
\end{aligned} \tag{4.23}$$

[4]For the two component order parameter this form is equivalent to Eq. 1.4. This is demonstrated in reference [Boe02].

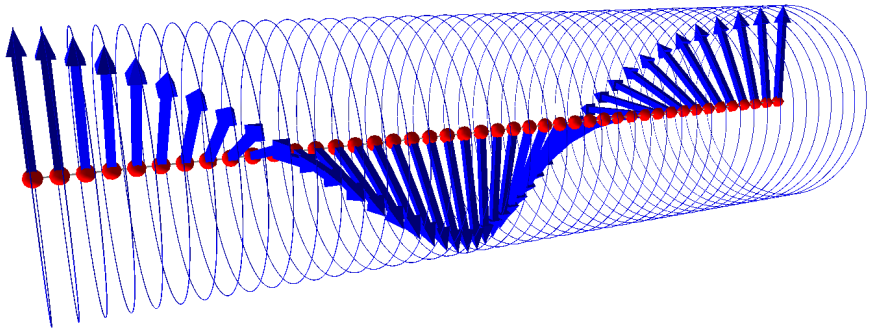

(a)

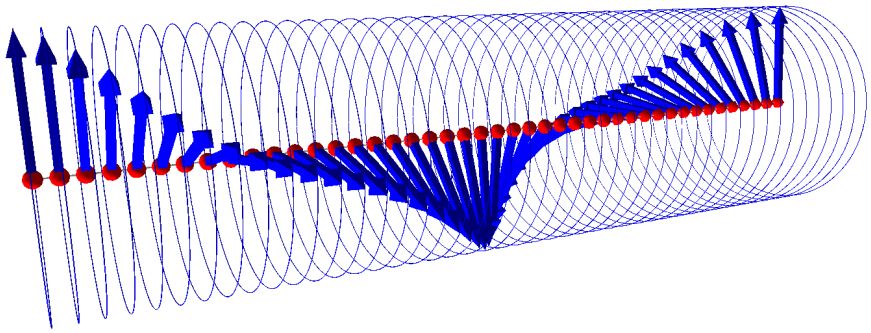

(b)

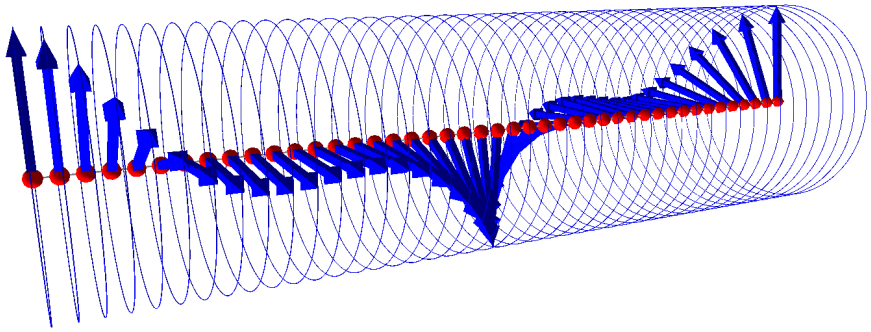

(c)

Figure 4.17: Transformation of a regular magnetic helix (a) into a magnetic soliton lattice (b),(c) due to the action of an increasing 2nd order magnetic anisotropy.

Eq. 4.23 shows that third order harmonics of the magnetic propagation vector can only be observed in a neutron scattering experiment if a 2nd (n=2) or 4th (n=4) order magnetic anisotropy is present in the plane perpendicular to the propagation vector. Tristan *et al.* have recently reported the observation of an anisotropy of the magnetic susceptibility for $NdFe_3(BO_3)_4$ within the hexagonal basal plane in addition to the easy plane character that was found in our measurements [TKH$^+$07]. They have measured the magnetic susceptibility parallel to crystallographic a axis and the b' axis (b' is perpencicular to crystallographic a and c axes) and found $\chi_a(T) > \chi_{b'}(T)$ below T_N. This suggest the presence of a 2nd order anisotropy in the hexagonal basal plane.
In Figs. 4.10 (b) to (d) we see that the intensities of the second order satellites are highest for temperatures T $\lesssim$ 13.5 K and the distortions of the incommensurate periodic structures seem to be largest near to the CM to ICM phase transition. We therefore assume that at T_{ICM} the interaction that favours a magnetic order that is incommensurate with respect to the underlying crystal lattice becomes non-negligible and leads to non-linear forces onto the magnetic subsystem slightly below T_{ICM} as it still wants to remain in its commensurate magnetic order. Within a small temperature regime below T_{ICM} the magnetic structure consequently is not yet completely incommensurate but can be rather viewed as a distorted commensurate magnetic structure with domain walls (cf Fig. 4.17). Alternating periods of commensurate parts and domains walls then lead to the observed third order harmonics. The observation of magnetic soliton lattice without the application of external forces like magnetic fields or mechanical stress are rather unlikely and to the best of our knowledge the only other compound for which a magnetic soliton lattice was reported without the application of an external magnetic field is CuB_2O_4 [RSP$^+$01]. The observed temperature dependence of the splitting of the propagation vector $k_z = \frac{3}{2} + \varepsilon$ where $\varepsilon \propto |(T_{ICM} - T)|^{0.58}$ is close to $k(T) \propto |(T_{ICM} - T)|^{0.48}$ reported in reference [RSP$^+$01]. In addition, similar to CuB_2O_4 the commensurate phase is realised when the temperature is increased, which is in contradiction to the prediction of the theory [IL83]. For CuB_2O_4 it was proposed that the difference to the theory can be explained by assuming that the change of the propagation vector is not due to a temperature dependent magnetic anisotropy as in reference [IL83] but rather due to the magnitude of the DMI that decreases as a function of increasing temperature [Boe02]. We assume that is is similarly true for $NdFe_3(^{11}BO_3)_4$. The principal difference is that for $NdFe_3(^{11}BO_3)_4$ the observed helix is 'antiferromagnetic' whereas for the compound CuB_2O_4 the helix is regular. in summary our experimental results are well described by the assumption of a magnetic soliton lattice.
Finally, we also want to briefly discuss the magneto-electric effect observed in $NdFe_3(BO_3)_4$ by Zvezdin and co-workers[ZVK$^+$06] in the light of the observed chirality. Even though the magnetic structure of $NdFe_3(^{11}BO_3)_4$ that we observed in the ICM phase shows magnetic chirality none of the models discussed in section 1.3.3 in which a spontaneous electric polarisation arises due to chiral magnetic ordering is adequate for this sample. The magnetic spirals that drive a spontaneous electric polarisation are cycloids where the magnetic moments rotate in a plane parallel to the propagation vector which is not the case for $NdFe_3(^{11}BO_3)_4$. In addition the electric polarisation due to the ME effect

did not develop spontaneously for $NdFe_3(BO_3)_4$ but was observed under application of a magnetic field. Apart from this, the temperature intervall below approximately 13.5 K where we observed the antiferromagnetic helix in $NdFe_3(BO_3)_4$ is not compatible with the observation of the ME effect below 25 K. Hence, new theoretical efforts for $NdFe_3(BO_3)_4$ that consider the influence of a magnetic field on the magnetic structure we have found in this investigations are highly desirable and may yield a better understanding of the ME effect in this material.

Chapter 5

The Helimagnet MnSi

We have already seen in section 1.3.4 that the itinerant helimagnet MnSi currently attracts a great deal of scientific interest as it displays exotic magnetic phases [PRP$^+$04] and a metallic non-Fermi-Liquid (NFL) phase that is not driven by a quantum critical point [PBK$^+$07]. In this chapter we will describe our experimental findings obtained by means of elastic and inelastic neutron scattering experiments with both unpolarised and polarised neutrons. Our experiments concentrate on the investigation of a possible intermediate phase between the helimagnetic and paramagnetic phase and the magnetic excitations in the helimagnetic phase. The intermediate phase was recently proposed by Roessler *et al.* based on experimental observations in the specific heat and neutron scattering [RBP06]. For the helical magnetic phase a novel magnetic excitation spectrum has been suggested independently by two theory groups [BKR07, Mal06]. The proposed magnetic excitations emerge in the helical phase as new Goldstone modes - the so-called *helimagnons* - due to the broken inversion symmetry in MnSi. Until now the excitation spectrum in the helical phase has not been explored in detail to the best of our knowledge and therefore no experimental confirmation of the helimagnons has been reported so far.
Before we will discuss the results we will summarise the known properties of MnSi and give an overview over recent theoretical developments that motivated our experimental work.

5.1 Properties

5.1.1 Chemical and magnetic structure

The 3d intermetallic compound MnSi crystallises in a cubic structure with the lattice constant a = 4.558 Å. The structure lacks inversion symmetry and is described by the space group $P2_13$. Four Mn and four Si ions are situated at the symmetry related sites

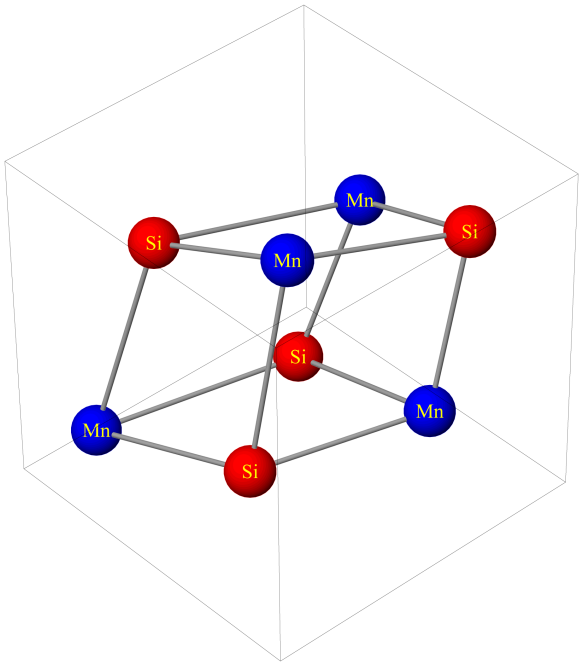

Figure 5.1: The chemical unit cell of MnSi is illustrated.

(x, x, x), $(\frac{1}{2} + x, \frac{1}{2} - x, -x)$, $(\frac{1}{2} - x, -x, \frac{1}{2} + x)$ and $(-x, \frac{1}{2} + x, \frac{1}{2} - x)$ with $x_{Mn} = 0.138$ and $x_{Si} = 0.814$, respectively. The chemical unit cell of MnSi is shown in Fig. 5.1.
MnSi is an itinerant-electron helimagnet with the ordering temperature T_c of 29.5 K and an ordered magnetic moment of 0.4 μ_B on each Mn atom. In absence of external magnetic fields the magnetic structure is a left-handed long-period ferromagnetic spiral with the propagation vector $\boldsymbol{k} = [\zeta, \zeta\, \zeta]$ with $\zeta = 0.016$ resulting in a period of approximately 180 Å as has been shown by means of polarised neutron scattering [SCM+83, IEM+85]. Bak and Jensen [BJ80] have shown theoretically that the magnetic helix in MnSi can be explained in terms of the Dzyaloshinsky-Moriya interaction (s. section 1.2.2 for a complete derivation). The handedness of the spiral is fixed to be left-handed due to the left-handed arrangement of the atoms in the chemical structure [IEM+85]. As we have already demonstrated in 3.3.1 the symmetry operators contained in the point group of MnSi (23) generate four configuration domains from the magnetic propagation vector $\boldsymbol{k}$ (s. also table 3.1) and therefore helices propagating parallel to all four cubic diagonal [111] directions are observed.
Alltogether the magnetic ground state of MnSi is a result of the complex interplay between three competing magnetic energy scales:

- On the largest energy scale, the ferromagnetic exchange interaction between the Mn ions leads to the ordered magnetic moment of 0.4 μ_B and favours parallel arrangement of neighbouring magnetic moments.

- The lack of inversion symmetry in MnSi allows for the weak antisymmetric DMI.

Thus, on the intermediate energy scale the DMI leads to mutually canted neighbouring spins (s. section 1.2 and Eq. 1.4). The interplay of the ferromagnetic exchange interaction and the DMI drive the formation of the observed magnetic spiral.

- The lowest magnetic energy scale is represented by crystal field interactions. They lead to cubic magnetic anisotropy that locks the propagation direction of the helix parallel to the [111] directions.

The described energy scales can be identified qualitatively with the phase boundaries in the magnetic phase diagram that is shown in Fig. 5.2 as a function of external magnetic field H and temperature T at ambient pressure. Below T_c and below external magnetic fields of $H_{c1} \approx 80$ mT the magnetic spirals are locked along the [111] directions. Above the critical field H_{c1} the helix is transformed in a conical helix that tends to orient its propagation direction $\boldsymbol{k}$ parallel to the field direction as shown by Ishikawa *et al.*[ITBR76]. With increasing magnetic field the helices align more and more with the direction of the applied magnetic field and a magnetic state with only one of the four configuration domains is generated. Simultaneously the cone angle α decreases and becomes zero at $H_{c2} = 600$ mT. Above H_{c2} the helical structure has transformed into a ferromagnetic arrangement of the spins with a spontaneous moment of of 0.4 μ_B per Mn ion. We note that the period of the helix only varies slightly below magnetic field H_{c2}.
An additional magnetic phase develops as pocket inside the conical helical phase slightly below T_c. The intensity of the Bragg reflections of helices oriented parallel to the applied field strongly decreases in a narrow range 130 mT < H < 200 mT, which is assumed to be caused by a rotation of the propagation vector perpendicular to the field [IA84, GMO$^+$06b, GMO$^+$07]. Moreover, a signature of this phase was observed in magnetic susceptibility measurements [TPSF97]. This magnetic phase is called A-phase and will not be considered further in this work.

5.1.2 Non-Fermi-liquid phase and partial magnetic order

At ambient pressure and low temperature MnSi is well described as a weakly ferromagnetic Fermi liquid (FL) [LT85, Mor85]. The magnetic transition temperature T_c to the helical ordered phase decreases by application of hydrostatic pressure and vanishes at a critical pressure $p_c = 14.6$ kbar as demonstrated in the phase diagram in Fig. 5.3(a). The suppression of the helical magnetic order may is of first order as suggested by ac susceptibility data[PMJL97]. The resistivity shows a sharp dip at the same pressure p_c from a FL temperature dependence T^α with $\alpha \approx 2$ to a non-FL (NFL) [Sch99] dependence with $\alpha \approx 3/2$. The NFL behaviour is observed over a temperature range of three orders of magnitude from a few mK to a crossover temperature of approximately 12 K (compare T_{TE} in Fig. 5.3(a) and α in Fig. 5.3(b)) [PJL01, DLWT$^+$].
In addition magnetic scattering intensity distributed over the surface of a sphere in reciprocal space with a radius k = 0.038 Å was observed by neutron scattering experiments even above p_c [PRP$^+$04]. This radius corresponds to the periodicity of the magnetic helix

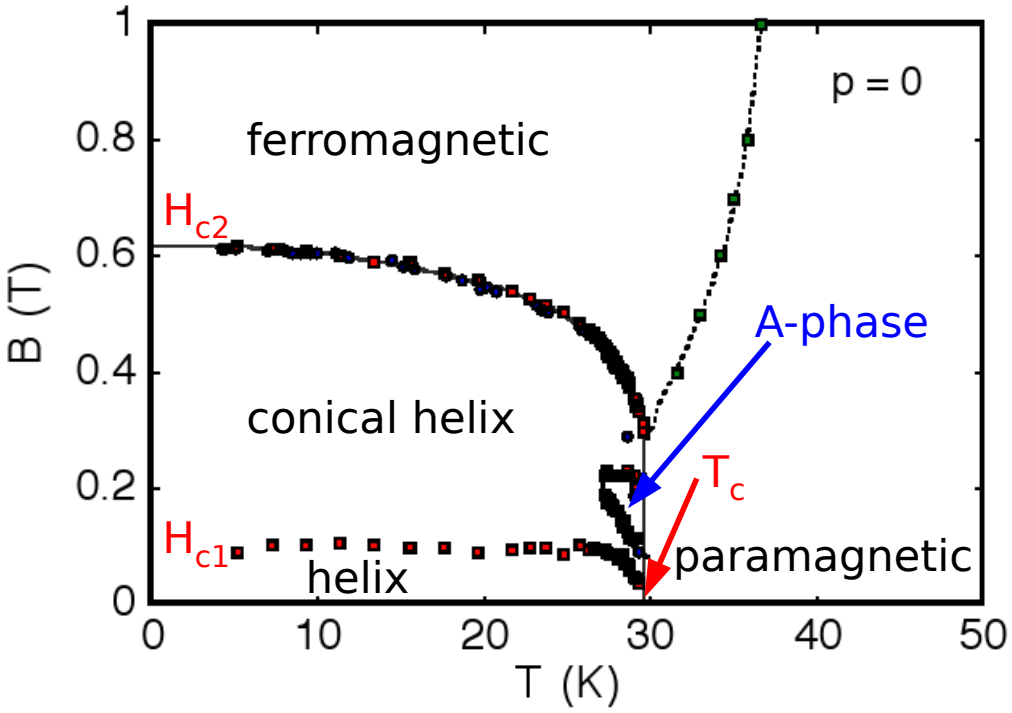

Figure 5.2: The graph shows the phase diagram of MnSi as a function of external magnetic field H and temperature T at ambient pressure.

that exist below p_c as shown in the left and right view graphs of Fig. 5.3(a). The intensity distribution with a broad maximum at [110] suggests that the direction of the helix that is fixed by crystal field interactions below p_c is unlocked above p_c. The intensity pattern is usually referred to as *partial magnetic order* due to its similarity to scattering patterns observed in liquid crystals. As the partial magnetic order appears at the same pressure p_c, where the FL phase of MnSi vanishes, the depinning of the helical order may be seen as a good candidate to drive the FL to NFL transition. However, the partial magnetic order is not observed for the complete NFL temperature range but only below a crossover temperature T_0 that vanishes at the pressure $p_0 \approx 21$ kbar. We note that the anomalies associated with T_0 are not seen in the resistivity and susceptibility and hence the partial magnetic order may fluctuate on time scales relevant for transport measurements. For an interpretation of the appearance of the observed neutron intensity pattern in the partial magnetic order phase, it has been speculated about several candidates for the magnetic structure:

1. The partial order consists of distinct regions with helices propagating in distinct directions that are independent from each other (similar to blue phases in liquid crystals, cf. [TBK06]).

2. Topological defects such as domains or vortex lattices (compare e.g. [BH94, RBP06]).
3. Spin crystals that are linear superpositions of spin spirals with different wave vectors [BVA06].
4. The helices remain intact, but meander through the crystal without being restricted to a specific direction [RBP06].

In recent μSR measurements performed by Uemera *et al.* [UGGM$^+$07] no magnetic signal was observed above p_c. This suggests that the partial order below T_0 is not static on the slower timescales probed by the muon and hence is dynamic on a time scale between 10^{-10} to 10^{-11} s. Further, the μSR data yield that the helical order below p_c occurs in a decreasing volume fraction for $T_c \rightarrow 0$ (s. Fig. 5.3(c) and dark blue shaded area in Fig. 5.3(a)). The abrupt drop at p_c of the zero field moun spin precession frequency shown in Fig. 5.3(c) additionally supports that the magnetic phase transition at p_c is first order. The combined results of decreasing volume fraction and the fluctuating partial magnetic order have been interpreted as metastable droplets of helimagnetic order of several 1000 Å diameter that form within a paramagnetic sea as remains of the first order transition.
A key question that has been discussed extensively until recently is whether the transition from the FL to the NFL regime is driven by a quantum critical point (QCP). For a three-dimensional metal like MnSi the breakdown of Fermi liquid theory is generally only expected at QCPs [Sch99]. A QCP is defined as zero-temperature second-order phase transition that is controlled by a nonthermal order parameter such as magnetic field or hydrostatic pressure. Since $T_c \longrightarrow 0$ at p_c it has been initially argued that the phase transition is only weakly first order and therefore has been been explained in terms of a ferromagnetic quantum critical point (QCP) [PMJL97] leading to the observed NFL behaviour in the resistivity. However, this explanation is contradicted by

- the previously mentioned signatures of a first order transition in the ac-susceptibility and μSR experiments .
- the fact that ferromagnetic exchange is only the strongest of the three magnetic energy scales present in MnSi. The existence of partial magnetic order clearly suggests that only the weakest energy scale, namely the cubic anisotropy energy is suppressed.

Pfleiderer *et al.* [PBK$^+$07] recently performed measurements of the thermal expansion in MnSi under pressure by means of Larmor diffraction. The thermal expansion is the conjugate variable to the control parameter pressure that is used to tune the system across the phase transition in question. Hence, it provides a unique handle to investigate the nature of the FL to NFL phase transition. Their results show no singularity of the thermal expansion at p_c and therefore demonstrate that the transition cannot be explained by a QCP. They also obtained similar results for the transition at p_0. This suggest that the NFL phase is rather a novel metallic state far from quantum criticality.

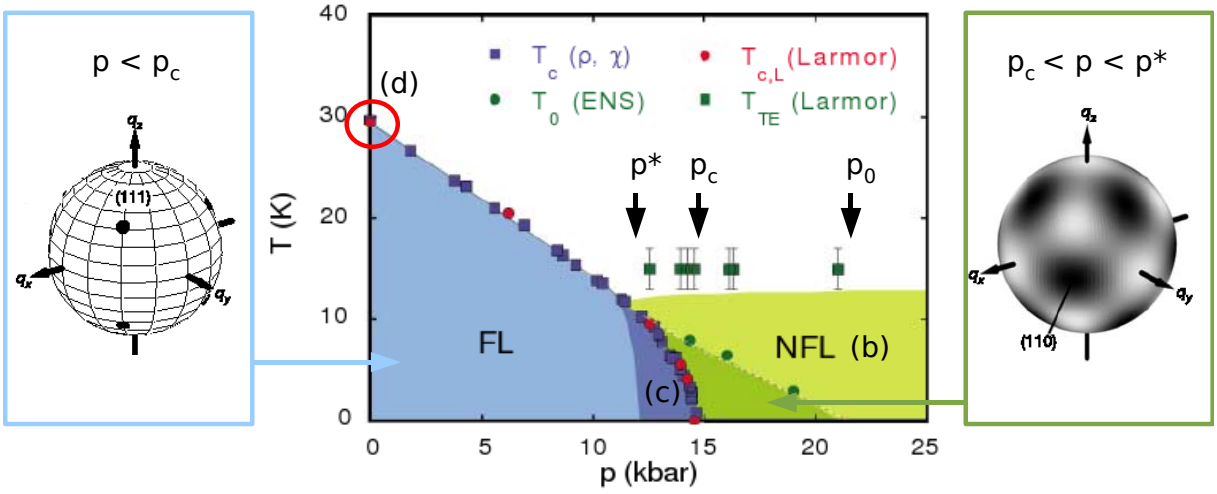

(a)

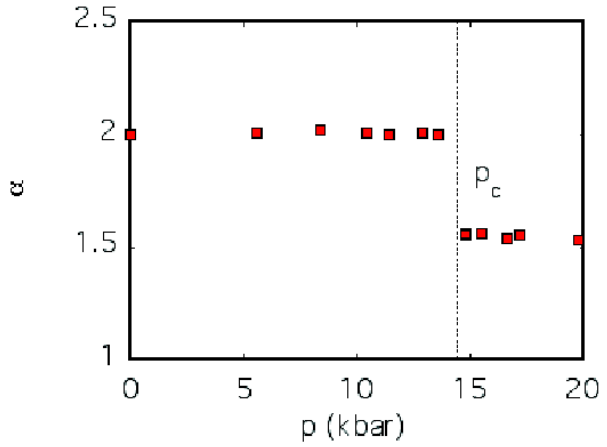

(b)

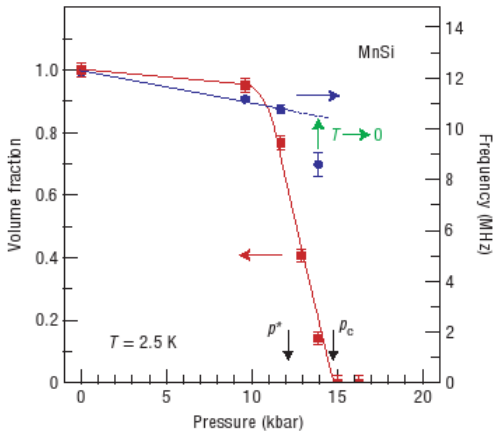

(c)

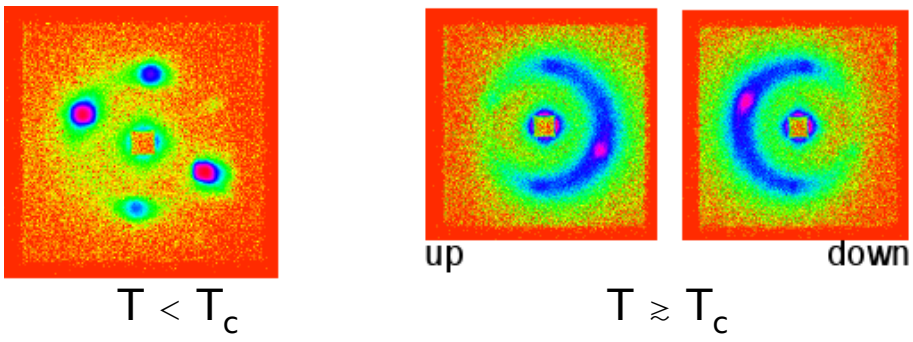

(d)

Figure 5.3: (a) Phase diagram of MnSi as a function of pressure is shown. The blue and green shaded areas represent the FL and NFL phases. The insets show the distribution of the magnetic neutron scattering intensity of the helically ordered magnetic phase below p_c (blue) and in the partial ordered phase between p_c and p_0 (green), respectively [PRP+04]. The consequent subfigures highlight the experimental findings summarised in the phase diagram. (b) The exponent α of the resistivity $\varrho(T) = AT^{\alpha}$ is shown as a function of pressure [PJL01]. (c) Volume fraction of the helical magnetic phase and zero field moun spin precession frequency as observed in μSR [UGGM+07]. (d) Distribution of magnetic neutron scattering intensity as observed by SANS at ambient pressure for $T < T_c$ and for $T \gtrsim T_c$, respectively. The position of the experiment is marked by the red circle in (a).

Finally small angle neutron scattering (SANS) results obtained under pressure and magnetic field show hysteresis effects in the magnetic scattering intensity. The observed hysteresis excludes the assumption of metastable magnet droplets as remains of the first order transition at p_c in the partial ordered phase and favours that the system is actively driven away from the helical ordered state above p_c [PRPH07]. However, the nature of the driving mechanism was not yet identified.

5.1.3 Possible intermediate phase and specific heat

A further experimental result that currently attracts a lot of interest is that in SANS measurements performed at ambient pressure a sphere of magnetic intensity is observed at $T \gtrsim T_c$ [GBL$^+$04, GMO$^+$05, Lam06] (s. Fig. 5.3(d)). The sphere is observed as a ring in the SANS measurement since only a single two-dimensional cut through reciprocal space can be observed at a time. Therefore, we will often also refer to the observed scattering as ring of magnetic intensity in the following. Again the radius of the sphere in reciprocal space corresponds to the periodicity of the helix below T_c and may be interpreted as the unpinning of the propagation vector of the helix similar to the partial magnetic order above p_c. The ring of intensity has been interpreted in different ways by different authors. Grigoriev *et al.* have discussed their SANS results in terms of paramagnetic critical fluctuations that appear at T_c [GMO$^+$05]. In contrast Lamago *et al.* [LGB05] observed a peak in the specific heat at 28.5 K with a change of slope in the wing of the peak at 28.8 K. Additionally they observed a kink in the integrated magnetic neutron intensity data at the same temperature of 28.8 K. They suggested that the observed ring of magnetic intensity may be due to an intermediate phase between the helical magnetic phase and the paramagnetic phase.
In Fig. 5.4 we show the specific heat data for MnSi from 2 K to 35 K as measured by Pfleiderer [Pfl06]. It shows two significant features around 30 K: (i) a Lambda-shaped peak at $T_{c1} = 29$ K that can be associated with the breakdown of the helical magnetic order (ii) a shoulder to the peak. We define $T_{c2} = 30.4$ K via the entropy conserving construction shown in the inset of Fig. 5.4. In the two lower view graphs we summarise again the results from small angle neutron scattering on MnSi for the helical magnetic phase and the possible intermediate phase for $T_{c1} < T < T_{c2}$.
In order to clarify whether such an intermediate magnetic phase may exist in MnSi several issues need to be investigated experimentally.

- If an intermediate magnetic phase exists we should be able to distinguish the associated magnetic structure experimentally. As we have seen in chapter 2 spherical neutron polarimetry is suitable to examine this question. However, we note that the observed magnetic intensity pattern may simply be interpreted as different regions in the crystal persisting with helices propagating in distinct directions as shown in the lower right viewgraph of Fig. 5.4.
- The exact structure of the sphere of scattering was not reported so far. It is unknown

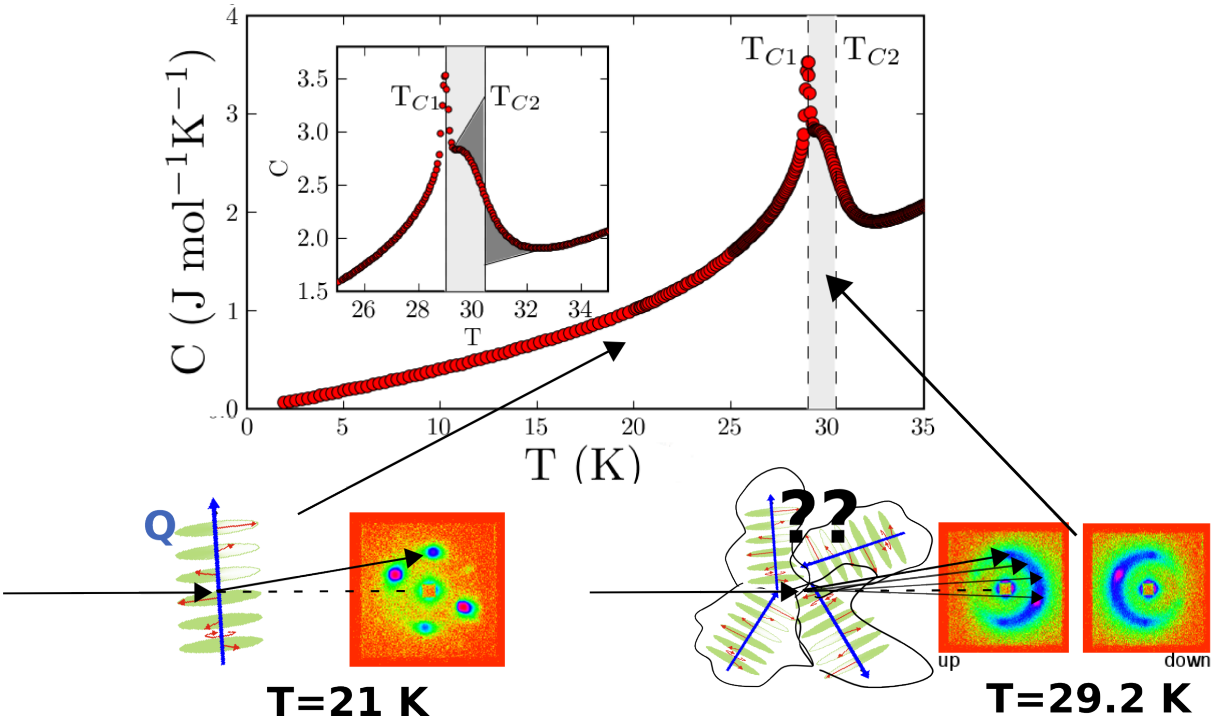

Figure 5.4: The specific heat for MnSi is shown for 2-35 K. It shows two significant features around 30 K: (i) a Lambda-shaped peak at $T_{c1} = 29$ K that can be associated with the breakdown of the helical magnetic order (ii) a shoulder to the peak. We can define $T_{c2} = 30.4$ K via the entropy conserving construction shown in the inset. The two lower view graphs show the results from small angle neutron scattering on MnSi below T_{c1} (left) and for $T_{c1} < T < T_{c2}$ (right). The ring-shaped magnetic intensity for the second case may be interpreted as the unlocking of the magnetic propagation vector of the helix as denoted by the distinct magnetic helices.

whether the magnetic intensity forms an isotropic sphere or if there are maxima of scattering on the sphere equivalent as for the partial magnetic order above p_c.

- Finally one may speculate that the partial magnetic order above p_c and the possible intermediate phase are not independent from each other. The intermediate phase could be imagined to be present along the whole phase transition line of T_c for all pressures up to p_C and to emerge into the partial magnetic order.

The possible existence of an intermediate phase also triggered theoretical efforts to explain the sphere of magnetic intensity that will be review in the theoretical section 5.2.

5.1.4 Magnetic excitations

The magnetic properties of 3d weak itinerant ferromagnets are governed by the conduction electrons. Hence, the magnetism in these compounds has to be described within

a band theory as opposed to insulating ferromagnets, where the magnetic properties are determined by local magnetic moments due to localised electrons that are treated within a Heisenberg model. Originally the difference between itinerant and local moment magnetism has been discussed quite controversially. The first model for itinerant ferromagnetism, namely the Stoner model [Sto38], was successful in the prediction of the saturation magnetisation per atom of ferromagnetic 3d metals like Fe, Co and Ni. However, it failed to explain the observed Curie-Weiss (CW) magnetic susceptibility above T_C that is observed in almost all ferromagnets. Moreover the predicted Curie temperatures were too high compared with the experimental values. Similar observations were made for $ZrZn_2$ and Sc_3In that were identified as weakly ferromagnetic metals[MB58, MCW$^+$61]. On the one hand they possess very low Curie temperatures (25 K and 6 K) and small magnetisations (0.12 μ_B and 0.04 μ_B per atom) which clearly excludes local magnetic moments, however, on the other hand the observed magnetic susceptibilities above T_c exactly obeyed the CW law for $T_c < T < 10T_c$ which could not be explained by the Stoner model. Additionally, the effective moments derived from the Curie constant by assuming the existence of local moments are much larger than those of the spontaneous moments. This discrepancy of the Stoner model in explaining the high temperature properties of itinerant magnets can be qualitatively understood by taking into account its magnetic excitations. In the Stoner theory of band magnetism the thermal excitations are spin flip excitations of single electrons across the Fermi surface or equivalently excitations of electron-hole pairs with opposite spins that move independently through the common mean field. Hence, only small spin density fluctuations are generated by thermal smearing out of the Fermi level and the high temperature magnetic properties derived from this model are inherently underestimated (s. e.g. [Mor85]).
The inability of band theory to describe the high temperature magnetic properties of 3d ferromagnetic metals was overcome by Moriya and Kawabata [Mor85] by means of their self-consistent renormalisation (SCR) theory. In addition to the single electron excitations of the Stoner theory they also considered mutually coupled modes of exchange enhanced spin flip fluctuations in a self-consistent way. Here the self-consistency indicates that the renormalisation of the thermal equilibrium state due to the presence of fluctuations is taken into account, which consequently also influences the excitation spectrum. For a complete review of this topic we refer to the book of Moriya [Mor85].
Historically, MnSi played a prominent role in the development of SCR theory for weak itinerant ferromagnets as it was the first compound for that the theory could be employed successfully. In spite of its helical magnetic structure in the absence of external magnetic fields MnSi is widely regarded as weak itinerant ferromagnet. This is (i) due to the spontaneous magnetic moment of 0.4 μ_B that is considerably smaller compared to the effective paramagnetic moment of 2.2 μ_B estimated from the CW law of the susceptibility in the paramagnetic regime [LLS72] and (ii) due to the fact that MnSi is ferromagnetic for external fields larger than 0.6 T. SCR theory predicts three types of magnetic excitations that are characteristic for a weak itinerant ferromagnet. For MnSi all of them were identified by Ishikawa *et al.* by means of inelastic neutron scattering experiments that were carried out in the ferromagnetic or paramagnetic phase:

- Single particle spin flip excitations in the so-called Stoner continuum are observed above the Stoner boundary that was found to be $E_{SB} = 2.6$ meV for MnSi. The excitations in the Stoner continuum are only weakly temperature dependent [ISTK77].
- Collective spin-waves with the dispersion $\epsilon = Dq^2 + \Delta$ ($D = 23.5$ meVÅ^2, $\Delta = 0.2$ meV) are present in the ferromagnetic phase below E_{SB} and merge tangentially into the Stoner continuum. They renormalise with increasing temperature and collapse into critical scattering above T_c at approximately 30 K [ISTK77, TBE$^+$98, SBE$^+$99].
- Low-energy paramagnetic excitations (critical scattering) with a unique q dependence of the linewidth $\Gamma(q)$ were identified. This linewidth is given by

$$\Gamma(q) = \frac{Cq}{\chi(q)} = \frac{Cq\{[\kappa(T)]^2 + q^2\}}{\chi_0}, \tag{5.1}$$

  which is different from the usual linewidth of critical scattering for local moment Heisenberg magnets that is described by a q^2-dependence with $\Gamma(q) = \frac{Cq^2}{\chi(q)}$[INFS82, INU$^+$85]. In both cases the magnetic coherence length is given by $[\kappa(T)]^2 = \kappa_0^2(T - T_c)$.

The different contributions to excitation spectrum are illustrated in Fig. 5.5.
We emphasise that despite the success of the SCR to describe the magnetic excitations in the ferromagnetic and paramagnetic phase and also the basic magnetic properties (e.g. T_c, CW susceptibility) of MnSi, it fails to reproduce the complex and non-understood magnetic phases and transport properties, that were described in the previous section. This is quite natural as SCR theory was proposed to explain the properties of weak ferromagnets and therefore ommits the Dzyaloshinsky-Moriya interaction. However, the unconventional magnetic and transport properties of MnSi are observed in regimes were MnSi is influenced by the Dzyaloshinsky-Moriya interaction and should be rather treated as a helimagnet. This is supported by the experimental work of different authors who demonstrated the existence of chiral magnetic correlations in the magnetic excitation spectrum by means of polarised neutron scattering. Shirane *et al.* reported that the lack of inversion symmetry in MnSi not only leads to a helical magnetic structure in zero external field but additionally to a chirality in the magnetic excitation spectrum in the ferromagnetic phase [SCM$^+$83]. Moreover, Roessli *et al* observed critical chiral magnetic fluctuations above T_c in the paramagnetic phase [RBFE02]. The maxima of the critical scattering lie on a sphere with a radius that corresponds to the pitch of the magnetic helix in the helimagnetic phase.
The presence of chiral fluctuation even outside the helical magnetic phase suggest that the magnetic chirality in MnSi is a key feature in order to understand its complex properties. However, to the best of our knowledge no detailed study of the excitations in the helical magnetic phase have been reported so far. In contrast to the experimental situation two theory groups have independently developed models for the a novel kind of excitation spectrum for the helical phase of MnSi that take into account the Dzyaloshinsky-Moriya interaction [BKR07, Mal06]. They will be reviewed in the next section.

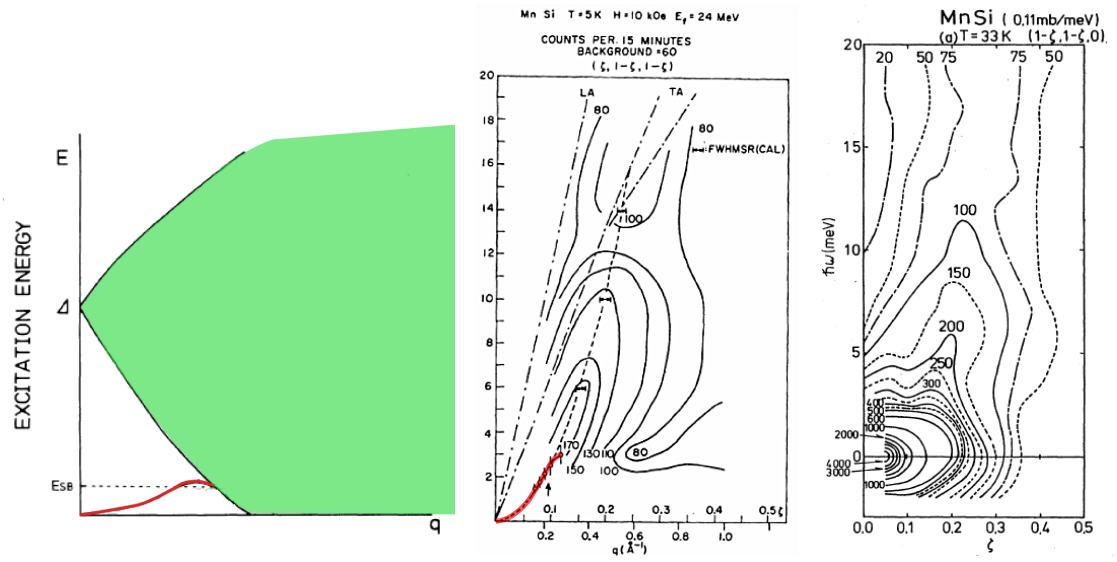

(a) (b) (c)

Figure 5.5: (a) A schematic view of the spin wave excitation (red) and the Stoner continuum (green) in MnSi is given (The figure is adapted from reference [ISTK77]) (b) The magnetic excitation spectrum of MnSi in the ferromagnetic phase at T = 5 K and H = 1 T as reported by Ishikawa *et al.* [ISTK77] is shown. The solid lines are contour lines with equal intensities. The red line denotes the collective spin wave excitation. (c) The critical scattering at T = 33 K is shown. The figure is taken from reference [INU+85].

5.2 Theoretical models

Before we will review our experiment results we would like to introduce the theories that are relevant for our work. The section is organised in three parts. In the first part new models that have been proposed to explain the existence of the possible intermediate magnetic phase are introduced. This is followed by section that describes a theory which explains the sphere-shaped magnetic intensity above T_c as paramagnetic critical scattering in a helimagnet. In the last part we present the models that cope with the magnetic excitation spectrum in the helical magnetic phase.

5.2.1 Intermediate magnetic phase and skyrmions

Due to former theoretical studies [WM89, BH94] it was commonly believed that only one-dimensional helical modulation as those shown in Fig. 5.6(a) may form spontaneous ground states in condensed matter systems. However, Rößler [RBP06] *et al.* showed by means of a phenomenological model that soft longitudinal magnetic fluctuations may stabilise multi-dimensional twisted modulations as well. They calculated the position

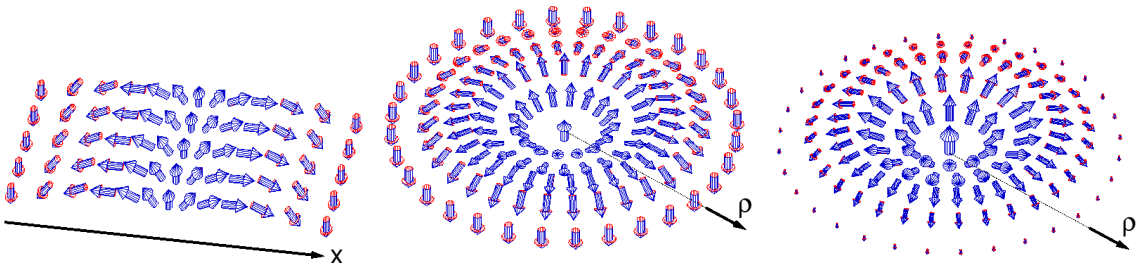

(a) (b) (c)

Figure 5.6: (a) A one-dimensional magnetic helix propagating along the x-direction with a constant magnitude m of the magnetic moments is shown. (b) A so called skyrmion structure is shown. For such a magnetic structure the propagation axis is not fixed in one direction but the structure is helical modulated radially in all directions from the centre. (c) The presented structure is similar to the skyrmion in (b) with the difference that additionally the amplitude m of the magnetic moment is allowed to vary. m has a maximum at the centre and decreases with increasing distance. All pictures are taken from reference [RBP06].

dependent energy density for several two-dimensional chiral structures (s. Fig. 5.6) and compared the results to a normal one-dimensional helix.
For the one-dimensional helix the energy density is a constant and independent of the position as shown in Fig. 5.7(a). Fig. 5.6(b) shows a two-dimensional magnetic structure where a helical modulation propagates circularly in all directions ϱ of a cylinder from the centre. Such a structure is called a *skyrmion*. The energy density of the skyrmion is no longer uniform and lower in the centre compared to the helical state. However, at a distance of the order of the pitch of the helix the energy density excess outweighs the initial reduction (s. Fig. 5.7(a)). Therefore, these kinds of skyrmion textures are not expected to form a spontaneous magnetic groundstate. However, if the amplitude of the magnetic moments in the skyrmion structure is allowed to vary as a function of the distance ϱ from the centre (5.6(c)), the energy density is lower with respect to the one-dimensional helix for all distances (cf. Fig. 5.7(a)) and a spontaneous skyrmion ground state can be realised. The temperature interval in which a magnetic skyrmion lattice may form is determined the longitudinal stiffness η of the magnetisation. If η is reduced from 1 ($\eta = 1 \Longrightarrow$ amplitude is not allowed to vary) the skyrmion phase is expected to be stable over a finite temperature range between the helix phase and the paramagnetic phase (see Fig. 5.7(b)).
In the electronic supplement to reference [RBP06] η is estimated to be $\eta \approx 0.4$ from experimental parameters to the theory. This implies a temperature range of $\approx 1K$ for the skyrmion phase which is consistent with the temperature interval of the shoulder appearing in the specific heat (compare 5.1.3). However, we emphasise that the model presented by Rößler et al. is for two-dimensional structures only. Yet, Fischer *et al.* [FSR08] proposed a three-dimensional magnetic structure that is formed by cylinders of skyrmions as illustrated in Fig. 5.8. This model also allows for an intermediate magnetic phase.

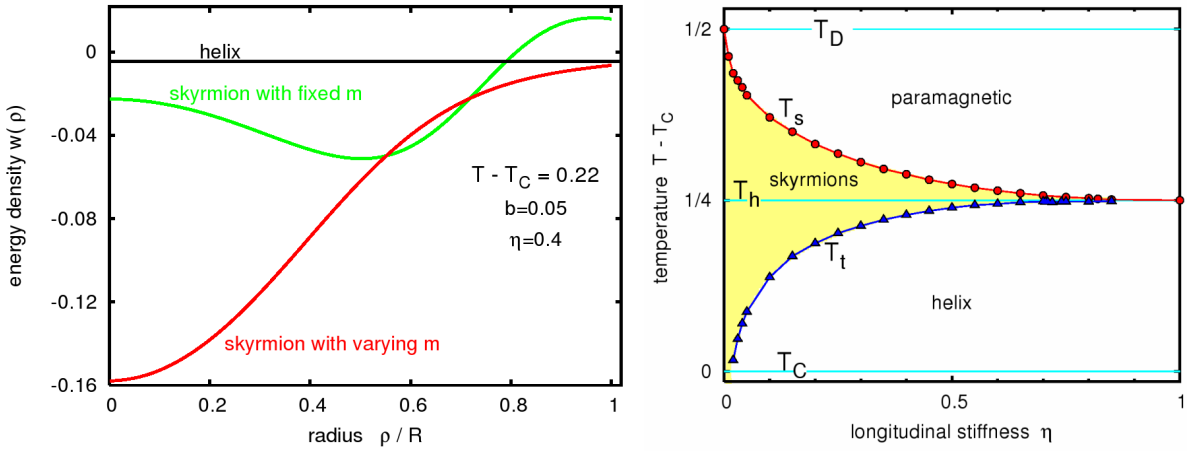

(a) (b)

Figure 5.7: (a) Comparison of the local energy densities for the one-dimensional helix and two-dimensional skyrmions with fixed and varying amplitudes of magnetisation [RBP06]. ϱ is the distance from the centre of the structure and R is the pitch of the helical structure in real space. (b) Phase diagram as a function of longitudinal moment stiffness η for a chiral magnet. The skyrmion phase is stable between two temperatures T_t and T_s that depend on η. Below T_D a double twisted texture is able to form, and below T_h a one-dimensional helix is stable [RBP06].

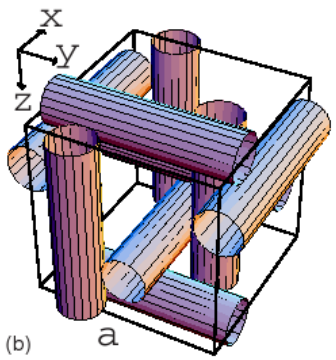

Figure 5.8: A three-dimensional magnetic structure constructed from skyrmions is illustrated. Each of the cylinders represents two-dimensional skyrmions (cf. Fig.5.6(c)). The skyrmions are stacked along the cylinder axis, i.e. the magnetic moments do not change when moving parallel to the cylinder axis.

5.2.2 Critical scattering above T_c

Maleyev *et al.* developed a mean-field model that explains the appearance of the sphere-shaped magnetic intensity above T_c by means of paramagnetic critical scattering [GMO+05]. Based on the Bak-Jensen model (cf. section 1.2.2) they derived the following expression

for the free energy of MnSi above T_c:

$$F(\boldsymbol{q}) = \sum_{\alpha,\beta} \left(\frac{A}{2}(q^2 + \kappa_0^2)\delta_{\alpha\beta} + iD\epsilon_{\alpha\beta\gamma}q_\gamma \right) S^\alpha_{\boldsymbol{q}} S^\beta_{-\boldsymbol{q}} + \frac{B_2}{2}\left(q_x^2|S^x_{\boldsymbol{q}}|^2 + q_y^2|S^y_{\boldsymbol{q}}|^2 + q_z^2|S^z_{\boldsymbol{q}}|^2 \right). \tag{5.2}$$

Here $\boldsymbol{q}$ is the reduced wave vector measured from the neighbouring reciprocal lattice vector. Additionally the non-renormalised inverse correlation length $\kappa_0^2 = C(T - T_{c0})$[1] was introduced according to mean-field theory. Further the indices $\alpha, \beta = x, y, z$ denote the components of the Fourier transform of the magnetic order parameter $\boldsymbol{S_q}$. We remind that A, D and B_2 are associated with the strength of the ferromagnetic exchange, the DMI and the cubic anisotropy, respectively. A is also called the spin wave stiffness constant. Using Eq. 5.2 the magnetic susceptibility tensor can be derived via $\chi^{-1}_{\alpha\beta}(\boldsymbol{q}) = \frac{\partial^2 F}{\partial S^\alpha_{\boldsymbol{q}} \partial S^\beta_{-\boldsymbol{q}}}$ (s. e.g. [CL95]). After several approximations (s. reference [GMO+05] for the complete derivation) the authors obtain the final expression for the susceptibility tensor as

$$\begin{aligned} \chi_{\alpha\beta} &= \frac{T}{AZ}\left((q^2 + \kappa^2 + k^2)\delta_{\alpha\beta} - 2i\frac{|D|}{D}kq_\gamma\epsilon_{\alpha\beta\gamma} - \frac{(2qk)^2}{q^2 + \kappa^2 + k^2}\hat{q}_\alpha\hat{q}_\beta \right), \\ Z &= [(q+k)^2 + \kappa^2]\left[(q-k)^2 + \kappa^2 + \frac{k^2|B_2|}{2A}\left(\{\hat{q}^4\} - \frac{1}{3} \right) \right]. \end{aligned} \tag{5.3}$$

Here $k = \frac{2\pi}{d} = \frac{|D|}{A}$ and d is the pitch of magnetic spiral below T_c. The renormalised inverse correlation length is defined by $\kappa^2 = \kappa_0^2 - k^2 = C(T - T_{c1})$. The expression $\{\hat{q}^4\} = \hat{q}_x^4 + \hat{q}_y^4 + \hat{q}_z^4$ is a cubic invariant that has a maximum for 1/3 in the case of MnSi and locks the helix propagation direction along the diagonals of the cubic unit cell if $B_2 > 0$.

From the magnetic susceptibility in Eq. 5.3 the magnetic scattering cross-section for the critical scattering above T_c can be derived as shown in the appendix C. Here we only provide the final result [GMO+05]:

$$\frac{d\sigma}{d\Omega} = 2\frac{(\gamma r_0 F_{Mn}(\boldsymbol{Q}))^2 T}{A\left((q+k)^2 + \kappa^2\right)} \cdot \frac{k^2 + q^2 + \kappa^2 - 2k\boldsymbol{q}\cdot\boldsymbol{P}_0}{(q-k)^2 + \kappa^2 + (\frac{|B_2|k^2}{2A})(\hat{q}_x^4 + \hat{q}_y^4 + \hat{q}_z^4 - 1/3)}. \tag{5.4}$$

Here $F_{Mn}(\boldsymbol{Q})$ is the magnetic form factor of the Mn ions (compare section 2.3.3). We note that this expression for the critical scattering depends on the initial polarisation vector $\boldsymbol{P}_0$ due to the DMI. Eq. 5.4 leads to a sphere of magnetic scattering with the radius k in reciprocal space and reproduces the data of Grigoriev *et al.* well.

For our measurements it is additionally important to consider how the polarisation vector of the neutrons scattered by paramagnetic critical fluctuations is changed. The expression for the final polarisation vector due to the critical scattering is also derived in appendix

[1] Here T_{c0} and T_{c1} (s. later in the text) are not necessarily connected to T_{c1} and T_{c2} that we have defined in section 5.1.3 from the specific heat. In reference [GMO+05] no statement is made about the exact meaning of the two temperatures!

C and is given by

$$\boldsymbol{P'} = \frac{\{2(q^2+\kappa^2+k^2)[(\delta_{\alpha\beta}-\hat{q}_\alpha\hat{q}_\beta)-1]\cdot\boldsymbol{P}_0+4k\boldsymbol{q}\}}{2(k^2+q^2+\kappa^2)-4k\boldsymbol{q}\cdot\boldsymbol{P}_0} \tag{5.5}$$

5.2.3 Goldstone modes in the helical phase

In 2006 the group of Belitz *et al.*[BKR07] and Maleyev[Mal06] independently developed theoretical models for the magnetic excitation spectrum in the helically ordered magnetic phase below T_c. We will introduce them here in separate sections and will compare them afterwards.

5.2.3.1 The model of Belitz

The theory of Belitz *et al.* [BKR07] was motivated by the strange properties of MnSi, e.g. the temperature dependence of the specific heat near T_C (compare section 5.1.3) and the NFL behaviour above p_c that is not observed in other metallic low-temperature magnets. The authors argue that the only significant difference between these other materials and MnSi is the existence of the DMI in the latter. They concluded that it is natural to assume that the exotic transport properties of MnSi are related to the helical order in MnSi.
In ferromagnetic metals (e.g. Fe, Ni) the spontaneous breaking of rotational symmetry in spin space leads to massless soft modes according to Goldstone's theorem. The soft modes are propagating ferromagnetic magnons with a dispersion relation $\omega(\boldsymbol{q}) \propto \boldsymbol{q}^2$. Is the rotational symmetry additionally broken explicitly due to external magnetic fields or due to spin-orbit coupling of the electronic spin to the underlying lattice the Goldstone modes additionally obtain a mass that corresponds to a gap of the excitation at $\boldsymbol{q} = 0$. In systems where the lattice possesses no inversion symmetry additional effects should be observed that are not related to the rotational symmetry of the spins. That is due to the DMI term $D\boldsymbol{M}(\nabla \times \boldsymbol{M})$ (cf. section 1.2.2) in the free energy that is invariant under simultaneous rotations of real space and $\boldsymbol{M}$ but breaks spatial inversion symmetry. Here $\boldsymbol{M}$ is the magnetisation. Belitz *et al.* predict a new helical Goldstone mode coupled to the emergence of the helical state which they call *helimagnon*, in analogy to ferromagnons and antiferromagnons.
In their paper Belitz *et al.* develop a theory for itinerant quantum helimagnets like MnSi based on Ginzburg-Landau theory that also permits to calculate other properties like transport properties or the specific heat as shown in reference [BKR06]. However, as a starting point they use a classical phenomenological Ginzburg-Landau theory in which they introduce the additional DMI term. We will briefly describe this approach as it is quite educational and refer to references [BKR07, BKR06] for the complete quantum-

mechanical derivation. The Hamiltonian they use for their model is given by

$$H = \frac{r}{2}\boldsymbol{M}^2(\boldsymbol{x}) + \frac{a}{2}[\boldsymbol{\nabla}\boldsymbol{M}(\boldsymbol{x})]^2 + \frac{D}{2}\boldsymbol{M}(\boldsymbol{x}) \cdot [\boldsymbol{\nabla} \times \boldsymbol{M}(\boldsymbol{x})] + \frac{u}{4}[\boldsymbol{M}^2(\boldsymbol{x})]^2 \tag{5.6}$$

and directly compares to the Bak-Jensen model (Eq. 1.5). As we have already seen in Eq. 1.7 a helical field configuration of the form

$$\boldsymbol{M}_{sp}(\boldsymbol{x}) = m_0(\cos kz, \sin kz, 0) \tag{5.7}$$

is the stable saddle-point solution of the corresponding action $S[\boldsymbol{M}] = \int d^3x H$. Here k is the pitch vector and the coordinate frame was chosen so that the helix propagates parallel to the z direction. This solution for the magnetisation breaks the translation symmetry of the lattice and leads to a new soft Goldstone mode that is called helimagnon.
As stated by Belitz an obvious guess for soft fluctuations about this saddle point associated with the soft mode are phase fluctuations of the form

$$\boldsymbol{M}(\boldsymbol{x}) = m_0(\cos(kz + \phi(\boldsymbol{x})), \sin(kz + \phi(\boldsymbol{x})), 0) \approx \boldsymbol{M}_{sp}(\boldsymbol{x}) + m_0\phi(\boldsymbol{x})(-\sin kz, \cos kz, 0), \tag{5.8}$$

where an expansion in $\phi(\boldsymbol{x})$ has been performed and only terms up to first order are taken into account. By substituting this epression in Eq. 5.6 one obtains for the kinetic energy of the mode $H_{fluct} = const \times \int d^3x[\boldsymbol{\nabla}\phi(\boldsymbol{x})]^2$. However, they also demonstrate that this solution can not be correct, by considering a simple rotation of the planes containing the spins perpendicular to the propagation vector, (α_1, α_2, k), which corresponds the the phase fluctuation $\phi(\boldsymbol{x}) = \alpha_1 x + \alpha_2 y$. This rotation should not cost any energy because a rotation of the spiral does not change its state due to the incommensurability of the spiral with respect to the underlying chemical lattice. But the evaluation of H_{fluct} yields $[\boldsymbol{\nabla}\phi(\boldsymbol{x})]^2 = \alpha_1^2 + \alpha_2^2 > 0$. This is due to the dependence of H_{fluct} on $\boldsymbol{\nabla}_\perp\phi$, with $\boldsymbol{\nabla} = (\boldsymbol{\nabla}_\perp, \partial_z)$. Belitz *et al.* proposed that the proper solution is obtained if the soft mode is a generalised phase $u(\boldsymbol{x})$ of the form $u(\boldsymbol{x}) = \phi(\boldsymbol{x}) + \boldsymbol{\nabla}_\perp\varphi(\boldsymbol{x})$ that gives

$$H_{fluct} = \frac{1}{2}\int d^3x\{c_z[\partial_z u(\boldsymbol{x})]^2 + c_\perp[\boldsymbol{\nabla}_\perp^2 u(\boldsymbol{x})]^2/k^2\}, \tag{5.9}$$

where c_z and $c_\perp$ are elastic constants. The corresponding dispersion relation of the helimagnons derived by the authors is given by

$$\omega_0(\boldsymbol{q}) = \text{const} \cdot r_0^{1/2}\sqrt{c_z q_z^2 + c_\perp q_\perp^4/k^2}, \tag{5.10}$$

with r_0 being the Goldstone mass of the $\boldsymbol{q} = 0$ mode and the damping coefficient γ is given by $\gamma(\boldsymbol{q}) = r_0\Gamma q_z^2$. The Goldstone mode has an anisotropic dispersion relation with fluctuations that are softer in the direction perpendicular to the pitch vector. As demonstrated in Fig. 5.9, the longitudinal mode corresponds to an excitation that squeezes and relaxes the period of the helix locally. The transverse modes correspond to an excitation where the direction of the helix fluctuates. Therefore it is quite intuitive that the

transverse mode is softer as rotating the complete helix should cost less energy compared to squeezing it. [2]. Further it is interesting to note that magnons in ferromagnets have a quadratic dispersion in $\boldsymbol{q}$ whereas antiferromagnets have a linear dispersion. For the helimagnon the branch of the dispersion that is parallel to the magnetic propagation vector $\boldsymbol{k}$ therefore shows antiferromagnetic character whereas the branch parallel to $\boldsymbol{k}$ can be associated with ferromagnetic fluctuations. This is expected as spins that are situated in the planes that are perpendicular to the propagation direction $\boldsymbol{k}$ of the helix are indeed coupled ferromagnetically. In the direction parallel to $\boldsymbol{k}$ neighbouring spins are mutually rotated and form the magnetic helix which corresponds to rather antiferromagnetic coupling when modes with small wave vectors q are considered (corresponding to large distances in real space).
Finally the magnetic susceptibility associated with the helimagnons is also anisotropic and described by the transverse and the longitudinal components

$$\chi^{\perp}(\boldsymbol{q},\omega) \sim \frac{1}{\omega_0^2(\boldsymbol{q}) - \omega^2 - i\omega\gamma(\boldsymbol{q})} \tag{5.11}$$

$$\chi^{L}(\boldsymbol{q},\omega) \sim \frac{q_{\perp}^2}{\omega_0^2(\boldsymbol{q}) - \omega^2 - i\omega\gamma(\boldsymbol{q})}. \tag{5.12}$$

As we have seen in section 2.3.6 the imaginary part of the magnetic susceptibility can be

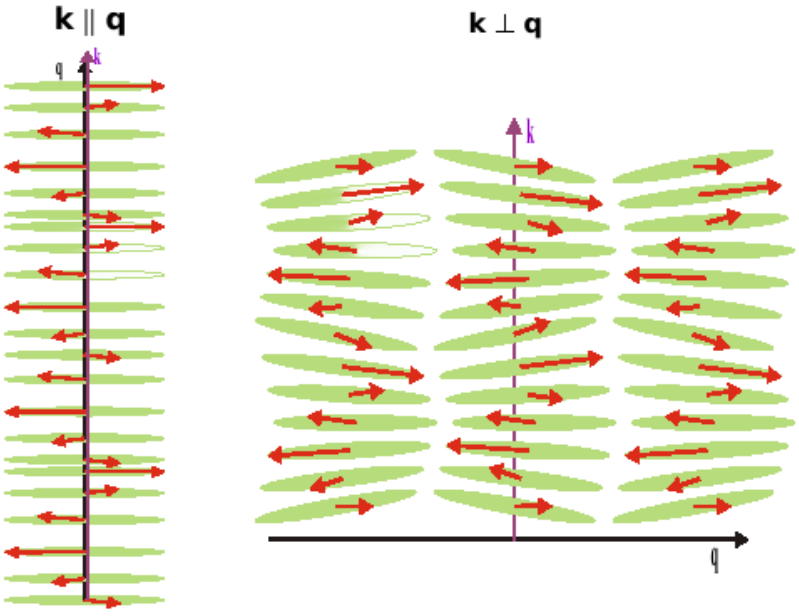

Figure 5.9: Left side: The longitudinal mode of a helimagnon that corresponds to a fluctuation of the *magnitude* of the propagation vector is demonstrated. Right side: The transverse mode of a helimagnon is shown. In this case the *direction* of the propagation vector is fluctuating.

[2] Compare this to a mechanical spring that you squeeze or rotate.

probed by magnetic neutron scattering and will allow us to verify the existence of the proposed helimagnons in our experiments.
One serious limitation of the Eqs. 5.10, 5.11 and 5.12 is that the model is only valid for $q < k$, which is a region that is experimentally difficult to access as we will see in the experimental section.

5.2.3.2 The model of Maleyev

Originally the theoretical model for the excitation spectrum in the helical phase by Maleyev [Mal06] was developed to explain the intensities of the magnetic satellite reflections in MnSi as a function of magnetic field that were observed in small angle neutron scattering experiments by Grigoriev [GMO$^+$06b, GMO$^+$06a]. The experimental data of Grigoriev *et al.*, especially the appearance of a second-order magnetic satellite peak at $2\boldsymbol{k}$ is well explained when a gap is introduced in the spin wave spectra. The gap stabilises the helices with respect to an external magnetic field that is applied perpendicular to the helix propagation direction $\boldsymbol{k}$. Maleyev finds that the gap originates microscopically due to the interaction between the spin waves and the small cubic anisotropy in MnSi. However, apart from the gap the proposed spin wave spectra are similar to the helimagnons that were proposed by Belitz *et al.* as they are also anisotropic.
Maleyev introduces a local three component spin operator $\boldsymbol{S_R}$ on each magnetic ion and derives the excitation spectrum in a linear spin-wave approximation. The following interactions are taken into account for the Hamiltonian of the spin system

$$
\begin{aligned}
H &= H_{EX} + H_{DM} + H_{AE} + H_D + H_Z && (5.13)\\
H_{EX} &= \frac{1}{2}\sum_{\boldsymbol{q}} J_{\boldsymbol{q}} \boldsymbol{S_q}\cdot\boldsymbol{S_{-q}}, && (5.14)\\
H_{DM} &= i\sum_{\boldsymbol{q}} D_{\boldsymbol{q}}\boldsymbol{q}\cdot[\boldsymbol{S_q}\times\boldsymbol{S_{-q}}], && (5.15)\\
H_{AE} &= \frac{1}{2}\sum_{\nu=x,y,z} F_{\boldsymbol{q}} q_\nu^2 S_{\boldsymbol{q}}^\nu S_{-\boldsymbol{q}}^\nu, && (5.16)\\
H_D &= \frac{\omega_0}{2}\sum[(\boldsymbol{S_q}\cdot\hat{q})(\boldsymbol{S_{-q}}\cdot\hat{q}) - 1/3(\boldsymbol{S_q}\cdot\boldsymbol{S_{-q}})], && (5.17)\\
H_Z &= \sqrt{N}\boldsymbol{H}\cdot S_0, && (5.18)
\end{aligned}
$$

they are the conventional isotropic exchange H_{EX}, the DMI H_{DM}, the anisotropic interaction H_{AE}, the magnetic dipolar interaction H_D and the Zeeman term H_Z. Here $\boldsymbol{S_q} = \sqrt{N}\sum \boldsymbol{S_R}\exp(-\boldsymbol{q}\cdot\boldsymbol{R})$ is the Fourier transform of the spin operator. $\omega_0 = \mu_0(g\mu_B)^2/a^3$ is the characteristic energy of the dipolar interaction. $\boldsymbol{H}$ is the magnetic field.
As all experiments within this work have been performed without the application of external magnetic fields we will consequently only consider the parts of Maleyev's work for $\boldsymbol{H} = 0$. Similar to Belitz, Maleyev also finds different dispersions parallel and perpendic-

ular to the propagation direction of the helix. For $\boldsymbol{q} \parallel \boldsymbol{k}$ he derives

$$\epsilon_{\parallel,\pm} = \sqrt{A(k \pm q_\parallel)^2[A(k \pm q)^2 + Ak^2 + S\omega_0]}. \tag{5.19}$$

Here A is the spin wave stiffness constant for $q \gg k$ and S = 0.2·4 is the spin of the unit cell of MnSi. The '+' and '-' branches emerge from $\pm\boldsymbol{k}$, respectively (see Fig. 5.10(a)). The corresponding magnetic susceptibility parallel to the propagation direction is given by

$$\begin{aligned} \chi_\parallel^{\alpha\beta} &= -(\delta_{\alpha\beta} - \hat{c}_\alpha \hat{c}_\beta)\frac{S}{4} \cdot \left(\frac{Z_+}{\omega^2 - \epsilon_{\parallel,+}^2} + \frac{Z_-}{\omega^2 - \epsilon_{\parallel,-}^2} \right), \\ \text{where} \quad Z_\pm &= A(k \pm q_\parallel)^2 + S\omega_0, \end{aligned} \tag{5.20}$$

For $\boldsymbol{q} \perp \boldsymbol{k}$ the dispersion is more complicated as umklapp processes mix the modes with $\boldsymbol{q} + \boldsymbol{k}$ and $\boldsymbol{q} - \boldsymbol{k}$. The corresponding dispersion is described by

$$\epsilon_{\perp,\pm} = Ak^2 \left(1 + 4\frac{q_\perp^2}{k^2} + \frac{q_\perp^4}{k^4} \pm \sqrt{1 + 8\frac{q_\perp^2}{k^2} + 17\frac{q_\perp^4}{k^4} + 8\frac{q_\perp^6}{k^6}}) \right)^{\frac{1}{2}} \tag{5.21}$$

Here the '+' and '-' branches have a different meaning, they correspond to the gaped and ungaped mode. The value of the gap is $\Delta\epsilon = \epsilon_{\perp,+}(0) - \epsilon_{\perp,-}(0) = Ak^2\sqrt{2}$. The dispersion is shown in Fig. 5.10(b). For the magnetic susceptibility perpendicular to the propagation direction we have

$$\begin{aligned} \chi_\perp^{\alpha\beta} &= -(\delta_{\alpha\beta} - \hat{c}_\alpha \hat{c}_\beta)\frac{S}{4(\epsilon_{\perp,+}^2 - \epsilon_{\perp,-}^2)} \cdot \left(\frac{Z_+}{\omega^2 - \epsilon_{\perp,+}^2} + \frac{Z_-}{\omega^2 - \epsilon_{\perp,-}^2} \right), \\ \text{where} \quad Z_\pm &= 2A^2 q_\perp^2 (2k^2 + q_\perp^2) \pm A(\epsilon_\pm^2 - \epsilon_1^2)(k^2 + q_\perp^2), \\ \epsilon_1^2 &= 2A^2 k^4 + S\omega_0 A k^2 + S^2 \omega_0^2 N_{cc} N_\perp / 2, \end{aligned} \tag{5.22}$$

where N_{cc} and $N_\perp$ are components of the demagnetisation tensor parallel and perpendicular to $\boldsymbol{k}$. $\hat{c}$ is a unit vector that is parallel to the propagation vector $\boldsymbol{k}$.
Maleyev also derived the asymmetric part of the magnetic susceptibility (compare also appendix C) that gives rise to an inelastic chiral contribution to the neutron scattering section. However, as we have seen in section 2.4.2 the chiral contribution is always zero for unpolarised neutron scattering and we have neglected it here as all our inelastic experiments have been performed with unpolarised neutrons. The dispersion relation corresponding to the model of Maleyev is illustrated in Fig 5.10.

5.2.3.3 Comparison of the models of Belitz and Maleyev

We have seen that both models predict a dispersion for the helimagnons that is anisotropic with respect to the propagation direction of the helix. For the limit of small values of q

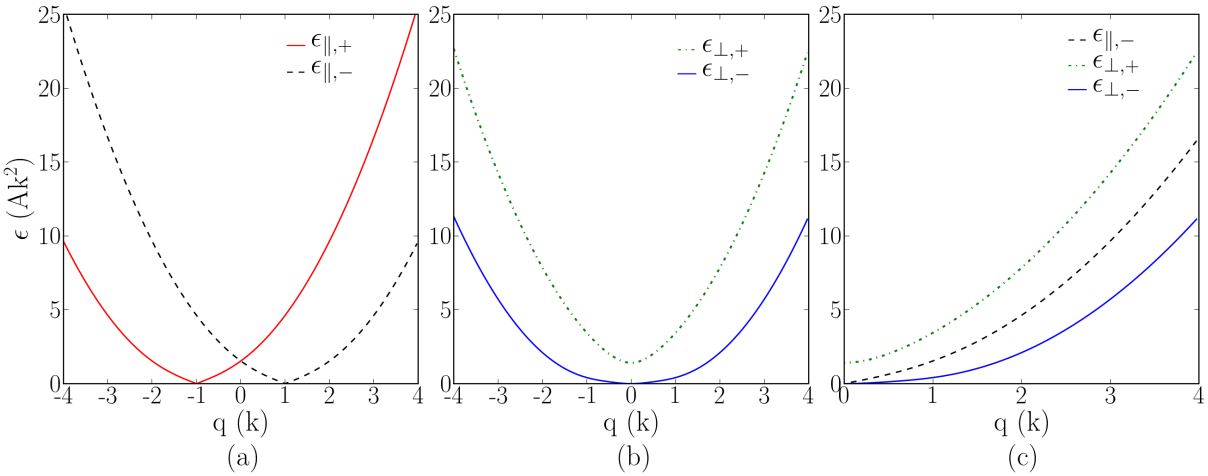

Figure 5.10: The dispersion relation of the magnetic excitations in MnSi as derived by Maleyev [Mal06] are shown. (a) The two dispersion branches parallel the propagation vector of the helix $\boldsymbol{k}$ are shown. Here '+' and '-' correspond to branches emerging from $\pm\boldsymbol{k}$, respectively. (b) The dispersion of the two excitations perpendicular $\boldsymbol{k}$ are illustrated. Here the meaning of the '+' and '-' branches is different, they correspond to the gaped and non-gaped modes, respectively. (c) To illustrate that the dispersion is anisotropic we show one parallel and the two perpendicular branches in one graph.

($q_{\parallel,\perp} << k$) Maleyev also derived an expression for the dispersion for arbitrary directions for the case of the gapless mode, namely

$$\epsilon_- = A(k^2 q_\parallel^2 + \frac{q_\perp^4}{2})^{1/2}, \tag{5.23}$$

This is similar to the Eq. 5.10 by Belitz *et al.* if we identify $c_\parallel = \text{const}^2 r_0 A^2 k^2$ and $c_\perp = \frac{c_\parallel}{2}$. However, the value of the gap of the ϵ_+ modes remains obviously unchanged in the Maleyev model. In contrast to this, Belitz argues that within low-energy theory all momenta are of the order of k, and umklapp scattering would only occur for a process of order $n \gtrsim G/k \approx 40$, where G is the modulus of a reciprocal lattice vector. Therefore, the resulting gap will be experimentally unobservable and negligibly small.
In summary we see that both models share the common feature of an anisotropic dispersion that can be directly compared for $q_{\parallel,\perp} << k$ but differ with respect to the prediction of a spin-wave gap.

5.3 Experimental work and results

The experimental section is organised in three parts. The first two sections report on our investigation of the possible intermediate phase in MnSi by means of elastic neutron scattering techniques with unpolarised and polarised neutrons, respectively. The third section

focuses on inelastic neutron scattering experiments that were conducted in the helimagnetic phase of MnSi in order to examine the dispersion of the proposed helimagnons.

5.3.1 Samples used for the investigation

For our experiments two different single crystal samples were used. The first sample is a big single crystal of cylindrical shape with a volume of approximately 8 cm^3. It was grown by the Bridgeman method starting from high purity materials. This crystal is well characterised as it was used in several previous experiments [RBFE02, SBE$^+$99] and has a crystal mosaic $\eta \approx 1.5°$. It will be referred to as *sample A* from now on and is shown in Fig. 5.11(a).
The second sample is a single crystal disc of 2 mm thickness at approximately 20mm diameter. It was cut from sample A and was used already in the reference [Lam06]. We will call the sample that is depicted in Fig. 5.11(b) sample B. The mosaic of sample B is $\eta \approx 0.15°$ [Lam06].

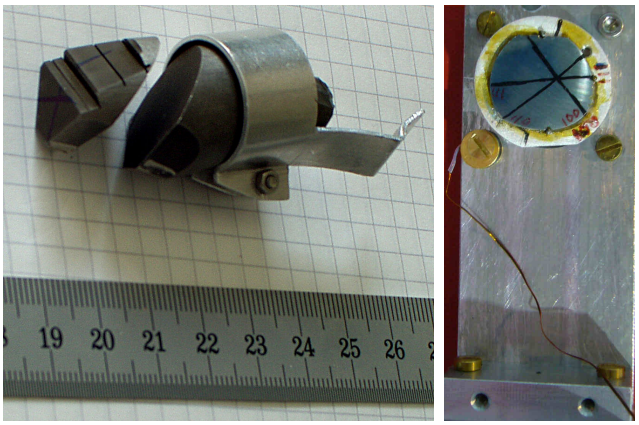

(a) (b)

Figure 5.11: The MnSi single crystal samples that were used in this work are shown mounted onto the holders that were employed in the experiments: (a) Sample A (b) Sample B.

5.3.2 Investigation of the possible intermediate phase by SANS

We examined the magnetic scattering intensity of MnSi near the transition from the helical phase to the paramagnetic phase at T_c by means of small angle neutron scattering (SANS) (s. also appendix A.4 for more details on this instrument type) on the very cold neutron multipurpose beamline MIRA [GBJ$^+$07] at the research reactor FRM-II in Germany. MIRA is equipped with a two-dimensional position sensitive detector (PSD) with an active area of 20 x 20 cm^2 and 256 x 256 pixels for the SANS geometry. The experiment was performed with the neutron wavelength $\lambda = 9.7$ Å that was

defined via a multilayer bandpass monochromator. The instrumental resolution was defined by a computer-controlled variable source aperture of rectangular cross-section that was installed after the monochromator and a cadmium aperture of approximately 15 mm diameter that was mounted directly on the sample holder. A moderate resolution was chosen in order to maximise the intensity for the detection of the faint magnetic scattering intensity above T_c. We will consider this in detail later. Additionally a flight tube filled with helium gas was used in front of the sample in order to minimise the experimental background due small angle scattering from air.[3] The two-dimensional data sets measured by means of the PSD were exclusively treated with the program $GRAS_{ans}P$ [Dew03].
For the experiment sample B has been used in an orientation where a $[11\bar{2}]$ zone axis was directed upwards. The sample was inserted into the standard toploading closed cycle cryostat available at FRM-II [CCR] in order to cool it into the magnetic phase.

5.3.2.1 Temperature dependence of the magnetic intensity

The sample was first cooled down to the lowest available temperature of approximately 1.8 K in order to orient it with respect to the magnetic reflections.[4] The orientation with the $[11\bar{2}]$ zone axis directed vertically allows to fulfil the Bragg condition for two pairs of satellites around the (0,0,0) position simultaneously, i.e. the satellites for $\boldsymbol{k}_1 = [\zeta, \zeta, \zeta]$ and $\boldsymbol{k}_2 = [\zeta, \zeta, \overline{\zeta}]$[5]. The sample was oriented to have similar intensities on magnetic satellites associated with the same propagation vector as shown in Fig. 5.12.
Consequently we followed the magnetic intensities as a function of temperature in order to identify the temperature interval where the ring of magnetic intensity is observed. This is illustrated in Fig. 5.12. The influence of the intensity of the direct beam was significantly reduced by covering the direct beam spot with a sheet of cadmium. Further a dataset measured at T = 31.5 K above T_c was subtracted from all datasets in order to consider background scattering and the remains of the direct beam intensity. At low temperature only the magnetic satellites are visible due to the helical magnetic order of MnSi. When the temperature is increased the magnetic Bragg peaks slowly move to larger values of q. Further, when T_c is approached the magnetic Bragg peaks start to broaden azymuthally and start to merge into a ring of intensity at approximately 29 K. The radius of the ring approximately corresponds to the pitch of the magnetic helix below T_c. As we have mentioned earlier in section 5.1.3 the magnetic intensity forms a sphere in reciprocal space and the observed ring is a two-dimensional cut through the sphere. The complete sphere will be investigated later in more detail. Accordingly, we will here often refer as ring to the intensity distribution. The magnetic scattering intensity is distributed more and

[3] Unfortunately no appropriate flight tube was available for the flight path between sample and detector at the time the experiment was performed.

[4] The usual approach of orienting the sample with respect to the nuclear reflections is not possible on MIRA as the neutron wavelength is to high to reach the reflections.

[5] It is possible to fulfil the Bragg condition for several Bragg reflections simultaneously in the SANS geometry due to the finite beam divergence and the finite magnetic mosaic spread of the sample.

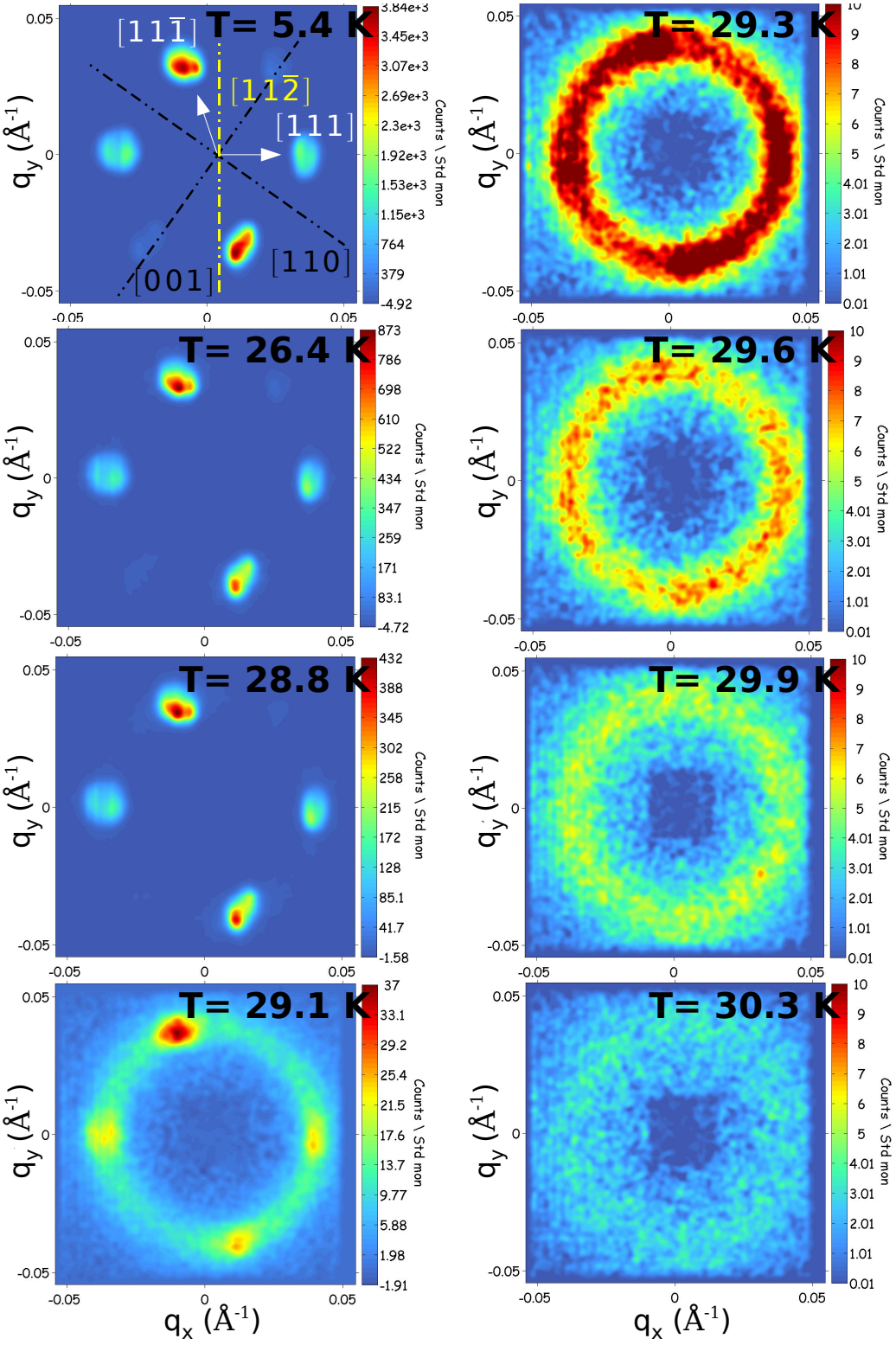

Figure 5.12: The magnetic scattering intensity of MnSi as function of temperature is shown. A dataset measured at T = 31.5 K has been subtracted for all temperatures. The data has been smoothed with a two-dimensional Gaussian smoothing kernel with 5 pixels full width half maximum. The magnetic satellites first move to slightly larger values of q. Then they begin to broaden azymuthally before they merge into a ring of magnetic scattering intensity at approximately 29 K. The ring finally disappears at approximately 30.5 K.

more isotropically on the ring while simultaneously the overall intensity decreases when the temperature is increased further. At T ≈ 29.5 K the magnetic Bragg intensity disappears completely.
In order to investigate the appearance of the ring-shaped magnetic intensity further we performed integrations over the measured intensity as a function of temperature. We defined circular regions of integration for the satellites and the ring, respectively, where only scattering of one kind was observed as illustrated in the top panels of Fig. 5.13.

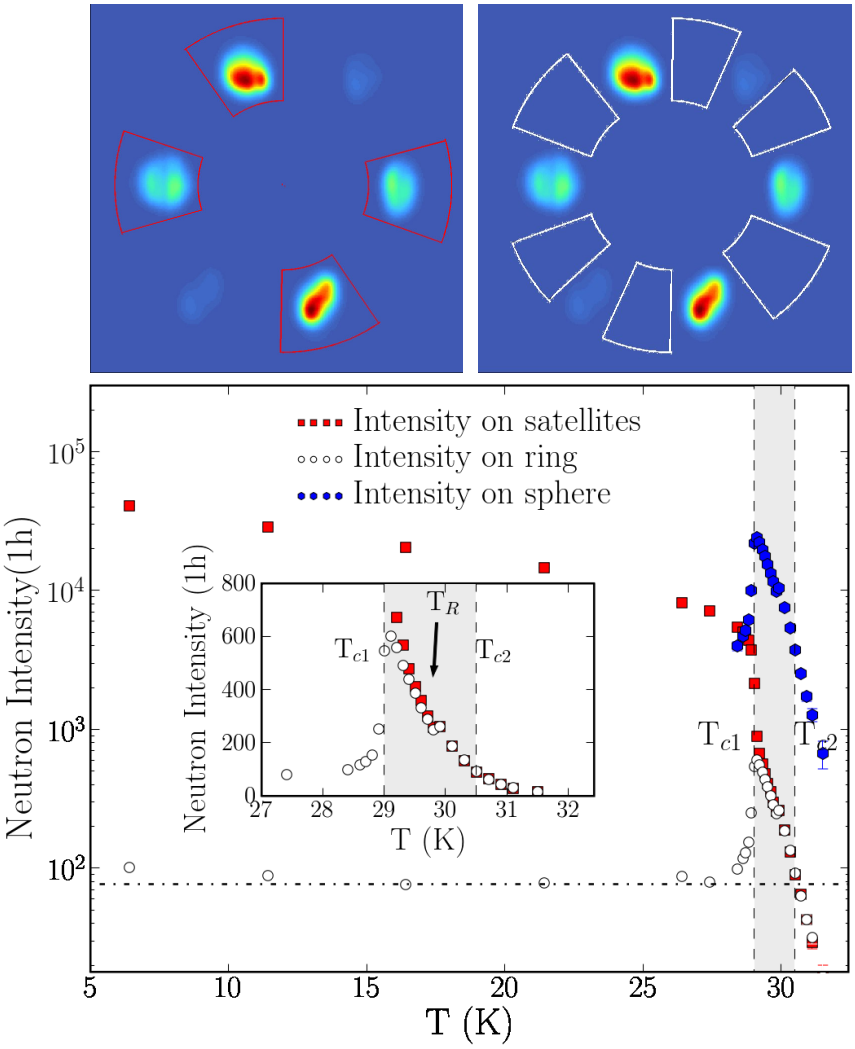

Figure 5.13: The figure shows the integrated intensity for the magnetic satellites and the ring as a function of temperature. The integration for the satellites and the ring were performed over the red and white circular box sectors shown in the top panels of figure, respectively. To compare the two integrated intensities each of them was normalised with respect to the arc length the corresponding circular box section cover, respectively (s. text for detailed explanation). The horizontal broken line signifies the background level below T_{c1}. The blue hexagons denote the intensity on the ring extrapolated to a sphere. This is explained in detail in section 5.3.2.3.

Hence, we were able to examine both types of magnetic scattering independently as function of temperature. Both integrated intensities were normalised with respect to the summed arc length that the corresponding circular box sections cover, respectively. This allows a comparison of both intensities on a absolute scale. The blue hexagons in Fig. 5.13 denote the intensity on the ring extrapolated to a sphere. This will be discussed in detail later in section 5.3.2.3. Fig. 5.13 demonstrates that at $T_{c1} = 29$ K the magnetic intensity on the satellites drops abruptly while the magnetic intensity on the ring section simultaneously makes a sharp upward jump from the background level towards the intensity level of the satellites. This indicates that at the temperature T_{c1} the intensity on the ring and the satellites is approximately identically and thus the ring of magnetic intensity has emerged. Above of T_{c1} both intensities decrease together. As shown in the inset of Fig. 5.13 the intensity on the magnetic satellites is still slightly higher compared to the intensity on the ring up to the temperature $T_R \approx 29.7$ K. This signifies that the intensity on the ring is not yet isotropically distributed between T_{c1} and T_R. That is consistent with the contour plots of Fig. 5.12 and shows that our normalisation is correct. Both intensities reach the level of the background intensity that is observed below T_{c1} at the temperature $T_{c2} \approx 30.5$ K. The intensity still decreases above this temperature which is because the overall background is significantly lower in the paramagnetic phase compared to the helimagnetic phase. We note that the temperatures T_{c1} and T_{c2} are in very good agreement with the temperatures defined from the specific heat data (cf. Fig. 5.4).

5.3.2.2 Fits of the magnetic intensity

We followed the temperature dependence of the pitch of the helix by means of $\boldsymbol{q}$-scans in radial direction through the magnetic intensity.[6] The $\boldsymbol{q}$-scans were extracted from the two-dimensional detector images in Fig. 5.12 by performing radial bins (see reference [Dew03] for an exact explanation of the binning procedure) with an azimuthal width of 20° which corresponds to the azimuthal width of the magnetic satellite reflections at low temperature. The result, namely the intensity as function of $q = |\boldsymbol{q}|$ and temperature is shown in the Figs. 5.14 and Fig. 5.15. The arrow in the small inset shows the direction of the respective $\boldsymbol{q}$-scans shown in each view graph.
The magnetic intensity on the satellite reflections below T_{c1} in the helical phase could be well fitted with Gaussian profiles of the form

$$I(q) = 2\frac{I_0}{\Delta k}\sqrt{\frac{\ln(2)}{\pi}}\exp\left\{-\frac{4\ln(2)(q-k)^2}{\Delta k^2}\right\} + \mathrm{BCK}, \tag{5.24}$$

where the given normalisation of the profile ensures that I_0 and Δk describe the integrated intensity and the full width at half maximum (FWHM), respectively. k is the peak centre

[6] We note that we use the reduced scattering vector $\boldsymbol{q}$ here as we are only interested in the scattering around the reciprocal lattice position (0,0,0) (direct beam) in the SANS geometry. $\boldsymbol{Q}$ and $\boldsymbol{q}$ are related via the relationship $\boldsymbol{Q} = \boldsymbol{\tau} + \boldsymbol{q}$ where $\boldsymbol{\tau}$ is a reciprocal lattice vector and for $\boldsymbol{\tau} = (0,0,0)$ we have $\boldsymbol{Q} = \boldsymbol{q}$.

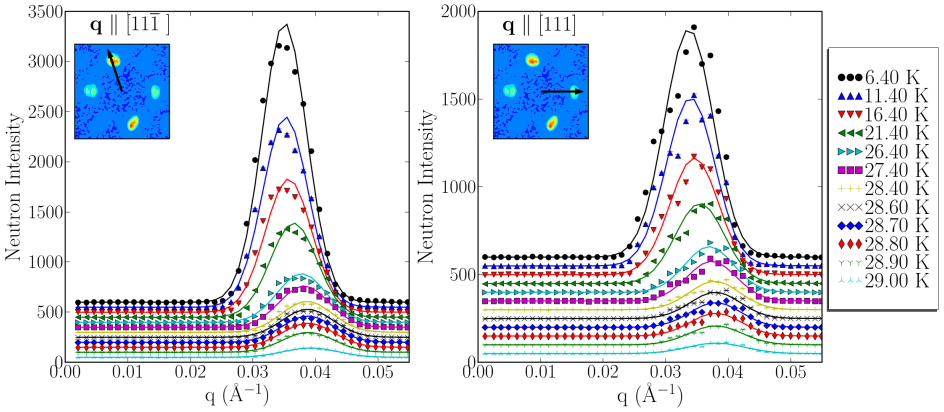

Figure 5.14: ***Q***-scans through the magnetic satellite reflections parallel to the direction denoted in the insets are shown for T $\leqq$ T$_{c1}$ in the helical phase. The scans were fitted with Gaussian profiles (s. Eq. 5.24). The data sets were shifted by a constant offset of 50 for clarity.

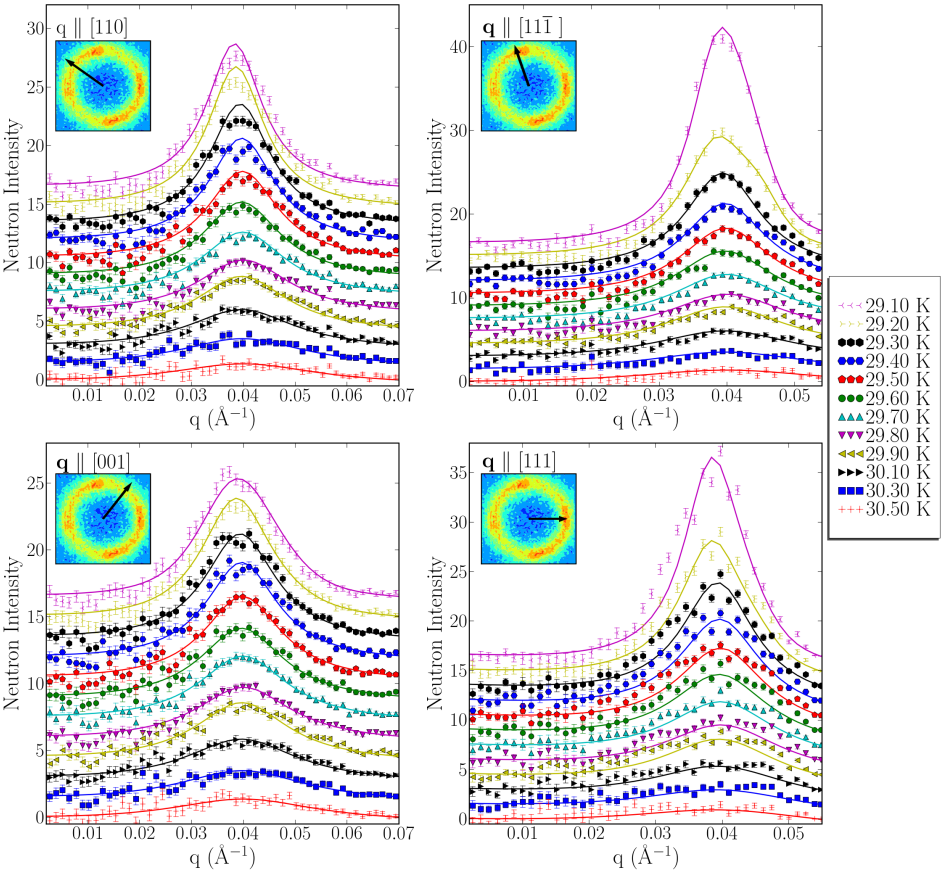

Figure 5.15: ***q***-scans through the magnetic ring-shaped intensity for T > T$_{c1}$ are shown for four directions that are denoted in the small insets of each subfigure. All four scans were fitted simultaneously with Eq. 5.4. The data sets were shifted by a constant offset of 1.5 for clarity.

and BCK describes a constant background. The position of the peak k in each data set corresponds to the modulus of the propagation vector $\boldsymbol{k}$ of the magnetic helix for the associated temperature. The fits were performed independently for the magnetic satellite reflections corresponding to $\boldsymbol{k}_1$ and $\boldsymbol{k}_2$. As the results of the fits are similar for both directions only the respective ones for $\boldsymbol{k}_1$ are shown in Figs. 5.16 (a)-(c). Fig. 5.16(a) shows clearly that the modulus of the propagation vector increases already within the helical magnetic phase. Before we discussed this in more detail we are going to describe the fits to the data above T_{c1}.

For temperatures larger than T_{c1} the $\boldsymbol{q}$-scans through the ring of magnetic intensity were better described by Lorentzian profiles as given by Eq. 5.4. We emphasise that the cubic invariant term $(\hat{q}_x^4+\hat{q}_y^4+\hat{q}_z^4-1/3)$ in the denominator of Eq. 5.4 is dependent of the direction of the performed $\boldsymbol{q}$-scan. Consequently the proper expression has to be introduced for each respective scan. As shown in Fig. 5.15 we fitted $\boldsymbol{q}$-scans for the four directions [110], [0,0,1], [1,1,1] and [1,1,$\overline{1}$]. The first two and last two directions correspond to the azimuthal positions with weakest and strongest magnetic intensity on the ring, respectively. Here the cubic invariant term describes the observed azimuthal dependence together with the coefficient B_2 that gives the magnitude of the cubic anisotropy energy. The larger B_2 the more anisotropic is the intensity distribution on the sphere of magnetic scattering described by Eq. 5.4. The correct expressions for the cubic invariant term for each of the four directions is given by

- [110]: $\hat{q}_x = \hat{q}_y = \tilde{q}/q$ and $\hat{q}_z = 0$ with $\tilde{q} = q/\sqrt{2}$,
- [001]: $\hat{q}_x = 1$ and $\hat{q}_y = \hat{q}_z = 0$,
- [111] and [1,1,$\overline{1}$]: $\hat{q}_x = \hat{q}_y = \hat{q}_z = \tilde{q}/q$ with $\tilde{q} = q/\sqrt{3}$.

As we have already discussed before (compare Fig. 5.12) the magnetic intensity on the ring becomes more and more isotropic with increasing temperature. In order to determine the cubic anisotropy energy coefficient B_2 as a function of temperature we performed least-squares fits to the data where we fitted the four $\boldsymbol{q}$-scans in Fig. 5.15 simultaneously. Additionally the inverse magnetic correlation length κ and the radius of the sphere given by k were correlated for all four scans. Similar to the fits for $T < T_{c1}$ we introduced a constant background in the fit. The magnetic form factor for the Mn ions $F_{Mn}(\boldsymbol{Q})$ does not differ significantly from 1 for the small values of $\boldsymbol{Q}$ in this experiment and was therefore neglected in the fits (s. also Fig. 2.4). Further we fixed the value of the spin wave stiffness constant to $A = 52$ meVÅ^2 as given in references [Mal06, GMO$^+$05]. Of course the incident polarisation vector was set to $\boldsymbol{P}_0 = 0$ in Eq. 5.4 as non-polarised neutrons were used in the experiment. For $T > 29.3$ K this model fitted the data well. However, for $T = 29.1$ K and 29.3 K Eq. 5.4 could not describe the $\boldsymbol{q}$-scans that were performed parallel to the [1,1,1] and [1,1,$\overline{1}$] directions as the intensities in the fits were always to low. These are the positions where the magnetic satellites are observed below T_{c1} in the helical phase. We therefore interpreted these findings as a cross-over regime where both the magnetic satellites due to the helical order and the magnetic critical scattering are observed simultaneously. The fits were significantly improved ($\chi^2 = 5.1$ instead 10.1) by

introducing an additional Gaussian profile in the fits for both directions and the data is described well due to this measure. The final fits are shown as the solid lines in Fig. 5.15 and the corresponding results for all parameters are summarised in Fig. 5.16.
The integrated intensities for magnetic satellites below T_{c1} and the critical scattering above T_{c1} shown in Fig. 5.16(a) are in good agreement with the intensities shown in Fig. 5.13. In Fig. 5.16(b) we see that the modulus of the propagation vector $\boldsymbol{k}$ of the magnetic helix in the helical phase increases smoothly as a function of temperature from k = 0.035 Å^{-1} to 0.039 Å^{-1}. Additionally a distinct change of slope in this increase is observed at the temperature T_{c1}. The radius of the sphere of magnetic scattering (not the satellites!) that is observed for $T \geq T_{c1}$ is found to be k = 0.038 Å^{-1} at T_{c1} and increases up to approximately $T_R = 29.6$ K where it stabilises at k ≈ 0.040 Å^{-1}. Thus, the temperature behaviour of the modulus of the helical propagation vector indicates that the period of the helix decreases smoothly as a function of increasing temperature in the helical magnetic phase and makes a sudden jump to an even smaller period at T_{c1} in the cross-over regime, where the magnetic satellites and the critical scattering are observed simultaneously. The width of the magnetic satellites in radial direction remains almost constant at $\Delta k \approx 0.009$ Å^{-1} below T_{c1} as shown in in Fig. 5.16(c). The inverse correlation length of the critical scattering is found to be $\kappa = 0.0051$ Å^{-1} at 29.1 K and diverges fast when the temperature is increased. For better comparison with the results obtained by Grigoriev *et al.* [GMO$^+$05] that are given in Fig. 5.16(f) we have plotted κ as a function of $\kappa^2 = C\tau^{2\nu}$ in Fig. 5.16(d). The solid line in the viewgraph is described by $\kappa^2 = C\tau^{2\nu}$ where $\nu = 0.62$ as obtained by Grigoriev. In contrast to our approach Grigoriev *et al.* have determined the inverse correlation length κ independently for $\boldsymbol{q}$-scans parallel to the [0,0,1] and [1,1,1] and refer to them as hard and easy magnetic axis, respectively. If this difference is considered our results are in good agreement with the result of Grigoriev. In addition, we note that only our approach of fitting the $\boldsymbol{q}$-scans in different directions simultaneously allows to determine B_2 as a function of temperature. The result obtained for B_2 is demonstrated in Fig. 5.16(e) and show that B_2 is not a constant. At T = 29.1 K we find $B_2 = 6.60(8)$ meVÅ^2 and it decreases for increasing temperature when the intensity on the ring is distributed more and more isotropically. The temperature dependence of B_2 could be well fitted by the power law $B_2 = a\tau^{-\varrho}$ with $\varrho = 0.840(9)$. Grigoriev *et al.* found that $B_2 = 4$ meV Å^2 at $T = T_{c1} + 0.3$ K, which is also in good agreement with our findings. In Fig. 5.13 we estimated that at $T_R \approx 29.7$ K the scattering on the observed ring is distributed isotropically. The values identified for B_2 show an identical trend since above T_R the anisotropy energy has decreased to $B_2 \lesssim 1$ meVÅ^2 and the intensity is therefore indeed distributed isotropically on the ring.
It is interesting to compare the obtained values with the instrumental resolution. In the case of the simple setup used in this experiment the experimental resolution is mainly defined by the aperture system installed in front of the sample. The resolution can be approximated by Eq. A.4 that is provided in the appendix. In the present experiment the distance between the sample and the source aperture was 800 mm and the sample-detector distance was 1180 mm. The rectangular source aperture was adjusted to a cross-section of 16 x 16 mm^2. We will approximate it as a circular aperture with a radius $r_1 = 8$ mm.

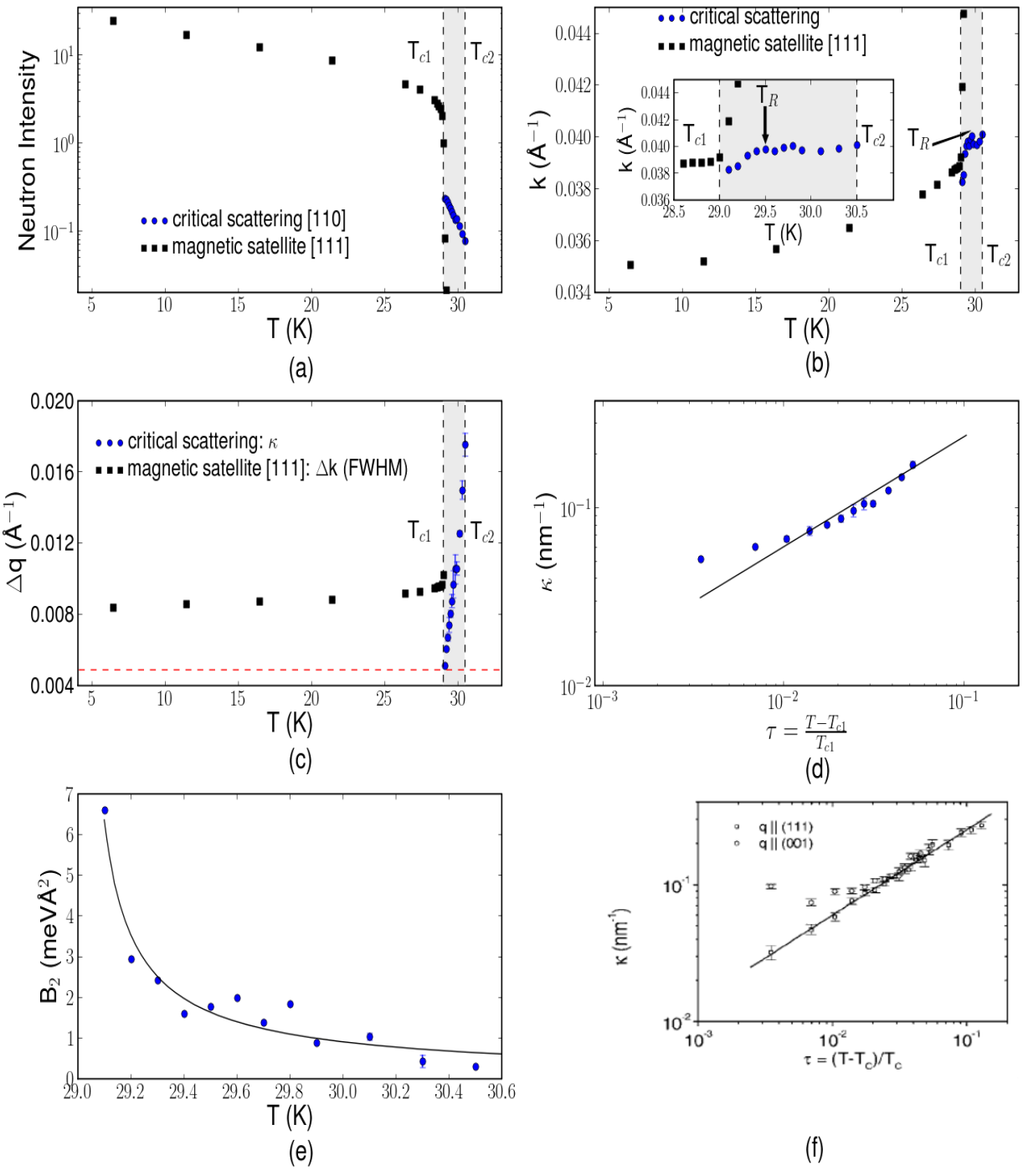

Figure 5.16: The results of the fits in Figs. 5.14 and 5.15 are summarised as a function of temperature: (a) the integrated intensities for the magnetic satellite $[\zeta, \zeta, \zeta]$ and for the critical scattering along the [110], (b) the position of magnetic satellite $[\zeta, \zeta, \zeta]$ and the critical scattering. (c) the width of the magnetic satellite Δk and the inverse correlation length κ of the critical scattering. (d) A detailed view of the inverse correlation length κ as a function of $\tau = (T - T_{c1})/T_{c1}$. The black line denotes the result of reference [GMO$^+$05] $\kappa^2 = C\tau^{2\nu}$ where $\nu = 0.62$. (e) The constant B_2 describing the cubic anisotropy energy as extracted from the fits as a function of temperature. The black line is a fit to the power law $B_2 = a\tau^{-\varrho}$ with $\varrho = 0.840(9)$. (f) The results for the inverse correlation length as they were obtained by Grigoriev *et al.*[GMO$^+$05].

The radius r_2 of the sample aperture is also 7.5 mm. The mean wave vector is $\langle K \rangle = \frac{2\pi}{9.7}$ Å^{-1} = 0.64 Å^{-1}. Therefore the values of the angular and $\boldsymbol{Q}$-resolution amount to $\Delta\beta_h = 0.439°$ and $\Delta Q_l = 0.0049$ Å^{-1}. We want to emphasise that this is a lower limit for the experimental resolution that is probably slightly larger in reality due to additional effects caused by a finite wavelength spread. However, as can be seen by the red line in Fig. 5.16(d) the calculated value seems reasonable when compared with our data below T_{c1}. The calculation demonstrates that the values found for the width of the peaks in the fits is certainly accurate. In addition, the position of the peaks is determined accurately, even though the shift of the peak is much smaller compared to the experimental resolution, since the width of the peaks has the same order of magnitude as the resolution.
In order to demonstrate that our results for the temperature dependence of the modulus of the magnetic propagation vector k, the inverse correlation length κ and the magnitude of the cubic anisotropy energy B_2 obtained by fitting the model in Eq. 5.4 to one-dimensional $\boldsymbol{q}$-scans also describe the two-dimensional data well, we performed the simulations that are shown in Fig. 5.17. The parameters that are shown in Fig. 5.16 were used in Eq. 5.4 to generate the simulations of the intensity patterns. Fig. 5.16 also demonstrates that for

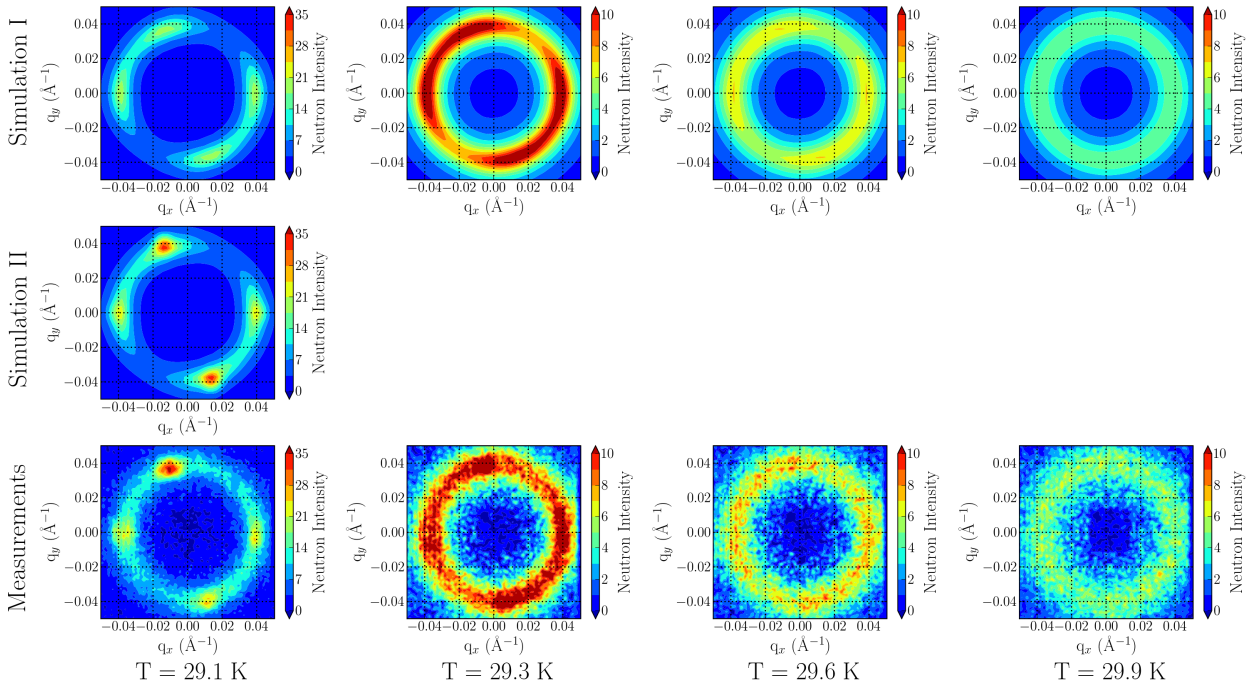

Figure 5.17: A comparison between the measured data (bottom row) and a simulation (two upper row) of the model for critical scattering as described by Eq. 5.4 is shown for different temperatures. For the simulation the parameters as obtained by the fits shown in Figs. 5.15 and 5.16 were used. For the simulation II two-dimensional Gaussian profiles have been added to the critical scattering intensity at the position of the magnetic satellite reflections. See the text for details.

T = 29.1 K the critical scattering described by Eq. 5.4 does not completely reproduce the data. However, if similar to the $\boldsymbol{q}$-scans in Fig. 5.15 two-dimensional Gaussians are inserted at the position of the magnetic satellite reflections the two-dimensional SANS data is described well by the simulation. This supports our assumption that there is a small temperature regime above T_{c1} where the magnetic critical scattering and the magnetic satellites due to the helical order coexist. Ultimately, we want to highlight, that for the simulation exactly the same expression was used, even without the use of a scale factor.

5.3.2.3 Rocking scans

Finally we carried out rocking scans at constant temperature, i.e. rotating the sample around the zone axis $[11\overline{2}]$ and measuring a detector image for several rocking angles ω. The result of the rocking scans is shown in Fig. 5.18 for 16.4 K and 29.4 K. For T = 16.4 K we observed that the magnetic satellite reflections associated with the propagation vector $\boldsymbol{k}_1 = [\zeta, \zeta, \zeta]$ decrease rather fast as a function of increasing rocking angle whereas the magnetic satellite reflections corresponding to $\boldsymbol{k}_2 = [\zeta, \zeta, \overline{\zeta}]$ only fade away at large rocking angles ω. This is expected as in the rocking scan the component of the scattering vector that is parallel to the rocking axis (q_y) is not changed. Further the modulus of the component of the scattering vector $\boldsymbol{Q}$ that is perpendicular to the rocking axis (q_x) remains constant, but its direction is varied with respect to the reciprocal lattice. As for the reflections corresponding to $\boldsymbol{k}_2$ $q_x = 0.0012$ Å^{-1} is small compared to $q_y = 0.0036$ Å^{-1} the scattering vector for the two corresponding magnetic reflections is only rotated slowly out of the condition for magnetic Bragg scattering.
In the second data set for T = 29.4 K the ring of magnetic intensity is visible for all measured rocking angles. Due to restrictions with the cryostat supply lines the maximum range of angles that could be covered with the used experimental setup was limited to -35° $\leq \omega \leq$ 35°. In Fig. 5.19 we show the intensity integrated within circular regions around the two magnetic satellites corresponding to $\boldsymbol{k}_1$ as a function of the rocking angle for several temperatures. The used integration regions are denoted by the red lines in the detector images for $\omega = 0°$ in Fig. 5.18. The integration regions were chosen to be independent of the intensity on the magnetic satellites associated with $\boldsymbol{k}_2$ and thus allow an easy comparison between the angular distribution of the magnetic intensity on the satellites in the helical phase and the ring above T_{c1}, respectively. The plots demonstrate that the intensity increases significantly at large rocking angles ω as soon as the ring shaped intensity arises at $T_{c1} = 29$ K. Further the intensity is almost independent of the rocking angles above T_{c1}. The small decrease of the intensity at large rocking angles has several reasons that we believe are not caused by the real intensity distribution of the sample but are due to experimental limitations:

- The circular sample aperture was fixed on the sample holder and therefore changes its size as a function of the rocking angle like cos(ω). At $\omega \pm 35°$ the aperture is

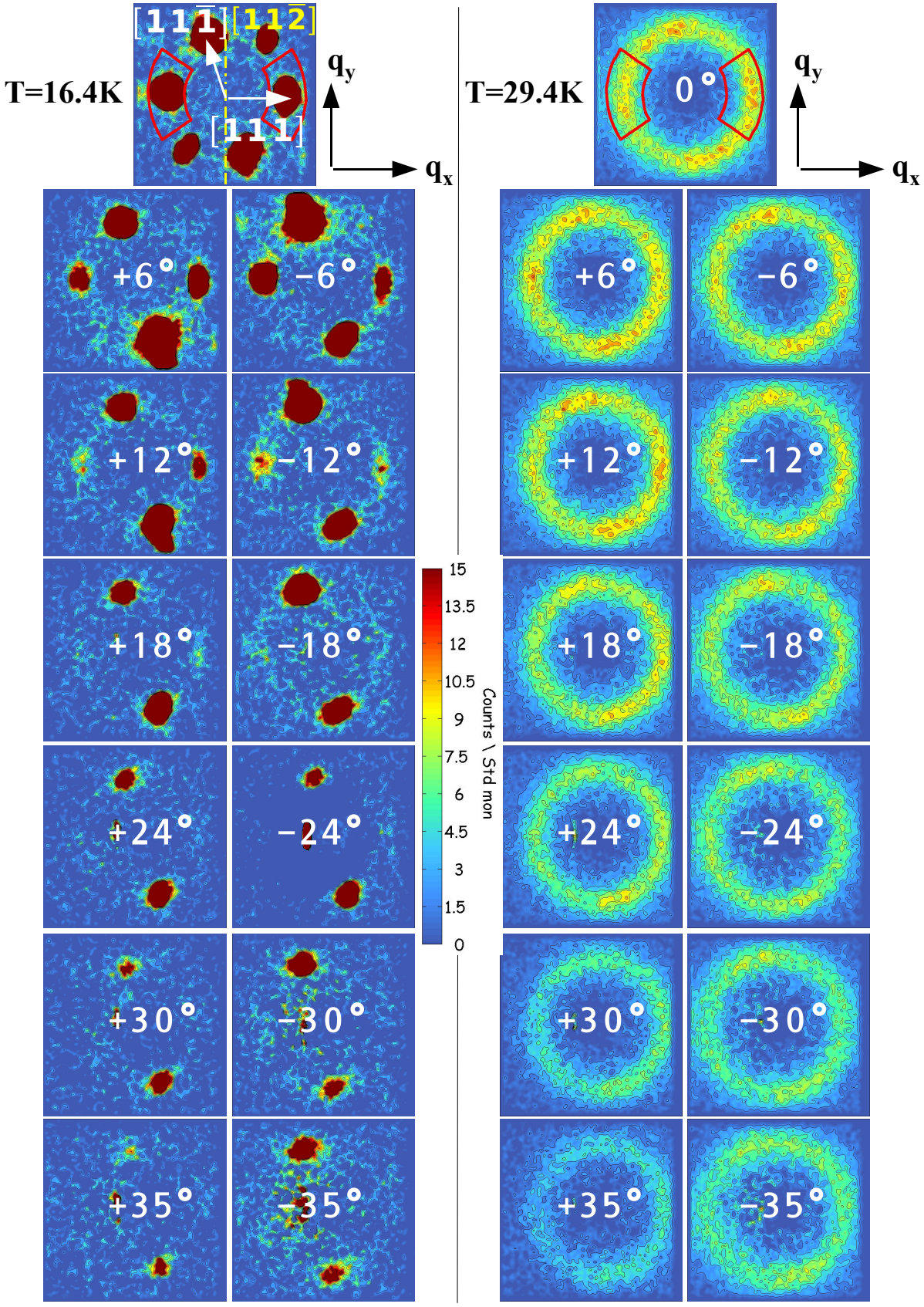

Figure 5.18: The figure shows the detector images for a rocking scan around the axis [11$\bar{2}$] for rocking angles -35° < ω < 35° for the two temperatures T = 16.4 K (left) and T = 29.4 K (right), respectively. The maximum intensity in the view graphs is set to the same value for both temperatures for the sake of better comparison. The real scans were made with half the step size (s. Fig. 5.19).

therefore reduced by 20%. This effect was alread taken into account in the graphs in Fig. 5.19 by normalising each point by $\cos(\omega)$. However, additionally the instrumental resolution changes with the size of the aperture, therefore also the intensity within the integration region. This effect cannot be considered easily. A deconvolution of resolution effects has to be performed with measured data which is an extensive task.[7].

- The used sample B is a disk that was mounted approximately perpendicular to the neutron beam. When the sample is rocked the effective path length of the neutrons through the samples increases and the neutron absorption due to the sample increases. This can be described by the *Beer-Lambert law* $I(l) = I_0 \exp(-\sigma_{abs} N l)$, where l is the path length in the sample, $N = \frac{n}{V}$ is the number density of absorbers (n number of absorbers, V volume of sample) and σ_{abs} is their corresponding absorption cross-section. This correction was also applied to the curves in Fig. 5.19 by normalising them to the angle dependent transmission $T = I(l)/I_0$ (for comparison one uncorrected curve is also shown).[8] For the correction we only used the additional path length due to the rocking of the sample that amounts to $l_{add} = d(\cos^{-1}(\omega) - 1)$, where d is the thickness of the used sample. The effect is however tiny and the correction at $\omega = 35°$ is only about 2.5%.

- The sample was not perfectly centred as can be seen by the asymmetric shape of the curves in Fig. 5.19 with respect to $\omega = 0°$. This effect also cannot be corrected properly. A better centering of the sample was not possible on MIRA as no nuclear Bragg reflections could be measured due to its long wavelength. With the magnetic reflections that were used to orient the sample the accuracy of the adjustment is limited within a view degrees.

If we take into account the above considerations we can conclude that the ring of magnetic intensity can be observed for all possible rocking angles. This indicates that between T_{c1} and T_{c2} the magnetic intensity is distributed over a sphere in reciprocal space whose radius is similar to the pitch of the magnetic helix below T_{c1}. The slight decrease of the intensity on the sphere for large rocking angles can be probably attributed to the fact that the magnitude of the anisotropy energy B_2 is not yet negligible for all measured temperatures (compare Fig. 5.16(e)). Therefore the intensity on the sphere is still slightly peaked at the direction of the cubic diagonals that correspond to the propagation direction of the magnetic helix in the helical phase.
In Fig. 5.13 we have compared the intensity of the magnetic satellites associated with $\boldsymbol{k}_1$ and $\boldsymbol{k}_2$ with the intensity of the observed ring above T_{c1}. However, as the intensity is distributed on a sphere the comparison should be also made for the intensity spread out on the whole sphere. As we have not measured the whole sphere a direct comparison is difficult, though. Nevertheless it is possible to extrapolate the intensity on the ring to

[7] 256^2=65536 data points and for each point one has to integrate numerically over the size of the resolution function

[8] We have used $\sigma_{Mn} = 13.3$ barn, $\sigma_{Si} = 0.017$ barn, N=$4/a^3$ where a is the lattice constant of MnSi.

obtain an estimate about the complete intensity above T_{c1}. From rocking scans of the magnetic satellites the magnetic mosaic was found to be approximately $\delta\omega = 4.5° = 0.025\pi$ (FWHM). If we assume that in a rocking scan the angular resolution is characterised by $\delta\omega$ we can calculate the portion of the sphere that is covered by a single position of ω. The surface of a spherical segment on a unit sphere is given in spherical coordinates by

$$dS = \sin(\theta) d\theta d\varphi. \tag{5.25}$$

Therefore the spherical segment covered in our measurements is

$$S = 2 \int_0^{\pi} \sin(\theta) d\theta \int_0^{\delta\omega} d\varphi = 2\delta\omega[-\cos(\theta)]_0^{\pi} = 4\delta\omega. \tag{5.26}$$

Here the factor 2 is because we have to cover spherical segments on both sides of the sphere. Finally, in order to extrapolate the intensity observed on the ring we consequently have to multiply the intensity on the ring by a factor $\frac{4\pi}{4\delta\omega} = \frac{\pi}{\delta\omega}$=40. The blue hexagons in Fig. 5.13 were obtained by scaling the intensity integrated over the ring by this factor 40. We note that for the comparison with the intensity on the magnetic satellite reflections we have to consider that the intensity of the magnetic satellites shown in Fig. 5.13 were obtained from measurements of only two pairs of magnetic satellites out of four. In conclusion our approximation for the magnetic intensity on the sphere shows that the magnetic intensity observed in the helical phase below T_{c1} is redistributed on the sphere when the direction of the propagation vector is unlocked.

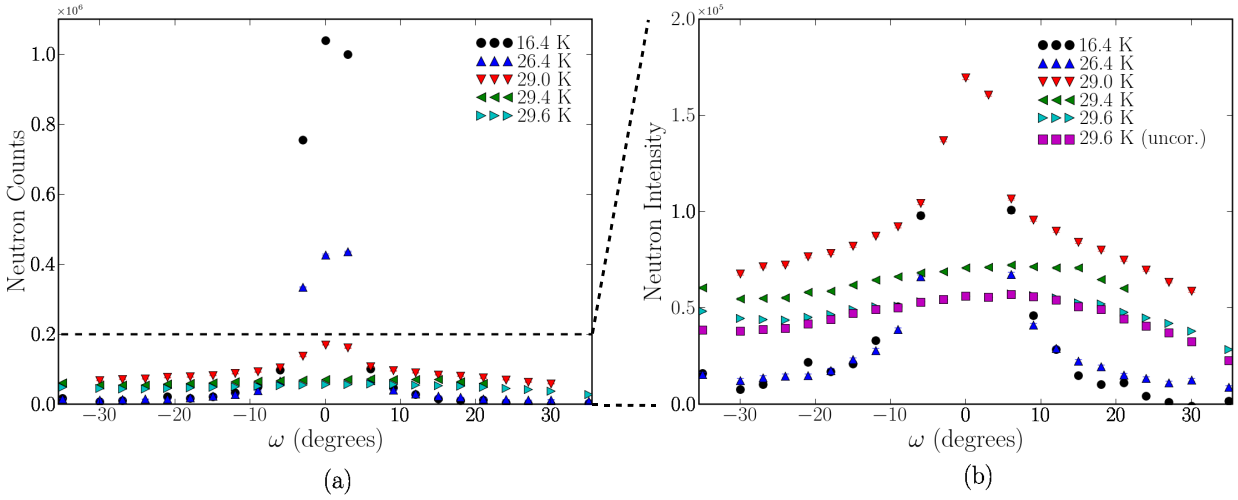

Figure 5.19: (a) Integrated intensities as a function of rocking angle are shown for different temperatures (s. text for details). (b) The same plots as in (a) are shown with a zoom on the lower intensities.

5.3.3 Spherical neutron polarimetry above T_c

A further experiment was conducted with polarised neutrons on MIRA in order to investigate in which way the magnetic structure of MnSi behaves in the temperature interval between T_{c1} and T_{c2}. The measurements were performed with the option MuPAD for spherical neutron polarimetry [JKR+07] (compare also section 2.5) installed on MIRA. The same neutron wavelength $\lambda = 9.7$ Å as for the unpolarised measurements has been used. The neutrons were polarised by means of a polarising supermirror bandpass that simultaneously operated as a monochromator. For the analysis of the polarisation after the scattering process a polarising supermirror bender was employed. With MuPAD the change of the polarisation vector can be only measured correctly at a single position in reciprocal space. Therefore the PSD was replaced by a single ^{3}He counting tube for the polarised measurements. Similar as for the experiment with unpolarised neutrons sample B has been used in an orientation where a $[11\bar{2}]$ zone axis was directed upwards. Also the same cryostat was used to cool the sample.
MIRA can only be operated with a single detector tube when MuPAD is installed[9] and therefore only the two satellite reflections associated with the magnetic propagation vector $\boldsymbol{k}_1$ could be accessed experimentally (both MIRA and MuPAD do not support to lift the detector out of the horizontal scattering plane). In order to maximise the intensity on the magnetic reflections the experiment was not performed in a SANS geometry where the sample is oriented in such a way that the Bragg condition is fulfilled for both satellites concurrently but in a small angle diffraction geometry where the sample is rotated (rocking scan) in such a way that the intensity is maximal for a single reflection at a time only. The two magnetic reflections $+\boldsymbol{k}_1 = [\zeta, \zeta, \zeta]$ and $-\boldsymbol{k}_1 = [\overline{\zeta}, \overline{\zeta}, \overline{\zeta}]$ on which the SNP experiment was carried out are shown in Fig. 5.20 as they were observed in a θ-2θ-scan.

5.3.3.1 Temperature dependence of the polarisation tensor

We measured polarisation tensors on both magnetic satellite peaks $+\boldsymbol{k}_1$ and $-\boldsymbol{k}_1$ as a function of temperature. The tensors were measured with the initial polarisation vector $\boldsymbol{P}_0$ directed parallel (+) and antiparallel (-) to the x,y and z-direction of the analysis frame defined in Fig. 2.3(b), respectively. As we have seen in section 2.4.3 a circular magnetic helix completely polarises the beam parallel to the x-direction independent of the direction of the initial polarisation vector $\boldsymbol{P}_0$ if the scattering vector $\boldsymbol{Q}$ is parallel to the magnetic propagation vector $\boldsymbol{k}$ (compare the polarisation tensors in table 2.2). Therefore the polarisation tensor in the helical phase of MnSi on both satellite reflections

[9] As described in section 2.4.2 the experimental coordinate frame used for SNP is rotated together with the scattering vector. Further MuPAD itself has only one exit channel which can be only oriented with respect to one scattering at a time (cf. section 2.5).

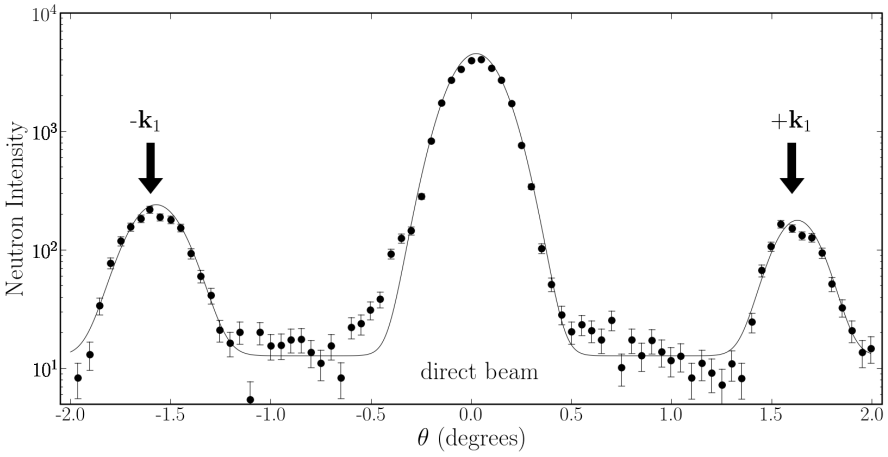

Figure 5.20: The θ-2θ-scan shows the two magnetic satellite reflections $+\boldsymbol{k}_1$ and $-\boldsymbol{k}_1$ on which the SNP experiment was carried out, as observed on MIRA in the single detector mode. The reflections are situated around the reciprocal space position (0,0,0), i.e. the direct beam position.

$+\boldsymbol{k}_1$ and $-\boldsymbol{k}_1$ should be

$$\mathrm{P} = \begin{pmatrix} 1 & 0 & 0 \\ 1 & 0 & 0 \\ 1 & 0 & 0 \end{pmatrix}. \tag{5.27}$$

The sign is reversed with respect to the tensor in table 2.2 since the helix in MnSi is left-handed. Further the tensor is identical for $+\boldsymbol{k}_1$ and $-\boldsymbol{k}_1$ because in contrast to the example in table 2.2 the scattering vector $\boldsymbol{Q}$ changes its direction between the measurements on the positions (0,0,0) $\pm$ $\boldsymbol{k}_1$. Hence, the coordinate frame for the measurement of the polarisation tensors is not identical for $\pm\boldsymbol{k}_1$ but rotated by π around the z-axis since the analysis frame for SNP measurements is defined by the direction of $\boldsymbol{Q}$ (s. Fig. 2.3(b)). In the example in table 2.2 this is not the case as the polarisation tensors were calculated for the reflections $\boldsymbol{Q}_\pm = (0, 0, 1 \pm k)$ where the direction of $\boldsymbol{Q}$ is identical for both satellites. For $\mathrm{T} < \mathrm{T}_{c1}$ the polarisation matrices that were observed in the experiment have the form of Eq. 5.27 as demonstrated in table 5.1 for T = 5 K. The reduction of the elements of the polarisation tensor P_{ix} (x-component of the final polarisation vector $\boldsymbol{P'}$ is analysed, compare Eq. 2.73) is due to the non-ideal supermirror benders used in the experiment. We note that the matrices show a deviation from zero on all elements P_{iz}. It has been discussed in detail in reference [Ber06] that the observed deviation in the elements is due to a stray field parallel to the y-axis of the MuPAD coordinate frame in the MuPAD zero field chamber. The stray field is located upstream of the MnSi sample and rotates the x-component of the final polarisation vector towards the z-direction. In this regard, we also want to highlight that for neutrons with a wavelength of $\lambda = 9.7$ Å already tiny fields have a significant impact on the polarisation vector. E.g. if neutrons with $\lambda = 9.7$ Å travel over 1.5 m (length of the MuPAD device) in a field of 5mG (approximately 1/100 of the Earths magnetic field) they are already rotated by 20°. Therefore, the performance

Table 5.1: Polarisation tensors for MnSi measured at T = 5 K on the two magnetic satellite reflections $\pm\boldsymbol{k}_1$ for the incident polarisation vector being $\boldsymbol{P}_0$ polarised parallel (+) and antiparallel (-) to the x,y and z-direction of the analysis frame defined in Fig. 2.3(b), respectively

	$\boldsymbol{P}'(+\boldsymbol{k}_1)$			$\boldsymbol{P}'(-\boldsymbol{k}_1)$		
$\boldsymbol{P}_0$	x	y	z	x	y	z
+x	+0.77(2)	+0.02(3)	+0.28(3)	+0.71(4)	−0.09(5)	−0.32(5)
+y	+0.778(7)	−0.03(1)	+0.27(1)	+0.816(8)	−0.00(1)	−0.35(1)
+z	+0.788(9)	+0.01(1)	+0.25(1)	+0.811(8)	−0.01(1)	−0.32(1)
-x	+0.783(7)	−0.01(1)	+0.29(1)	+0.819(6)	+0.02(1)	−0.33(1)
-y	+0.79(1)	−0.04(2)	+0.29(1)	+0.814(9)	−0.02(2)	−0.32(2)
-z	+0.769(8)	−0.01(1)	+0.31(1)	+0.81(1)	+0.01(2)	−0.32(2)

of MuPAD is still quite impressive under these tough conditions. Finally, as we are interested in measuring a change of the polarisation matrix as a function of temperature we can neglect this problem anyway as we will see in the following.
The elements of polarisation tensor P_{ix} remain at about 0.8 for both magnetic satellites until the transition temperature is approached at around 29.8 K as demonstrated in Fig. 5.21. The elements P_{iz} show a temperature dependence that follows exactly the behaviour for the elements P_{ix}, however scaled to the smaller value of approximately 0.25. This supports our statement in the previous section that there is a stray field in the zero field chamber of MuPAD downstream of the sample that rotates the x-components of the polarisation vector towards z. The elements P_{iy} are approximately equal to zero over the whole temperature region. From here on, we will neglect the elements P_{iy} and P_{iz} and focus on the elements P_{ix} that show a significant change around the critical temperature interval.
Within the helical magnetic phase the polarisation tensor stays essentially unchanged and the interesting temperature interval is in the vicinity of the transition temperature. The temperature interval between 20 and 32 K is shown in a detailed view in Fig. 5.22, where for convenience only the elements P_{ix} are presented. For the (-)-polarisation tensor the three elements are identical below T_{c1} = 29 K. Above T_{c1} they start to decrease and it seems that the elements yx and zx decrease slightly faster compared to the element xx. We note that at T_{c1} additionally the magnetic intensity drops significantly similar to the unpolarised experiment. Above T_{c2} = 30.5 K all elements are reduced to zero within the errorbars and all magnetic intensity has vanished. For the (+)-polarisation tensor the differences between the element xx and the other two are more significant. As for the (-)-tensor yx and zy do not change below T_{c1}, however, the xx-element already starts to decrease from its original value at $T^* \approx 22$ K and reaches $P_{xx} \approx 0.6$ at T_{c1}. At T_{c1} also the yx- and zy-elements start to decrease and the xx-element drops with a steeper slope. On the (+)-tensor the elements behave inverted with respect to the (-)-tensor and xx is reduced faster. The temperature behaviour of the yx and zy elements is however identical for both the (+) and (-) tensors. Similarly to the (-)-tensor all elements are reduced to zero at T_{c2}.

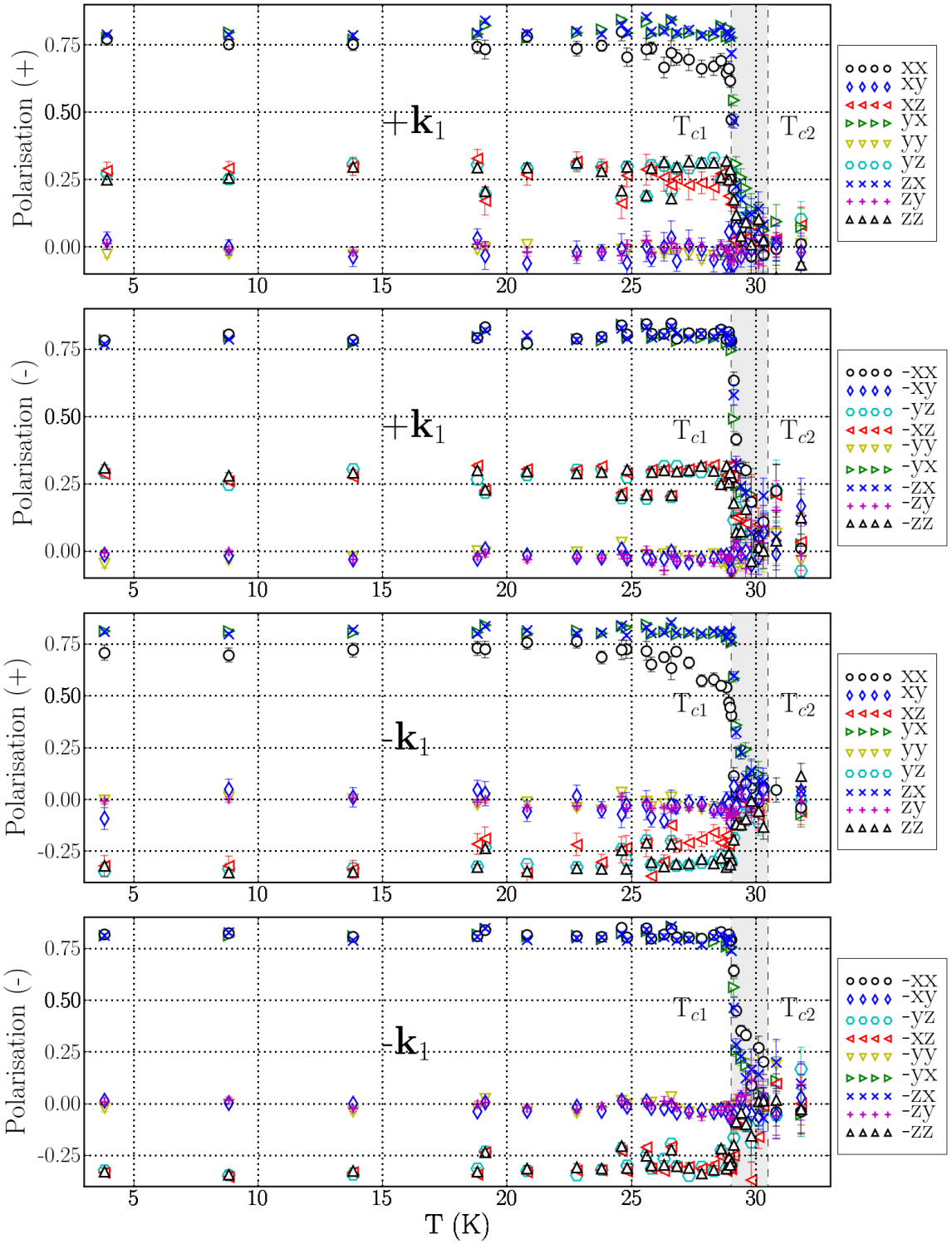

Figure 5.21: The temperature dependence of the polarisation tensors for MnSi measured on the two magnetic satellite reflections $+\boldsymbol{k}_1$ and $-\boldsymbol{k}_1$ around the direct beam position. The polarisation tensors have been measured with the initial polarisation vector $\boldsymbol{P}_0$ being directed parallel (+) and antiparallel (-) to the x,y and z-direction of the analysis frame defined in Fig. 2.3(b), respectively

Two independent experiment have been carried out to verify the observed temperature dependence of the polarisation tensor. The figures shown so far have been measured in 2007 and will be referred to as 2007 experiment from now on. In a previous experiment carried out in 2006 we have observed an identical temperature dependence of the polarisation tensor as shown in Fig. 5.23. In 2006 we have only measured the polarisation behaviour on the magnetic satellite reflection $-\boldsymbol{k}_1$ though, and additionally the measurement was limited to the polarisation tensor with positive incoming polarisation vector (+). The temperatures T^* and T_{c1} identified in 2006 are identical to the ones found in 2007. However, the temperature T_{c2} is found to be 31 K in 2006, and additionally the difference between the elements yx/zy and xx is much more pronounced compared to 2007.
Both measurements were carried out under identical conditions (both on MIRA; same wavelength, same cryostat). The only significant difference between the two experiments is the setting of the apertures used in front of the sample, hence, the $\vec{Q}$-resolution in the respective experiments was different.

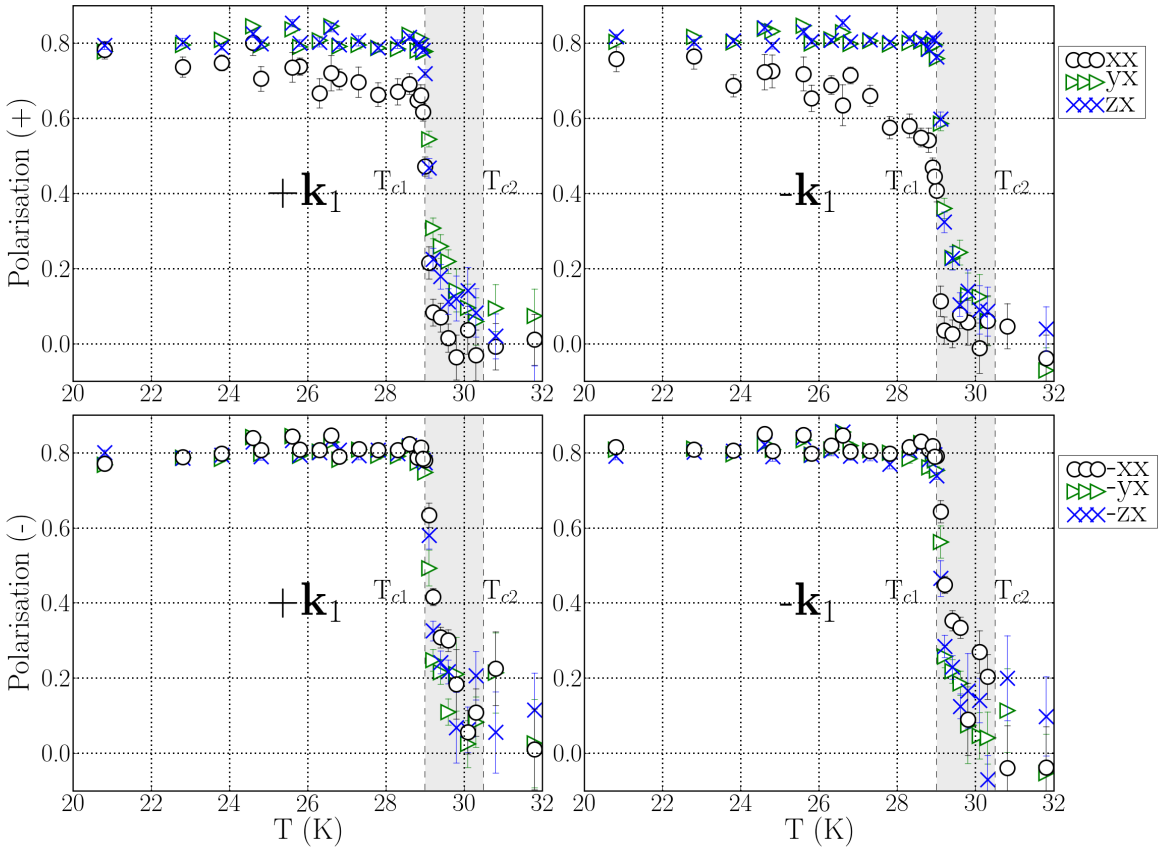

Figure 5.22: A detailed view of the temperature dependence of the relevant polarisation tensor elements P_{ix} in the interesting temperature interval is shown. The complete observed temperature range and all elements are provided in Fig.5.21.

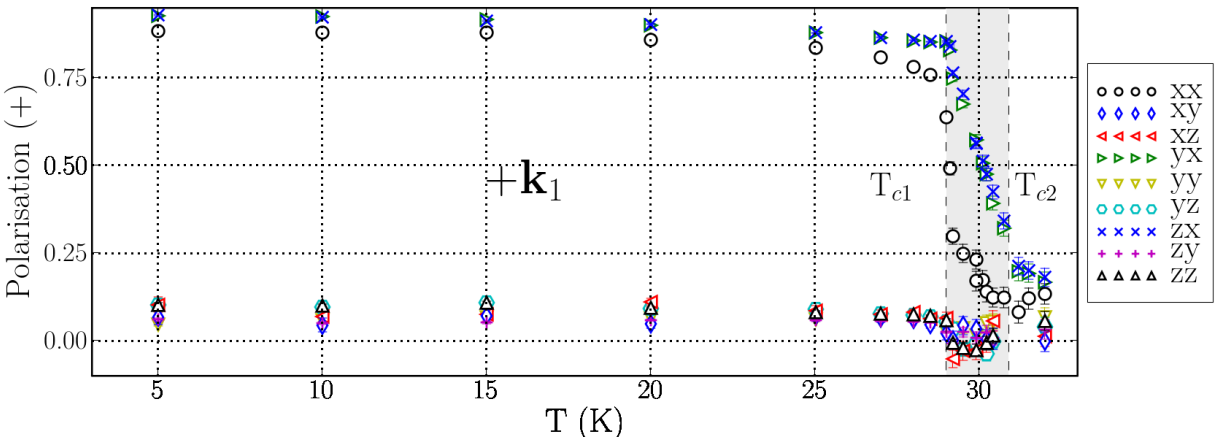

Figure 5.23: The temperature dependence of the polarisation tensor as observed in second experiment performed in 2007 is provided. The tensor was only measured on the satellite $-\boldsymbol{k}_1$ and with the initial polarisation vector $\boldsymbol{P}_0$ directed parallel to the x, y, and z-direction (+).

5.3.3.2 Considerations concerning the Q-resolution

Before we discuss the temperature dependence of the polarisation tensor with respect to possible models we want to clarify the difference between the experiments carried out in 2006 and 2007, respectively. Similar to the SANS experiment performed with unpolarised neutrons on MIRA (compare section 5.3.2) the neutron beam was collimated by a computer-controlled variable source aperture of rectangular cross-section that was installed directly after the monochromator and a cadmium aperture of approximately 15 mm diameter that was mounted directly on the sample holder. In table 5.2 an overview over the used distances and aperture sizes is provided.
We will approximate the resulting $\boldsymbol{Q}$-resolution in an identical manner as for the SANS experiment, since the only difference is the replacement of the area detector with a single ^{3}He counting tube. Based on the Eq. A.4 presented in appendix according to reference [PPM90] we calculated the resolution for both experiments. For the calculation for the experiment in 2006, we have treated the problem in two cases for the different horizontal and vertical extent of the source aperture, respectively. Eq. A.4 is derived for circular apertures, however the difference for apertures where only the extent in one dimension is considered at a time is negligible for our case (compare e.g. Fig. 3 in reference [PPM90]). This is because we are only interested in the order of magnitude of the difference between the 2006 and 2007 experiments. The results are presented in table. 5.3. Here *horizontal* denotes the resolution parallel to scattering vector and *vertical* the resolution perpendicular to the scattering plane.
We see that the $\boldsymbol{Q}$-resolution parallel to the scattering vector is almost identical for both experiments. In contrast to this the transverse resolution ΔQ_t is more than a factor 2 larger for the experiment in 2006 compared to the experiment in 2007. We will see in the following that this difference qualitatively explains the difference in the two experiments.

Table 5.2: Instrument parameters that determine the $\boldsymbol{Q}$-resolution for the two SNP measurements performed with MIRA/MuPAD in 2006 and 2007.

Instrument Parameter	Variable	2006	2007
Incoming wave vector (Å^{-1})	K	0.64	0.64
Scattering angle (degrees)	θ	1.7	1.7
Source aperture horizontal (mm)	$r_{1,h}$	8	5
Source aperture vertical (mm)	$r_{1,v}$	21	5
Defining aperture horizontal (mm)	$r_{2,h}$	7.5	7.5
Defining aperture vertical (mm)	$r_{2,v}$	7.5	7.5
Distance Source aperture - defining aperture (mm)	L	750	800
Distance Defining aperture - detector (mm)	l	2100	2100

Table 5.3: Results for the approximation of the $\boldsymbol{Q}$-resolution for the two SNP measurements performed with MIRA/MuPAD in 2006 and 2007.

Resolution parameter	Variable	2006	2007
horizontal angular resolution (degrees)	$\Delta\beta_h$	1.4	1.4
vertical angular resolution (degrees)	$\Delta\beta_v$	3.0	1.4
horizontal $\boldsymbol{Q}$-resolution, FWHM (Å^{-1})	ΔQ_l	0.015	0.016
vertical $\boldsymbol{Q}$-resolution, FWHM (Å^{-1})	ΔQ_t	0.034	0.016

5.3.3.3 Interpretation of the polarisation tensor

As has been discussed in section 5.1.3 the appearance of magnetic intensity on a sphere in reciprocal space above T_c may be interpreted as unpinning of the helix vector. Our results with unpolarised neutrons presented in section 5.3.2 are also in agreement with this assumption since we have observed that the cubic anisotropic energy that fixes the direction of the helix along the cubic diagonals decreases significantly above T_{c1}.
In terms of the skyrmion model that was introduced in section 5.2.1 we can imagine the underlying magnetic structure as magnetic helices that propagate in multiple directions simultaneously (s. Fig. 5.6(c)). Alternatively one could think that the crystal splits up in many domains with a unique propagation direction $\boldsymbol{k}_i$ of the magnetic helix in each of them. This was already illustrated in the lower right inset of Fig. 5.4. These two models for the magnetic structure can hardly be distinguished in neutron scattering as configuration domains that only differ with respect to their propagation vector (cf. section 3.3.1) just show up as additional magnetic satellite reflections. The same is true for a magnetic structure with multiple propagation vectors within one domain (multi-$\boldsymbol{k}$-structure). The only difference might be due different domain populations in the case of the configuration domains. Therefore we will not distinguish between the two models in the following.
In Fig. 5.24 such a magnetic structure is depicted schematically in reciprocal space around the position (0,0,0) that corresponds to the direct beam. Each of the magnetic helices

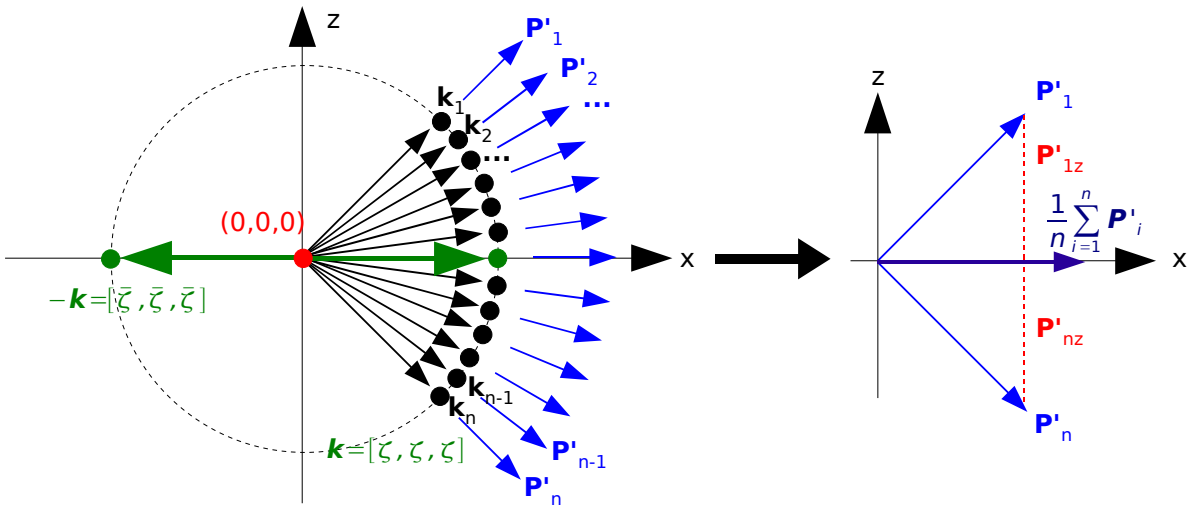

Figure 5.24: A possible toy model with multiple magnetic helices for the magnetic structure of MnSi above T_{c1} is shown in reciprocal space around the (0,0,0) position. Each of the black arrows denotes the propagation vector $\boldsymbol{k}_i$ of the helix i. Each of the helices polarises the beam parallel to its propagation vector as illustrated by the blue arrows. On the right side it is demonstated that an average over the different final polarisation vectors $\boldsymbol{P}'_i$ associated with each helix in the SNP analysis frame leads to a final propagation vector $\boldsymbol{P}' = \frac{1}{n}\sum_{i=1}^{n}\boldsymbol{P}'_i$ that is parallel to the x-direction of the analysis frame.

i will polarise the beam parallel to its propagation vector $\boldsymbol{k}_i$ as denoted by the blue arrows in the figure. In our experiment we would average over a certain number of the magnetic satellite reflections depending on the resolution perpendicular to the direction x in the drawing. Hence, we would also average over the final polarisation vectors $\boldsymbol{P}'_i$ associated with each of the reflections. Our measurements have been performed in the analysis frame defined via the original reflection $\boldsymbol{k}_1 = [\zeta,\zeta,\zeta]$ (cf. Fig. 2.3(b)) in the helical phase that is also denoted in the figure. As shown on the right hand side of Fig. 5.24 the average over the corresponding final polarisation vectors $\boldsymbol{P}' = \frac{1}{n}\sum_{i=1}^{n}\boldsymbol{P}'_i$ always results in a final polarisation vector that is parallel to the x-direction. We note that this result is independent of the number of different helices over that we average. Consequently, this toy-model for the magnetic structure above T_{c1} does not explain our results. This has also been verified in a numerical integration.
In section 5.3.2 we have successfully described our results obtained by unpolarised SANS measurements by the model for helical critical scattering as derived by Maleyev [GMO+05]. Starting from the magnetic susceptibility proposed by Maleyev we have additionally derived the expression for the final polarisation vector due to this model provided in Eq. 5.5. In Fig. 5.25 we have plotted the magnetic intensity as function of $\boldsymbol{q}$ as described by Eq. 5.4 that already has been used in section 5.3.2. However, here we have considered an incident neutron beam that is polarised parallel to the $x-$,$y-$ and z-direction of the analysis frame (top row of subfigures) in contrast to e.g. Fig. 5.17. Further the polarisation values for all terms of the polarisation tensor described by Eq. 5.5 are illustrated (three lower rows

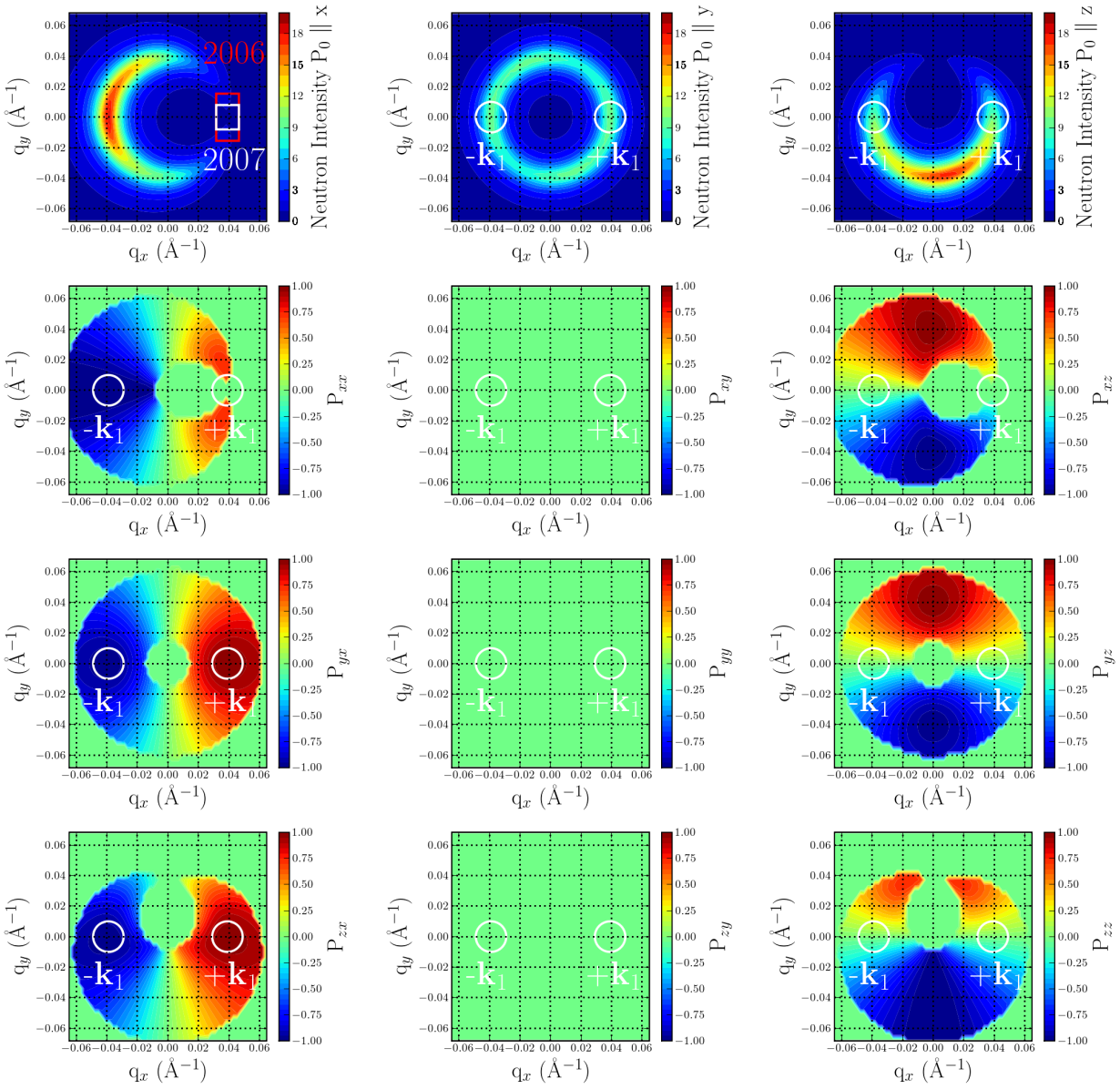

Figure 5.25: The upper row of subfigures shows a simulation of the magnetic intensity distributions according to Eq. 5.4 for the initial polarisation vector $\boldsymbol{P}_0$ being directed parallel to the $x-$,$y-$ and $z-$direction of the analysis frame of the magnetic reflection $+\boldsymbol{k}_1$. The remaining subfigures show a simulation of the polarisation values for all elements of the polarisation tensor as described by Eq. 5.5. For the simulation we have considered $|\boldsymbol{P}_0| = 0.9$. Further the simulation has been performed with the parameters $B_2 = 1.61$ meVÅ^2 and $\kappa = 0.00743$ Å^{-1} for Eqs. 5.4 and 5.5 as they have been found by fits in section 5.3.2 for T = 29.4 K.

of subfigures). For the plots of the polarisation we have additionally considered that if no magnetic scattering is observed at a distinct position in reciprocal space also the polarisation has to be equal to zero. The plots presented in Fig. 5.25 have been simulated using the values for the parameters that have been obtained in the fits of the magnetic intensities to Eq. 5.4 for T = 29.4 K in section 5.3.2. These are $B_2 = 1.61$ meVÅ^2 and $\kappa = 0.00743$ Å^{-1}. Otherwise the same parameters as in section 5.3.2 have been used. We have set the magnitude of the incident polarisation vector to $|\boldsymbol{P}_0| = 0.9$ to take into account that the used polariser is non-ideal and does not polarise the beam perfectly. The plots correspond to the polarisation tensor in the (+) setting.
By inspecting the values of the polarisation for the different elements of the polarisation at the reciprocal lattice position corresponding to the magnetic satellite $\boldsymbol{k}_1$ (the position is denoted by the white circles in Fig. 5.25), we see that they are qualitatively very similar to what we have observed in the experiments. The elements P_{iy} and P_{iy} are equal to zero. In addition the elements yx and zx are fully polarised, whereas the element xx is significantly reduced. In order to verify if the model for the helical critical scattering can reproduce our experimental results we calculated the polarisation tensor for different temperatures with the help of Eq. 5.5 by using the values for B_2 and κ that were obtained in the fits of the magnetic intensities in section 5.3.2. The polarisation values were consequently averaged over the size of the $\boldsymbol{Q}$-resolution that has been calculated in the previous paragraph. The resolution for the two experiments carried out in 2006 and 2007 are denoted by the red and white rectangular in the upper left subfigure in Fig. 5.25, respectively. The result of this calculation is shown in Fig. 5.26 for $29.1 \leq T \leq 31.5$ K and for the elements P_{ix}. The other elements are not shown for the clarity of the presentation as they are equal to zero for all temperatures. This averaging calculation has been performed for positive and negative incident polarisation vector.
For the (+) polarisation tensors the polarisation values in Fig. 5.26 describe the observed

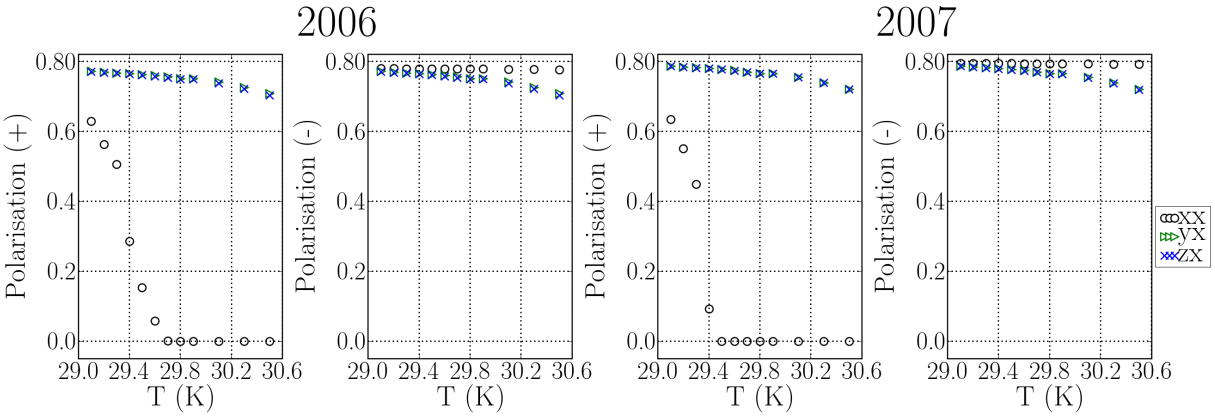

Figure 5.26: A simulation of the polarisation tensor elements P_{ix} as a function of temperature is shown. The resolution of the two experiments performed in 2006 and 2007 has been taken into account. The respective resolutions for 2006 and 2007 are denoted by the red and white rectangle in the upper left subfigure in Fig. 5.25 .

effect that the element xx is smaller than the other two elements yx/zx already for T_{c1} well. Similar to the experiment this is not the case for the (-) polarisation tensor. Additionally the xx element decreases fast as function of increasing temperature for the (+) tensor, whereas the other two elements decrease slowly. The temperature dependence of the yx/zx elements is identical for both the (+) and the (-) polarisation tensor, as it was also observed in the experiment. Additionally the xx element for the (-) tensor decreases slower as a function of temperature compared to the yx/zx elements, which is also very similar to the experiment. Thus, we conclude that the main features of the experiments are described qualitatively by the model for the helical critical scattering. The main difference is that the decrease of the elements yx/zx for the (+) and (-) cases and for xx in the (+) case is too slow as a function of increasing temperature.
Finally we also want to review the difference between the experiments performed in 2006 and 2007 with respect to the $\boldsymbol{Q}$-resolution. The simulation summarised in Fig. 5.26 for both experiments shows that due to the better $\boldsymbol{Q}$-resolution in the experiment of 2007 the xx term decreases faster as a function of temperature when compared to the 2006 experiment. However, the calculated effect is much smaller than the difference that has been observed between the two experiments. Yet, our calculations based on the theory for helical critical scattering proposed by Maleyev [GMO$^+$05] reproduce the change of the polarisation tensor in the critical temperature interval above T_{c1} qualitatively well. In contrast, the first model for the magnetic structure (s. Fig. 5.24) does not predict any change of the polarisation tensor in the critical temperature interval. Therefore, we conclude that the model of Maleyev provides the correct description of our experimental findings.

5.3.4 Investigation of the helical Goldstone modes

We examined the existence of the proposed helimagnons (cf. section 5.2.3) using the triple-axis spectrometer TASP [SRB01] situated at the end position of a cold supermirror guide of the continuous spallation neutron source SINQ at Paul Scherrer Institut. In order to avoid second order contamination of the neutron beam a beryllium filter was inserted between the sample and the analyser. For the experiment the single crystal sample A (s. section 5.3.1) was inserted in an ILL-type orange He-cryostat[ora] and was oriented with the [1,1,0] and [0,0,1] crystallographic directions within in the scattering plane.

5.3.4.1 Experimental constraints and setup

As mentioned earlier in section 5.2.3, the specific anisotropic shape of the excitations in the helical phase is expected to become visible for small magnitudes of the reduced scattering vector $\boldsymbol{q}$. This constraint of small q can be understood qualitatively as follows. Due to the long period of the magnetic helix in MnSi (180 Å), its magnetic structure is locally, i.e. over length scales corresponding to a few lattice constants (a = 4.558 Å),

almost ferromagnetic. If magnetic correlations over such small distances, that correspond to rather large reduced scattering vectors q, are measured, a ferromagnetic dispersion will be observed. Consquently, in order to investigate the characteristic properties of helimagnetic fluctuations, we have to probe magnetic correlations over length scales of the order of the period of the helix. Hence, the experiment is basically restricted to a relatively small portion of reciprocal space around a magnetic satellite reflection that fulfils the constraint $q \simeq k$.
The experiment was performed around the nuclear Bragg reflection (1, 1, 0) due to the large magnetic structure factor of the corresponding magnetic Bragg reflections (compare e.g. table I in reference [ISTK77]). The reciprocal lattice in the proximity of this reflection is illustrated in Fig. 5.27 together with the positions where constant-$\boldsymbol{Q}$ scans have been carried out to probe the magnetic excitations. We emphasise that the constraint $q \simeq k$ requires an excellent instrumental resolution in both $\boldsymbol{Q}$ and energy. E.g. from Maleyev's model we can estimate that the energy of the dispersion branch that propagates parallel to the propagation vector at $q = k = 0.035$ Å^{-1} [10] is $\epsilon_{\parallel,-} = 97.8$ μeV.[11] Thus a high energy resolution is essential to be able to resolve the excitations from the incoherent scattering at $\hbar\omega = 0$ (cf. section 2.2.2).
Finally all scans were performed in two setups that had their respective emphasis on resolution and intensity. For setup I the triple-axis spectrometer was operated with fixed final wave vector $k_f = 1.2$ Å^{-1}. Additionally 20' Soller collimators were installed in the incident beam and in front of the analyser whereas 40' have been used in front of the detector. For setup II the resolution was slightly relaxed in favour of higher intensity. The final wave vector was fixed at $k_f = 1.4$ Å^{-1} and the collimation in front of the sample and the analyser was replaced by 40' and in front of the detector by 80', respectively. The energy resolution in setup I and II is approximately 70 μeV and 90 μeV, respectively. The corresponding $\boldsymbol{Q}$-resolution is depicted in Fig. 5.27.

5.3.4.2 Measurements and results

All scans that will be shown in the following have been performed at a temperature of 20 K. This choice for the temperature assures on the one hand that the intensity is not unduly suppressed due to the Bose factor (cf. Eq 2.53) and on the other hand that the measurements have been performed significantly below T_c and therefore in the helical phase. Both theories by Maleyev and Belitz propose magnetic excitations in the helical phase with an anisotropic dispersion for the directions parallel and perpendicular to the magnetic propagation vector of the helix. We have therefore carried out inelastic scans at reciprocal lattice positions, where the reduced scattering vector $\boldsymbol{q}$ was parallel or perpendicular to the propagation vector $\boldsymbol{k}_1 = [\zeta, \zeta, \zeta]$ of configuration domain 1. The reciprocal lattice positions where scans have been performed are denoted by the red squares and

[10] Here, we measure q from the magnetic satellite.

[11] Here we used the parameters estimated in Maleyev's paper [Mal06], namely: A = 52 meVÅ^2, S = 0.8, $\omega_0 = 28.5$ μeV, $k = 0.035$ Å^{-1}.

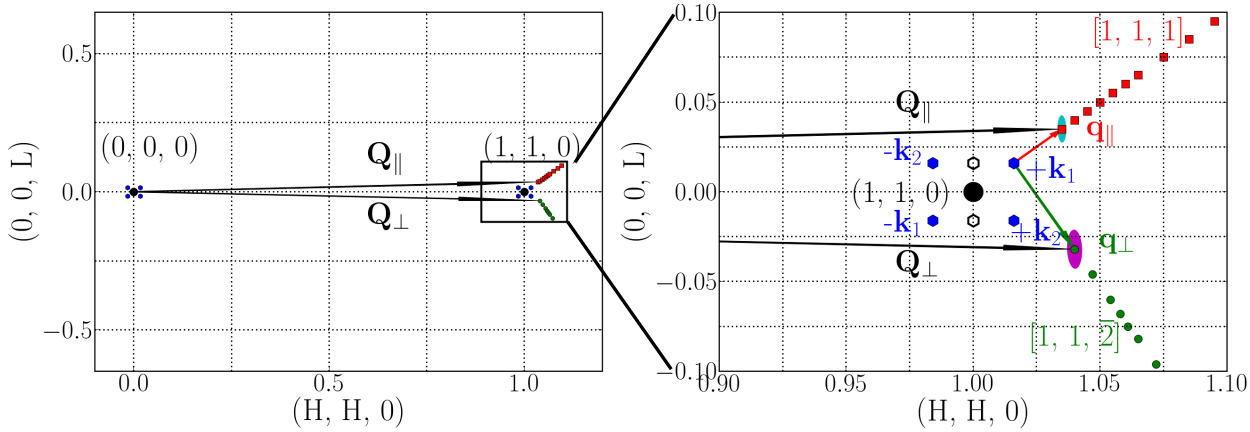

Figure 5.27: The reciprocal lattice in the proximity of the (110) nuclear Bragg reflection, where all inelastic scans were performed is illustrated to scale. Black circles denote nuclear Bragg reflections whereas the blue hexagons denote magnetic satellite reflections. White hexagons illustrate the positions of the out of plane satellites. For clarity of the presentation the interesting region is displayed magnified on the right hand side. Red squares and green circles indicate positions on the reciprocal lattice corresponding to to the directions that are parallel and perpendicular to the propagation vector $\boldsymbol{k}_1$, respectively. On these positions constant-$\boldsymbol{Q}$ scans have been performed in order to probe the dispersion of the helimagnons. The cyan and and magenta ellipsoids denote the $\boldsymbol{Q}$-resolution of setups I and II, respectively (s. text for detail).

green circles in Fig. 5.27 for the parallel and perpendicular directions, respectively. However, we note that in the orientation of the sample used for this experiment additionally the magnetic satellite reflections due to configuration domain 2 associated with the magnetic propagation vector $\boldsymbol{k}_2$ are present in the scattering plane (compare section 5.1.1 and section 3.3.1) and additional contributions from magnetic excitations emerging from this magnetic configuration domain might be expected.

We probed the dispersion of the excitations in the helical phase by means of constant-$\boldsymbol{Q}$-scans. This allowed for easy separation of the dispersion branches with respect to their energy. Some typical scans are shown in Fig. 5.28. Before we discuss the results of the measurements we want to emphasise that the flux of the SINQ neutron source was about 170% [Roe06] for the scans parallel to $\boldsymbol{k}$ when compared to scans perpendicular to $\boldsymbol{k}$.[12]. The intensity of the observed magnetic excitations was weak and the couting time per point was approximately 25 mins. In order to compensate for the smaller source flux we used setup II (s. proceeding section) with a slightly relaxed resolution setting for the scans along the perpendicular direction.

We discuss now the data shown in Fig. 5.28. The strong elastic peak at 0 meV is due to incoherent scattering (s. section 2.2.2). The scans with $\boldsymbol{q} \parallel \boldsymbol{k}_1$ clearly show only one

[12]The solid lead target of the SINQ neutron source at the PSI was temporarely replaced by the liquid metal target *MEGAPIE*[GFJK+04] in the year 2006 for test purposes, which led to an increase of the neutron flux by 70%.

dispersion branch is visible. Further, in the direction perpendicular to $\boldsymbol{k}_1$ two distinct peaks corresponding to two dispersion branches are observed. This already demonstrates that the dispersion of the magnetic excitations in the helical magnetic phase is anisotropic as it was proposed by theory.

5.3.4.3 Fits with the model of Maleyev

We have performed fits of our data to the model of Maleyev by using Eq. 5.19 for scans in the direction parallel to $\boldsymbol{k}_1$, whereas Eq. 5.21 has been employed for the perpendicular direction. Here the respective expressions for the inelastic neutron scattering cross-section have been obtained by inserting the imaginary parts of the corresponding magnetic susceptibilities Eqs. 5.20 and 5.22 in Eq.2.53. For the fits of the scans the neutron cross-section has been convoluted with the four-dimensional resolution function of the spectrometer with the help of the program *tasresfit* (s. appendix D). We note that the imaginary part of the magnetic susceptibilities calculated by Maleyev are obtained by substituting [Mal07] (s. also reference [Mal02])

$$\frac{-1}{\omega^2 - \epsilon^2} \longrightarrow \frac{\pi}{2\epsilon} \left[\delta(\omega - \epsilon) - \delta(\omega + \epsilon)\right]. \tag{5.28}$$

Since δ-functions are difficult to model in the numerical four-dimensional resolution deconvolution we have replaced them by damped harmonic oscillator (DHO) profiles with a finite linewidth Γ:

$$\frac{\omega\Gamma}{(\omega^2 - \Gamma^2)^2 - (\omega\Gamma)^2}. \tag{5.29}$$

The parameters that were varied in the fits were the spin wave constant A, the linewidth Γ and an overall scale parameters to match the intensities. The components of the demagnetisation tensor parallel and perpendicular to $\boldsymbol{k}$, namely N_{cc} and $N_{\perp}$ were fixed at zero as the experiment was carried out without an external field. The dipolar energy was fixed at its values $\omega_0 = 28.5$ μeV. For the modulus of the propagation vector we employed the value we found in the experiments by $\boldsymbol{Q}$-scans over the magnetic satellites, namely k = 0.037 Å^{-1}. Finally we introduced a constant background and a Gaussian profile centred at $\hbar\omega$= 0.01 meV to describe the incoherent scattering.
Each scan was fitted individually with the obtained cross-section. The resulting best fits are shown as solid lines in Fig. 5.28 and the obtained value for the spin wave stiffness constant A is provided for each scan. The dispersion that was calculated from the fitted values is shown for both the parallel and perpendicular directions in Fig. 5.29(a). The differences of the spin wave stiffness between distinct scans might appear rather large, however, we note that the observed deviations only lead to small differences in the shape of the dispersions represented by Eqs. 5.19 and 5.21. To obtain a single value of the spin wave stiffness constant A we fitted Eqs. 5.19 and 5.21 to the peak positions as defined by the fitted parameters A found in the individual scans. The resulting dispersion curves are

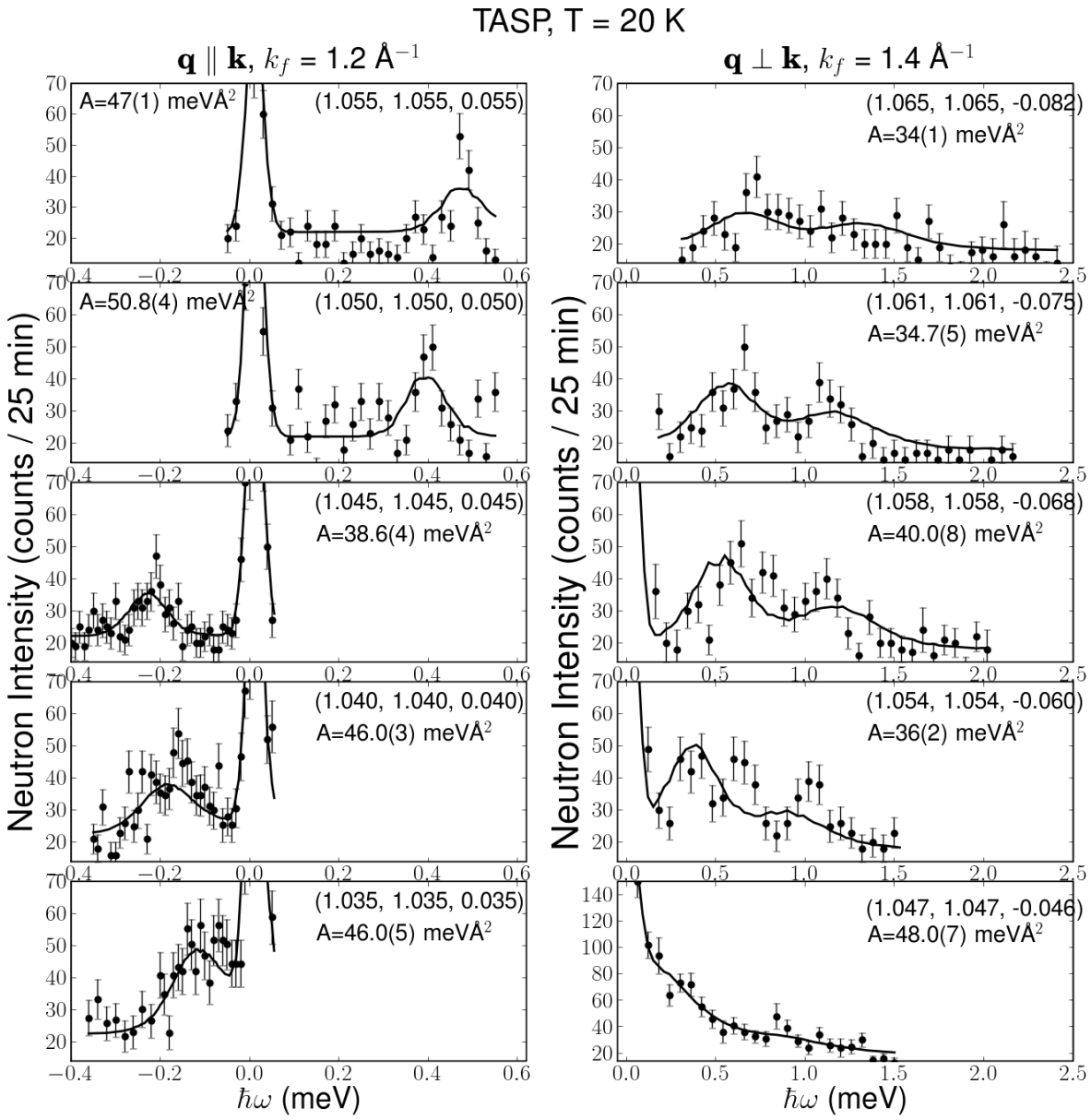

Figure 5.28: The results of the inelastic scans performed on TASP at T = 20 K in the helical magnetic phase are shown. The left and right hand side show scans that were performed at reciprocal lattice positions, where the reduced vector $\boldsymbol{q}$ is parallel and perpendicular to the propagation vector $\boldsymbol{k}$, respectively. The solid lines are fits to the data with the model of Maleyev (s. section 5.2.3). The large peak at $\hbar\omega \approx 0$ is due to incoherent scattering (s. section 2.2.2). For clarity of the presentation we have omitted its upper part. We note that the counting time per point was approximately 25 min.

given by the black and the green/blue lines in Fig. 5.29(a) for the parallel and perpendicular directions, respectively. The value for the spin wave stiffness constant obtained

from this fit amounts to $A = 43.7(7)$ meVÅ^2. In reference [GMO$^+$06a] the temperature dependence of the spin wave stiffness constant was determined to be

$$A(T) = A_0 \left[1 - c \left(\frac{T}{T_c}\right)^z\right], \tag{5.30}$$

with $A_0 = 50$ meVÅ^2, $c = 0.35$ and z = 2.4. Our measurements were performed at T = 20 K and by using $T_c = 29$ K we obtain $A(20\text{ K}) = 43.8$ meVÅ^2, which is in excellent agreement with our result based on the helimagnons. For comparison the magenta line in Fig. 5.29(a) shows the dispersion $\epsilon = Aq^2$ of ferromagnetic magnons as observed in the ferromagnetic phase of MnSi [SBE$^+$99, TBE$^+$98]. For large values of the wave vector $q \gg k$ (ferromagnetic limit) we expect that all the observed dispersion branches converge to follow this ferromagnetic dispersion. However, for $q \gg k$ the spectral weight of the observed modes becomes weak (cf. Fig. 5.28), because the collective magnetic excitations merge into the Stoner continuum of single particle excitations (s. also section 5.1.4), since MnSi is an itinerant magnet.
Further, our data indicate, that the branch $\epsilon_{\perp,+}$ of the dispersion indeed shows a small gap as predicted by Maleyev [Mal06]. From the fitted value of A it can be estimated to be $\Delta\epsilon = Ak^2\sqrt{2}$=85 μeV (s. section 5.2.3.2). As can be seen from the experimentally obtained positions of the $\epsilon_{\perp,+}$-branch (green triangles in Fig. 5.29(a)) this value is probably underestimated.
The linewidth found in the fits is provided in Fig. 5.29(b). For the direction parallel to $\boldsymbol{k}_1$ it is of the order of 2 μeV for all points apart for the two lowest values of q. This value is beyond the resolution limit of the used spectrometer, however this shows that the resolution deconvolution calculations in the fits were performed correctly. For the perpendicular directions it is significantly larger and of the order of 100 μeV. Here also the scans with smaller q's show a tendency to larger values of Γ. However, we believe that this is no systematic dependency, but rather a result of our approach for the fits. The equations derived by Maleyev only provide the shape of the dispersion branches for the directions that are exactly parallel and perpendicular to the propagation vector, and the dispersion for general directions are not known. Therefore, the $\boldsymbol{Q}$-resolution of the spectrometer in directions deviating from the special directions are not taken into account properly. The good agreement for the dispersion branches found via the fits and the theoretical model nevertheless justifies our approach. In addition a better procedure for the fits is only possible if appropriate theoretical equations for general directions are available. Another interpretation of the apbrupt changes of the linewidth, especially in the perpendicular direction, is that we see contributions from the second configuration domain. However, it is difficult to fit the data with both domains, due to the low statistics in the scans.

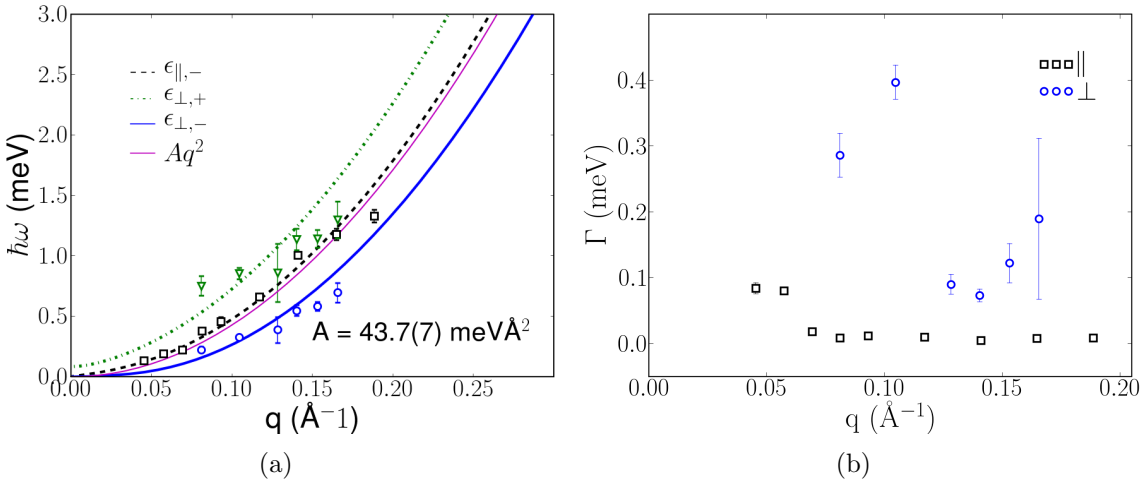

Figure 5.29: The figure summarises the results of the fits of the scans in Fig. 5.28 with the model of Maleyev (s. section 5.2.3). (a) The dispersion as found in the fits of the inelastic scans in Fig. 5.28 is illustrated. The green, black and blue lines are fits of the Eqs. 5.19 and 5.21, that describe the dispersions calculated by Maleyev, to the dispersions found in the measurements. For comparison the magenta line shows the dispersion $\epsilon = Dq^2$ of ferromagnetic spin waves with an identical spin wave stiffness $D = 43.8$ meVÅ^2. (b) The linewidth as function of q that we obtained in the fits.

5.3.4.4 First results with the model of Belitz

All the inelastic scans have been performed at reciprocal lattice positions, where $q > k$. Hence, Eqs. 5.10, 5.11 and 5.12 that provide the dispersion and magnetic dynamic susceptibility for the model of Belitz are not suitable to fit the measured scans since they were derived in the limit $q < k$ [Ros08]. However, based on the same model that we have introduced in section 5.2.3.1 Rosch also calculated numerical expressions for the dispersions of the helimagnons for $q > k$ [Ros08]. Similar to the analytical calculations of Maleyev presented in section 5.2.3.2 this numerical calculations take the occurance of umklapp processes into account. The interaction of the modes with wave vectors $\boldsymbol{q}$, $\boldsymbol{q} \pm n\boldsymbol{k}$ ($n = 1,\ldots, \infty$) also leads to a gap at $\boldsymbol{q} = 0$. The calculations of Maleyev are limited to a single umklapp interaction, whereas Rosch *et al.* consider a finite number of interactions. This essentially leads to much more modes with different spectral weights (depending on the number of umklapp interactions) that, however, still show the characteristic anisotropic shape. The presentation of these numerical derivations is rather involved and here we only show result of the calculations in Fig. 5.30. The size of the poins in the figure denotes the spectral weight of the corresponding mode.
The four dimesional convolution of the spectrometer resolution with the large number of dispersion branches, including the calculations of the respective spectral weights is rather complicated and time consuming and not completely finished. As a first result we show

the constant-$\boldsymbol{Q}$ scan carried out at the reciprocal lattice position (1.058, 1.058, -0.067), where Rosch has convoluted his theory with the spectrometer resolution. The result is shown by the solid line in Fig. 5.31. It shows that the agreement between measurement and theory is reasonable. The analysis of the other scans with respect to this model is still in preparation. However, this first result is already rather promising.

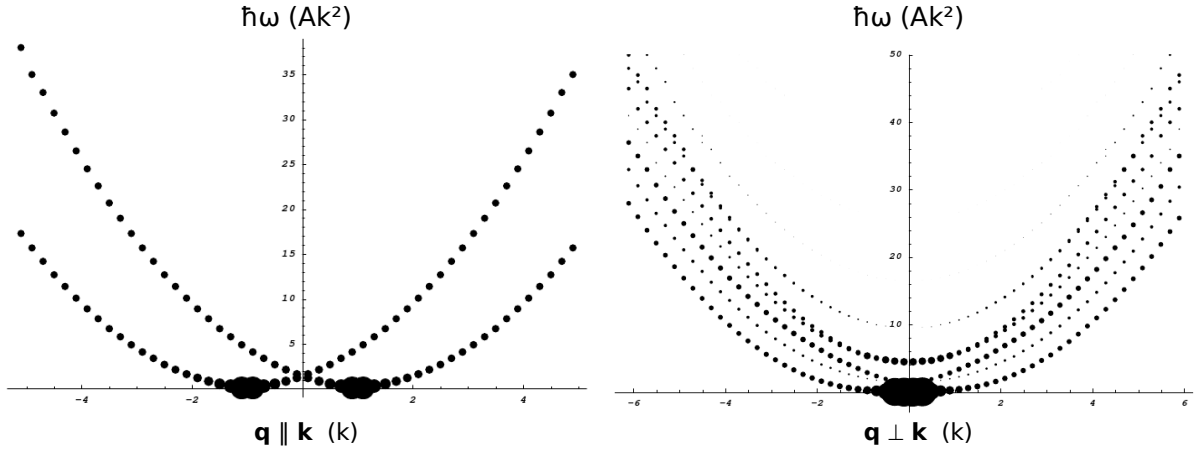

(a) (b)

Figure 5.30: The dispersion relation for the the helimagnons for $q > k$ obtained in numerical calculations by Rosch [Ros08] for the directions (a) parallel and (b) perpendicular to the propagation vector $\boldsymbol{k}$. The size of the points corresponds to their respective weight.

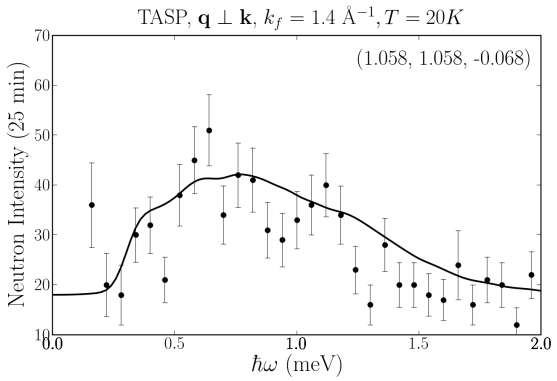

Figure 5.31: The solid line in the figure denotes the convolution of the dispersion of the helimagnons shown in Fig.5.30 with the spectrometer resolution for the reciprocal lattice position (1.058, 1.058, -0.067).

5.4 Discussion

In chapter 5 we investigated the existence of an intermediate magnetic phase in MnSi between the helically ordered and the paramagnetic phase that was recently proposed by theory [RBP06]. Additionally, extensive measurements of the collective magnetic excitations in the helical ordered phase were performed, as a new type of Goldstone mode for helimagnets without a centre of inversion has been recently discussed extensively [BKR07, Mal06].
We have carried out a detailed neutron scattering study of the diffuse magnetic scattering intensity that is observed in MnSi in a small temperature interval of approximately 2 K above $T_{c1} \approx 29$ K with both unpolarised and polarised neutrons. This magnetic scattering intensity is distributed over a sphere in reciprocal space that has a radius corresponding approximately to the pitch of the magnetic helix in the helical phase below T_{c1}. The appearance of this sphere is widely interpreted as the unlocking of the helix vector above T_{c1}. However, there is an ongoing discussion whether the magnetic intensity on the sphere can be regarded as a new intermediate magnetic phase formed by magnetic skyrmion patterns (cf. sections 5.4 and 5.2.1) or represents the critical scattering from a helimagnet (s. section 5.2.2).
Our unpolarised SANS results are well-fitted with the model for critical scattering from a helimagnet developed by Maleyev [GMO$^+$05]. The data clearly illustrates, that the magnetic intensity on the sphere is not distributed isotropically. Distinct maxima are visible on the sphere at the reciprocal lattice positions where the magnetic satellites are situated in the helical phase below T_{c1}. The intensity smears out more and more isotropically on the sphere when the temperature is increased. In our fits we were able to show that the parameter B_2 that describes the strength of the cubic anisotropy energy vanishes fast as function of temperature above T_{c1} described by the power law $B_2 = a\tau^{-\varrho}$ with $\varrho = 0.840(9)$. Since the cubic anisotropy locks the direction of the helix below T_{c1} this result clearly supports the scenario that the emergence of the sphere of magnetic intensity is linked to the unlocking of the propagation direction of the helix. Our data also indicates that the magnetic intensity observed on the magnetic satellite reflections in the helical phase is redistributed on a sphere above T_{c1}, which additionally supports this unlocking scenario. The fits to the model of Maleyev also showed that for a small temperature interval of approximately 0.3 K the observed anisotropic intensity on the sphere is not solely explained by the yet finite cubic anisotropy energy in the magnetic neutron cross-section described by Eq. 5.4. Additional intensity is observed on the sphere, indicating a cross-over regime, where both the magnetic satellite reflections due to persisting helical magnetic order and critical scattering coexist. Therefore, the theory of Maleyev, which is based on the model of a 2nd order phase transition, describes the experimental findings well in a first approximation, however, it has to be adapted to explain the coexistance of the magnetic Bragg reflections and the critical scattering in the cross-over regime.
In connection with this behaviour we also observed that the modulus of the propagation vector of the helix increases from k = 0.035 Å^{-1} at T = 6.4 K to 0.039 Å^{-1} at T_{c1}.

Thus, the pitch of the helix decreases from approximately 180 Å at low temperature to 161 Å at T_{c1}. This indicates that the second strongest energy scale in MnSi, namely the Dzyaloshinsky-Moriya interaction, becomes more significant with increasing temperature. Therefore, the angle between neighbouring spins in the helix increases, i.e. the system becomes less ferromagnetic. In the intermediate phase the radius of the sphere saturates at k $\approx$ 0.04 Å^{-1} corresponding to a period of 157 Å. The coexistence of the magnetic satellites and the critical scattering, together with the saturation of the propagation vector indicate a first order phase transition.

Further we have performed full polarisation analysis of the magnetic intensity above T_{c1}. The results indicate that a model of magnetic spirals propagating in multiple directions does not explain the observed polarisation tensors. Similar as for the unpolarised data, the temperature dependence of the measured polarisation tensors is in qualitative agreement with the model for critical magnetic scattering. We note that in the model for the skyrmions [RBP06] so far the term for the cubic anisotropy energy has been neglected because it is the weakest energy scale in MnSi. However, the fits and calculations for both the unpolarised and polarised neutron data clearly indicate that the cubic anisotropy energy is the decisive energy scale that drives the observed behaviour of MnSi between the temperatures T_{c1} and T_{c2}. A further interesting detail is that the element xx of the polarisation tensor measured on the magnetic satellites of MnSi already starts to deviate from its maximal value of approximately 0.8 at $T^* \approx 22$ K. As we identified that this decrease is at least qualitatively explained by the presence of magnetic critical scattering, indicating that already between T^* and T_{c1} critical magnetic fluctuations that drive the unlocking of the helix direction are present. This assumption is also in agreement with the unpolarised SANS data that shows that the magnetic satellite reflections already start to broaden azymuthally below T_{c1}. It will be interesting to characterise these fluctuations by measuring the corresponding quasielastic neutron scattering intensities by neutron spin echo methods.

In section 5.4 we have illustrated that the shoulder observed in the specific heat of MnSi at $T_{c2} = 30.5$ K may be interpreted as a second phase transition. Here we propose, based on our experimental findings, that the Lambda-shaped peak at $T_{c1} = 29$ K can be associated with the melting of the propagation direction of the helical magnetic order. However, the order breaks down due to transversal fluctuations of $\boldsymbol{k}$ that essentially leaves the magnetic helices intact but alters their propagation direction, which leads to the observed intensity on the sphere. The shoulder to the peak observed at $T_{c2} = 30.5$ K may then be interpreted as the temperature, where additionally the helical order of the spins breaks down. This is supported by the observation that the magnetic intensity from the magnetic satellites is redistributed on the sphere above T_{c1}. Therefore, it will be useful to carry out a more detailed study of the magnetic intensity on the sphere were the whole intensity is mapped out in rocking scans over a larger angular range and with finer steps compared to this work. Furthermore, such experiments will provide additional information about the cross-over regime, where both the helical magnetic order and the critical scattering coexist.

Finally we also investigated the dynamic magnetic susceptibility below T_{c1} by means

of inelastic neutron scattering. Our experiments clearly demonstrate that the specific magnetic excitations that were proposed independently by Belitz *et al.* [BKR07] and Maleyev [Mal06] for a helimagnet with Dzyaloshinsky-Moriya interaction are present in MnSi. The observed helimagnons show the distinct anisotropic dispersion with respect to the propagation direction of the magnetic helix as it was calculated by theory. The data could be well fitted by the dispersion relations calculated by Maleyev and a spin wave stiffness constant A = 43.7(7) meVÅ^2 was obtained for T = 20 K. This is in excellent agreement with the value $A(\mathrm{T} = 20\ \mathrm{K}) = 43.8$ meVÅ^2 calculated from the relation $A(T) = A_0\,[1 - c\,(T/T_c)^z]$ published in reference [GMO$^+$06a]. In addition our results indicate the existence of a small gap $\Delta\epsilon = Ak^2\sqrt{2}$=85 μeV for the dispersion branch perpendicular to the propagation vector. This gap is a result of the interaction between different helimagnon modes due to umklapp processes. The size of the gap is small due to the small size of the propagation vector $\boldsymbol{k}$, as $k/G \approx 40$ (G is the modulus of a reciprocal lattice vector). This leads to the occcurance of a large number of umklapp interactions that renormalise the size of the gap.

For the model of Belitz *et al.* only preliminary fits have been performed and the analysis is still going on. The first results presented in this work are promising, though. They essentially agree with the results obtained by the fits to the model of Maleyev.

Our experiments show that one mode of the helimagnons perpendicular to the propagation vector $\boldsymbol{k}$ is softer compared to the modes parallel to $\boldsymbol{k}$. This indicates that soft modes with $\boldsymbol{q} \perp \boldsymbol{k}$ are related to the unlocking of the propagation directions of the magnetic spirals that is observed in the SANS experiments at $\mathrm{T}_{c1} = 29$ K, whereas the hard mode with $\boldsymbol{q} \parallel \boldsymbol{k}$ is responsible for the destruction of the helical order at $\mathrm{T}_{c2} = 30.5$ K. The hardest mode perpendicular to $\boldsymbol{k}$ is related to the transition from the helical phase to the ferromagnetic phase in an applied external field. Hence, the observation of the proposed helimagnons also provides an intuitive explanation for the appearance of consecutive magnetic phase transitions in a rather small temperature interval of 1.5 K in MnSi.

A question that remains unanswered so far is the influence of the four different configuration domains that in principle should give four distinct contributions to the magnetic excitations in the helical magnetic phase. This issue is difficult to overcome with our current data set that suffers from relatively low statistics. However, we plan to overcome these difficulties by further experiments that will be carried out on the triple-axis spectrometer PANDA situated at the cold source of the high flux neutron source FRM-II in Munich. For the proposed experiment we will field-cool the MnSi crystal in a weak magnetic field, which is larger than 80 mT ($H \gtrsim H_{c1}$, see section 5.1.1). This procedure will prepare the sample in a state with a single configuration domain without destroying the magnetic helix. The data shall also provide more accurate estimates for the gap. The proposal for this experiment has already been accepted and the experiment is planned for October 2008.

Chapter 6

Conclusion and Outlook

The chiral magnetism in the multiferroic compound $NdFe_3(^{11}BO_3)_4$ and the itinerant helimagnet MnSi has been investigated by neutron scattering. In the first chapter we give an overview over the domain of chiral magnetism, which currently attracts a great deal of scientific interest in various fields of condensed matter physics, e.g. magnetic surfaces and interfaces [BHvB$^+$07, BR01], spintronics [HBBB06], multiferroics[Kim07, CM07] and superconductivity [BHM$^+$04, FAKS04, KAS05]. In chapter 2 we establish the basic theory of neutron scattering that was used as primary tool for the investigations in this work. The high potential of this microscopic probe for the investigation of chiral magnetism was highlighted, especially when polarised neutron scattering techniques are applied. Further, we summarise how the use of symmetry analysis facilitates magnetic structure analysis based on magnetic neutron diffraction data in chapter 3.

In chapter 4 the results of bulk properties combined with a detailed neutron diffraction study with unpolarised and polarised neutrons on the non-centrosymmetric multiferroic compound $NdFe_3(^{11}BO_3)_4$ were presented. This compound is a member of the family of borates $RM_3(BO_3)_4$ (R = Y,La-Lu, M = Al, Ga, Cr, Fe, Sc) that currently attract much attention because of their special optical properties [Jaq01, HCC$^+$02, CLJ$^+$01] that are important for laser techniques. Our study identified that $NdFe_3(^{11}BO_3)_4$ displays antiferromagnetic long-range order below $T_N \approx 30$ K in agreement with the literature, however, we could additionally establish that below $T_{ICM} \approx 13.5$ K the antiferromagnetic order becomes incommensurate with respect to the underlying chemical structure. By means of magnetic representation analysis and Rietvield refinement of the powder diffraction patterns two different magnetic models for the commensurate phase could be identified that explain the data sets measured with unpolarised neutrons equally well. The use of spherical neutron polarimetry ultimately allowed to exclude one model. For the correct structure the magnetic moments of both magnetic ions Fe^{3+} and Nd^{3+} are oriented parallel to the hexagonal basal plane. Magnetic moments in adjacent hexagonal planes are coupled antiferromagnetically corresponding to a magnetic propagation vector $\boldsymbol{k}^{hex} = [0,$

0, $\frac{3}{2}$]. The magnetic moments of all three Fe sublattices have the same amplitude and are mutually parallel. Further the SNP data suggests that also the magnetic moments of the Nd ions are parallel to the Fe magnetic moments. However, we note that the preliminary analysis of more recent data measured on a second sample at HEIDI at FRM-II (that has not been considered in this work) favour a non-zero angle of approximately 45° at 1.6 K between the magnetic moments of the Fe and Nd ions within the hexagonal basal plane. Yet, the result from the single crystal experiments suffer from problems with extinction due to a rather large crystal and additionally the SNP data is more sensitive to the orientation of magnetic moments. Moreover, this suggests that the angle between the moments of the Fe and Nd sublattices is sample dependent.
Below T_{ICM} the observed incommensurate propagation vector amounts to $\boldsymbol{k}_i^{hex} = [0,\ 0,\ \frac{3}{2} + \varepsilon]$ where $\varepsilon(1.6\ K)$ was determined to be 0.00667 at 1.6 K. By means of polarised neutron diffraction below T_{ICM} we identified that the magnetic structure is transformed into a long-period antiferromagnetic spiral that propagates parallel to the c-direction with a pitch of approximately 1140 Å. In addition our data suggests that there is only a single chirality domain in $NdFe_3(^{11}BO_3)_4$. This is quite interesting as generally both chirality domains are expected to be present and thus this might be related to the fact that the chemical structure is non-centrosymmetric, similar to the magnetic helices in MnSi or UPtGe [Bro01] that both possess no inversion symmetry.
At T = 1.6 K the magnetic moment of the Fe^{3+} ions amounts to approximately 5.1 μ_B (4.9 μ_B if a non-zero angle between Fe and Nd sublattices is assumed) which is closed to the value for free Fe^{3+}. The magnetic moment of the Nd^{3+} sublattices saturates at 1.51 μ_B (2.7 μ_B if a non-zero angle between Fe and Nd sublattices is assumed), and is therefore reduced of the value 3.3-3.7 μ_B for free Nd^{3+} (s. e.g. [Blu01]), which is presumably due to the crystal fields that were observed and calculated in reference [PCS+07].
The observation of third order harmonics of the magnetic satellites at the positions (0, 0, 3/2 ± 3ε) additionally indicates the formation of a magnetic soliton lattice in $NdFe_3(^{11}BO_3)_4$. A soliton is the appearance of localised or topological defects in periodic structures due to the presence of non-linear forces. Such non-linear forces can be due to an external magnetic field that interacts with the magnetic moments or due to magnetic anisotropy in the plane perpendicular to the propagation vector. A magnetic soliton lattice can be imagined as a magnetic helix that is not yet completely incommensurate, e.g. a distorted commensurate magnetic structure with domain walls (cf. Fig. 4.17). Alternating periods of commensurate parts and domain walls then lead to the observed third order harmonics. The observation of magnetic soliton lattice without the application of external forces like magnetic fields or mechanical stress are rather unlikely and to the best of our knowledge the only other compound for which a magnetic soliton lattice was reported without the application of an external magnetic field is CuB_2O_4 [RSP+01]. For $NdFe_3(^{11}BO_3)_4$ we propose that the magnetic soliton lattice arises due to a magnetic anisotropy in the basal hexagonal plane that is presumably of second order type. This assumption is based on the magnetic susceptibility data reported in reference [TKH+07]. However, the assumption of the appearance of a magnetic soliton lattice is only based on the observation of the third order harmonics of the magnetic satellites and we have no de-

tailed knowledge of the spin-Hamiltonian leading to the observed behaviour. Consequently it would be interesting to carry out further inelastic neutron scattering experiments in order to probe the magnetic interactions being responsible for the magnetic ground state of $NdFe_3(^{11}BO_3)_4$.

In chapter 5 we reported on our experiments on the helimagnet MnSi. We investigated the magnetic intensity that is spread over a sphere in reciprocal space in a small temperature interval of approximately 2 K above the magnetic ordering temperature T_{c1} by means of unpolarised and polarised neutron diffraction experiments. The sphere has a radius corresponding approximately to the pitch of the magnetic helix in the helical phase below T_{c1} and is usually interpreted as the unlocking of the helix propagation vector above T_{c1}. Roessler *et al.* [RBP06] recently demonstrated theoretically that the Dzyaloshinsky-Moriya interaction may not only stabilise straight-forward helical order, but additionally complex magnetic textures, when the amplitude of the local magnetisation is soft and supports strong longitudinal fluctuations, e.g. near critical phase transitions. It was speculated that the observed magnetic scattering on the sphere at $T \gtrsim T_{c1}$ in MnSi may originate from such a magnetic texture. In contrast, Grigoriev *et al.* have interpreted this experimental result as critical scattering from a helimagnet [GMO$^+$05]. Our experimental results are partly compatible with the latter scenario. The theory proposed by Maleyev [GMO$^+$05] for the critical scattering in MnSi above T_c explains the observation of the magnetic intensity on the sphere, however, it fails to explain a cross-over regime, that was identified in our measurements. In the cross-over regime the magnetic Bragg reflections from the helical magnetic order and the critical scattering coexist in a small temperature interval of 0.3 K. Further the fits of our data to the model for the critical scattering published in reference [GMO$^+$05] illustrate that the magnetic anisotropy energy quickly decreases above T_{c1} as a function of temperature described by the power law $B_2 = a\tau^{-\varrho}$ with $\varrho = 0.840(9)$. This clearly supports the scenario that the emergence of the sphere of magnetic intensity is linked to the unlocking of the propagation direction of the helix. Furthermore this illustrates that the magnetic anisotropy in MnSi is the decisive energy scale that drives the observed behaviour of MnSi between the temperatures T_{c1} and T_{c2} despite being the smallest magnetic energy scale. Hence, it has to be included in the theoretical models. For instance the calculations in reference [RBP06] do not take the cubic anisotropy energy into account. In this context it is also interesting to note that the pitch of the helix decreases from approximately 180 Å at low temperature to 161 Å at T_{c1}. This indicates that the second strongest energy scale in MnSi, namely the Dzyaloshinsky-Moriya interaction, becomes more significant with increasing temperature and the angle between neighbouring spins in the helix increases, i.e. the system becomes less ferromagnetic.
The decrease of the element xx of the polarisation tensor measured on the magnetic satellites of MnSi already $T^* \approx 22$ K additionally indicates that already between T^* and T_{c1} critical magnetic fluctuations that drive the unlocking of the helix direction are present. This assumption is also in agreement with the unpolarised SANS data that shows that the magnetic satellite reflections already start to broaden azymuthally below T_{c1}. The

neutron resonance spin echo spectrometers TRISP and RESEDA situated at the FRM-II provide a unique possibility to study the critical dynamics in MnSi. First measurements on TRISP have already been performed but the analysis of the corresponding data is not yet finished. Additionally a project has been started with a new master student on RESEDA in order to further investigate the dynamics of the critical scattering in MnSi.
Finally we have also carried out extensive inelastic measurements on a triple-axis spectrometer in the helical phase. Our experimental observations clearly demonstrate that the specific magnetic excitations that were proposed independently by Belitz *et al.* [BKR07] and Maleyev [Mal06] for a helimagnet with Dzyaloshinsky-Moriya interaction occur in MnSi. The observed helimagnons show the distinct anisotropic dispersion with respect to the propagation direction of the magnetic helix as it was calculated by theory. The data could be well fitted to the equations calculated by Maleyev and a spin wave stiffness constant A = 43.7(7) meVÅ^2 was obtained for T = 20 K, which agrees perfectly with the value A = 43.8 meVÅ^2 published in reference [GMO$^+$06a]. Moreover, our results show the existence of a small gap $\Delta\epsilon = Ak^2\sqrt{2}$=85 μeV that was also predicted by theory of Maleyev [Mal06]. For the model of Belitz *et al.* only preliminary fits have been performed and the analysis is still going on. The first results presented in this work are promising and essentially agree with the results obtained by the fits to the model of Maleyev.
The mode of the helimagnons perpendicular to the propagation vector $\boldsymbol{k}$ is softer compared to the mode parallel to $\boldsymbol{k}$. This suggests that soft modes with $\boldsymbol{q} \perp \boldsymbol{k}$ are related to the melting of the propagation directions of the magnetic spirals that is observed in the SANS experiments at T_{c1} = 29 K. In contrast the hard mode parallel to the propagation directions is responsible for the destruction of the helical order at T_{c2} = 30.5 K. Finally the transition from the helical phase to the ferromagnetic phase in an applied external field then is related to the hardest mode perpendicular to $\boldsymbol{k}$. Hence, the observation of the proposed helimagnons also provides an intuitive explanation for the appearance of consecutive magnetic phase transitions in a small temperature interval of 1.5 K in MnSi.
In further experiments we plan to investigate the dispersion of the identified helimagnons in more detail. In order to resolve possible problems in our fits due to the presence of the four configuration domains in MnSi we will carry out experiments with a MnSi crystal that will be field-cool in a weak magnetic field. This procedure will prepare a crystal with a single configuration domain without destroying the magnetic helix. The proposal for this experiment has already been accepted and the experiment is planned for October 2008. In addition we intend to examine the influence of temperature and pressure on the dispersion of the helimagnons. This will allow to determine whether these magnetic excitations that are characteristic for a helimagnet are able to explain some of the peculiar properties of MnSi.
As we have seen in section 1.3 chiral magnetism was identified as an essential driving mechanism in different fields of condensed matter physics. The theoretical concepts that lead to the proposition of the helimagnons are not limited to the specific case of MnSi but can be transferred to other compounds that display the Dzyaloshinsky-Moriya interaction. Therefore the experimental identification of the helimagnons may be of fundamental importance in a whole series of materials.

Appendix A

Neutron scattering instruments

Here we will briefly describe the different types of neutron scattering instruments that were used during this work.

A.1 Powder diffractometer

Neutron powder diffraction is used for the determination of chemical and magnetic structures of specimen. The method relies on the specific preparation of the samples that consists of milling crystalline samples into fine powders with typical crystallite sizes of mm-μm. The orientation of the crystallites in the powder is assumed to be completely random. A monochromatic beam prepared by a monochromator crystal is scattered at the powder sample. Due to the large number of crystallites and their respective random orientation a part of them will always fullfil the Bragg condition in Eq. 2.19 for a specific conditions. This gives rise to a so-called *Debye-Scherrer cone* for each Bragg reflection as it is shown in Fig. A.1(a). To observe these cones generally large multi-detector arrays that cut the cones in one plane (denoted by the cylinder in Fig. A.1(a)) are used. A schematic layout of a powder diffractometer is shown in Fig.A.1(b).

A.2 Single crystal diffractometer

In a single crystal diffraction setup monochromatic neutrons prepared by a monochromator crystal are impinged on a single crystal sample. A movable detector that can be positioned around the sample and only covers a small part of the solid angle is used to detect neutrons scattered by the sample (s. Fig A.2). Consequently only specific orientations of the sample with respect to the detector fulfil the condition for Bragg scattering in Eq. 2.19 for a given Bragg reflection reflection. The sample is therefore mounted on a

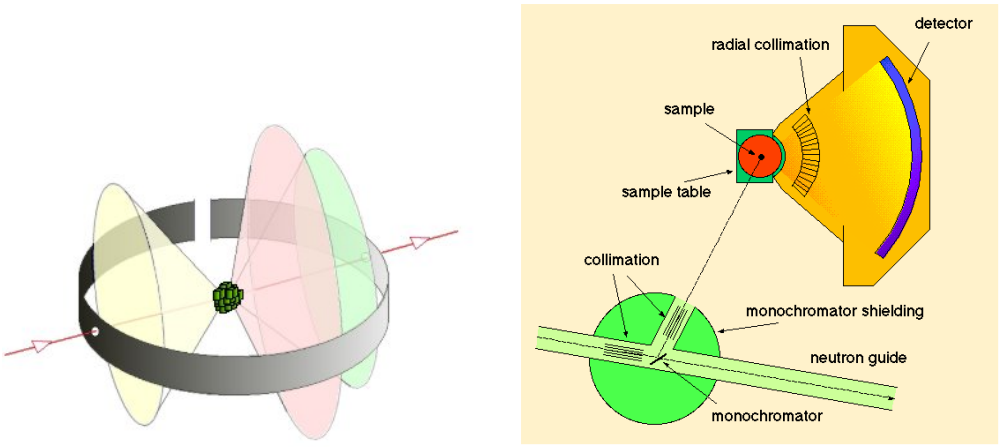

(a) (b)

Figure A.1: (a) Debye-Scherrer cones as they appear from the diffraction of a monochromatic beam from a powder sample are shown. The grey cylinder schematically displays the position of a multi-detector array that will be used to experimentally observe the cones. The picture is taken from the webpage: `http://www.matter.org.uk/diffraction/x-ray/powder_method.htm`. (b) A schematic of the powder diffractometer DMC at Paul Scherrer Institut that was used for this work is shown [FKSK00].

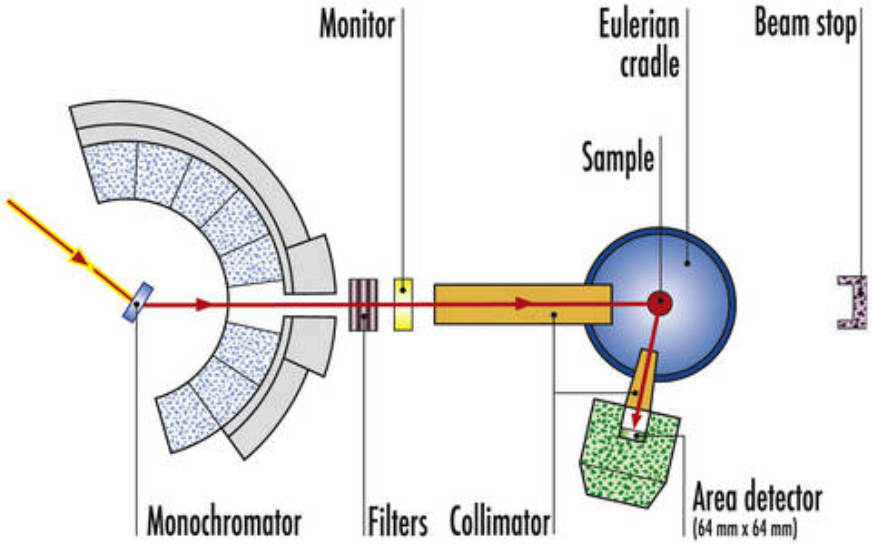

Figure A.2: A schematic layout of a single crystal diffractometer is shown.

Eulerian cradle that allows for almost free orientation of the sample with respect to the detector and allows to rotate it into the Bragg condition. For chemical or magnetic structure determination one needs to compare the relative intensities on a large set of different reflections. For a precise comparison integrated intensities of Bragg reflections are measured by rotating the sample through the Bragg condition. There are two modes of operation that are typically used:

- ω-scans: only the sample is rotated with respect to the detector. The angle for this rotation is generally called ω. In such a scan the modulus of the scattering vector is not changed but its direction is changed as the Bragg reflections are rotated through the Ewald sphere (approximately a transverse $\boldsymbol{Q}$-scan).
- $\omega/2\theta$-scan or $\theta/2\theta$: 2θ is the angle between the incident and final neutron wave vectors (s. also Fig.2.14) and therefore corresponds to the orientation of the detector with respect to the incident beam. Both angles are changed simultaneously in the same direction, where the angular steps of 2θ are chosen to be twice as large as in ω. Such a scan corresponds keeping the direction of the scattering vector fixed but changing its modulus (longitudinal $\boldsymbol{Q}$-scan).

A.3 Triple-axis spectrometer

Triple-axis spectroscopy (TAS) is in general used to measure the dispersion of excitations in condensed matter systems. Two well-characterised crystals up- and downstream of the sample are used as monochromator and analyser, respectively. Both can be rotated in order to select a specific incident wave vector $\boldsymbol{k}_i$ and a specific final wave vector $\boldsymbol{k}_f$ via Bragg's law in Eq. 2.19. Additionally the mutual orientation between $\boldsymbol{k}_i$ and $\boldsymbol{k}_f$, and thus the scattering vector $\boldsymbol{Q}$, can be chosen via a third axis on which the specimen to be investigated is mounted. A schematic layout and a photograph of a triple-axis spectrometer (TAS) are shown in Fig. A.3(a) and A.3(b), respectively. By a distinct choice of orientations between the three axes for the monochromator, sample and analyser a specific momentum transfer $\hbar\boldsymbol{Q}$ and energy transfer $\hbar\omega$ (compare Eq. 2.1) on the sample is selected and the neutron scattering cross-section is determined at the corresponding point in $(\boldsymbol{Q}, \omega)$-space.
There a two typical operation modes for a TAS:

- constant-$\boldsymbol{Q}$ scan: the instrument is adjusted to a specific scattering vector $\boldsymbol{Q}$ and the energy transfer $\hbar\omega$ is varied throughout a scan. This is achieved by leaving e.g. $\boldsymbol{k}_f$ fixed and varying the modulus of $\boldsymbol{k}_i$ during the scan. However, in order to fulfil the condition of momentum and energy conservation (compare Eq. 2.1) the orientation of $\boldsymbol{k}_f$ with respect to $\boldsymbol{k}_i$ has to to be changed (for a constant modulus!) by changing the sample angle $2\theta_S$ (s. Fig. A.3(a)).
- constant-energy scan: the situation is reversed, in a scan the scattering vector is

varied for a constant energy transfer $\hbar\omega$. A constant-energy scan is realised by fixing the modulus of $\boldsymbol{k}_i$ and $\boldsymbol{k}_f$ and changing their mutual orientation.

In Fig. A.4(a) a constant-$\boldsymbol{Q}$ scan is shown in reciprocal space. The result of both types of scans in a measurement to determine the dispersion of a phonon is shown in Fig. A.4(b). Fig. A.4(b) also illustrates that the resolution of a TAS in ($\boldsymbol{Q}$,ω)-space is finite due to the finite mosaicity of the crystals employed as monochromator andanalyser and the finite beam divergence. The resolution function of a TAS is a four-dimensional ellipsoid whose shape depends on the actual spectrometer configuration [Pop75]. A nice introduction to the complex calculation of the resolution function and to the deconvolution of it from experimental data is provided in [Ber06]. We note that also the type of scan that will be performed mostly depends on the orientation of the resolution ellipsoid with respect to the dispersion of the excitation and is chosen in such a way that the resolution is optimised.

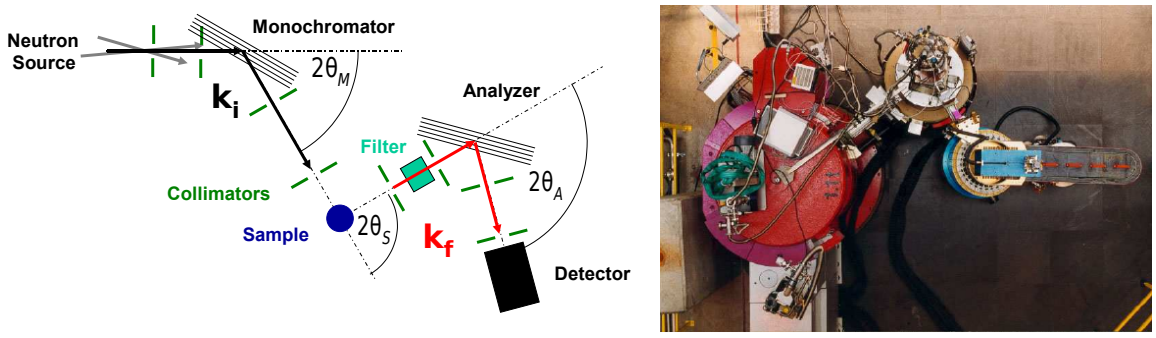

(a) (b)

Figure A.3: (a) A schematic layout of a triple-axis spectrometer. (b) The triple-axis spectrometer TASP [SRB01] at the Paul Scherrer Institut that was used for this work is shown.

A.4 Small angle neutron scattering

Small angle neutron scattering (SANS) is an elastic scattering method that allows to probe spatial correlations in a sample on a rather large length scale (compared to interatomic distances) that ranges between nm and μm. We have seen in chapter 2 that in neutron scattering spatial correlations in real space lead to an intensity distribution $I(\boldsymbol{Q})$ in reciprocal space. As distances in real space d and reciprocal space τ are related via $d\tau = 2\pi$ (s. Eq. 2.14), spatial correlation over large distances in real space are observed at small scattering vectors $\boldsymbol{Q}$. For elastic scattering the modulus of the scattering vector can be described as a function of the neutron wavelength λ and the scattering angle θ (cf. Fig. 2.1) as

$$Q = \frac{4\pi}{\lambda}\sin(\theta). \tag{A.1}$$

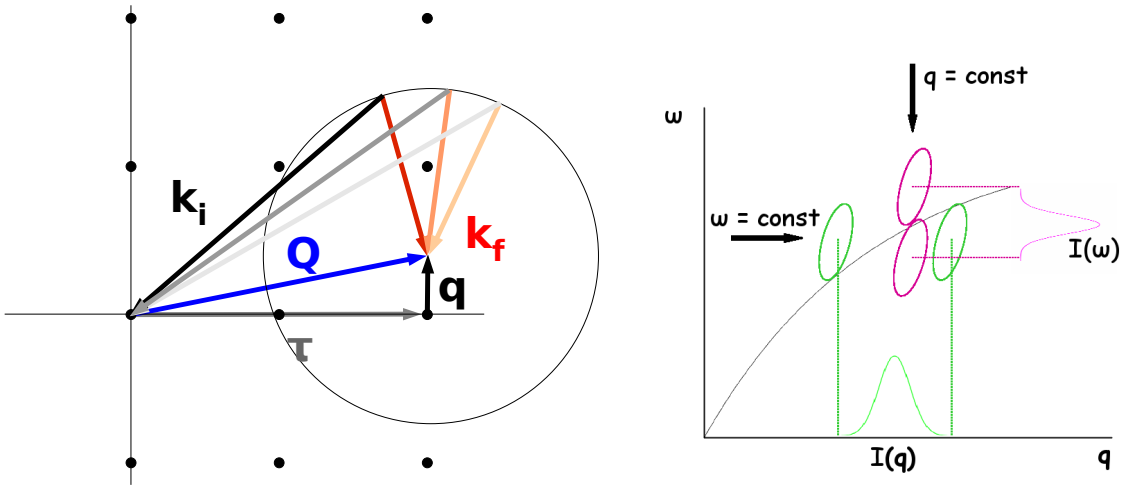

(a) (b)

Figure A.4: (a) A constant-$\boldsymbol{Q}$ scan with fixed modulus of $\boldsymbol{k}_f$ is demonstrated (b) The result of a constant-$\boldsymbol{Q}$ scan (red) and a constant-energy scan (green)over over the acoustic branch of a phonon a demonstrated.

Consequently small values of Q are achieved in an experimental setup by either increasing the neutron wavelength or decreasing the scattering angle. To improve the angular resolution in order to perform scattering experiments with small scattering angles generally the flight path between the sample and the detector is increased. The simple SANS setup on the instrument MIRA at the research reactor FRM-II in Munich that was used during this work is displayed in Fig. A.5.
In the case of the simple setup shown in Fig. A.5 the experimental resolution in the detector plain is mainly defined by the aperture system installed in front of the sample. Given that the distance between the source aperture and the sample is denoted by L, the distance between the sample and detector denoted by l, and the radii r_1 and r_2 of the source and sample apertures, respectively, are known, the angular FWHM resolution on the detector parallel to the scattering vector $\boldsymbol{Q}$ can be approximated by the analytical expression (s. [PPM90])

$$\begin{aligned}
\Delta\beta_h &= 2\frac{r_1}{L} - \frac{1}{2}\frac{r_2^2}{r_1}\frac{\cos^4\langle 2\theta\rangle}{l^2 L}(L + l/\cos^2\langle 2\theta\rangle)^2, \quad \text{for} \quad r_1 \geqslant r_2, \\
\Delta\beta_h &= 2r_2\left(\frac{1}{L} + \frac{\cos^2\langle 2\theta\rangle}{l}\right) - \frac{1}{2}\frac{r_1^2}{r_2}\frac{l}{L}\frac{1}{\cos^2\langle 2\theta\rangle(L + l/\cos^2\langle 2\theta\rangle)}, \quad \text{for} \quad r_1 < r_2,
\end{aligned} \tag{A.2}$$

where $\langle 2\theta \rangle$ is the mean scattering angle for which the resolution is calculated. Similarly the angular resolution perpendicular to the scattering vector $\boldsymbol{Q}$ is given by:

$$\begin{aligned} \Delta\beta_v &= 2\frac{r_1}{L} - \frac{1}{2}\frac{r_2^2}{r_1}\frac{\cos^2\langle 2\theta\rangle}{l^2 L}(L + l/\cos\langle 2\theta\rangle)^2, \quad \text{for} \quad r_1 \geqslant r_2, \\ \Delta\beta_v &= 2r_2\left(\frac{1}{L} + \frac{\cos\langle 2\theta\rangle}{l}\right) - \frac{1}{2}\frac{r_1^2}{r_2}\frac{l}{L}\frac{1}{\cos\langle 2\theta\rangle(L + l/\cos\langle 2\theta\rangle)}, \quad \text{for} \quad r_1 < r_2, \end{aligned} \tag{A.3}$$

The corresponding longitudinal (radial) and transverse $\boldsymbol{Q}$-resolutions are further given by

$$\begin{aligned} \Delta Q_l &= \langle K\rangle \cos\langle\theta\rangle \Delta\beta_1, \\ \Delta Q_t &= \langle K\rangle \Delta\beta_2. \end{aligned} \tag{A.4}$$

Here $\langle K\rangle = k_i = k_f$ is the mean modulus of the experimental wave vector. Of course this is only a lower limit for the approximation of the resolution function as there are additional effects due to a finite wavelength spread.

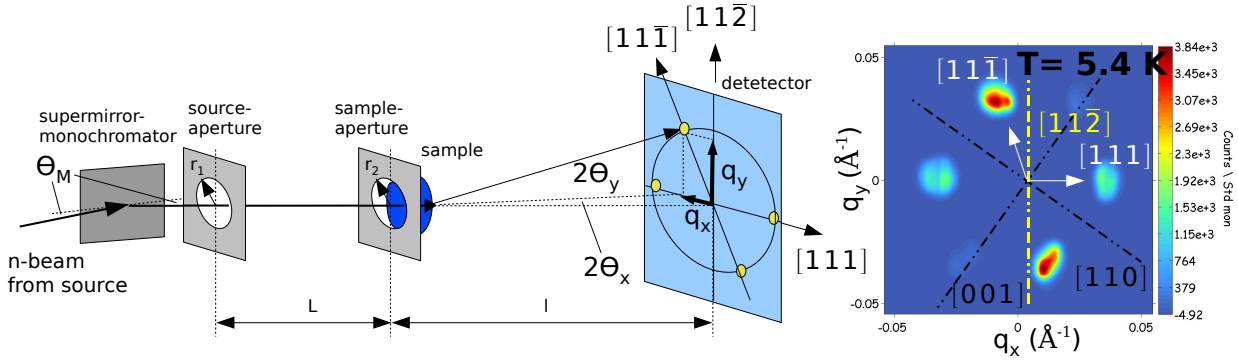

Figure A.5: (a) A schematic layout of small angle neutron scattering (SANS) setup is demonstrated. The instrumental resolution of the instrument can be generally tuned by changing the radii r_1 and r_2 of the source and sample aperture and the sample-detector distance l. The right panel shows a typical image measured by a position-sensitive detector (PSD) in a SANS experiment in one of the experiments on MnSi described in this work. On usual SANS instruments a velocity selector is used as a monochromator; the supermirror monochromator is specific to the instrument MIRA [GBJ+07] used in our experiments.

Appendix B

Useful mathematical relationships concerning the neutron polarisation

In this short paragraph we want to summarise some useful mathematical formula that concern the experiments with polarised neutrons.

B.1 Statistical errors and background

In section 2.4.4 we have defined the experimentally measured polarisation in Eq. 2.82 as

$$P'_z = \frac{I^+ - I^-}{I^+ + I^-}, \tag{B.1}$$

where I^+ and I^- are the intensities for the neutron flipper being switched on or off (neutrons with spins parallel and antiparallel to the quantisation axis). First we want to derive the statistical error of the measured polarisation. Neutron detectors are generally assumed to show Poisson statistics and therefore the error for the neutron count rate is given by $\Delta I = \sqrt{I}$ where I is the number of neutron counts. Therefore it is straightforward to calculate the statistical error of the experimental polarisation by using Gaussian error propagation:

$$\begin{aligned} P'_z &= \sqrt{\left(\Delta I^+ \frac{\partial P'_z}{\partial I^+}\right)^2 + \left(\Delta I^- \frac{\partial P'_z}{\partial I^-}\right)^2} \\ &= 2\sqrt{\frac{I^+ I^-}{(I^+ + I^-)^3}}. \end{aligned} \tag{B.2}$$

If the polarisation is measured on a signal that is contaminated by a strong background signal (e.g. incoherent scattering, that may also be polarised) then it can be helpful to

subtract the background scattering from the signal of interest. The background can be estimated e.g. by measuring the intensities for both polarisation channels on a position in reciprocal space near to the signal of interest.[1] This can be achieved by rotating the sample by 2-3° from the position where the signal was measured. We denote the intensities measured on the background as B^+ and B^- for the flipper being switched on and off, respectively. Additionally, as the background signal and the signal are often not measured with the same monitor we will consider this and will consequently call the corresponding monitor counts with M^+, M^-, M_B^+ and M_B^-, where the B in the subscript indicates the monitor for measurement of the background. The correct expression for the polarisation is then given by

$$P'_z = \frac{\left(\frac{I^+}{M^+} - \frac{B^+}{M_B^+}\right) - \left(\frac{I^-}{M^-} - \frac{B^-}{M_B^-}\right)}{\left(\frac{I^+}{M^+} - \frac{B^+}{M_B^+}\right) + \left(\frac{I^-}{M^-} - \frac{B^-}{M_B^-}\right)}. \tag{B.3}$$

Again we can calculate the statistical error of the polarisation via the Gaussian error propagation where we will denote $\Delta B^{\pm} = \sqrt{(}B^{\pm})$ as the statistical errors of the respective background counts. We will not consider the statistical error of the monitor. The error is then described by:

$$\begin{aligned} P'_z &= \sqrt{\left(\Delta I^+ \frac{\partial P'_z}{\partial I^+}\right)^2 + \left(\Delta B^+ \frac{\partial P'_z}{\partial B^+}\right)^2 + \left(\Delta I^- \frac{\partial P'_z}{\partial I^-}\right)^2 + \left(\Delta B^- \frac{\partial P'_z}{\partial B^-}\right)^2} \\ &= 2\sqrt{\frac{\left(\frac{I^+}{M^{+2}} + \frac{B^+}{M_B^{+2}}\right)\left(\frac{I^-}{M^-} - \frac{B^-}{M_B^-}\right)^2 + \left(\frac{I^+}{M^{+2}} + \frac{B^+}{M_B^{+2}}\right)\left(\frac{I^+}{M^+} - \frac{B^+}{M_B^+}\right)^2}{\left(\frac{I^+}{M^+} - \frac{B^+}{M_B^+}\right) + \left(\frac{I^-}{M^-} - \frac{B^-}{M_B^-}\right)^4}}. \end{aligned} \tag{B.4}$$

B.2 Relationships between the polarisation, flipping ratio and polarisation efficiency

Often the polarisation of the beam is expressed in terms of the so-called *flipping ratio* that is defined as the ratio between the intensities of the neutrons with spins being parallel and antiparallel to the chosen quantisation axis, respectively:

$$R = \frac{I^+}{I^-}. \tag{B.5}$$

It is obvious that the relationship between the value for the experimental polarisation in Eq. B.1 and the the flipping ratio is given via the expression

$$P'_z = \frac{R-1}{R+1}. \tag{B.6}$$

[1] We note that incoherent scattering is generally isotropic.

In addition we have defined the value of the polarisation efficiency P_1 and P_2 for the polariser and polarisation analyser in Eq. 2.84, respectively. As the meaning of this two values is less clear we will review it here. If the polarisation efficiency of a polariser is $P_1 = 0.5$ it signifies that the neutrons that leave the device are not polarised at all, and therefore $I^+ = I^-$. Further if $P_1 = 0.9$ this means that 90% of the neutrons are in the spin up and 10% in the spin down state. This means that from a given polarisation efficiency P_1 we can calculate the flipping ratio as

$$R = \frac{P_1}{1 - P_1}. \tag{B.7}$$

Consequently the experimental polarisation amounts to

$$P'_z = \frac{R-1}{R+1} = \frac{\frac{P_1}{1-P_1} - 1}{\frac{P_1}{1-P_1} + 1} = 2P_1 - 1. \tag{B.8}$$

We emphasise that if this equation for the conversion between P_1 and $|\boldsymbol{P_0}|$ is used, also the Blume-Maleyev-equations (Eqs.2.70, 2.71) can be used to calculate the polarisation tensor for the case that the modulus of the initial polarisation vector $|\boldsymbol{P_0}|$ is reduced from one instead of Eqs. 2.83 and 2.84. However, if also the flipping efficiencies of the flippers are considered Eqs. 2.83 and 2.84 have to be employed.

Appendix C

Final polarisation due to the critical scattering in MnSi

Here we want to derive the results given in Eqs. 5.4 and 5.5 that describe the magnetic quasi-elastic neutron cross-section and final polarisations of neutrons scattered from critical paramagnetic fluctuations above T_c in MnSi as derived in reference [GMO$^+$05]. In section 2.3.6 we already have derived that the inelastic magnetic neutron cross-section can be expressed via the the imaginary part of the magnetic susceptibility $\chi_{\alpha\beta}(\boldsymbol{Q},\omega)$ (s. Eq. 2.53). In reference [Mal02] Maleyev showed that also the Blume-Maleyev equations (s. Eqs.2.70, 2.71) that take into account the polarisation of the neutron beam can be expressed through the magnetic susceptibility. For simplicity we only provide the terms of these equations that contain pure magnetic parts and neglect the nuclear contributions and the nuclear-magnetic interference terms that are non-existent in MnSi.
Maleyev introduces a symmetric and an antisymmetric part of the magnetic susceptibility as follows:

$$\chi_{\alpha\beta}(\boldsymbol{Q},\omega) = \chi^{(S)}_{\alpha\beta}(\boldsymbol{Q},\omega) + \chi^{(A)}_{\alpha\beta}(\boldsymbol{Q},\omega), \tag{C.1}$$

where $\chi^{(S)}_{\alpha\beta}(\boldsymbol{Q},\omega) = \chi^{(S)}_{\beta\alpha}(\boldsymbol{Q},\omega)$ and $\chi^{(A)}_{\alpha\beta}(\boldsymbol{Q},\omega) = -\chi^{(A)}_{\beta\alpha}(\boldsymbol{Q},\omega)$. The antisymmetric part is uniquely related to an axial vector and can thus be written as

$$\chi^{(A)}_{\alpha\beta}(\boldsymbol{Q},\omega) = -i\epsilon_{\alpha\beta\gamma}C_{\gamma}(\boldsymbol{Q},\omega). \tag{C.2}$$

The pure magnetic cross-section that takes into account the incident polarisation vector $\boldsymbol{P}_0$ is then given by

$$\begin{aligned}\frac{d^2\sigma}{d\Omega dE'} &= \frac{(\gamma r_0)^2}{\pi\hbar}\frac{k_f}{k_i}\left(F(\boldsymbol{Q})\right)^2\{n(\omega)+1\} \\ &\times \left[\sum_{\alpha,\beta}(\delta_{\alpha\beta}-\hat{Q}_\alpha\hat{Q}_\beta)Im\left(\chi^{(S)}_{\alpha\beta}(\boldsymbol{Q},\omega)\right) + 2(\boldsymbol{P}_0\cdot\hat{\boldsymbol{Q}})\left(\hat{\boldsymbol{Q}}\cdot Im\left(\boldsymbol{C}(\boldsymbol{Q},\omega)\right)\right)\right],\end{aligned} \tag{C.3}$$

where $n(\omega)$ is the *Bose-Einstein function* (compare Eq. 2.53), $\hat{\boldsymbol{Q}}$ is a unit vector parallel to the scattering vector and $F(\boldsymbol{Q})$ is the magnetic form factor. Further the final polarisation vector is given by

$$\begin{aligned} \boldsymbol{P'}\frac{d^2\sigma}{d\Omega dE'} &= \frac{(\gamma r_0)^2}{\pi\hbar}\frac{k_f}{k_i}\left(F(\boldsymbol{Q})\right)^2\{n(\omega)+1\} \\ &\times \left[2Im\left(\chi_\perp^{(S)}(\boldsymbol{Q},\omega)\right)\cdot\boldsymbol{P}_0 - Im\left(\chi_{\perp\alpha\alpha}^{(S)}(\boldsymbol{Q},\omega)\right)\boldsymbol{P}_0 - 2\hat{\boldsymbol{Q}}\left(\hat{\boldsymbol{Q}}\cdot Im\left(\boldsymbol{C}(\boldsymbol{Q},\omega)\right)\right)\right], \end{aligned} \tag{C.4}$$

where the tensor $\chi_\perp^{(S)}(\boldsymbol{Q},\omega)$ has the components

$$\chi_{\perp\alpha\beta}^{(S)}(\boldsymbol{Q},\omega) = \sum_{\alpha_1,\beta_1}(\delta_{\alpha\alpha_1}-\hat{Q}_\alpha\hat{Q}_{\alpha_1})\chi_{\alpha_1\beta_1}^{(S)}(\delta_{\beta_1\beta}-\hat{Q}_{\beta_1}\hat{Q}_\beta) \tag{C.5}$$

and is always perpendicular to the scattering vector: $\chi_\perp^{(S)}\cdot\hat{\boldsymbol{Q}} = \hat{\boldsymbol{Q}}\cdot\chi_\perp^{(S)} = 0$. This is because due to the magnetic selection rule only components of the magnetisation that are perpendicular to the scattering vector contribute to the magnetic cross-section (compare section 2.3.2).

Starting out from the magnetic susceptibility tensor for the critical magnetic scattering that was derived in reference [GMO+05] and is given in Eq. 5.3 we can now derive the magnetic cross-section and final polarisation vector for the critical scattering in MnSi. By investigating Eq. 5.3 we see that the symmetric part of the susceptibility $\chi_{\alpha\beta}^{(S)}$ and the axial vector $\boldsymbol{C}$ are defined as

$$\chi_{\alpha\beta}^{(S)}(\boldsymbol{q}) = \frac{T}{AZ}\left((q^2+\kappa^2+k^2)\delta_{\alpha\beta} - \frac{(2qk)^2}{q^2+\kappa^2+k^2}\hat{q}_\alpha\hat{q}_\beta\right) \tag{C.6}$$

$$\boldsymbol{C} = 2\frac{T}{AZ}\frac{|D|}{D}k\boldsymbol{q} = -2\frac{T}{AZ}k\boldsymbol{q}, \tag{C.7}$$

where we have taken into account that D is negative, since the helix in MnSi is left-handed[IEM+85]. We note that in the above equations the reduced scattering vector $\boldsymbol{q}$ is used as we are only interested in the scattering around the reciprocal lattice position (0,0,0) (direct beam) in the SANS geometry. $\boldsymbol{Q}$ and $\boldsymbol{q}$ are related via the relationship $\boldsymbol{Q} = \boldsymbol{\tau} + \boldsymbol{q}$ where $\boldsymbol{\tau}$ is a reciprocal lattice vector and for $\boldsymbol{\tau} = (0,0,0)$ we have $\boldsymbol{Q} = \boldsymbol{q}$. Consequently we will replace the scattering vector $\boldsymbol{Q}$ by $\boldsymbol{q}$ for our calculations.

To proceed we need the imaginary parts of $\chi_{\alpha\beta}^{(S)}$ and $\boldsymbol{C}$. According to reference [Mal02] the full expression for the magnetic susceptibility taking into account also the energy dependence is given by multiplying Eq. 5.3 by the expression $\lim_{\delta\to 0^+}(\hbar\omega-\hbar\omega_0+i\delta)^{-1} = P/(\hbar\omega-\hbar\omega_0) - i\hbar\pi\delta(\omega-\omega_0)$, where P is the Cauchy principal value. Therefore the δ-function in energy describes the imaginary part and we have $\omega_0 = 0$ as the expression is for quasi-elastic scattering. Therefore to consider the imaginary part we just multiply Eqs. C.6 and C.7 by $\hbar\pi\delta(\omega)$.

Now we will evaluate the expression $\sum_{\alpha,\beta}(\delta_{\alpha\beta}-\hat{q}_\alpha\hat{q}_\beta)Im\left(\chi_{\alpha\beta}^{(S)}(\boldsymbol{q},\omega)\right)$ and Eq. C.5 before

we write down the full Eqs. C.3 and C.4. To simplify the presentation we will not write the constant factor $\frac{T}{AZ}$ and the δ-function in energy.

$$\begin{aligned}
&\sum_{\alpha,\beta}(\delta_{\alpha\beta}-\hat{q}_\alpha\hat{q}_\beta)Im\left(\chi^{(S)}_{\alpha\beta}(\boldsymbol{q},\omega)\right)\\
=&\sum_{\alpha,\beta}(\delta_{\alpha\beta}-\hat{q}_\alpha\hat{q}_\beta)\left((q^2+\kappa^2+k^2)\delta_{\alpha\beta}-\frac{(2qk)^2}{q^2+\kappa^2+k^2}\hat{q}_\alpha\hat{q}_\beta\right)\\
=&(3-\underbrace{\sum_\alpha\hat{q}^2_\alpha}_{=1})(q^2+\kappa^2+k^2)-\left(\sum_\alpha\hat{q}^2_\alpha(1-\underbrace{\sum_\beta\hat{q}^2_\beta}_{=1})\right)\frac{(2qk)^2}{q^2+\kappa^2+k^2}\\
=&\ 2(q^2+\kappa^2+k^2) \qquad \text{(C.8)}
\end{aligned}$$

Here we used that $\hat{\boldsymbol{q}}$ is a unit vector and consequently $\sum_\alpha\hat{q}^2_\alpha=1$. Further we have for Eq. C.5

$$\begin{aligned}
\chi^{(S)}_{\perp\alpha\beta}(\boldsymbol{q},\omega)=&\sum_{\alpha_1,\beta_1}(\delta_{\alpha\alpha_1}-\hat{q}_\alpha\hat{q}_{\alpha_1})\chi^{(S)}_{\alpha_1\beta_1}(\delta_{\beta_1\beta}-\hat{q}_{\beta_1}\hat{q}_\beta)\\
=&\sum_{\alpha_1,\beta_1}(\delta_{\alpha\alpha_1}-\hat{q}_\alpha\hat{q}_{\alpha_1})\left((q^2+\kappa^2+k^2)\delta_{\alpha_1\beta_1}-\frac{(2qk)^2}{q^2+\kappa^2+k^2}\hat{q}_{\alpha_1}\hat{q}_{\beta_1}\right)(\delta_{\beta_1\beta}-\hat{q}_{\beta_1}\hat{q}_\beta)\\
=&\sum_{\alpha_1}(\delta_{\alpha\alpha_1}-\hat{q}_\alpha\hat{q}_{\alpha_1})\times\\
\times&\left[(q^2+\kappa^2+k^2)(\delta_{\alpha_1\beta}-\hat{q}_\beta\hat{q}_{\alpha_1})-\frac{(2qk)^2}{q^2+\kappa^2+k^2}\left(\hat{q}_{\alpha_1}\hat{q}_\beta-\hat{q}_{\alpha_1}\hat{q}_\beta\sum_{\beta_1}\hat{q}^2_{\beta_1}\right)\right]\\
=&(q^2+\kappa^2+k^2)\left(\delta_{\alpha\beta}-\hat{q}_\beta\hat{q}_\alpha-\hat{q}_\alpha\hat{q}_\beta+\hat{q}_\alpha\hat{q}_\beta\underbrace{\sum_{\alpha_1}\hat{q}^2_{\alpha_1}}_{=1}\right)-\\
-&\frac{(2qk)^2}{q^2+\kappa^2+k^2}\underbrace{\left(\hat{q}_\alpha\hat{q}_\beta-\hat{q}_\alpha\hat{q}_\beta-\hat{q}_\alpha\hat{q}_\beta\sum_{\alpha_1}\hat{q}^2_{\alpha_1}+\hat{q}_\alpha\hat{q}_\beta\sum_{\alpha_1}\hat{q}^2_{\alpha_1}\right)}_{=0}\\
=&(q^2+\kappa^2+k^2)(\delta_{\alpha\beta}-\hat{q}_\beta\hat{q}_\alpha) \qquad \text{(C.9)}
\end{aligned}$$

Inserting the obtained expressions in the Eqs C.3 and C.4 we can write down the polarisation dependent cross-section

$$\frac{d\sigma}{d\Omega}=2\frac{(\gamma r_0F_{Mn}(\boldsymbol{Q}))^2T}{A\left((q+k)^2+\kappa^2\right)}\cdot\frac{k^2+q^2+\kappa^2-2k\boldsymbol{q}\cdot\boldsymbol{P}_0}{(q-k)^2+\kappa^2+(\frac{|B_2|k^2}{2A})(\hat{q}^4_x+\hat{q}^4_y+\hat{q}^4_z-1/3)}, \qquad \text{(C.10)}$$

and the final polarisation vector

$$\boldsymbol{P'} = \frac{\{2(q^2+\kappa^2+k^2)[(\delta_{\alpha\beta}-\hat{q}_\alpha\hat{q}_\beta)-1]\cdot\boldsymbol{P}_0+4k\boldsymbol{q}\}}{2(k^2+q^2+\kappa^2)-4k\boldsymbol{q}\cdot\boldsymbol{P}_0}. \tag{C.11}$$

for the critical scattering in MnSi. We have thus derived the Eqs. 5.4 and 5.5 given in section 5.2.2.

Appendix D

The neutrons python package

The *neutrons* python package is an extension for the python scripting language [vRD01] that was essentially written by the author in order to treat different types of neutron data. The reasons why python was used for this project are:

- Python is distributed freely by the Python Software Foundation (PSF) under a GPL compatible open source license (s. `http://www.python.org/psf/license/`).
- Python is available for many operating systems (Windows, Linux, other *NIXes, Mac OS X, to name a view) and therefore porting of the code to other systems should be possible with minor efforts. The current version of the python package was however only developed for the use with Linux.
- Python has a big standard library that allows to perform many tasks with a standard python distribution. Additionally a huge number of third party packages are available for all kinds of tasks (s. `http://pypi.python.org/pypi/`).
- Python is a scripting language and all extension and packages written for python can be used interactively in the python shell. Hence, it is possible to do fast data analysis by writting scripts that import the neutrons package functionality. In addition development is much faster since the usual compilation cycle can be skipped. Of course a scripting language performs worse in terms of speed when compared to compiled languages as C, C++ or FORTRAN, however with today's modern computers this becomes less and less important and we think that the advantages outweight this minor drawback.
- Python is object-oriented, which allows to model data types as objects and therefore complex tasks can be realised more easily.

The current version of the package that was also used during this thesis is 0.3.9. The package consists of different submodules that are dedicated to distinct tasks. This is illustrated in Fig. D.1.

```
neutrons/
├─data/ ..............Submodules to load data from different instrument data files and to convert
│                      them to internal formats for further treatment.
│ ├─scans.py ........ Classes to save data for further treatment of data (e.g. summing two scans,
│ │                    normalisation, flipping ratio correction,...). There is on class for one
│ │                    dimensional scans and a second one that is able to treat four-dimensional scans
│ │                    (H, K, L, energy) from a triple-axis spectrometer correctly.
│ ├─polardat.py .... Class to save polarisation data from MuPAD for further treatment (e.g. summing
│ │                    two polarisation tensors, normalisation, background correction,...).
│ ├─tasdat.py ...... Importfilters to import data from different triple-axis spectrometers.
│ │                    Currently the data formats of the following instruments are supported: TASP,
│ │                    PANDA, IN14 and TRISP.
│ ├─miradat.py ..... Importfilters to import data from the multi-purpose beamline MIRA including
│ │                    polarisation data.
│ ├─general.py ..... This is the most important submodule for the loading of instrument data. It
│ │                    contains the function load(filename) that loads the data contained in the file
│ │                    filename. The function automatically detects which import filter from the
│ │                    other specialised submodules needs to be used to load the data and returns an
│ │                    error in case the data file format is unknown.
│ └─graspdat.py .... Importfilters to import binned data from the program GRAS$_{ans}$P [Dew03] for the
│                      treatment of SANS data.
├─crystal/ ......... Submodules dedicated to crystallography.
│ ├─atoms.py ........ Class that describes the properties of atoms and magnetic atoms for a crystal
│ │                    structure.
│ ├─magsymmetry.py . Functions to treat magnetic symmetry operations.
│ ├─structure.py ... Class to describe a crystal structure and calculate nuclear and magnetic
│ │                    structure factors.
│ ├─symmetry.py .... Functions to treat symmetry operations in a crystal. Further the symmetry
│ │                    operations associated with a specific space group can be generated from
│ │                    the space group number or name. Not all space groups have been tested for
│ │                    correctness yet.
│ └─unitcell.py .... Class to describe the unitcell of a crystal and perform calculations in real
│                      and reciprocal space.
├─instruments/ ..... Instrument specific submodules.
│ ├─snp/ ............ Submodules for spherical neutron polarimetry.
│ │ ├─mucurrents.py  Contains functions to calculate the currents in the coils of MuPAD.
│ │ └─polar.py ...... Contains functions to calculate the polarisation tensor from given nuclear
│ │                    and magnetic structure factors, and polarising efficiencies of polariser and
│ │                    analyser.
│ └─tas/ ............ Contains submodules for triple-axis spectrometers.
│   └─tasres.py .... Contains functions to calculate the resolution function of a triple-axis
│                      spectrometer. Further a function to perform the four-dimensional convolution
│                      of a given scattering cross-section and the resolution is available.
├─fit/ .............. Contains submodules that are used to perform fits.
│ ├─fit.py .......... Class that wraps the least-squares and simulated annealing fit algorithms from
│ │                    scipy for more a comfortable handling of fit parameters and fits.
│ ├─snpfit.py ...... Functions devoted to the fits of spherical neutron polarimetry data.
│ └─intensfit.py ... Functions devoted to the fit of single crystal diffraction data. They are
│                      still under development.
├─tables/............ Submodules containting different tabulated information.
│ ├─elements.py .... Contains tables with information about all elements such as atomic weight,
│ │                    scattering factors and so on.
│ └─magformfac.py .. Contains tabulated magnetic structure factors for magnetic ions.
└─io/ ............... Submodules that are devoted to input and output functions.
  ├─read.py ......... Functions to read the different input files that contain information for
  │                    different tasks performed by the neutrons package.
  ├─write.py ........ Functions to write information into different output file formats.
  └─format.py ...... Functions to format information before it printed or saved.
```

Figure D.1: The different submodules of the neutrons package and their features.

The package makes extensive use of some other python packages, these are:

- **matplotlib** [Hun07]: All plotting functionality is handled via the functions included in this package. It provides the possibility to do publication-quality image generation. Many of the images and graphs shown in this thesis work have been produced by means of python and matplotlib.
- **scipy/numpy** [JOP+01]: These packages provide powerful object-oriented array and matrix types that are implemented in fast C code. Therefore complex array and matrix calculations can be performed easily and fast. This functionality is mainly used to handle the neutron scattering data (summing of scans, data normalisation and so on).

The submodule *tasres.py* has been developed in collaboration with Florian Bernlochner (s. also reference [Ber06]). This module contains the functions to calculate the resolution function of a triple-axis spectrometer for a given instrument setup and to perform the four-dimensional convolution of the resolution with a provided cross-section. To large extent this submodule has been ported from the octave program of Bertrand Roessli that performs the identical tasks. Parts of the modules for crystallography (s. subfolder *crystal* in Fig. D.1) have been ported from the Crystallographic Fortran Modules Library (CrysFML) written primarily by Juan Rodriguez-Carvajal (`http://www.ill.eu/sites/fullprof/php/programs24b7.html?pagina=Crysfml`).
Based on the functionality that is available in the modules of the neutrons package several programs that have been used to treat parts of the data presented in this thesis have been written. Here we will introduce the two most important ones. The entire neutron package and programs based on it are distributed freely to interested persons. Please mail to marc.janoschek@frm2.tum.de if you are interested.

D.1 spfit

spfit is a program to fit a magnetic structure to spherical neutron polarimetry data. The magnetic structure is defined in a input file. The most important parameters in the file are:

- orientation of the crystal,
- unitcell dimensions and angles,
- atom types, positions, Debye-Waller factors and occupancy,
- magnetic moments defined directly as magnetic moments or Fourier components (s. e.g. chapter 3.),
- magnetic domains.

In Fig. D.2 we show the input file for the 'constant Fe moment model' that gave the best fits of the SNP data in chapter 4. The input was designed to be as similar as possible to the imput file for the program Fullprof [RC06] for the fit of powder diffraction data. This approach makes it easier to fit the SNP data with the same model as for a preceding powder fit. The definition of fit codes works identical to Fullprof. Of course much less options are available for the definition of the structure. The program reads in the input file and then calculates the nuclear and magnetic structure factors via the Eqs. 2.20 and 2.45. The polarisation tensors for given reflections are then determined via Eqs. 2.83 and 2.84. Finally a least-squares fit to refine the model parameters can be performed.

D.2 tasresfit

tasresfit was developed in collaboration with Florian Bernlochner to perform four-dimensional resolution deconvolution fits that are necessary to treat triple-axis spectrometer data (s. also A.3). The program internally uses the approach developed by Popovici [Pop75] to calculate the four dimensional resolution function of a triple-axis spectrometer for a given instrument setup (e.g. collimation, focussing options, sample size and form, monochromator and analyser sizes, ...). To fit the measured data the following steps are performed:

- calculation of the resolution function at EACH data point with the given spectrometer congurations and sample parameters,
- transformation of the resolution function into the appropriate coordinate frame,
- numerical convolution of this resolution function and a provided theoretical cross sections via a monte-carlo integration,
- fitting the convoluted cross section to the provided data sets.

Additionally tasresfit was developed to perform standard tasks without signicant effort. Therefore it allows for direct import of instrumental data files through the import filter framework provided by the neutrons package (currently: TASP, IN14, PANDA and TRISP). The import filter system is powerful and easily extendable and hence new instruments can be added without significant effort. Moreover, the loaded data can be treated further within the program (e.g. correct monitor, flipping ratio, sum and merge scans). This makes it straight forward to start fits to the data immediately. The user interface is command line based. After the acquisition of some simple commands the program can be therefore controlled in an extremely simple and fast way. Additionally this makes it even easy to install the program on a more powerful, external computer and to do the fits over a network connection. Further features are:

- The neutron cross-section to be fitted to the data can be easily loaded into the program.

```
#instrument related stuff
#Flipping Efficiencies of benders/polarizers
PE 0.966 0.966

#zone vector for polarisation frame
zone 1.0 0.0 0.0

#crystal structure input file for neutrons library
#Spacegroup or structure
SPG R 3 2

#nuclear structure
# Label Sym    x         y         z         biso     occ
atom     ND1    ND  0.00000   0.00000   0.00000   0.200    0.16670
                    0.00      0.00      0.00      0.00     0.00
atom     FE1    FE  0.55000   0.00000   0.00000   0.200    0.50000
                    0.00      0.00      0.00      0.00     0.00
atom     B01    B   0.00000   0.00000   0.50000   0.200    0.16667
                    0.00      0.00      0.00      0.00     0.00
atom     B02    B   0.44630   0.00000   0.50000   0.200    0.50000
                    0.00      0.00      0.00      0.00     0.00
atom     O01    O   0.85390   0.00000   0.50000   0.500    0.50000
                    0.00      0.00      0.00      0.00     0.00
atom     O02    O   0.59480   0.00000   0.50000   0.500    0.50000
                    0.00      0.00      0.00      0.00     0.00
atom     O03    O   0.45460   0.14480   0.51740   0.500    1.00000
                    0.00      0.00      0.00      0.00     0.00

#nuclear unitcell
# a b c  alpha  beta  gamma
unit     9.5946  9.5946  7.6037   90.00  90.00   120.00
          0.00    0.00    0.00     0.00   0.00    0.00

#magnetic structure (asumes basic unit cell)

#Domains (if two populations are given chiral domains are assumed)
# SymOp                                          Phase Pop       Code
dom  1       0    0   0       1    0   0 0  1    0.0   0.16667  0.000
dom -0.5  -0.8667 0   0.8667 -0.5  0   0 0  1    0.0   0.16667  0.000
dom -0.5   0.8667 0  -0.8667 -0.5  0   0 0  1    0.0   0.16667  0.000
dom  1       0    0   0      -1    0   0 0 -1    0.0   0.16667  0.000
dom -0.5  -0.8667 0  -0.8667  0.5  0   0 0 -1    0.0   0.16667  0.000
dom -0.5   0.8667 0   0.8667  0.5  0   0 0 -1    0.0   0.16667  0.000

#magnetic symmetry operators
sym x,y,z
msym     u,v,w 0.00
sym -y,x-y,z
msym     u,v,w 0.00
sym -x+y+1,-x+1,z
msym     u,v,w 0.00
sym x+2/3,y+1/3,z+1/3
msym     u,v,w 0.00
sym      -y+2/3,x-y+1/3,z+1/3
msym     u,v,w 0.00
sym      -x+y+1+2/3,-x+1+1/3,z+1/3
msym     u,v,w 0.00
sym      x+1/3,y+2/3,z+2/3
msym     u,v,w 0.00
sym      -y+1/3,x-y+2/3,z+2/3
msym     u,v,w 0.00
sym      -x+y+1+1/3,-x+1+2/3,z+2/3
msym     u,v,w 0.00

#coordinate system (0 = crystal, 1 = spherical)
sys 1
#phi is angle in xy plane and theta angle between moment and z axis
#         Label   FF      x          y          z          biso      occ
#         positional codes
#         knr onr  m r          phir     thetar       mi          phii        thetai       phas
#         magnetic codes
matom     Fe1     MFE3    0.55030    0.00000   0.00000     0.000    1.00000
                            0.00       0.00      0.00       0.00      0.00
      1   1   3.926       0.000     90.000     3.936   90.000     90.000     0.00000
              0.00      0.00       0.00       0.00      0.00       0.00       0.00

matom     Nd1     JND3    0.00000    0.00000   0.00000     0.000    0.33333
                            0.00       0.00      0.00       0.00      0.00
      1   1   0.277       0.000     90.000     0.277   90.000     90.000     0.000000
              0.00      0.00       0.00       0.00      0.00       0.00       61.00

#magnetic unitcell
# a b c  alpha  beta  gamma
munit 9.5946  9.5946  7.6037   90.00  90.00   120.00
       0.00    0.00    0.00     0.00   0.00    0.00

#kvecs (0 = not k and -k are not equivalent, 1 = they are)
#     h     k     l     equiv
kvec  0.0   0.0   1.5   1
```

Figure D.2: The input file for the 'constant Fe moment model' that gave fits of the SNP data in chapter 4 for the program *spfit* is shown .

- Fit parameters for the cross-section can be easily changed or fixed within the program without the need to edit an input file.
- The changes to the cross-section that were conducted within the program can be saved to a cross-section file.
- Simulation of scans taking into account the loaded cross-sections can be performed, e.g. for the preparation of an experiment.
- Most of the resolution parameters (e.g. collimators) can be changed from within the program without the need to edit configuration files.
- The resolution function can be simulated and plotted at single positions in reciprocal space or over a scan.
- A complete program session can be saved to a session file to continue fits and calculations at a later time.
- After successful execution of a command the last state of the session is saved automatically and can be restored whenever needed.
- Successful fits can be saved together with the cross-section and fit parameters in a human-readable ASCII-file to be used in other programs.
- Plots of data and fits can be directly printed on printer connected to the computer.

Fig. D.3 illustrates a typical tasresfit session.

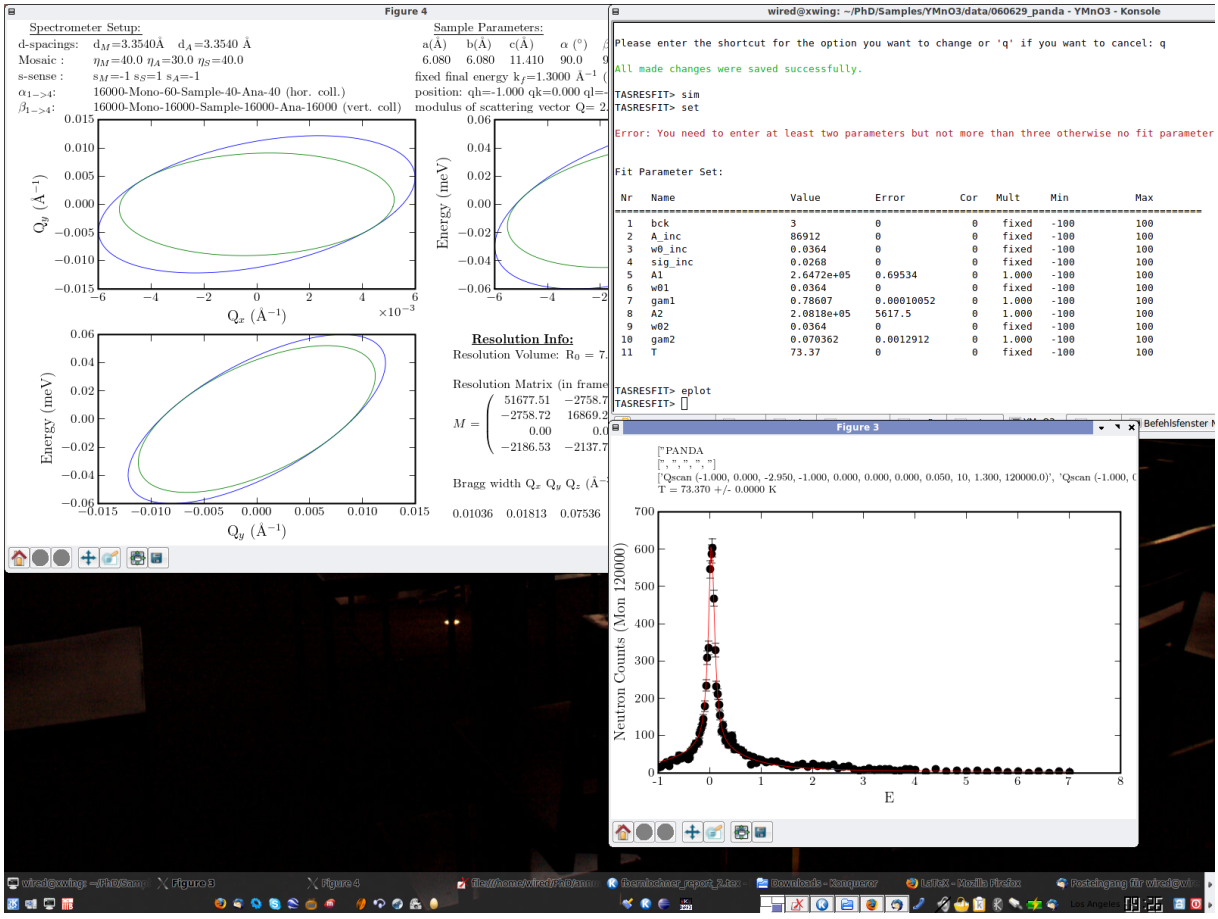

Figure D.3: A typical tasresfit session is shown. The upper left window shows the plot of a resolution function. On the upper right side the main window where the commands can be entered can be seen. The lower right window shows a successful fit to a data set.

Appendix E

Publications

During this work different projects were persued. Here we list the resulting publications:

1. H. Nozaki, J. Sugiyama, M. Janoschek, B. Roessli, V. Pomjakushin, L. Keller, H. Yoshida and Z. Hiroi. Neutron diffraction study of layered Ni dioxides: Ag_2NiO_2, J. Phys.: Condens. Matter 20, 104236 (2008)

2. Y. Bodenthin, U. Staub, M. Garcia-Fernandez, M. Janoschek, J. Schlappa, E. I. Golovenchits, V. A. Sanina, and S. G. Lushnikov. Manipulating the magnetic structure by electric fields in multiferroic $ErMn_2O_5$, Phys. Rev. Lett. 100, 027201 (2008)

3. A. Cervellino,M. Janoschek, L. Keller, V. Pomjakushin, J. Schefer, G. Schuck, D. Sheptyakov, U. Stuhr, O. Zaharko. 10 years of neutron diffraction at the Swiss spallation neutron source SINQ, SGK/SSCr Newsletter No. 73 (2007)

4. H. Nozaki , M. Janoschek, B. Roessli, J. Sugiyama, L. Keller, J. H. Brewer, E. J. Ansaldo, G. D. Morris, T. Takami, and H. Ikuta. Antiferromagnetic spin structure in $BaCoO_3$ below 15 K determined by neutron and muSR, J. Phys. Chem. Sol. 68, 2162-2165 (2007)

5. H. Nozaki , M. Janoschek, B. Roessli, J. Sugiyama, L. Keller, J. H. Brewer, E. J. Ansaldo, G. D. Morris, T. Takami, and H. Ikuta. Neutron diffraction and muSR study on the antiferromagnet $BaCoO_3$, Phys. Rev. B 76, 014402 (2007)

6. T. Lancaster, S. J. Blundell, D. Andreica, M. Janoschek, B. Roessli, S. N. Gvasaliya, K. Conder, E. Pomjakushina, M. L. Brooks, P. J. Baker, D. Prabhakaran, W. Hayes, and F. L. Pratt. Magnetism in geometrically frustrated $YMnO_3$ under hydrostatic pressure studied with muon spin relaxation, Phys. Rev. Lett. 98, 197203 (2007)

7. R. Georgii, P. Böni, M. Janoschek, C. Schanzer and S. Valloppilly. MIRA A flexible instrument for VCN, Physica B: Condensed Matter 397(1), 150-152 (2007)

8. M. Janoschek, S. Klimko, R. Gähler, B. Roessli and P. Böni. Spherical neutron

polarimetry with MuPAD, Physica B: Condensed Matter 397(1), 125-130 (2007)

9. P. Fischer, V. Pomjakushin, D. Sheptyakov, L. Keller, M. Janoschek, B. Roessli, J. Schefer, G. Petrakovskii, L. Bezmaternikh, V. Temerov and D. Velikanov. Simultaneous antiferromagnetic Fe^{3+} and Nd^{3+} ordering in $NdFe_3(^{11}BO_3)_4$, J. Phys.: Condens. Matter 18, 7975-7989 (2006)

10. S. Gvasaliya, L. Keller, M. Kenzelmann, B. Roessli, J. Schefer, K. Conder, E. Pomjakushina, M. Janoschek, B. Harris, S. Jonas, C. Broholm, O. Vajk, Jeff W. Lynn, S. B. Kim, C.L. Zhang and S.-W. Cheong. Low temperature magneto-ferroelectrics, PSI Scientific Report 2005, Vol. I, p. 42-43

11. M. Janoschek, B. Roessli, L. Keller, S.N. Gvasaliya, K. Conder and E. Pomjakushina. Reduction of the ordered magnetic moment in $YMnO_3$ with hydrostatic pressure, J. Phys.: Condens. Matter 17, 425-430 (2005)

Bibliography

[And59] P. W. Anderson. New Approach to the Theory of Superexchange Interactions. *Phys. Rev.*, 115:2, 1959.

[Ast60] D. N. Astrov. The magnetoelectric effect in antiferromagnets. *Sov. Phys. JETP*, 38:984, 1960.

[Bar86] L. D. Barron. Symmetry and Molecular Chirality. *Rev. Chem. SOC.*, 15:189–223, 1986.

[BBG+03] A.D. Balaeva, L.N. Bezmaternykh, I.A. Gudima, V.L. Temerova, S.G. Ovchinnikova, and S.A. Kharlamovaa. Magnetic properties of trigonal $GdFe_3(BO_3)_4$. *J. Magn. Magn. Mater.*, 258259:532534, 2003.

[Ber06] F. Bernlochner. Magnetic Structure and Excitations in the Helimagnet MnSi studied by Neutron Scattering. Master's thesis, Technical Universtiy Munich, 2006.

[BH94] A. Bogdanov and A. Hubert. Thermodynamically stable magnetic vortex states in magnetic crystals. *Jour. Mag. Mag. Mater.*, 138:255–259, 1994.

[BHM+04] E. Bauer, G. Hilscher, H. Michor, Ch. Paul, E.W. Scheidt, A. Gribanov, Yu. Seropegin, H. Noel, M. Sigrist, and P. Rogl. Heavy Fermion Superconductivity and Magnetic Order in Noncentrosymmetric $CePt_3Si$. *Phys. Rev. Lett.*, 92(2):027003, Jan 2004.

[BHvB+07] M. Bode, M. Heide, K. von Bergmann, P. Ferriani, S. Heinze, G. Bihlmayer, A. Kubetzka, O. Pietzsch, S. Blugel, and R. Wiesendanger. Chiral magnetic order at surfaces driven by inversion asymmetry. *Nature*, 447:190, 2007.

[BJ80] P. Bak and M. Høgh Jensen. Theory of helical magnetic structures and phase transitions in $MnSi$ and $FeGe$. *J.Phys C: Solid St. Phys.*, 12:L881–5, 1980.

[BKR06] D. Belitz, T. R. Kirkpatrick, and A. Rosch. Theory of helimagnons in itinerant quantum systems. II. Nonanalytic corrections to Fermi-liquid behavior. *Phys. Rev. B*, 74(2):024409, 2006.

[BKR07] D. Belitz, T. R. Kirkpatrick, and A. Rosch. Theory of helimagnons in itinerant quantum systems. *Phys. Rev. B*, 73:054431, 2007.

[BKT04] L. N. Bezmaternykh, S. A. Kharlamovaand, and V. L. Temerov. Flux Crystallization of Trigonal $GdFe_3(BO_3)_4$ Competing with the Crystallization of α-Fe_2O_3. *Krystallografiya*, 49:855, 2004.

[Blu63] M. Blume. Polarization Effects in the Magnetic Elastic Scattering of Slow Neutrons. *Phys. Rev.*, 130:1670–1676, 1963.

[Blu64] M. Blume. Polarization effects in slow neutron scattering II. - Spin orbit scattering and Interference. *Phys. Rev.*, 133(5A), 1964.

[Blu01] S. Blundell. *Magnetism in Condensed Matter*. Oxford University Press, 2001.

[Boe02] M. Boehm. *Magnetic Structures and Interactions in the Insulating Copper-Oxygen Compound* CuB_2O_4. PhD in Physics, 2002.

[Bön00] P. Böni. Novel concepts in neutron instrumentation. *Physica B*, 6:1, 2000.

[Boy92] R. Boyd. *Non Linear Optics*. Academic Press, New York, USA, 1992.

[BR01] A. N. Bogdanov and U. K. Rößler. Chiral Symmetry Breaking in Magnetic Thin Films and Multilayers. *Phys. Rev. Lett.*, 87(3):037203, Jun 2001.

[Bro01] P. J. Brown. Polarised neutrons and complex antiferromagnets: an overview. *Physica B*, 297:198–203, 2001.

[Bro04] P.J. Brown. *International Tables for Crystallography, Volume C*, chapter Magnetic form factors, pages 454–461. Springer, International Union of Crystallography, 2004.

[Bro05] P.J. Brown. *Neutron Scattering From Magnetic Materials*, chapter Spherical Neutron Polarimetry, pages 215–244. Elsevier, 2005.

[Bro06] P. J. Brown. Neutron Polarimetry: II Polarisation Analysis. In *Francesco Ricci School, Neutron Scattering from Magnetic Systems*, 2006.

[BVA06] B. Binz, A. Vishwanath, and V. Aji. Theory of the Helical Spin Crystal: A Candidate for the Partially Ordered State of MnSi. *Phys. Rev. Lett.*, 96(20):207202, 2006.

[CCGP+97] J. A. Campaá, C. Cascales, E. Gutieérrez-Puebla, M. A. Monge, , I. Rasines, and C. Ruíz-Valero. Crystal Structure, Magnetic Order, and Vibrational Behavior in Iron Rare-Earth Borates. *Chem. Mater.*, 9:237–240, 1997.

[CCR] `http://www.frm2.tum.de/dienste/probenumgebung/ausstattung/ccr/index.html`.

[CKP+04] E.P. Chukalina, D.Yu. Kuritsin, M.N. Popova, L.N. Bezmaternykh, S.A. Kharlamova, and V.L. Temerov. Magnetic ordering of $NdFe_3(BO_3)_4$ studied by infrared absorption spectroscopy. *Phys. Lett. A*, 322:239–243, 2004.

[CL95] P. M. Chaikin and T. C. Lubensky. *Principles of Condensed Matter Physics*. Cambridge University Press, 1995.

[CLJ+01] X. Chen, Z. Luo, D. Jaque, J. J. Romero, J. G. Sole, Y. Huang, A. Jiang, and Ch. Tu. Comparison of optical spectra of Nd^{3+} in $NdAl_3(BO_3)_4$(NAB), Nd:$GdAl_3(BO_3)_4$(NGAB) and Nd:$Gd_{0.2}Y_{0.8}Al_3(BO_3)_4$ (NGYAB) crystals. *J. Phys.: Condens. Matt.*, 13:1171, 2001.

[CM07] S.-G. Cheong and M. Mostovoy. Multiferroics: a magnetic twist for ferroelectricity. *Nature*, 6:13, 2007.

[Cot90] F. A. Cotton. *hemical Applications of Group Theory*. John Wiley & Sons; New York, 1990.

[cti] `http://lns00.psi.ch/sinqwiki/Wiki.jsp?page=ClosedCycleRefrigerators`.

[Cur94] P. Curie. Symmétrie dun champ électrique et dun champ magnétique. *J. Physique*, 3:392, 1894.

[Cyw06] B. Cywinski. Lecture notes on polarised neutrons. In *Hercules Course 2006*, 2006.

[DAN67] O. W. Dietrich and J. Als-Nielsen. Neutron Diffraction Study of the Magnetic Long-Range Order in Tb. *Phys. Rev.*, 162(2):315–320, Oct 1967.

[Dar67] M. I. Darby. Tables of the Brillouin function and of the related function for the spontaneous magnetization. *Br. J. Appl. Phys.*, 18(10):1415–1417, 1967.

[DD90] S. Datta and B. Das. Electronic analog of the electro-optic modulator. *Appl. Phys. Lett.*, 56:665, 1990.

[Deb13] P. Debye. Interferenz von Röntgenstrahlen und Wärmebewegung. *Ann. d. Phys.*, 348:49, 1913.

[Dew03] C. Dewhurst. `http://www.ill.eu/sites/grasp/download.html`. *GRASansP Manual*, 2003.

[DLWT+] N. Doiron-Leyraud, I. R. Walker, L. Taillefer, M. J. Steiner, S. R. Julian, and G. G. Lonzarich. Fermi-liquid breakdown in the paramagnetic phase of a pure metal. *Nature*, 425:595–599.

[Dow06] E. Dowty. Program ATOMS. *Shape Software*, 2006.

[Dzy58] I. E. Dzyaloshinskii. A Thermodynamic theory of weak ferromagnetism of Antiferromagnets. *J. Phys. Chem Solids*, 4:241, 1958.

[Dzy59] I. E. Dzyaloshinskii. On the magneto-electral effect in antferromagnets. *Sov. Phys. JETP*, 10:628, 1959.

[Dzy64] I. E. Dzyaloshinskii. Theory of helicoidal structures in Antiferromagnets .I. Nonmetals. *Sov. Phys. JETP*, 19:960, 1964.

[FAKS04] P. A. Frigeri, D. F. Agterberg, A. Koga, and M. Sigrist. Superconductivity without Inversion Symmetry: MnSi versus $CePt_3Si$. *Phys. Rev. Lett.*, 92(9):097001, Mar 2004.

[Fan57] U. Fano. Description of States in Quantum Mechanics by Density Matrix and Operator Techniques. *Rev. Mod. Phys.*, 29(74-93), 1957.

[FFK+00] P. Fischer, G. Frey, M. Koch, M. Könnecke, V. Pomjakushin, J. Schefer, R. Thut, N. Schlumpf, R. Bürge, U. Greuter, S. Bondt, and E. Berruyer. High-resolution powder diffractometer HRPT for thermal neutrons at SINQ. *Neutron News*, 276-278:146–147, 2000.

[Fie05] M. Fiebig. Revival of the magnetoelectric effect. *J. Phys D: Appl: Phys.*, 38(8):R123–R152, 2005.

[FKSK00] P. Fischer, L. Keller, J. Schefer, and J. Kohlbrecher. Neutron Diffraction at SINQ. *Neutron News*, 11:19–21, 2000.

[FL06] Eric Francotte and Wolfgang Lindner. *Chirality in drug research.* KGaA, Weinheim, DE : Wiley-VCH, 2006.

[FPS+06] P. Fischer, V. Pomjakushin, D. Sheptyakov, L. Keller, M. Janoschek, B. Roessli, J. Schefer, G. Petrakovskii, L. Bezmaternikh, V. Temerov, and D. Velikanov. Simultaneous antiferromagnetic Fe3+ and Nd3+ ordering in NdFe3(11BO3)4. *J. Phys.: Condens. Matter*, 18(34):7975–7989, 2006.

[FSR08] Inga Fischer, Nayana Shah, and Achim Rosch. Crystalline phases in chiral ferromagnets: Destabilization of helical order. *Phys. Rev. B*, 77(2):024415, 2008.

[GBJ+07] R. Georgii, P. Böni, M. Janoschek, C. Schanzer, and S. Valloppilly. MIRA–A flexible instrument for VCN. *Physica B*, 397:150–152, 2007.

[GBL+04] R. Georgii, P. Böni, D. Lamago, S. Stüber, S. V. Grigoriev, S. V. Maleyev, A. I. Okorokov, H. Eckerlebe, P. K. Pranzas, B. Roessli, and W. E. Fischer. Critical small-angle scattering of polarised neutrons in MnSi. *Physica B*, 350:45–47, 2004.

[GFJK+04] F. Groeschel, C. Fazio, Ch. Perret J. Knebel, A. Janett, G. Laffont andL. Cachon, Th. Kirchner, A. Cadiou, A. Guertin, and P. Agostini. The MEGAPIE

1 MW target in support to ADS development: status of R&D and design. *J. Nucl. Mater.*, 335:156–162, 2004.

[GMO+05] S. V. Grigoriev, S. V. Maleyev, A. I. Okorokov, Yu. O. Chetverikov, R. Georgii, P. Böni, D. Lamago, H. Eckerlebe, and K. Pranzas. Critical fluctuations in MnSi near T_C: A polarized neutron scattering study. *Phys. Rev. B*, 72(13):134420, 2005.

[GMO+06a] S. V. Grigoriev, S. V. Maleyev, A. I. Okorokov, Yu. O. Chetverikov, P. Böni, R. Georgii, D. Lamago, H. Eckerlebe, and K. Pranzas. Magnetic structure of MnSi under an applied field probed by polarized small-angle neutron scattering. *Phys. Rev. B*, 74(21):214414, 2006.

[GMO+06b] S. V. Grigoriev, S. V. Maleyev, A. I. Okorokov, Yu. O. Chetverikov, and H. Eckerlebe. Field-induced reorientation of the spin helix in MnSi near T_c. *Phys. Rev. B*, 73(22):224440, 2006.

[GMO+07] S. Grigoriev, S.V. Maleyev, A.I. Okorokov, Yu.O. Chetverikov, and H. Eckerlebe. Field-induced reorientation of helix in MnSi near T_c. *J. Magn. Magn. Mater.*, 310:1599–1601, 2007.

[Güt32] P. Güttinger. Das Verhalten von Atomen im magnetischen Drehfeld. *Z.Phys.*, 73:169–184, 1932.

[Hah06] T. Hahn, editor. *International Tables for Crystallography, Volume A*. Springer, International Union of Crystallography, 2006.

[HBBB06] M. Heide, G. Bihlmayer, Ph. Mavropoulosand A. Bringer, and S. Blügel. Spin Orbit Driven Physics at Surfaces. *psi-k newsletter*, (78):111, 2006.

[HCC+02] M. Huang, Y. Chen, X. Chen, Y. Huang, and Z. Luo. A CW blue laser emission by self-sum-frequency-mixing in Nd^{3+} : $GdAl_3(BO_3)_4$ crystal. *Opt. Commun.*, 208:163, 2002.

[HDI+03] Y. Hinatsu, Y. Doi, K. Ito, M. Wakeshima, and A. Alemi. Magnetic and calorimetric studies on rare-earth iron borates $LnFe_3(BO_3)_4$ (Ln=Y, La-Nd, Sm-Ho). *J. Solid State Chem.*, 172:438, 2003.

[Hei28] W. Heisenberg. Zur Theorie des Ferromagnetismus. *Z. f. Physik*, 49:28, 1928.

[Hil00] N. A. Hill. Why Are There so Few Magnetic Ferroelectrics. *J. Phys. Chem. B*, 104:6694, 2000.

[HPS+04a] N. Hur, S. Park, P. A. Sharma, J. S. Ahn, S. Guha, and S-W Cheong. Electric polarization reversal and memory in a multiferroic material induced by magnetic fields. *Nature*, 429(6990):392–395, 2004.

[HPS+04b] N. Hur, S. Park, P. A. Sharma, S. Guha, and S-W Cheong. Colossal Magnetodielectric Effects in DyMn[sub 2]O[sub 5]. *Phys Rev Lett*, 93(10):107207–4, 2004.

[Hun07] J.D. Hunter. Matplotlib: A 2D Graphics Environment. *Computing in Science & Engineering*, 9(3):90–95, May-June 2007.

[IA84] Y. Ishikawa and M. Arai. Magnetic Phase Diagram of MnSi near Critical Temperature Studied by Neutron Small Angle Scattering. *J. Phys. Soc. Jpn.*, 53:2726–2733, 1984.

[icvcvIT01] M. Žukovič, T. Idogaki, and K. Takeda. Chiral universality class behavior of a nonchiral antiferroquadrupole system. *Phys. Rev. B*, 63(17):172412, Apr 2001.

[IEM+85] M. Ishida, Y. Endoh, S. Mitsuda, Y. Ishikawa, and M. Tanaka. Crystal Chirality and Helicity of the Helical Spin Density Wave in MnSi. II. Polarized Neutron Diffraction. *J. Phys. Soc. Jpn.*, 54:2975–2982, 1985.

[IL83] Yu. A. Izyumov and V. M. Laptev. Neutron diffraction by incommensurate magnetic strcutures. *Sov. Phys. JETP*, 58:1267–1274, 1983.

[IM62] Yu. A. Izyumov and S.V. Maleyev. *Sov. Phys. JETP*, 14:1668, 1962.

[IN79] Yu. A. Izyumov and V. E. Naish. Symmetry analysis in neutron diffraction studies of magnetic structures 1. A phase transition concept to describe magnetic structures in crystals. *J. Magn. Magn. Mater.*, 12:239–248, 1979.

[INFS82] Y. Ishikawa, Y. Noda, C. Fincher, and G. Shirane. Low-energy paramagnetic spin fluctuations in the weak itinerant ferromagnet MnSi. *Phys. Rev. B*, 25(1):254–263, Jan 1982.

[INO91] Y. A. Izyumov, V. E. Naish, and R. P. Ozerov. *Neutron Diffraction of Magnetic Materials*. Plenum Publishing Corporation, New York, 1991.

[INU+85] Y. Ishikawa, Y. Noda, Y. J. Uemura, C. F. Majkrzak, and G. Shirane. Paramagnetic spin fluctuations in the weak itinerant-electron ferromagnet MnSi. *Phys. Rev. B*, 31(9):5884–5893, May 1985.

[ISTK77] Y. Ishikawa, G. Shirane, J. A. Tarvin, and M. Koghi. Magnetic excitations in the weak intinerant ferromagnet MnSi. *Phys. Rev. B*, 16:4956–4870, 1977.

[ITBR76] Y. Ishikawa, K. Tajima, D. Bloch, and M. Roth. Helical spin structure in manganese silicide MnSi. *Solid State Commun.*, 19:525, 1976.

[Izy63] Yu. A. Izyumov. *Sov. Phys. Usp*, 16:359, 1963.

[Izy84] Y. A. Izyumov. Modulated, or long-periodic, magnetic structures of crystals. *Usp. Fiz. Nauk*, 144:439–474, 1984.

[Jan04] M. Janoschek. MuPAD - 3D Polarization Analysis in magnetic Neutron Scattering. Master's thesis, Technical Universtiy Munich, `http://mupad.wired-things.de`, 2004.

[Jaq01] D. Jaque. Self-frequency-sum mixing in Nd doped nonlinear crystals for laser generation in the three fundamental colours: The NYAB case. *J. Alloys Compd.*, 323:204, 2001.

[Jen96] J. Jensen. Theory of commensurable magnetic structures in holmium. *Phys. Rev. B*, 54(6):4021–4032, Aug 1996.

[JKR+07] M. Janoschek, S. Klimko, B. Roessli, R. Gähler, and P. Böni. Spherical neutron polarimetry with MuPAD. *Physica B*, 397:125–130, 2007.

[JM91] J. Jensen and A.R. Mackintosh. *Rare Earth Magnetism: Structure and Excitations*. Clarendon Press, Oxford, 1991.

[JOP+01] E. Jones, T. Oliphant, P. Peterson, et al. SciPy: Open source scientific tools for Python, 2001.

[Kam81] A. A. Kaminskii. *Laser Crystals*. Springer Verlag, Berlin, Germany, 1981.

[Kam96] A. A. Kaminskii. *Crystalline Lasers: Physical Processes and Operating Schemes*. CRC Press, Boca Raton, FL 33487, USA, 1996.

[Kap59] T. A. Kaplan. Classical Spin-Configuration Stability in the Presence of Competing Exchange Forces. *PR*, 116:888, 1959.

[Kas56] T. Kasuya. A Theory of Metallic Ferro- and Antiferromagnetism on Zener's Model. *Prog. Theor. Phys.*, 16:45, 1956.

[KAS05] R. P. Kaur, D. F. Agterberg, and M. Sigrist. Helical Vortex Phase in the Noncentrosymmetric $CePt_3Si$. *Phys. Rev. Lett.*, 94(13):137002, 2005.

[Kaw85] H. Kawamura. Phase Transition of the Three-Dimensional Heisenberg Antiferromagnet on the Layered-Triangular Lattice. *J. Phys. Soc. Japan*, 54:3220, 1985.

[Kaw86] H. Kawamura. Phase Transition of the Three-Dimensional XY Antiferromagnet on the Layered-Triangular Lattice. *J. Phys. Soc. Japan*, 55:2095, 1986.

[Kaw87] H. Kawamura. New Critical Behavior I-Heisenberg Antiferromagnet on the Layered-Triangular Lattice. *J. Phys. Soc. Japan*, 56:474, 1987.

[Kaw98] H. Kawamura. Univerality of phase transitions of frustrated antiferromagnets. *J. Phys.: Condens. Matter*, 10:4707, 1998.

[KCWC63] W. C. Koehler, H. R. Child, E. O. Wollan, and J. W. Cable. Some Magnetic Structure Properties of Terbium and of Terbium-Yttrium Alloys. *Journal of Applied Physics*, 34(4):1335–1336, 1963.

[KCWW66] W. C. Koehler, J. W. Cable, M. K. Wilkinson, and E. O. Wollan. Magnetic Structures of Holmium. I. The Virgin State. *Phys. Rev.*, 151(2):414–424, Nov 1966.

[Kel04] Lord Kelvin. *Baltimore Lectures*. Clay, London, 1904.

[KFM+05] S.A. Klimin, D. Fausti, A. Meetsma, L.N. Bezmaternykh, P. H. M. van Loosdrecht, and T. T. M. Palstra. . *cond-mat*, (0502423), 2005.

[KGS+03] T. Kimura, T. Goto, H. Shintani, K. Ishizaka, T. Arima, and Y. Tokura. Magnetic control of ferroelectric polarization. *Nature*, 426(6962):55–58, 2003.

[KHJ+05] M. Kenzelmann, A. B. Harris, S. Jonas, C. Broholm, J. Schefer, S. B. Kim, C. L. Zhang, S.-W. Cheong, O. P. Vajk, and J. W. Lynn. Magnetic Inversion Symmetry Breaking and Ferroelectricity in $TbMnO_3$. *Phys. Rev. Lett.*, 95(8):087206, 2005.

[Kho06] D.I. Khomskii. Multiferroics: Different ways to combine magnetism and ferroelectricity. *Jour. Magn. Magn. Mat.*, 306:1, 2006.

[Kim07] T. Kimura. Spiral Magnets as Magnetoelectrics. *Annu. Rev. Mater. Res.*, 37:387, 2007.

[Kit54] M. A Ruderman C. Kittel. Indirect Exchange Coupling of Nuclear Magnetic Moments by Conduction Electrons. *Phys. Rev.*, 96(1):99, Oct 1954.

[KNB05] H. Katsura, N. Nagaosa, and A. V. Balatsky. Spin Current and Magnetoelectric Effect in Noncollinear Magnets. *Phys. Rev. Lett.*, 95(057205), 2005.

[Koe65] W. C. Koehler. Magnetic Properties of Rare-Earth Metals and Alloys. *Journal of Applied Physics*, 36(3):1078–1087, 1965.

[Kov65] O. V. Kovalev. *Representations of the Crystallographic Space Groups*. Gordon and Breach, New York, 1965.

[Lam06] D. Lamago. *Critical Magnetic Fluctuations in Localized and Itinerant Magnets studied by Neutron Scattering*. PhD in Physics, Technische Unitversität München, 2006.

[LGB05] D. Lamago, R. Georgii, and P. Böni. Magnetic susceptibility and specific heat of the itinerant ferromagnet MnSi. *Physica B*, 359-361:1171, 2005.

[LHK+05] G. Lawes, A. B. Harris, T. Kimura, N. Rogado, R. J. Cava, A. Aharony, O. Entin-Wohlman, T. Yildirim, M. Kenzelmann, C. Broholm, and A. P.

Ramirez. Magnetically Driven Ferroelectric Order in $Ni_3V_2O_8$. *Phys. Rev. Lett.*, 95(8):087205, 2005.

[LLS72] L. M. Levinson, G. H. Lander, and M. O. Steinitz. Anomalous Magnetic Behavior of MnSi. *AIP Conf. Proc.*, 10:1138, 1972.

[Lov84] S. W. Lovesey. *Theory of Neutron Scattering from Condensed Matter Vol I/II.* Oxford Science Publications, 1984.

[LT85] G. G. Lonzarich and L. Taillefer. Effect of spin fluctuations on the magnetic equation of state of ferromagnetic or nearly ferromagnetic metals. *J. Phys. C: Solid State Phys.*, 18:4339, 1985.

[Mal99] S. V. Malayev. Nuclear-magnetic interference in the inelastic scattering of the polarized neutrons. *Physica B*, 267-268:236–242, 1999.

[Mal02] S. V. Maleyev. Polarized neutron scattering in magnets. *Physics-Uspekhi*, 45:569–596, 2002.

[Mal06] S. V. Maleyev. Cubic magnets with Dzyaloshinskii-Moriya interaction at low temperature. *Phys. Rev. B*, 73(17):174402, 2006.

[Mal07] S. V. Maleyev. private communication, 2007.

[MB58] B. T. Matthias and R. M. Bozorth. Ferromagnetism of a Zirconium-Zinc Compound. *Phys. Rev.*, 109(2):604–605, Jan 1958.

[MCW+61] B. T. Matthias, A. M. Clogston, H. J. Williams, E. Corenzwit, and R. C. Sherwood. Ferromagnetism in Solid Solutions of Scandium and Indium. *Phys. Rev. Lett.*, 7(1):7–9, Jul 1961.

[Mez93] F. Mezei. *Neutron and Synchrotron Radiation for Condensed Matter Studies, Volume I*, chapter Polarized Neutrons, pages 454–461. Springer-Verlag & EDP Sciences, 1993.

[Mor60] T. Moriya. Anisotropic superexchange interaction and weak ferromagnetism. *Phys. Rev.*, 120:91, 1960.

[Mor85] T. Moriya. *Spin Fluctuations in itinerant electron magnetism.* Springer, 1985.

[Mos06] M. Mostovoy. Ferroelectricity in Spiral Magnets. *Phys. Rev. Lett.*, 96(6):067601, 2006.

[MRK69] R. M. Moon, T. Riste, and W.C. Koehler. Polarization analysis of thermal neutron scattering. *Phys. Rev.*, 181(920), 1969.

[nob57] `http://nobelprize.org/nobel_prizes/physics/laureates/1957/`, 1957.

[nob01] http://nobelprize.org/nobel_prizes/chemistry/laureates/2001/public.html, 2001.

[ora] http://lns00.psi.ch/sinqwiki/Wiki.jsp?page=HeCryostats.

[PBK+07] C. Pfleiderer, P. Böni, T. Keller, U. K. Rößler, and A. Rosch. NonFermi Liquid Metal Without Quantum Criticality. *Science*, 2871:8330–8338, 2007.

[PCS+07] M. N. Popova, E. P. Chukalina, T. N. Stanislavchuk, B. Z. Malkin, A. R. Zakirov, E. A. Popova, L. N. Bezmaternykh, and V. L. Temerov. Optical spectra, crystal-field parameters, and magnetic susceptibility of the new multiferroic $NdFe_3(BO_3)_4$. *Phys. Rev. B*, 75(224435), 2007.

[Pfl06] C. Pfleiderer. private communication, 2006.

[PJL01] C. Pfleiderer, S. R. Julian, and G. G. Lonzarich. *Nature*, 414:427, 2001.

[PMJL97] C. Pfleiderer, G. J. McMullan, S. R. Julian, and G. G. Lonzarich. Magnetic quantum phase transition in MnSi under hydrostatic pressure. *Phys. Rev. B*, 55:8330–8338, 1997.

[PMK+99] V. P. Plakhty, S. V. Maleyev, J. Kulda, J. Wosnitza, D. Visser, and E. Moskvin. Inelastic polarised neutron scattering in the triangular-lattice antiferromagnet $CsMnBr_3$: An experimental proof of the chiral universality. *Europhys. Lett.*, 48:215–220, 1999.

[Pop75] M. Popovici. On the Resolution of Slow-Neutron Spectrometers. IV. The Triple-Axis Spectrometer Resolution Function, Spatial Effects Included. *Acta. Cryst. A*, 31:507, 1975.

[PPBB04] A. I. Pankrats, G. A. Petrakovskii, L. N. Bezmaternykh, and O. A. Bayukov. Antiferromagnetic Resonance and Phase Diagrams of Gadolinium Ferroborate $GdFe_3(BO_3)_4$. *J. Exp. Theo. Phys.*, 99:766775, 2004.

[PPM90] J. S. Pedersen, D. Posselt, and K. Mortensen. Analytical Treatment of the Resolution Function for Small-Angle Scattering. *J. Appl. Cryst.*, 23:321, 1990.

[PRP+04] C. Pfleiderer, D. Reznik, L. Pintschovius, H. v. Lohneysen, M. Garst, and A. Rosch. *Nature*, 427:227, 2004.

[PRPH07] C. Pfleiderer, D. Reznik, L. Pintschovius, and J. Haug. Magnetic Field and Pressure Dependence of Small Angle Neutron Scattering in MnSi. *Phys. Rev. Lett.*, 99(15):156406, 2007.

[Ras60] E. I. Rashba. Properties of semiconductors with an extremum loop. *Sov. Phys. Solid State*, 2:1109, 1960.

[RBFE02] B. Roessli, P. Böni, W.E. Fischer, and Y. Endoh. Chiral Fluctuations in MnSi above the Curie Temperature. *Phys. Rev. Lett.*, 88(23), 2002.

[RBP06] U. K. Rößler, A. N. Bogdanov, and C. Pfleiderer. *Nature*, 442:797–801, 2006.

[RBV+07] C. Ritter, A. Balaev, A. Vorotynov, G. Petrakovskii, D. Velikanov, V. Temerov, and I. Gudim. Magnetic structure, magnetic interactions and metamagnetism in terbium iron borate $TbFe_3(BO_3)_4$: a neutron diffraction and magnetization study. *J. Phys.: Condens. Matter*, 19:196227, 2007.

[RC06] J. Rodriguez-Carvajal. Recent Advances in Magnetic Structure Determination by Neutron Powder Diffraction. *Physica B*, 192:55, 2006.

[Roe06] B. Roessli. private communication, 2006.

[Rön88] W. C. Röntgen. Über die durch Bewegung eines im homogen elektrischen Felde befindlichen Dielectrikums hervorgerufene elektrodynamische Kraft. *Ann. Phys.*, 35:264, 1888.

[Ros08] A. Rosch. private communication, 2008.

[RSP+01] B. Roessli, J. Schefer, G. A. Petrakovskii, B. Ouladdiaf, M. Boehm, U. Staub, A. Vorotinov, , and L. Bezmaternikh. Formation of a Magnetic Soliton Lattice in Copper Metaborate. *Phys. Rev. Lett.*, 86:1885, 2001.

[SB68] R. I. Schermer and M. Blume. Polarization Effects in Slow-Neutron Scattering. III. Nuclear Polarization. *Phys. Rev.*, 166:554, 1968.

[SBE+99] F. Semadeni, P. Böni, Y. Endoh, B. Roessli, and G. Shirane. Direct observation of spin-flip excitations in MnSi. *Physica B*, 267-268:248, 1999.

[SBP04] W. Sikora, F. Bialas, and L. Pytlik. MODY: a program for calculation of symmetry-adapted functions for ordered structures in crystals. *J. Appl. Cryst.*, 37:1015–1019, 2004.

[Sch94] H. Schmid. Multiferroics: Different ways to combine magnetism and ferroelectricity. *Ferroelectrics*, 162:19, 1994.

[Sch97] F. Schwabl. *Quantenmechanik für Fortgeschrittene*. Springer Verlag, 1997.

[Sch99] A. J. Schofield. Non-Fermi liquids. *Cont. Phys.*, 40:95–112, 1999.

[SCM+83] G. Shirane, R. Cowley, C. Majkrzak, J.B. Sokoloff, B. Pagonis, C. H. Perry, and Y. Ishikawa. Spiral magnetic correlation in cubic MnSi. *Physical Review B*, 28(11), 1983.

[SD06] I. A. Sergienko and E. Dagotto. Role of the Dzyaloshinskii-Moriya interaction in multiferroic perovskites. *Phys. Rev. B*, 73(9):094434, 2006.

[SDD98] R. Saito, G. Dresselhaus, and M. S. Dresselhaus. *Physical Properties of Carbon Nanotubes*. Imperial College Press, London, 1998.

[SKM+00] J. Schefer, M. Könnecke, A. Murasik, A. Czopnik, Th. Strässle, P. Keller, and N. Schlumpf. Single-crystal diffraction instrument TriCS at SINQ. *Neutron News*, 276-278:168–169, 2000.

[Squ78] G. L. Squires. *Introduction to the theory of thermal neutron scattering.* Dover Publications, 1978.

[SRB01] F. Semadeni, B. Roessli, and P. Böni. Three-axis Spectroscopy with Remanent Benders. *Physica B*, 297:152, 2001.

[Sto38] E. C. Stoner. Collective Electron Ferromagnetism. *Proc. Roy. Soc. A*, 165(922):372–414, 1938.

[Tas89] F. Tasset. Zero field neutron polarimetry. *Physica B*, 156-157:627, 1989.

[TAT+06] K. Taniguchi, N. Abe, T. Takenobu, Y. Iwasa, and T. Arima. Ferroelectric Polarization Flop in a Frustrated Magnet $MnWO_4$ Induced by a Magnetic Field. *Phys. Rev. Lett.*, 97(9):097203, 2006.

[TBE+98] S. Tixier, P. Böoni, Y. Endoh, B. Roessli, and G. Shirane. Polarisation dependence of the magnetic fluctuations in the weak itinerant ferromagnet MnSi below T_C. *Physica B*, 241-243:613, 1998.

[TBK06] S. Tewari, D. Belitz, and T. R. Kirkpatrick. Blue Quantum Fog: Chiral Condensation in Quantum Helimagnets. *Phys. Rev. Lett.*, 96(4):047207, 2006.

[TKH+07] N. Tristan, R. Klingeler, C. Hess, B. Buchner, E. Popova, I.A. Gudim, and L.N. Bezmaternykh. Thermodynamic properties of $NdFe_3(BO_3)_4$. *J Magn. and Magn. Mater.*, 316:e621–e623, 2007.

[TPSF97] C. Thessieu, C. Pfleiderer, A. N. Stepanov, and J. Flouquet. Field Dependence of the Magnetic Quantum Phase Transition in MnSi. *Phys. Rev. Lett.*, 9:6677, 1997.

[TR95] F. Tasset and E. Ressouche. Optimum transmission for a ^{3}He neutron polarizer. *Nuclear Instruments and Methods in Physics Research*, A(359):537–541, 1995.

[UGGM+07] Y. J. Uemura, T. Goko, I. M. Gat-Malureanu, J. P. Carlo, P. L. Russo, A. T. Savici, A. Aczel, G. J. Macdougall, J. A. Rodriguez, G. M. Luke, S. R. Dunsiger, A. Mccollam, J. Arai, C. Pfleiderer, P. Böni, K. Yoshimura, E. Baggio-Saitovitch, M. B. Fontes, J. Larrea, Y. V. Sushko, and J. Sereni. Phase separation and suppression of critical dynamics at quantum phase transitions of MnSi and $(Sr_{1x}Ca_x)RuO_3$. *Nature*, 3:29, 2007.

[VDK07] D. V. Volkov, A. A. Demidov, , and N. P. Kolmakova. Magnetic Properties of an Easy-Plane Trigonal $NdFe_3(BO_3)_4$ Antiferromagnet. *JETP*, 104:897–905, 2007.

[Vil59] J. Villain. La structure des substances magnetiques. *J. Phys. Chem. Solids*, 11:303, 1959.

[Vil77] J. Villain. Two-level systems in a spin-glass model: I. General formalism and two-dimensional model. *J. Phys. C: Solid State Phys.*, 9:4793, 1977.

[Vle62] J. H. Van Vleck. Note on the Interactions between the Spins of Magnetic Ions or Nuclei in Metals. *Rev. Mod. Phys.*, 34(4):681–686, Oct 1962.

[VPSB+01] W. V.P. Plakhty, Schweika, Th. Brückel, J. Kulda, S. V. Gavrilov, L.-P. Regnault, and D. Visser. Chiral criticality in helimagnet Ho studied by polarized neutron scattering. *Phys. Rev. B*, 64(10):100402, Aug 2001.

[vRD01] G. van Rossum and F.L. Drake. `http://www.python.org`. *Python Reference Manual, PythonLabs, Virginia, USA*, 2001.

[WA73] V. E. Wood and A. E. Austin. . *Int. J. Magn.*, 5:303, 1973.

[Wal23] I. Waller. Zur Frage der Einwirkung der Wärmebewegung auf die Interferenz von Röntgenstrahlen. *Z. Phys.*, 17:398–408, 1923.

[wik] `http://en.wikipedia.org/wiki/Chirality_chemistry`.

[Wil05] H. A. Wilson. . *Phil. trans. R. Soc. A*, 204:129, 1905.

[Wil83] K. G. Wilson. The renormalization group and critical phenomena. *Rev. Mod. Phys.*, 55(3):583–600, Jul 1983.

[Wil88] W. G. Williams. *Polarized Neutrons*. Clarendon Press, 1988.

[WK74] K. G Wilson and J. Kogut. The renormalization group and the ϵ expansion. *Phys. Reports*, 12:75–199, August 1974.

[WM66] C.-S. Wu and S. A. Moszkowski. *Beta decay*. Interscience Publishers, 1966.

[WM89] D. C. Wright and N. D. Mermin. Crystalline liquids: the blue phases. *Rev. Mod. Phys.*, 61(2):385–432, Apr 1989.

[YLS+06] F. Yen, B. Lorenz, Y. Y. Sun, C. W. Chu, L. N. Bezmaternykh, and A. N. Vasiliev. Magnetic eld effect and dielectric anomalies at the spin reorientation phase transition $GdFe_3(BO_3)_4$. *Phys. Rev. B*, 73(054435), 2006.

[Yos57] K. Yosida. Magnetic Properties of Cu-Mn Alloys. *Phys. Rev.*, 106(5):893–898, Jun 1957.

[Yos59] A. Yoshimori. A New Type of Antiferromagnetic Structure in the Rutile Type Crystal. *J. Phys. Soc. Japan*, 14:807, 1959.

[YSG+07] Y. Yamasaki, H. Sagayama, T. Goto, M. Matsuura, K. Hirota, T. Arima, and Y. Tokura. Electric Control of Spin Helicity in a Magnetic Ferroelectric. *Phys. Rev. Lett.*, 98(147204), 2007.

[ZKK+05] A. K. Zvezdin, S. S. Krotov, A. M. Kadomtseva, G. P. Vorob'ev, Y. F. Popov, A. P. Pyatakov, L. N. Bezmaternykh, and E. A. Popova. Magnetoelectric Effects in Gadolinium Iron Borate $GdFe_3(BO_3)_4$. *JETP Lett.*, 81:335, 2005.

[ZVK+06] A. K. Zvezdin, G. P. Vorob'ev, A. M. Kadomtseva, Yu. F. Popov, A. P. Pyatakova, L. N. Bezmaternykh, A. V. Kuvardin, and E. A. Popova. Magnetoelectric and Magnetoelastic Interactions in $NdFe_3(BO_3)_4$ Multiferroics. *JETP Lett.*, 83:509, 2006.